

Waves in Cylindrical Systems

Theodore J. Mapes
Submarine Sonar Department



19960719 000

Naval Undersea Warfare Center Division
Newport, Rhode Island

PREFACE

This report was prepared as a Ph.D. dissertation for the degree of Doctor of Philosophy in Ocean Engineering awarded by the University of Rhode Island. The major advisor for this work was Professor Peter R. Stepanishen. Associate advisors were Professor James Hu and Professor Stephen V. Letcher. The research was partially sponsored by the Long Term Training Program at NUWC Detachment New London.

The technical reviewer for this report was Professor Peter R. Stepanishen.

The author is deeply grateful to Professor Stepanishen for his patient guidance and advice during the course of the study. His profound knowledge of acoustics and unique ability to make difficult concepts easily understood were essential to the successful completion of this work. Sincerest appreciation is also extended to my good friends Kenneth Webman and Daniel Miller and my wife Elizabeth Phillips for their unwavering encouragement and support.

Reviewed and Approved: 7 June 1996

A handwritten signature in black ink, appearing to read "R. J. Martin". The signature is fluid and cursive, with the first letters of the first and last names being capitalized and prominent.

R. J. Martin
Acting Head, Submarine Sonar Department

REPORT DOCUMENTATION PAGE			Form Approved OMB No. 0704-0188	
<small>Public reporting burden for this collection of information is estimated to average 1 hour per response, including the time for reviewing instructions, searching existing data sources, gathering and maintaining the data needed, and completing and reviewing the collection of information. Send comments regarding this burden estimate or any other aspect of this collection of information, including suggestions for reducing this burden, to Washington Headquarters Services, Directorate for Information Operations and Reports, 1215 Jefferson Davis Highway, Suite 1204, Arlington, VA 22202-4302, and to the Office of Management and Budget, Paperwork Reduction Project (0704-0188), Washington, DC 20503.</small>				
1. AGENCY USE ONLY (Leave Blank)		2. REPORT DATE 7 June 1996		3. REPORT TYPE AND DATES COVERED Ph.D. Thesis
4. TITLE AND SUBTITLE Waves in Cylindrical Systems			5. FUNDING NUMBERS	
6. AUTHOR(S) Theodore J. Mapes				
7. PERFORMING ORGANIZATION NAME(S) AND ADDRESS(ES) Naval Undersea Warfare Center Detachment New London New London, Connecticut 06320			8. PERFORMING ORGANIZATION REPORT NUMBER TR 11,153	
9. SPONSORING/MONITORING AGENCY NAME(S) AND ADDRESS(ES) Long Term Training Program Naval Undersea Warfare Center Detachment New London, CT 06320			10. SPONSORING/MONITORING AGENCY REPORT NUMBER	
11. SUPPLEMENTARY NOTES				
12a. DISTRIBUTION/AVAILABILITY STATEMENT Approved for public release; distribution is unlimited.			12b. DISTRIBUTION CODE	
13. ABSTRACT (Maximum 200 words) <p>This report is a study of the propagation of acoustical waves in contiguous fluid and elastic cylinders. A transfer matrix approach is used to develop models of a fluid cylinder, a fluid tube, the external medium, and thin elastic shells.</p> <p>An analytical and experimental investigation of the dispersion of transient impulses in thin elastic shells is presented using transform techniques and joint time-frequency distributions.</p>				
14. SUBJECT TERMS Acoustic Waves, Cylindrical System, Elastic Cylinder, Fluid Cylinder, Thin Elastic Shell, Wave Propagation			15. NUMBER OF PAGES 240	
			16. PRICE CODE	
17. SECURITY CLASSIFICATION OF REPORT UNCLASSIFIED	18. SECURITY CLASSIFICATION OF THIS PAGE UNCLASSIFIED	19. SECURITY CLASSIFICATION OF ABSTRACT UNCLASSIFIED	20. LIMITATION OF ABSTRACT SAR	

TABLE OF CONTENTS

ACKNOWLEDGMENTS	iii
LIST OF TABLES	vi
LIST OF ILLUSTRATIONS	vii
Chapter	
1 Introduction	1
1.1 Objective	1
1.2 Background	1
1.3 Organization of the Study	2
1.4 Transfer Matrix Approach	4
1.5 Wavevectors	6
1.6 Synthesis of a Cylindrical Wave from Plane Waves	9
2 Fluid Media	12
2.1 Analytical Approach	12
2.2 Fluid Cylinder	17
2.3 Fluid Tube	25
2.4 External Fluid	47
3 Elastic Media	57
3.1 Introduction	57
3.2 Thin Shell Theory	59
3.3 Transfer Matrix Model of a Thin Shell	61
3.4 Analysis of Thin Shell in Wavenumber-Frequency Space	62

3.5	Modes in Harmonically Driven Finite Length Tube	65
3.6	Membrane Transition Frequencies	69
3.7	Transient Response of Thin Shell	71
3.8	Discussion of $w(f,z)$ and $u(f,z)$ Transfer Functions	82
3.10	Joint Time-Frequency Distributions	90
4	Composite Systems	96
4.1	Introduction	96
4.2	Fluid Systems	96
4.3	Fluid Loaded Elastic Shells	108
5	Experimental Work	114
5.1	Introduction	114
5.2	Design of Experiment	114
5.3	Transient Measurements	132
6	Conclusions	136
6.1	Transfer Matrix Method	136
6.2	Elastic Media	137
6.3	Experimental Work	140
	ILLUSTRATIONS	142
	TABLES	211
	BIBLIOGRAPHY	218

LIST OF TABLES

Table		Page
2-1	Roots of Free-Free Characteristic Equation	212
2-2	Roots of Free-Fixed Characteristic Equation	213
2-3	Roots of Fixed-Free Characteristic Equation	214
2-4	Roots of Fixed-Fixed Characteristic Equation	215
4-1	Parameter Matrix for Two-Fluid Problems	98
5-1	Published Data on Brass	216
5-2	Comparison of Measured and Calculated Modal Frequencies	217

LIST OF ILLUSTRATIONS

Figure	Title	Page
1-1	Classification of cylindrical models	143
1-2	General cylindrical system	144
1-3	Transfer matrix for fluid tube	144
1-4	Wavevector domain	145
1-5	Wavevector-frequency space	145
1-6	Wavevector in cylindrical coordinates	146
1-7	Geometry for synthesis of cylindrical wave	146
1-8	Diverging cylindrical wave	147
2-1	Cylindrical coordinate system	147
2-2	Modified quotient of Bessel functions vs. non-dimensional radial wavenumber, K_{ra}	148
2-3	Spectral impedance of fluid cylinder vs K_{ra} , computed for $K_a = 1$	148
2-4	Normalized spectral impedance of fluid cylinder as a function of non-dimensional wavenumber K_a , for $K_z = 0$	149
2-5	Normalized phase and group velocities for a fluid cylinder with free radial boundary	150
2-6	Normalized pressure vs non-dimensional radius for a fluid cylinder with free radial boundary	151
2-7	Normalized phase and group velocities for a fluid cylinder with fixed radial boundary	152
2-8	Normalized pressure vs non-dimensional radius for a fluid cylinder with fixed radial boundary	153

2-9	Fluid tube model	154
2-10	ABCD Parameters as a function of K_{ra} for three values of radii ratio S	155
2-11	Surface plot of parameter A vs S and K_{ra}	156
2-12	Surface plot of parameter B vs S and K_{ra}	156
2-13	Surface plot of parameter C vs S and K_{ra}	157
2-14	Surface plot of parameter D vs S and K_{ra}	157
2-15	Error in the asymptotic expression for the roots of the free-free modes in a fluid tube	158
2-16	Error in the asymptotic expression for the roots of the free-fixed modes in a fluid tube	158
2-17	Error in the asymptotic expression for the roots of the fixed-free modes in a fluid tube	159
2-18	Error in the asymptotic expression for the roots of the fixed-fixed modes in a fluid tube	159
2-19	Characteristic equations for free-free and fixed-fixed modes of a fluid tube for $S = 1.5, 2$, and 3	160
2-20	Characteristic equations for free-fixed and fixed-free modes of a fluid tube for $S = 1.5, 2$, and 3	161
2-21	Pressure and radial velocity vs. non-dimensional radius for the first three free-free modes in a fluid tube	162
2-22	Pressure and radial velocity vs. non-dimensional radius for the first three free-fixed modes in a fluid tube	163
2-23	Pressure and radial velocity vs. non-dimensional radius for the first three fixed-free modes in a fluid tube	164
2-24	Pressure and radial velocity vs. non-dimensional radius for fixed-fixed modes in a fluid tube	165
2-25	Wavevectors and wavefronts in external fluid	166

2-26	Real and imaginary components of normalized specific acoustic impedance of external fluid with $k_z = 0$	167
2-27	Real and imaginary components of normalized specific acoustic impedance of external fluid for four values of axial wavenumber	168
3-1	Branch 1 and Branch 2 frequencies vs wavenumber	169
3-2	Branch 1 and Branch 2 phase velocities vs wavenumber	169
3-3	Branch 1 and Branch 2 group velocities vs wavenumber	170
3-4	Ratio of radial to axial displacements vs wavenumber for branch 1 and branch 2	170
3-5	Variation of Q roots with frequency	171
3-6	Variation of Q roots in transition region	172
3-7	Magnitude of Q roots in transition zone	174
3-8	Magnitude of Q roots near lower transition frequency	174
3-9	Loci of Q and S roots at low and high frequencies	175
3-10	Magnitude of S roots in transition zone	177
3-11	Components of S3 in transition zone as functions of Beta	177
3-12	Contour for inversion of Laplace transform	180
3-13	Magnitude of $W(f,z)$ vs distance and frequency (far field)	181
3-14	Magnitude of $U(f,z)$ vs distance and frequency (far field)	182
3-15	Magnitude of $W(f,z)$ vs distance and frequency (near field)	183
3-16	Magnitude of $U(f,z)$ vs distance and frequency (near field)	184
3-17	Magnitude of $W(f,z)$ vs frequency at fixed distances	185
3-18	Magnitude of $U(f,z)$ vs frequency at fixed distances	186
3-19	Magnitude of $W(f,z)$ vs distance at fixed frequencies (near field)	188

3-20	Magnitude of $U(f,z)$ vs distance at fixed frequencies (near field)	188
3-21	Magnitude of $W(f,z)$ vs distance at fixed frequencies (far field)	189
3-22	Magnitude of $U(f,z)$ vs distance at fixed frequencies (far field)	189
3-23	Weighted transfer function $W(f)$ at $Z = 6$ cm	190
3-24	Weighted transfer function $U(f)$ at $Z = 6$ cm	190
3-25	Radial displacement $W(t)$ at $Z = 6$ cm	191
3-26	Axial displacement $U(t)$ at $Z = 6$ cm	191
3-27	Spectrogram contour plot of $W(t)$ at $Z = 6$ cm	192
3-28	Spectrogram contour plot of $U(t)$ at $Z = 6$ cm	192
3-29	3 D spectrogram contour plot of $W(t)$ at $Z = 6$ cm	193
3-30	3 D spectrogram contour plot of $U(t)$ at $Z = 6$ cm	193
4-1	Normalized spectral impedance of a fluid tube in an external fluid, parametric in radius ratio S	194
4-2	Normalized spectral impedance of a fluid tube in an external fluid, parametric in impedance ratio R_z	195
4-3	Normalized spectral impedance of a fluid tube in an external fluid, parametric in sound speed ratio R_c	196
5-1	Experimental apparatus	197
5-2	Admittance of disk near first radial mode	198
5-3	Admittance of disk vs frequency	198
5-4	Complex admittance locus of PZT disk	199
5-5	Early spectrum at gage C-1	199
5-6	Equivalent electrical circuits for dummy load design	200
5-7	Performance improvement with dummy load	201

5-8	Comparison of measured and computed modal frequencies	202
5-9	Standard deviation of difference between measured and computed modal frequencies	202
5-10	Difference between computed and measured modal frequencies as a percentage of the measured frequency	203
5-11	Radial displacements vs time and distance	204
5-12	Spectra of radial displacements at four distances	205
5-13	Spectrogram contour plot of waveform at gage C-3	206
5-14	Spectrogram contour plot of waveform at gage C-1	206
5-15	Spectrogram contour plot of waveform at gage C-4	207
5-16	Spectrogram contour plot of waveform at gage C-2	207
5-17	3 D Contour plot of spectrogram of waveform at gage C-3	208
5-18	3 D Contour plot of spectrogram of waveform at gage C-1	208
5-19	3 D Contour plot of spectrogram of waveform at gage C-4	209
5-20	3 D Contour plot of spectrogram of waveform at gage C-2	209
5-21	Computed waveform at gage C-1	210
5-22	Spectrogram contour plot of computed waveform at gage C-1	210

CHAPTER 1

Introduction

1.1 Objective

The objective of this study is to investigate the propagation of acoustic waves in contiguous concentric cylinders of solid and fluid media. Wavenumber-frequency and/or transform methods are applied to several configurations of interest to determine the characteristics of acoustic wave propagation as functions of the spatial variables and the properties of the media. In the experimental work, joint time-frequency distribution functions such as the spectrogram are used to study the propagation of transient disturbances in dispersive systems. The study is limited to systems of infinite extent in the axial direction.

1.2 Background

There are many practical situations in which it is desirable to understand the characteristics of the propagation of acoustical energy in physical systems which may be modeled in a cylindrical coordinate system. For example, in noise control problems, the objective is to reduce the transmission of sound from one region into another. Cases of interest include aircraft fuselages and submarine hulls in which turbulent boundary layer noise is generated by the motion of the platform through an external fluid medium. Another case is noise generated by fluid flow in pipes and ducts. Another problem of interest relates to sonar transducers, arrays, and

domes of cylindrical geometry, in which it is desired to enhance the transmission of propagating acoustic waves in the external medium while discriminating against evanescent waves generated by turbulence or structural vibration.

There is an extensive body of literature, including both textbooks and monographs in technical journals, that deals with the problems considered in this dissertation. Specific subjects of interest include the propagation of acoustic waves in ducts, acoustic radiation in an infinite fluid medium, the transmission of acoustical waves in layered media, and the vibration of shells.

In problems which involve fluid-structure interaction, the most complex task is analysis of the motion of the structure. Thus it is customary to first consider the vibration of the structure in vacuo and then to attempt to determine the effects of coupling to the fluid.

1.3 Organization of the Study

The general schema of the models studied in this work is outlined in Figure 1-1. The general category of cylindrical models branches into fluid media and solid media. Under fluid media, models are developed for the fluid cylinder, a fluid tube, and the external fluid medium. The branch comprising elastic media is subdivided to include models which may be represented by thin shell theory, and those for which elasticity theory is required. This latter category includes thick shells, concentric elastic shells, and the external solid medium. Composite system models are constructed by combining the elementary models of system components through the transfer matrix approach.

In this introductory chapter, we describe the transfer matrix method which was suggested by previous work on the propagation of plane waves through layered media. This is followed by a discussion of wavevectors in cylindrical coordinates, and the synthesis of cylindrical waves from plane waves.

Chapter 2 begins with a discussion of the analytical approach followed for the study of fluid media. These methods are applied to the fluid cylinder, the fluid tube, and the external medium. For each of these components, the radial spectral impedance is computed. The dispersion equation is developed and used to study the propagation of free waves. The transfer matrix for each component is determined.

In Chapter 3 we develop the transfer matrix for a thin elastic cylinder, using Donnell's formulation (Donnell 1933; Krauss 1967; Junger and Feit 1986). Dispersion of harmonic waves for the axisymmetric mode is studied in the frequency domain. An analysis of low frequency axisymmetric longitudinal modes of a harmonically driven finite length cylinder is presented. The transient response of a semi-infinite, radially excited elastic cylinder is studied using Laplace and Fourier transforms in the wavenumber and frequency domains.

The models developed in the first three chapters are combined in Chapter 4 to describe several composite systems of interest.

Chapter 5 describes the results of transient measurements on a thin brass cylinder. These results are compared to the predictions made in Chapter 3.

1.4 Transfer Matrix Approach

The transfer matrix approach followed in this study is similar to that employed by previous authors in analyzing the propagation of plane waves in layered media. Thomson (1950) introduced the matrix method to study the transmission of plane elastic waves through any number of parallel plates of solid or fluid material. Shaw and Bugl (1969) employed matrix methods to study harmonic plane waves in viscoelastic media, using complex and frequency dependent Lamé constants to describe the viscoelastic behavior. Folds and Loggins (1977) extended this work to include calculations of the transmission and reflection coefficients. They report experimental work which agrees well with the theory. Stepanishen and Strozski (1982) employed transfer matrix and Fourier transform methods to analyze the response of layered viscoelastic media to a time dependent plane wave excitation.

In this study models are constructed for each component of the concentric cylindrical system. Typical components include, for example, a fluid cylinder, a fluid tube, an elastic shell, and the external medium.

For each component, the governing equations for the field variables in terms of time and spatial coordinates are converted via a two dimensional Fourier transform into a representation in wavevector-frequency space. The transfer function of the component is then formulated in terms of the state variables at the radial interfaces. The resulting matrix model is two by two (two port) for fluid-solid and fluid-fluid interfaces, for which the boundary conditions are continuity of pressure and radial velocity. For contiguous elastic solids in which shear stresses exist, continuity of the

three components of displacement and stress results in a six port transfer matrix.

A system model for any combination of components is constructed by cascading the component transfer matrices to obtain an overall transfer function. Specification of an appropriate spectral excitation function in one region of the system model enables the computation of state and field variables throughout the system. Non-axisymmetric excitations may be represented using a Fourier series expansion in terms of a discrete circumferential wavenumber.

Thus the general problem of interest comprises a number of concentric circular cylinders imbedded in an infinite fluid medium. This system is excited by a pressure or velocity function specified at one of the radial interfaces. Figure 1-2 indicates the coordinates of a general cylindrical system with m components in which the center component is a cylinder of radius a_1 , surrounded by a tube of inner radius a_1 and outer radius a_2 , etc. terminating in the $(m - 1)th$ tube of inner radius a_j and outer radius a_m , which marks the boundary with the external medium. The general cylindrical coordinates are r, θ , and z , representing the radius, azimuthal angle, and cylindrical axis, respectively.

The two-port model for a fluid tube is shown in Figure 1-3. If this is the j th component in the system, with inner radius $a_{(j-1)}$ and outer radius a_j , the state variables of pressure $P_{(j-1)}$ and velocity $V_{(j-1)}$ at the inner radius are related to the pressure P_j and velocity V_j at the outer radius by a transfer matrix $[T_j]$, viz.

$$\begin{bmatrix} P_j \\ V_j \end{bmatrix} \equiv [T_j] \times \begin{bmatrix} P_{(j-1)} \\ V_{(j-1)} \end{bmatrix}$$

The outermost cylinder is surrounded by a fluid presumed to extend to infinity

in the radial and axial directions. Application of the radiation condition that the pressure must decrease to zero at infinity leads to equations for the specific acoustic impedance at the last radial interface at $r = a_m$.

A further requirement is that all concentric layers must exhibit the same pressure dependence in the axial direction as the excitation.

For example, if the excitation is a traveling wave represented by

$$p_n(z, \theta, a_j) = P_e \cos(n\theta) \exp(i(k_z z - \omega t))$$

where k_z is the axial wavenumber of the excitation, ω is the angular frequency, t represents time, and n is the circumferential mode number, then each component of the system must have the same variation with k_z and n . This condition results from the continuity of normal particle velocity and pressure across the interface between contiguous layers.

1.5 Wavevectors

The concept of a wavevector, also known as a vector wavenumber (Elmore & Heald, 1985) is highly useful in describing complex wave phenomena. We define the wavevector \mathbf{k} for a monochromatic wave as a quantity having the magnitude of a wavenumber, $|\mathbf{k}| = \frac{\omega}{c}$ and the direction of a unit vector which is normal to the wavefront, or surfaces of constant phase. For example, a propagating wave of frequency ω may be expressed compactly as

$$p(\mathbf{r}, t) = \text{Re} \left\{ \widetilde{P}_o e^{i(\mathbf{r} \cdot \mathbf{k} - \omega t)} \right\} \quad (1.1)$$

where \widetilde{P}_o represents the complex wave amplitude and \mathbf{r} is the spatial vector. In

rectangular coordinates, $\mathbf{r} = \mathbf{e}_x x + \mathbf{e}_y y + \mathbf{e}_z z$ where $\mathbf{e}_x, \mathbf{e}_y, \mathbf{e}_z$ are unit vectors along the x, y , and z axes, respectively. In this formulation, surfaces of constant phase are described by $\mathbf{r} \cdot \mathbf{k} = \text{constant}$. In a region with no acoustic sources, equation (1.1) must satisfy the reduced (Helmholtz) wave equation, $(\nabla^2 + |\mathbf{k}|^2)p = 0$; application of this to (1.1) yields the result $|\mathbf{k}|^2 = \left(\frac{\omega}{c}\right)^2 = k_x^2 + k_y^2 + k_z^2$. The domain of the wavevector \mathbf{k} is thus described by a sphere of radius $|\mathbf{k}|$, as indicated in Figure 1-4. Propagating acoustic waves are represented by points on the surface of this sphere. Wavevectors falling within the surface of the sphere, where $|\mathbf{k}| < \frac{\omega}{c}$, describe supersonic waves. Wavevectors exterior to the surface of the sphere describe evanescent sub-sonic waves. Note that the quantities $\frac{k_x}{k}, \frac{k_y}{k}$, and $\frac{k_z}{k}$ are the direction cosines of \mathbf{k} with respect to the x, y , and z axes. We identify $c_x = \frac{\omega}{k_x}, c_y = \frac{\omega}{k_y}$, and $c_z = \frac{\omega}{k_z}$ as the trace velocities of the wave along the respective axes. Similarly, since $k = \frac{2\pi}{\lambda}$ where λ is the wavelength of the propagating wave, the trace wavelengths are expressed as $\lambda_x = \frac{2\pi}{k_x}, \lambda_y = \frac{2\pi}{k_y}$, and $\lambda_z = \frac{2\pi}{k_z}$.

We note that as the wavevector \mathbf{k} approaches perpendicularity with respect to one of the coordinate axes, the trace velocity and wavelength tend to infinity along that axis. This concept is useful in understanding the cutoff phenomenon which occurs under certain conditions in a propagating wave which is constrained by some physical boundary, such as within a waveguide.

If $p(\mathbf{r}, t)$ describes a complex wave field for which the principle of superposition applies, we may define a wavevector spectrum in terms of a three dimensional

spatial Fourier transform,

$$\hat{p}(\mathbf{k}, t) = \iiint_{-\infty}^{\infty} p(\mathbf{r}, t) e^{-i\mathbf{k} \cdot \mathbf{r}} d\mathbf{r}$$

in which $\hat{p}(\mathbf{k}, t) = \hat{p}(k_x, k_y, k_z, t)$ represents the spectral components of the wavefield in the wavevector domain in the same manner that the Fourier transform of a time dependent function depicts the spectral composition of the function in the frequency domain.

In this study we are primarily concerned with wave propagation in cylindrical configurations with coordinates (r, θ, z) and unit vectors $(\mathbf{e}_r, \mathbf{e}_\theta, \mathbf{e}_z)$. In this notation, the wavevector may be written $\mathbf{k}_{cyl} = \mathbf{e}_r k_r + \mathbf{e}_\theta k_\theta + \mathbf{e}_z k_z$. A vector \mathbf{k}_{rect} in rectangular coordinates may be transformed into a cylindrical wavevector \mathbf{k}_{cyl} in cylindrical coordinates by means of an orthogonal transformation matrix $[S]$ which has the following properties (Hughes and Gaylord 1964):

1. The inverse of $[S]$ is equal to the transpose of $[S]$, $[S]^{-1} = [S]^T$, and $[S] \cdot [S]^{-1} = [I]$, the identity matrix.
2. The determinant of $[S] = \pm 1$.

The transformation equations are: $\mathbf{k}_{cyl} = [S] \cdot \mathbf{k}_{rect}$, and $\mathbf{k}_{rect} = [S]^T \cdot \mathbf{k}_{cyl}$.

where

$$[S] = \begin{bmatrix} \cos \theta & \sin \theta & 0 \\ -\sin \theta & \cos \theta & 0 \\ 0 & 0 & 1 \end{bmatrix}$$

and

$$[S]^T = \begin{bmatrix} \cos \theta & -\sin \theta & 0 \\ \sin \theta & \cos \theta & 0 \\ 0 & 0 & 1 \end{bmatrix}$$

Applying this to the present case, the components of the cylindrical wavevector in terms of the elements of a rectangular wavevector are:

$$k_r = k_x \cos \theta + k_y \sin \theta; \quad k_\theta = -k_x \sin \theta + k_y \cos \theta; \quad \text{and} \quad k_z = k_z.$$

The inverse transformation results in:

$$k_x = k_r \cos \theta - k_\theta \sin \theta; \quad k_y = k_r \sin \theta + k_\theta \cos \theta; \quad \text{and} \quad k_z = k_z.$$

Propagating cylindrical waves must satisfy the equation

$$|\mathbf{k}|^2 = k_r^2 + k_\theta^2 + k_z^2 \quad (1.2)$$

Now let $k_\theta = 0$. For this case, Eq. (1.2) defines a cone in $k - \omega$ space, Figure 1-5. Points on the surface of this cone correspond to propagating acoustic waves. A plane at some particular frequency ω_0 which is parallel to the $\omega = 0$ plane intersects the cone and defines a circle of radius k_0 , Figure 1-6. The two-dimensional wavevector $\mathbf{k} = \mathbf{e}_r k_r + \mathbf{e}_z k_z$ represents propagating waves when $|\mathbf{k}| = k_0$, supersonic waves when \mathbf{k} is inside the circle, and sub-sonic evanescent waves when \mathbf{k} is outside the circle.

1.6 Synthesis of a Cylindrical Wave from Plane Waves

A construction which is useful in the description of cylindrical waves comprises the synthesis of such waves from an infinite number of plane waves. (Lamont 1950; Redwood 1960)

Consider a plane wave of wavenumber k propagating in a rectangular (x, y, z) coordinate system, with wavevector \mathbf{k} making an angle ϕ with respect to the z axis, and oriented so that there is no component in the y direction, i. e., $k_y = 0$. Such a wave may be described by

$$p(x, y, z, t) = \text{Re} \left\{ A e^{i(k_x x + k_z z - \omega t)} \right\}$$

in which $k_x = k \sin \phi$ and $k_z = k \cos \phi$.

Now we hold the angle ϕ constant and sum up an infinite number of such plane waves by rotating the x, y axes around the z axis. We consider a point at $(r, \theta, 0)$ in the plane $z = 0$, Figure 1.7. The x axis is shown at an angle ψ with respect to the polar coordinates $(r, \theta, 0)$ and thus $x = r \cos \psi$. Now let the amplitude of the elementary wave associated with the point (r, θ, z) be represented by

$$dp = \text{Re} \left\{ A \cos n(\theta + \psi) e^{i(k_x r \cos \psi + k_z z - \omega t)} d\psi \right\}$$

The total pressure at (r, θ, z) is obtained by integrating ψ over the range $0 \leq \psi \leq 2\pi$,

$$p(r, \theta, z, t) = \text{Re} \left\{ \int_0^{2\pi} A \cos n(\theta + \psi) e^{i(k r \sin \phi \cos \psi)} e^{i(k z \cos \phi - \omega t)} d\psi \right\}$$

Using the identity (Gradshteyn and Ryzhik 1980)

$$J_n(u) = \frac{i^{-n}}{2\pi} \int_0^{2\pi} e^{i(u \cos \psi)} \cos(n\psi) d\psi$$

and substituting $u = kr \sin \phi$, we obtain

$$p(r, \theta, z, t) = \text{Re} \left\{ 2\pi i^n A \cos n\theta J_n(kr \sin \phi) e^{i(kz \cos \theta - \omega t)} \right\} \quad (1.3)$$

Making the substitutions $k_r = k \sin \phi$ and $k_z = k \cos \phi$ in Eq. (1.3) yields

$$p(r, \theta, z, t) = \text{Re} \left\{ 2\pi i^n A \cos n\theta J_n(k_r r) e^{i(k_z z - \omega t)} \right\} \quad (1.4)$$

which is recognized as one solution of the cylindrical wave equation, and k_r and k_z are components of the cylindrical wave vector. For the axisymmetric ($n = 0$) case, Eq (1.4) specializes to

$$p(r, z, t) = \text{Re} \left\{ 2\pi A J_0(k_r r) e^{i(k_z z - \omega t)} \right\}$$

This describes a wave diverging from the origin in a cone of half-angle ϕ , as indicated in Figure 1.8. If the amplitude constant A is real, this may be written

$$p(r, z, t) = 2\pi A J_0(k_r r) \cos(k_z z - \omega t)$$

Using the asymptotic expression for the Bessel function for large values of the argument $k_r r$, we find

$$p(r, z, t)_{k_r r \rightarrow \infty} = 2\pi A \sqrt{\frac{2}{\pi k_r r}} \cos\left(k_r r - \frac{\pi}{4}\right) \cos(k_z z - \omega t)$$

which describes a wave propagating in the z direction and with amplitude decreasing as $(r)^{-\frac{1}{2}}$ in the radial direction.

Using the momentum equation, the radial and axial components of velocity are determined to be:

$$\text{Radial: } v_r(r, z, t) = -2\pi \frac{A}{\rho c} \sin \phi J_1(k_r r) \sin(k_z z - \omega t)$$

$$\text{and Axial: } v_z(r, z, t) = 2\pi \frac{A}{\rho c} \cos \phi J_0(k_r r) \cos(k_z z - \omega t)$$

Since the axial velocity and the pressure are in phase, energy is propagating in the axial direction. The radial velocity is orthogonal to the the pressure.

CHAPTER 2

Fluid Media

2.1 Analytical Approach

In this chapter we develop the transfer matrices for three cylindrical fluid components of interest: a fluid cylinder, a fluid tube, and the external fluid. Wave propagation in these components is studied for limiting boundary conditions (rigid and soft) as a prelude to understanding the more complicated situation which obtains when composite (cascaded) systems are considered.

For all fluid models we shall assume the fluid is inviscid and that the amplitudes of the field variables (pressure and particle velocity) are sufficiently small that the linearized wave equation is applicable. Thus we are concerned with solutions to

$$\nabla^2 p = \frac{1}{c^2} \frac{\partial^2 p}{\partial t^2}$$

where p is the acoustic pressure in the fluid, c is the acoustic wave speed in the fluid, and ∇^2 is the three-dimensional Laplacian operator. The particle velocity \mathbf{v} is related to the pressure via the linearized momentum equation,

$$\nabla p = -\rho_0 \frac{\partial \mathbf{v}}{\partial t}$$

where ρ_0 is the equilibrium (static) density of the fluid.

2.1.1 Wave Equation in Cylindrical Coordinates

Consider the cylindrical coordinate system shown in Figure 2.1, in which r, z and

θ are the radial, axial, and angular variables, respectively; and \mathbf{e}_r , \mathbf{e}_θ , \mathbf{e}_z are the corresponding unit vectors. The wave equation for the pressure is

$$\frac{1}{r} \frac{\partial}{\partial r} \left(r \frac{\partial p}{\partial r} \right) + \frac{1}{r^2} \frac{\partial^2 p}{\partial \theta^2} + \frac{\partial^2 p}{\partial z^2} = \frac{1}{c^2} \frac{\partial^2 p}{\partial t^2} \quad (2.1)$$

and the momentum equation is

$$\mathbf{e}_r \frac{\partial p}{\partial r} + \mathbf{e}_\theta \frac{1}{r} \frac{\partial p}{\partial \theta} + \mathbf{e}_z \frac{\partial p}{\partial z} = -\rho_0 \frac{\partial \mathbf{v}}{\partial t} \quad (2.2)$$

Two approaches in solving the cylindrical wave equation (2.1) are the separation of variables and the use of integral transforms, such as the Fourier or Laplace transforms.

In the separation of variables method, the solution is assumed to consist of the product of independent functions of r, z, θ and t , such as

$$p(r, \theta, z, t) = R(r) \Theta(\theta) Z(z) T(t) \quad (2.3)$$

If harmonic time dependence of the form $T(t) = \exp(-i\omega t)$ is assumed, the reduced (harmonic) Helmholtz equation is obtained,

$$(\nabla^2 + k^2)p(r, \theta, z) = 0 \quad (2.4)$$

where ω is the angular frequency and $k = \frac{\omega}{c}$ is the acoustic wavenumber.

Operating on Eq.2.3 using Eq.2.4, and suppressing the time dependence, three independent ordinary differential equations are obtained:

$$\frac{d^2 Z}{dz^2} + k_z Z = 0 \quad (2.5)$$

$$\frac{d^2 \Theta}{d\theta^2} + n^2 \Theta = 0 \quad (2.6)$$

$$\frac{d^2 R}{dr^2} + \frac{1}{r} \frac{dR}{dr} + k_r^2 R = 0 \quad (2.7)$$

In these equations, k_z , k_r , and n are separation constants, related by the expression $k^2 = k_r^2 + k_z^2 + \left(\frac{n}{r}\right)^2$.

Solutions to 2.5 may be either exponential, $Z(z) = Ae^{\pm ik_z z}$, representing traveling waves, or sinusoidal, $A \begin{Bmatrix} \sin(k_z z) \\ \cos(k_z z) \end{Bmatrix}$, for standing waves.

Since $\Theta(\theta)$ repeats periodically with period 2π , that is, $\Theta(\theta) = \Theta(\theta + 2\pi)$, n must be an integer, and solutions of 2.6 must be combinations of trigonometric functions, such as $\Theta(\theta) = B_1 \cos(n\theta) + B_2 \sin(n\theta)$.

Equation 2.7 is recognized as Bessel's equation of integer order n , solutions to which comprise various linear combinations of Bessel functions of argument $k_r r$, such as:

$$R_n(r) = C_1 J_n(k_r r) + i C_2 Y_n(k_r r)$$

or alternatively,

$$R_n(r) = D_1 H_n^{(1)}(k_r r) + D_2 H_n^{(2)}(k_r r)$$

In these equations, k_z may be identified as an axial wavenumber, and k_r as a radial wavenumber. At a particular value of the radial coordinate, $r = a$, we may define $k_n = \frac{n}{a}$, a discrete circumferential wavenumber. By use of the momentum equation at the radial interfaces $r = a_1, a_2, \dots, a_m$ for a particular cylindrical fluid component, and recognizing that k_z and n must be identical for each component in the system to insure the continuity of the radial particle velocity across each radial interface, the various coefficients A, B, C etc may be evaluated.

2.1.2 Integral Transform Approach

A major advantage of integral transforms, such as the Fourier or Laplace transforms, is the reduction of differential equations to algebraic equations. In the solution of transient problems, the Laplace transform is advantageous since it permits the initial conditions to be included in the formulation of the problem.

To illustrate the application of integral transforms we will construct a Fourier transformed version of the cylindrical wave equation, transforming on the time t , and the spatial coordinates z and θ .

For the continuous variables z and t we define the forward transform

$$\hat{p}(k_z, \omega) = \iint_{-\infty}^{\infty} p(z, t) e^{-i(\omega t + k_z z)} dt dz \quad (2.8)$$

The inverse transform is defined as

$$p(z, t) = \frac{1}{(2\pi)^2} \iint_{-\infty}^{\infty} \hat{p}(k_z, \omega) e^{i(\omega t + k_z z)} d\omega dk_z$$

Since the circumferential variation is periodic, we may expand $p(\theta)$ in a Fourier series, viz.

$$p(\theta) = \sum_{n=-\infty}^{\infty} \frac{\hat{p}(n) e^{in\theta}}{2\pi} \quad (2.9)$$

Multiplying both sides of Eq. (2.9) by $e^{-im\theta}$ and integrating over the range $-\pi, \pi$ we have

$$\int_{-\pi}^{\pi} p(\theta) e^{-im\theta} d\theta = \sum_{n=-\infty}^{\infty} \int_{-\pi}^{\pi} \frac{\hat{p}(n)}{2\pi} e^{i(n-m)\theta} d\theta \quad (2.10)$$

From the orthogonality of trigonometric functions, the integral on the right hand side of Eq. (2.10) is zero for all values of $n \neq m$ and therefore

$$\hat{p}(n) = \int_{-\pi}^{\pi} p(\theta) e^{-in\theta} d\theta \quad (2.11)$$

Equations (2.9) and (2.11) define a transform pair on the circumferential coordinate θ .

Transforms of Derivatives Differentiating Eq. (2.9) m times yields

$$\frac{d^m p(\theta)}{d\theta^m} = (in)^m \sum_{n=-\infty}^{\infty} \frac{\hat{p}(n)}{2\pi} e^{in\theta}$$

and transforming both sides of this equation gives for the transform of the derivative:

$$\mathcal{F} \left[\frac{d^m p(\theta)}{d\theta^m} \right] = (in)^m \hat{p}(\theta)$$

The derivatives of the transforms of the continuous variables z and t are obtained by differentiating Eq. (2.8), viz

$$\mathcal{F} \left[\frac{d^m p(t)}{dt^m} \right] = (-i\omega)^m \hat{p}(\omega)$$

and

$$\mathcal{F} \left[\frac{d^m p(z)}{dz^m} \right] = (-ik_z)^m \hat{p}(k_z)$$

2.1.3 Transformed Cylindrical Wave Equation

Applying these transforms to the cylindrical wave equation (2.1) results in an ordinary differential equation in r and in $\hat{p}(k_z, \omega, n)$,

$$\frac{d^2 \hat{p}}{dr^2} + \frac{1}{r} \frac{d\hat{p}}{dr} + \left(k^2 - k_z^2 - \frac{n^2}{r^2} \right) \hat{p} = 0 \quad (2.12)$$

which is identical in form to Eq. (2.7) obtained by the method of separation of variables. Thus solutions of (2.12) will consist of combinations of Bessel functions of argument $k_r r$ and coefficients determined by the boundary conditions which apply to the model of interest.

2.2 Fluid Cylinder

2.2.1 Introduction

The propagation of acoustic waves in a confined fluid has received extensive study in the literature. Redwood (1906) discusses continuous and transient (pulsed) propagation in rectangular and cylindrical fluid waveguides with both free and rigid boundaries. Morse and Ingard (1968) devote a chapter to "Sound Waves in Ducts and Rooms" in which both plane wave and higher order modes are considered. Their analysis includes an intermediate boundary condition in which the stiffness and mass of the duct walls are considered. A similar analysis is presented by Junger and Feit (1986).

Anderson and Barnes (1953) studied the dispersion of a damped sinusoidal ultrasonic pulse in a water-filled thin walled cylinder lined with rubber to create a free radial boundary. Their experimental results agreed with the theoretical dispersion curve for the first axisymmetric (0,1) mode. They also developed an expression for the transient response as a function of time and axial distance for an impulsive (delta function) velocity input and related this result to the dispersion predicted from group velocity concepts.

The dispersion of a rectangular narrow band pulse (tone burst) in a rectangular fluid waveguide with free boundaries was studied by Proud, Tamarkin, and Kornhauser (1956). They measured the phase velocity as a function of frequency for the (1,1) and (2,1) modes of the waveguide. The pulse envelopes were measured at various distances along the waveguide and compared with the predictions from

a theoretical model by Pearson (1953).

Jacobi (1949) made an extensive theoretical and experimental study of the propagation of acoustic waves in fluid cylinders. His models included a fluid cylinder with rigid and free walls, a fluid cylinder imbedded in an infinite fluid, a fluid cylinder with fluid walls, and a fluid cylinder within a thin elastic cylinder. Experimental results were obtained for the fluid cylinder with free boundaries and for the fluid cylinder in a thin shell.

2.2.2 Physical Description

Consider a cylinder of fluid of radius a , sound speed c , and density ρ extending infinitely in the axial (z) direction. The solution of the transformed wave equation (2.12) appropriate for this case is

$$\hat{p}(n, k_z, \omega, r) = \hat{p}(n, k_z, \omega) J_n(k_r r),$$

where $k_r^2 = \left(\frac{\omega}{c}\right)^2 - k_z^2 - \left(\frac{n}{r}\right)^2$. (The Neumann function $N_n(k_r r)$ is excluded because of the singularity at $r = 0$.)

The transformed momentum equation is

$$\mathbf{e}_r \frac{d\hat{p}}{dr} + \mathbf{e}_\theta \frac{(in)}{r} \hat{p} + \mathbf{e}_z (ik_z) \hat{p} = \rho (i\omega) \hat{\mathbf{v}} = i\rho ck \hat{\mathbf{v}}$$

Application of the momentum equation to the transformed wave equation results in the three components of particle velocity:

Axial:

$$\hat{v}_z = \frac{k_z}{\rho ck} \hat{p} J_n(k_r r)$$

Circumferential:

$$\hat{v}_\theta = \frac{n}{\rho c k r} \hat{p} J_n(k_r r)$$

Radial:

$$\hat{v}_r = -\frac{i}{\rho c k} \hat{p} J'_n(k_r r) \quad (2.13)$$

where the prime denotes the derivative with respect to the argument $(k_r r)$.

These relationships will be used to develop the radial spectral impedance of the fluid cylinder, and to study the propagation of free waves in a fluid cylinder.

2.2.3 Radial Spectral Impedance

We define a radial spectral impedance as the ratio of the transformed pressure to the transformed radial component of velocity;

$$Z(n, \omega, k_z, r) = \frac{\hat{p}}{\hat{v}_r} = \frac{i \rho c k J_n(k_r r)}{J'_n(k_r r)}$$

We now specialize this to the axisymmetric ($n = 0$) mode. The justification for this simplification is that any arbitrary circumferential excitation function may be expanded in a Fourier series as indicated in Eq. (2.9). Solutions would then consist of a summation of terms representing the harmonic components of the excitation.

For the axisymmetric case, $J'_0(k_r r) = -k_r J_1(k_r r)$ and the spectral impedance of the fluid cylinder is

$$Z(\omega, k_z, r) = \frac{-i \rho c k J_0(k_r r)}{k_r J_1(k_r r)}$$

At the surface of the cylinder, $r = a$, we define the state variables of pressure \hat{P}_a and \hat{V}_a in terms of the spectral impedance, viz:

$$Z_a = \frac{\hat{P}_a}{\hat{V}_a} = \frac{-i \rho c k J_0(k_r a)}{k_r J_1(k_r a)} \quad (2.14)$$

The notation may be simplified somewhat by using the definition for the modified quotients of Bessel functions (Onoe 1958). Therefore we define $\widetilde{\mathcal{J}}_n(k_r a)$ as

$$\widetilde{\mathcal{J}}_n(k_r a) = \frac{(k_r a) J_{n+1}(k_r a)}{J_n(k_r a)}$$

This function is plotted in Figure 2.2 for $n = 0$ and values of the argument from 0 to 15.

With this definition, the radial spectral impedance of Eq. (2.14) is written as

$$Z_a = \frac{-i\rho c k a}{\widetilde{\mathcal{J}}_0(k_r a)}$$

To study the spectral impedance of the fluid cylinder, consider an excitation consisting of a spectrally pure traveling wave of pressure of arbitrary frequency ω and axial wavenumber k_z applied at the boundary $r = a$. This condition could be physically realized, for example, by a membrane or thin elastic cylinder enclosing the fluid and driven by some external force.

The waves in the fluid cylinder must satisfy the dispersion equation $k_r^2 = \left(\frac{\omega}{c}\right)^2 - k_z^2$. Thus as ω and k_z take on all possible values the radial wavenumber k_r may be real, zero, or imaginary.

Case 1 - k_r Real, Propagating Axial Wave For $k > k_z$, k_r is real, and $k_r = \sqrt{k^2 - k_z^2}$. The normalized spectral impedance, $Z_a/\rho c$, is plotted in Figure 2.3 as a function of the argument $k_r a$ for $ka = 1$.

The spectral impedance is purely reactive, alternating between stiffness and mass type reactances as the radial wavenumber $k_r a$ increases. With k_z real, waves may propagate along the z axis of the fluid cylinder.

Case 2 - No Axial Wave Propagation Now if we let $k_z = 0$, (i. e. there is no axial propagation in the fluid cylinder) then $k_r = k$, and

$$Z_a = \frac{-i\rho c J_0(ka)}{J_1(ka)} \quad (2.15)$$

For low frequencies ($ka \ll 1$, or $\omega \ll c/a$), $J_0(ka) \approx 1$, and $J_1(ka) \approx \frac{ka}{2}$, so that

$$Z_a \approx \frac{2\rho c^2}{i\omega a}$$

Noting that $\rho c^2 = \beta$, the adiabatic bulk modulus of the fluid (Kinsler and Frey, 1982; Junger and Feit, 1986), we may write $Z_a \approx 2\beta/i\omega a$. Now consider a section of the fluid cylinder of length l and area $2\pi al$. The mechanical impedance of the section is $2\pi al Z_a$, thus,

$$Z_M \approx \frac{4\pi l \beta}{i\omega}, \quad \omega \ll \frac{c}{a}$$

Thus for very low frequencies the fluid cylinder acts like a spring of stiffness $4\pi l \beta$ Newtons per meter.

For values of the argument $ka > 2\pi$, the Bessel function is approximated as

$J_n(ka) \approx \sqrt{\frac{2}{\pi ka}} \cos\left(ka - \frac{n\pi}{2} - \frac{\pi}{4}\right)$. Using this relationship, the expression for the spectral impedance (with $k_z = 0$) at high frequencies is

$$Z_a \approx -i\rho c \cot\left(ka - \frac{\pi}{4}\right), \quad ka > 2\pi$$

The exact value of normalized spectral impedance from Eq. (2.15) is shown in Figure 2.4. As in Case 1, it is purely reactive, alternating between stiffness and mass type reactance. The impedance is zero at the zeros of $J_0(ka)$, and infinite at the zeros of $J_1(ka)$.

Case 3 - k_r Imaginary When the axial wavenumber k_z exceeds the acoustic wavenumber k , the radial wavenumber is imaginary, and $k_r = i\sqrt{k_z^2 - k^2} = i\bar{k}_r$. For an imaginary argument, the Bessel function of the first kind is replaced with the modified Bessel function of the first kind. Thus $J_n(i\bar{k}_r a) = i^n I_n(\bar{k}_r a)$. Substituting in (2.14), the spectral impedance is given by

$$Z_a = \frac{i\rho ck I_0(\bar{k}_r a)}{\bar{k}_r I_1(\bar{k}_r a)} \quad (2.16)$$

For small values of the argument, $I_n(\bar{k}_r a) \rightarrow \frac{(\bar{k}_r a)^n}{2^n n!}$ and the spectral impedance is approximated as

$$Z_a \approx \frac{2i\beta}{\omega a \left[\left(\frac{k_z}{k} \right)^2 - 1 \right]}$$

Now when $k_z \gg k$, $\bar{k}_r \approx k_z$ and for large values of $\bar{k}_r a$ the large argument approximations for $I_n(\bar{k}_r a)$ yield

$$Z_a \approx \frac{-\rho ck}{ik_z} = \frac{i\rho\omega}{k_z} \quad (2.17)$$

2.2.4 Free Wave Propagation

We now consider the propagation of free waves in a fluid cylinder for the limiting cases of a rigid and a free boundary. In contrast to the preceding discussion of spectral impedance in which both the frequency and the axial wavenumber were permitted to be free variables, we now seek values of the radial wavenumber k_r which will satisfy specific boundary conditions. These particular values of k_r determine the modes of free wave propagation. Again, the analysis is restricted to the axisymmetric case.

Free Radial Boundary The pressure must vanish at a free boundary, so we set $\hat{P}_a = 0$ in Eq. (2.14). To satisfy this condition requires that $J_0(k_r a) = 0$. Designating the roots of this equation as $j_{0,m}$, the allowable values of k_r are given by

$$k_{r,m}a = j_{0,m}, \quad m = 1, 2, 3, \dots$$

$$\text{and } j_{0,1} = 2.40, \quad j_{0,2} = 5.52, \quad j_{0,3} = 8.65, \quad \text{etc.}$$

For values of m greater than 2 the roots may be approximated by $j_{0,m} \approx \frac{\pi}{4}(4m - 1)$ with an error of less than 0.1%.

Each root determines the characteristics of wave propagation of a particular mode in the fluid cylinder. Since the axial wavenumber must be real for propagation to occur, each mode will exhibit a cutoff frequency ω_m , determined from the dispersion equation by setting $k_{z,m} = 0$, as

$$\omega_m = \frac{j_{0,m}c}{a}$$

The phase velocity of the wave, c_ϕ , is computed from the axial wavenumber $k_{z,m}$,

$$c_{\phi,m} = \frac{\omega}{k_{z,m}} = c \left[1 - \left(\frac{j_{0,m}c}{\omega a} \right)^2 \right]^{-\frac{1}{2}}$$

and the group velocity c_g is given by

$$c_{g,m} = \frac{d\omega}{dk_{z,m}} = c \left[1 - \left(\frac{j_{0,m}c}{\omega a} \right)^2 \right]^{\frac{1}{2}}$$

The variation with frequency of the phase and group velocities for a fluid cylinder with a free radial boundary are shown in Figure 2.5. This is an example of

"normal" dispersion, in which the phase velocity decreases with frequency. (Elmore and Heald, 1985)

Substitution of the modal radial wavenumber $k_{r,m} = j_{0,m}/a$ into the wave equation yields the characteristic function describing the radial variation in pressure for the m th mode:

$$p_m(r) = A_m J_0\left(j_{0,m} \frac{r}{a}\right)$$

where A_m is a modal amplitude coefficient. The normalized modal amplitude, p_m/A_m is plotted as a function of the normalized radius r/a in Figure 2.6 for the first three modes. We note that there is no plane wave mode ($m = 0$) for this case, since the pressure must be zero at $r = a$. For any mode, the pressure is a maximum at the center of the cylinder and zero at the boundary.

As discussed in section 1.6, the wave in the fluid cylinder may be constructed from an infinite number of plane waves whose wavevector \mathbf{k} makes an angle ϕ with the z axis. This angle is determined from $\tan \phi = \frac{k_r}{k_z}$ and the angle for a particular mode is

$$\phi_m = \arctan \left[\left(\frac{\omega c}{j_{0,m} a} \right)^2 - 1 \right]^{-\frac{1}{2}}$$

Rigid Radial Boundary The presence of a rigid boundary requires that the radial component of velocity be zero at $r = a$. From Eq.(2.13) this condition is satisfied when $J_1(k_r a) = 0$. Letting $j_{1,m}$ represent the roots of this equation, modes exist for values of k_r given by

$$k_{r,m} a = j_{1,m}, \quad m = 0, 1, 2, \dots$$

where $j_{1,0} = 0$, $j_{1,1} = 3.83$, $j_{1,2} = 7.01$, $j_{1,3} = 10.17$ For m greater than 5 the approximation $j_{1,m} \approx \frac{\pi}{4}(4m + 1)$ may be used with an error of less than 0.1%.

The phase and group velocities for a fluid cylinder with a rigid boundary are presented in Figure 2.7. The $j_{1,0} = 0$ root characterizes the plane wave mode which is supported by the rigid wall boundary condition. There is no cut-off frequency for this mode, and the phase and group velocities are independent of frequency and equal to the sound speed in the fluid.

The modeshapes for this case are given by $p_m(r) = A_m J_0(j_{1,m} \frac{r}{a})$ and are shown in Figure 2.8. For the plane wave mode, the pressure is independent of the radius.

2.3 Fluid Tube

2.3.1 Introduction

We now consider a cylindrical tube of fluid, infinite in length, with inner radius a , outer radius b , sound speed c , and density ρ . Such a fluid cylinder could be physically realized, for example, by a fluid contained in the annular space between two concentric cylindrical shells.

We seek to develop a transfer function relating the state variables of pressure P and radial velocity V at the inner boundary, $r = a$, to those at the outer boundary, $r = b$, for an arbitrary excitation comprising an axisymmetric traveling pressure wave at either boundary. The analysis is restricted to the axisymmetric case for clarity, but it may easily be extended to the more general non-axisymmetric case using the transform pair defined in equations 2.9 and 2.11 to describe the

circumferential variation. This will result in an infinite sum of transfer functions to represent the fluid tube.

Figure 2.9 describes the model in block diagram form. P_a and V_a represent the state variables of pressure and velocity at the inner radius, and P_b and V_b those at the outer radius.

The desired transfer function is a matrix of the form

$$\begin{bmatrix} P_b \\ V_b \end{bmatrix} = \begin{bmatrix} A & B \\ C & D \end{bmatrix} \begin{bmatrix} P_a \\ V_a \end{bmatrix}$$

where the parameters A , B , C , and D are defined as:

$$A = \frac{P_b}{P_a} \big|_{V_a=0}, \quad B = \frac{P_b}{V_a} \big|_{P_a=0}, \quad C = \frac{V_b}{P_a} \big|_{V_a=0} \quad \text{and} \quad D = \frac{V_b}{V_a} \big|_{P_a=0}$$

2.3.2 Development of Transfer Function

The pressure within the fluid tube must satisfy the scalar Helmholtz equation,

$$(\nabla_r^2 + k^2) \hat{p}(k_z, \omega, r) = 0$$

where $\hat{p}(k_z, \omega, r)$ is the double Fourier transform of the pressure as described in equation 2.8 and $\nabla_r^2 = \frac{1}{r} \frac{\partial}{\partial r} \left[r \frac{\partial}{\partial r} \right]$.

Now we assume a solution of the form

$$\hat{p}(k_z, \omega, r) = \left[E H_0^{(1)}(k_r r) + F H_0^{(2)}(k_r r) \right] e^{i(k_z z - \omega t)} \quad (2.18)$$

where $H_0^{(1)}(k_r r)$ is the Hankel function of the first kind, order 0, representing waves traveling outward in the positive r direction, and $H_0^{(2)}(k_r r)$ is the Hankel function of the second kind, representing waves traveling inward. A radial wavenumber k_r is computed from $k_r^2 = k^2 - k_z^2 = \left(\frac{\omega}{c}\right)^2 - k_z^2$; and E and F are

complex coefficients to be determined. The radial velocity \hat{v}_r is found using the momentum equation,

$$-\nabla_r \hat{p}(k_z, \omega, r) = \rho \frac{\partial}{\partial t} \hat{v}_r(k_z, \omega, r) = -i\rho\omega \hat{v}_r(k_z, \omega, r)$$

Applying this to equation 2.18 results in

$$\hat{v}_r(k_z, \omega, r) = \frac{ik_r}{\omega\rho} \left[E H_1^{(1)}(k_r r) + F H_1^{(2)}(k_r r) \right] e^{i(k_z z - \omega t)}$$

Defining the radial spectral impedance of the fluid in the tube as

$$Z = \frac{\rho c k}{k_r}$$

the radial velocity may be expressed as

$$\hat{v}_r(k_z, \omega, r) = \frac{i}{Z} \left[E H_1^{(1)}(k_r r) + F H_1^{(2)}(k_r r) \right] e^{i(k_z z - \omega t)} \quad (2.19)$$

The transformed state variables P_a , V_a , P_b , and V_b are found by substituting $r = a$ and $r = b$ into equations 2.18 and 2.19. This results in the following four equations which must be solved to determine the complex coefficients E and F . The exponential function $\exp i(k_z z - \omega t)$ will be suppressed in subsequent equations for brevity.

$$\hat{P}_a = E H_0^{(1)}(k_r a) + F H_0^{(2)}(k_r a)$$

$$\hat{V}_a = \frac{i}{Z} \left[E H_1^{(1)}(k_r a) + F H_1^{(2)}(k_r a) \right]$$

$$\hat{P}_b = E H_0^{(1)}(k_r b) + F H_0^{(2)}(k_r b)$$

$$\hat{V}_b = \frac{i}{Z} \left[E H_1^{(1)}(k_r b) + F H_1^{(2)}(k_r b) \right]$$

These equations may be written in matrix form as

$$\begin{bmatrix} \hat{P}_b \\ \hat{V}_b \end{bmatrix} = \begin{bmatrix} M_b \end{bmatrix} \begin{bmatrix} E \\ F \end{bmatrix} \quad (2.20)$$

and

$$\begin{bmatrix} \hat{P}_a \\ \hat{V}_a \end{bmatrix} = \begin{bmatrix} M_a \end{bmatrix} \begin{bmatrix} E \\ F \end{bmatrix} \quad (2.21)$$

where

$$\begin{bmatrix} M_a \end{bmatrix} = \begin{bmatrix} H_0^{(1)}(k_r a) & H_0^{(2)}(k_r a) \\ \frac{i}{Z} H_1^{(1)}(k_r a) & \frac{i}{Z} H_1^{(2)}(k_r a) \end{bmatrix} = \begin{bmatrix} a_1 & a_2 \\ a_3 & a_4 \end{bmatrix} \quad (2.22)$$

and

$$\begin{bmatrix} M_b \end{bmatrix} = \begin{bmatrix} H_0^{(1)}(k_r b) & H_0^{(2)}(k_r b) \\ \frac{i}{Z} H_1^{(1)}(k_r b) & \frac{i}{Z} H_1^{(2)}(k_r b) \end{bmatrix} = \begin{bmatrix} b_1 & b_2 \\ b_3 & b_4 \end{bmatrix} \quad (2.23)$$

Multiplying 2.20 by the inverse of 2.23 and 2.21 by the inverse of 2.22 leads to the elimination of the complex coefficients E and F , viz.

$$\begin{bmatrix} E \\ F \end{bmatrix} = \begin{bmatrix} M_b \end{bmatrix}^{-1} \begin{bmatrix} \hat{P}_b \\ \hat{V}_b \end{bmatrix} = \begin{bmatrix} M_a \end{bmatrix}^{-1} \begin{bmatrix} \hat{P}_a \\ \hat{V}_a \end{bmatrix} \quad (2.24)$$

Multiplying 2.24 by $\begin{bmatrix} M_b \end{bmatrix}$ and noting that $\begin{bmatrix} M_b \end{bmatrix} \begin{bmatrix} M_b \end{bmatrix}^{-1} = \begin{bmatrix} I \end{bmatrix}$, the identity matrix, result in:

$$\begin{bmatrix} \hat{P}_b \\ \hat{V}_b \end{bmatrix} = \begin{bmatrix} M_b \end{bmatrix} \begin{bmatrix} M_a \end{bmatrix}^{-1} \begin{bmatrix} \hat{P}_a \\ \hat{V}_a \end{bmatrix}$$

By a similar method we obtain

$$\begin{bmatrix} \hat{P}_a \\ \hat{V}_a \end{bmatrix} = \begin{bmatrix} M_a \end{bmatrix} \begin{bmatrix} M_b \end{bmatrix}^{-1} \begin{bmatrix} \hat{P}_b \\ \hat{V}_b \end{bmatrix}$$

Thus $\begin{bmatrix} M_b \end{bmatrix} \begin{bmatrix} M_a \end{bmatrix}^{-1}$ is the transfer matrix from the inner surface of the fluid tube to the outer surface, and $\begin{bmatrix} M_a \end{bmatrix} \begin{bmatrix} M_b \end{bmatrix}^{-1}$ is the transfer matrix from the outer surface to the inner surface. Substituting the expressions for $\begin{bmatrix} M_a \end{bmatrix}$ and $\begin{bmatrix} M_b \end{bmatrix}$ from (2.22) and (2.23) we have

$$\begin{bmatrix} M_{ab} \end{bmatrix} = \frac{\begin{bmatrix} (b_1 a_4 - b_2 a_3) & (-b_1 a_2 + b_2 a_1) \\ (b_3 a_4 - b_4 a_3) & (-b_3 a_2 + b_4 a_1) \end{bmatrix}}{\Delta a}$$

where $\Delta a = a_1 a_2 - a_2 a$ and $[M_{ab}]$ represents the transfer matrix from the inner surface of the fluid tube at $r = a$ to the outer surface, $r = b$.

Substituting the Hankel functions into the expression for Δa we have

$$\Delta a = \frac{i}{Z} \left[H_0^{(1)}(k_r a) H_1^{(2)}(k_r a) - H_0^{(2)}(k_r a) H_1^{(1)}(k_r a) \right]$$

The Wronskian for the Hankel functions is

$$W \{ H_n^{(1)}(x), H_n^{(2)}(x) \} = \frac{-4i}{\pi x} = H_{n+1}^{(1)}(x) H_n^{(2)}(x) - H_n^{(1)}(x) H_{n+1}^{(2)}(x)$$

therefore $\Delta a = \frac{-4i}{\pi Z k_r a}$, and the desired A, B, C, D parameters are:

$$A = -i \frac{\pi}{4} k_r a \left[H_0^{(1)}(k_r b) H_1^{(2)}(k_r a) - H_0^{(2)}(k_r b) H_1^{(1)}(k_r a) \right] \quad (2.25)$$

$$B = \frac{\pi}{4} k_r a Z \left[H_0^{(1)}(k_r b) H_0^{(2)}(k_r a) - H_0^{(2)}(k_r b) H_0^{(1)}(k_r a) \right] \quad (2.26)$$

$$C = \frac{\pi}{4} \frac{k_r a}{Z} \left[H_1^{(1)}(k_r b) H_1^{(2)}(k_r a) - H_1^{(2)}(k_r b) H_1^{(1)}(k_r a) \right] \quad (2.27)$$

$$D = -i \frac{\pi}{4} k_r a \left[H_1^{(2)}(k_r b) H_0^{(1)}(k_r a) - H_1^{(1)}(k_r b) H_0^{(2)}(k_r a) \right] \quad (2.28)$$

A B C D Parameters Expressed in Bessel Functions

Using the definitions of the Hankel functions, $H_n^{(1)}(x) = J_n(x) + iY_n(x)$ and $H_n^{(2)}(x) = J_n(x) - iY_n(x)$ the A B C D parameters may be expressed in the form

$$A = \frac{\pi}{2} k_r a [J_1(k_r a) Y_0(k_r b) - J_0(k_r b) Y_1(k_r a)] \quad (2.29)$$

$$B = i \frac{\pi}{2} k_r a Z [J_0(k_r a) Y_0(k_r b) - J_0(k_r b) Y_0(k_r a)] \quad (2.30)$$

$$C = i \frac{\pi}{2} \frac{k_r a}{Z} [J_1(k_r a) Y_1(k_r b) - J_1(k_r b) Y_1(k_r a)] \quad (2.31)$$

$$D = \frac{\pi}{2} k_r a [J_1(k_r b) Y_0(k_r a) - J_0(k_r a) Y_1(k_r b)] \quad (2.32)$$

Note that A and D are real, whereas B and C are imaginary.

A Compact Notation for A B C D Parameters

Hermann and Mirsky (1956) defined a new symbol to represent combinations of Bessel functions of the form shown above. Their definition is:

$$Q_{mn}(k_r) = J_m(k_r a) Y_n(k_r b) - J_n(k_r b) Y_m(k_r a)$$

Using this definition facilitates a more compact expression of the A B C D parameters, viz.

$$A = \frac{\pi}{2} k_r a Q_{10}(k_r)$$

$$B = i \frac{\pi}{2} k_r a Z Q_{00}(k_r)$$

$$C = i \frac{\pi}{2} \frac{k_r a}{Z} Q_{11}(k_r)$$

$$D = -\frac{\pi}{2} k_r a Q_{01}(k_r)$$

Zero Thickness Fluid Tube

As a check on the preceding results, let $a = b$, that is, the tube has zero thickness.

Substituting $a = b$ in Equation 2.29 we have

$$A = \frac{\pi}{2} k_r a [J_1(k_r a) Y_0(k_r a) - J_0(k_r a) Y_1(k_r a)]$$

The expression in brackets is the Wronskian, which equals $\frac{2}{\pi k_r a}$, thus for this case, $A = 1$. The product terms in B and C cancel, so that $B = C = 0$. In similar fashion, $D = 1$. Therefore the transfer matrix reduces to

$$\begin{bmatrix} \hat{P}_b \\ \hat{V}_b \end{bmatrix} = \begin{bmatrix} 1 & 0 \\ 0 & 1 \end{bmatrix} \begin{bmatrix} \hat{P}_a \\ \hat{V}_a \end{bmatrix}$$

That is, $\hat{P}_b = \hat{P}_a$ and $\hat{V}_b = \hat{V}_a$, as expected.

A B C D For Imaginary Radial Wavenumber

When the axial wavenumber k_z exceeds the acoustic wavenumber k , the radial wavenumber is imaginary. Using the same notation as in Case 3 for the fluid cylinder we substitute $k_r = i\bar{k}_r$ into Equations 2.25 to 2.28 and replace the Hankel functions with the modified Bessel functions, viz.

$$H_n^{(1)}(i\bar{k}_r a) = \frac{2}{\pi i^{n+1}} K_n(\bar{k}_r a)$$

and

$$H_n^{(2)}(i\bar{k}_r a) = 2i^n I_n(\bar{k}_r a) - \frac{2}{\pi i^{n+1}} K_n(\bar{k}_r a)$$

The resulting $A B C D$ values for the fluid tube with imaginary radial wavenumber are

$$A = \bar{k}_r a [K_0(\bar{k}_r b) I_1(\bar{k}_r a) + K_0(\bar{k}_r a) I_1(\bar{k}_r b)] \quad (2.33)$$

$$B = i\rho c \bar{k}_r a \left[K_0(\bar{k}_r a) I_0(\bar{k}_r b) - K_0(\bar{k}_r b) I_0(\bar{k}_r a) \right] \quad (2.34)$$

$$C = \frac{i\bar{k}_r^2 a}{\rho c k} \left[K_1(\bar{k}_r b) I_1(\bar{k}_r a) - K_1(\bar{k}_r a) I_1(\bar{k}_r b) \right] \quad (2.35)$$

$$D = \bar{k}_r a \left[K_0(\bar{k}_r a) I_1(\bar{k}_r b) + K_1(\bar{k}_r b) I_0(\bar{k}_r a) \right] \quad (2.36)$$

Again we note that A and D are real, whereas B and C are imaginary.

2.3.3 Transfer Function From b to a

As mentioned earlier, the transfer function from the outer surface at $r = b$ to the inner surface at $r = a$ is defined by

$$[M_{ba}] = [M_a] [M_b]^{-1}$$

When this is solved for the $A B C D$ parameters in the same manner as for the preceding case, the expressions take the same form but with the values of a and b interchanged, viz.

$$A = \frac{\pi}{2} k_r b \left[J_1(k_r b) Y_0(k_r a) - J_0(k_r a) Y_1(k_r b) \right] \quad (2.37)$$

$$B = i\frac{\pi}{2} k_r b Z \left[J_0(k_r b) Y_0(k_r a) - J_0(k_r a) Y_0(k_r b) \right] \quad (2.38)$$

$$C = i\frac{\pi}{2} \frac{k_r b}{Z} \left[J_1(k_r b) Y_1(k_r a) - J_1(k_r a) Y_1(k_r b) \right] \quad (2.39)$$

$$D = \frac{\pi}{2} k_r b \left[J_1(k_r a) Y_0(k_r b) - J_0(k_r b) Y_1(k_r a) \right] \quad (2.40)$$

2.3.4 Large Argument Approximations for Transfer Functions

The $A B C D$ parameters for large values of the argument are determined using the asymptotic values of the Hankel functions,

$$H_n^{(1)}(z) \approx \sqrt{\frac{2}{\pi z}} e^{i(z - n\frac{\pi}{2} - \frac{\pi}{4})}, \quad z \gg 2\pi$$

and

$$H_n^{(2)}(z) \approx \sqrt{\frac{2}{\pi z}} e^{-i(z - n\frac{\pi}{2} - \frac{\pi}{4})}$$

Substituting these relationships into Equations 2.25 to 2.28 and simplifying the results yields the following expressions for $A B C D$ for large real values of the non-dimensional radial wavenumbers, $k_r a$ and $k_r b$:

$$A \approx \sqrt{\frac{a}{b}} \cos k_r (b - a) \quad (2.41)$$

$$B \approx iZ \sqrt{\frac{a}{b}} \sin k_r (b - a) \quad (2.42)$$

$$C \approx \frac{i}{Z} \sqrt{\frac{a}{b}} \sin k_r (b - a) \quad (2.43)$$

$$D \approx \sqrt{\frac{a}{b}} \cos k_r (b - a) \quad (2.44)$$

Now if we let h represent the thickness of the fluid tube, that is $h = b - a$, and assume that h is very small compared to b , so that

$$\sqrt{\frac{a}{b}} = \sqrt{1 - \frac{h}{b}} \approx 1, \quad h \ll b$$

then

$$A = D \approx \cos k_r h$$

$$B \approx iZ \sin k_r h$$

$$C \approx \frac{i}{Z} \sin k_r h$$

Recalling that $Z = \frac{\rho ck}{k_r}$, $k = \frac{\omega}{c}$, and $k_r = \sqrt{k^2 - k_z^2}$, we observe that the asymptotic expressions for the two port model of a fluid tube reduce to those developed for plane waves in another study. (Stepanishen, 1985)

Imaginary Large Argument

When the non-dimensional radial wavenumber is large and imaginary, $\bar{k}_r a \gg 2\pi$, the modified Bessel functions are replaced with $I_n(\bar{k}_r a) \approx \frac{\exp(\bar{k}_r a)}{\sqrt{2\pi \bar{k}_r a}}$ and $K_n(\bar{k}_r a) \approx \sqrt{\frac{\pi}{2\bar{k}_r a}} \exp(-\bar{k}_r a)$

Using these expressions in Equations 2.33 to 2.36 yields the following equations for the $A B C D$ parameters for large imaginary values of the argument $\bar{k}_r a$:

$$A = D \approx \sqrt{\frac{a}{b}} \cosh\left(\frac{b}{a} - 1\right) \exp(\bar{k}_r a)$$

$$B \approx \frac{i\rho ck}{\bar{k}_r} \sqrt{\frac{a}{b}} \sinh\left(\frac{b}{a} - 1\right) \exp(\bar{k}_r a)$$

$$C \approx \frac{-i\bar{k}_r}{\rho ck} \sqrt{\frac{a}{b}} \sinh\left(\frac{b}{a} - 1\right) \exp(\bar{k}_r a)$$

We note that these expressions indicate that the negative square root must be chosen for \bar{k}_r in order to represent an evanescent wave which decays with radial distance.

2.3.5 Discussion of Fluid Tube Transfer Function

We now consider the behavior of the fluid tube $A B C D$ parameters as functions of the radial wavenumber and the fluid tube radial dimensions.

It is convenient to begin with the asymptotic approximations for large arguments since the trigonometric functions involved are simpler than the exact relationships which are the products of Bessel functions.

We also introduce the dimensionless ratio of the outer to inner radius, $s = b/a$.

Substituting into Equations 2.41 to 2.44 we have

$$A = D \approx \frac{1}{\sqrt{s}} \cos [k_r a (s - 1)]$$

$$B \approx \frac{i \rho c k}{k_r \sqrt{s}} \sin [k_r a (s - 1)]$$

$$C \approx \frac{i k_r}{\rho c k \sqrt{s}} \sin [k_r a (s - 1)]$$

These functions are periodic with period $k_{r,n} s (s - 1) = 2\pi n$. The amplitude coefficient $1/\sqrt{s} = \sqrt{\frac{a}{b}}$ reflects the decrease in magnitude of the pressure and velocity at b relative to a due to cylindrical spreading.

As s is increased the frequency of variation with radial wavenumber $k_r a$ also increases; that is, there is a larger number of pressure and velocity cycles between the inner and outer radii.

Now let the axial wavenumber $k_z = 0$ so that there is no propagation in the axial direction. For this case the radial wavenumber k_r equals the acoustic wavenumber k . The equations of state for this case are:

$$\hat{P}_b = \frac{\hat{P}_a}{\sqrt{s}} \cos [ka(s-1)] + i \frac{\rho c}{\sqrt{s}} \hat{V}_a \sin [ka(s-1)]$$

$$\hat{V}_b = \frac{i \hat{P}_a}{\rho c \sqrt{s}} \sin [ka(s-1)] + \frac{\hat{V}_a}{\sqrt{s}} \cos [ka(s-1)]$$

Now when $ka(s-1) = n\pi$, $n = 0, 1, 2, \dots$ the sine terms vanish, and the cosine terms equal $(-1)^n$. The transfer equations reduce to

$$\hat{P}_b = (-1)^n \frac{\hat{P}_a}{\sqrt{s}}$$

and

$$\hat{V}_b = (-1)^n \frac{\hat{V}_a}{\sqrt{s}}$$

Thus the pressure and velocity at b are either in phase, or 180° out of phase with those at a . This condition occurs when the tube thickness, $h = (b - a)$ is an integral number of half wavelengths, $h = n\lambda_n/2$ or at a frequency $\omega_n = \pi n c / h$.

Similarly, when $ka(s-1) = (2n+1)\pi/2$, the sine terms equal $(-1)^n$ and the cosine terms vanish. The result is

$$\hat{P}_b = i(-1)^n \rho c \frac{\hat{V}_a}{\sqrt{s}}$$

and

$$\hat{V}_b = i(-1)^n \frac{\hat{P}_a}{\rho c \sqrt{s}}$$

This will be true when the thickness h is an odd number of quarter wavelengths, i. e. $h = (2n+1)\lambda/4$, or $\omega_n = (2n+1)\pi c / 2h$

The conditions just discussed describe a radial standing wave in the fluid tube.

For the general case of interest in which the large argument approximations are not valid, the $A B C D$ parameters are computed using one of the sets of expressions presented earlier, such as Equations 2.29 to 2.32. The parameters are plotted in Figure 2-10 as a function of the non-dimensional wavenumber $k_r a$ for three values of the ratio of radii, $s = 1.5, 2$, and 3 . The plots for B and C are normalized with respect to the spectral impedance Z , that is, $C' = -iCZ$ and $B' = -iB/Z$.

The behavior of the $A B C D$ parameters in gross aspect follows the pattern indicated by the asymptotic approximations. Both A and D are similar to cosine functions, whereas B and C resemble sine functions. The amplitude of the envelope of the parameters decreases with increasing values of s .

Using the asymptotic expressions for the Bessel functions with small argument in Equations 2.29 to 2.32 and taking the limit as $k_r \rightarrow 0$, we find:

$$\lim_{k_r \rightarrow 0} A = 1; \quad \lim_{k_r \rightarrow 0} B = \lim_{k_r \rightarrow 0} C = 0; \quad \lim_{k_r \rightarrow 0} D = \frac{1}{s}$$

This condition will occur when the axial wavenumber k_z equals the acoustic wavenumber k . For this case, the pressures at a and b are equal, and $\hat{V}_b = \hat{V}_a/s$. This would be the situation for a plane wave propagating in the fluid tube with no radial component.

Figures 2-11 to 2-14 depict the $A B C D$ parameters as three dimensional surfaces for values of $k_r a$ ranging from 0 to 5, and for s ranging from 2 to 5. The features described above are clearly indicated in these plots.

2.3.6 Free Wave Propagation

We now consider the propagation of free waves in a fluid tube. In contrast to the preceding analysis, in which both the axial wavenumber k_z and frequency were assumed to be independent variables, now their relationship is determined by the radial wavenumber k_r , which in turn takes on discrete values that are established by the boundary conditions.

The transfer function parameters provide a convenient means for determining the conditions which govern the propagation of free waves in the fluid tube. We recall that the transfer equations are:

$$\hat{P}_b = \hat{P}_a A + \hat{V}_a B \quad (2.45)$$

$$\hat{V}_b = \hat{P}_a C + \hat{V}_a D \quad (2.46)$$

in which $\hat{P}_a, \hat{P}_b, \hat{V}_a$ and \hat{V}_b are the state variables at the surfaces $r = a$ and $r = b$, respectively. Four cases for free wave propagation may be defined in terms of the state variables at the boundaries:

Case	Description	Boundary Conditions
I	Free-Free	$P_a = 0, P_b = 0$
II	Free-Fixed	$P_a = 0, V_b = 0$
III	Fixed-Free	$V_a = 0, P_b = 0$
IV	Fixed-Fixed	$V_a = 0, V_b = 0$

Case I, Free-Free Boundary

Now consider Case I. For the free-free case, the pressure must be zero at both the inner and outer surfaces of the fluid cylinder. Setting $P_a = P_b = 0$ in Equations 2.45 and 2.46 results in the following two equations: $V_a B = 0$ and $V_b = V_a D$. This in turn requires that $B = 0$. Substituting for B in Equation 2.26 yields the characteristic equation for the propagation of free waves:

$$H_0^{(1)}(k_r a s) H_0^{(2)}(k_r a) - H_0^{(2)}(k_r a s) H_0^{(1)}(k_r a) = 0 \quad (2.47)$$

Denoting the roots of this equation as h_m , free waves may exist for values of the radial wavenumber such that

$$k_{r,m} = \frac{h_m}{a}$$

To investigate these roots, we first consider the case for which the argument $k_{r,m} a$ is large. Using the asymptotic expressions for the Hankel functions, the roots of Equation 2.47 occur at values of k_r which satisfy the following relation:

$$\exp[i(2k_r a \{s - 1\})] = 1$$

This condition is met for values of the radial wavenumber $k_{r,m}$ such that

$$k_{r,m} = \frac{m\pi}{a(s-1)}, \quad m = 1, 2, 3, \dots \quad (2.48)$$

Expressing this in terms of the tube thickness $(b - a)$,

$$k_{r,m} = \frac{m\pi}{(b - a)}$$

we see that the radial wavenumber $k_{r,m}$ for a given mode number m decreases as the tube thickness increases.

The exact values of the roots h_m must be determined by numerical solution of the characteristic equation, 2.47. The asymptotic value of the root $k_{r,m}a$ for a particular mode number m is used as the estimated root in a root solving algorithm. The roots for the first ten modes are listed in Table I for four values of s : 1.5, 2, 3, and 5. Also shown in Table I is the error (expressed as a percentage of the exact value) which results when the asymptotic approximation for the root is used. For a particular mode number, the error increases as the ratio $s = b/a$ increases.

The error is plotted as a function of the mode number for four values of s in Figure 2-15.

Case II, Free-Fixed Boundary

In Case II, the inner surface of the fluid tube is free, and the outer surface is blocked. Thus in Equations 2.45 and 2.46, P_a and V_b are zero. This is satisfied if the parameter D equals zero. From Equation 2.28, the characteristic equation for Case II is

$$H_1^{(2)}(k_r a s) H_0^{(1)}(k_r a) - H_1^{(1)}(k_r a s) H_0^{(2)}(k_r a) = 0 \quad (2.49)$$

Again, using the asymptotic expressions for the Hankel functions to determine the approximate roots of 2.49 we obtain

$$\exp[i2(k_r a \{s - 1\} - \frac{\pi}{2})] = 1$$

Thus the approximate values of the roots for this case are given by

$$h_m = k_{r,m}a = \frac{(2m+1)\pi}{2(s-1)}, \quad m = 1, 2, 3, \dots \quad (2.50)$$

This result was used in the characteristic equation to determine the exact values of the roots for the first ten modes as in Case I. The results are presented in Table II. Figure 2-16 shows the error as a function of the mode number for four values of s .

Case III, Fixed-Free Boundary Case III is the reverse of Case II in that the inner boundary is rigid and the outer boundary is free, so that V_a and P_b are zero. Thus $A = 0$ and the characteristic equation is

$$H_0^{(1)}(k_ras) H_1^{(2)}(k_ra) - H_0^{(2)}(k_ras) H_1^{(1)}(k_ra) = 0 \quad (2.51)$$

For large values of the argument k_ra the asymptotic form of this equation is

$$\exp[i2(k_ra\{s-1\} - \frac{\pi}{2})] = 1.$$

This is identical with the result for Case II, hence the approximate values for the roots of Equation 2.51 are given by Equation 2.50. Table III lists the exact values of the roots for the first ten modes of Case III for four values of s . Figure 2-17 shows the error as a function of mode number for the same values of s .

Comparing Figure 2-16 with Figure 2-17 we note that the approximate formula predicts a value of the roots which is too large in Case II, and too small in Case III.

Case IV, Fixed-Fixed Boundary Finally, for Case IV, the fixed boundaries at a and b imply that the radial velocities V_a and V_b vanish, which in turn requires that $C = 0$. The characteristic equation for this case is

$$\frac{(k_r a)^2}{\rho c k a} [H_1^{(1)}(k_r a s) H_1^{(2)}(k_r a) - H_1^{(2)}(k_r a s) H_1^{(1)}(k_r a)] = 0 \quad (2.52)$$

The asymptotic solution to this is identical with that for Case I, and the approximate roots are given by Equation 2.48. The exact roots for the first ten modes are listed in Table IV, and Figure 2-18 shows the error as a function of mode number and s . Comparing the results for Case I with those for Case IV, we note that the asymptotic formula yields a positive error for the free-free case, and a negative error for the fixed-fixed case. We note that Case IV is the only one to which supports a plane-wave mode.

Up to this point in the analysis we have used the characteristic equations in complex form for ease of manipulation in determining the asymptotic expressions for the roots. The $A B C D$ parameters may also be cast in the form given in Equations 2.29 to 2.32, which results in the following expressions for the characteristic equations:

Case I:

$$J_0(k_r a) Y_0(k_r a s) - J_0(k_r a s) Y_0(k_r a) = 0$$

Case II:

$$J_1(k_r a s) Y_0(k_r a) - J_0(k_r a) Y_1(k_r a s) = 0$$

Case III:

$$J_1(k_r a) Y_0(k_r a s) - J_0(k_r a s) Y_1(k_r a) = 0$$

Case IV:

$$\frac{(k_r a)^2}{\rho c k a} [J_1(k_r a) Y_1(k_r a s) - J_1(k_r a s) Y_1(k_r a)] = 0$$

The characteristic equations for the four cases analyzed for the fluid tube are plotted as a function of the non-dimensional wavenumber $k_r a$ in Figures 2-19 to 2-22 for radii ratios of 1.5, 2, and 3. We note that as the ratio of radii s increases, the number of zeros for a given range of the non-dimensional wavenumber also increases. Physically this simply means that the modal density is greater in a thick walled fluid tube than in a thin one.

2.3.7 Mode Shapes in a Fluid Tube

We now consider the mode shapes of the pressure and velocity in a fluid tube with the four sets of boundary conditions described above. Guidance for this effort is provided by the analysis of a rectangular fluid waveguide (Redwood, 1960). The rectangular waveguide is the limiting case of a fluid tube of infinite radius. The mode shapes in the rectangular waveguide comprise simple sinusoidal functions, considerably simpler than those of the finite radius fluid tube.

To proceed, we use Equation 2.18 for pressure and Equation 2.19 for the radial velocity. Using the appropriate boundary conditions in these equations establishes the relation between the unknown coefficients E and F .

For example, in Case I, substitution of $r = a$ and $p = 0$ yields

$$F = -E \frac{H_0^{(1)}(h_m)}{H_0^{(2)}(h_m)}$$

where $h_m = k_{r,m} a$ is the m th root of the characteristic equation.

Thus the pressure for the m th mode is given by

$$p_m(r, \omega, z) = E \left[H_0^{(1)} \left(h_m \frac{r}{a} \right) - \frac{H_0^{(1)}(h_m)}{H_0^{(2)}(h_m)} H_0^{(2)} \left(h_m \frac{r}{a} \right) \right] \exp [i (k_z z - \omega t)]$$

where the axial and time dependence have been included.

The Hankel functions may be written in polar form as $H_n^{(1)}(h_m) = M_n(h_m) \exp(i\theta_m)$

and $H_n^{(2)}(h_m) = M_n(h_m) \exp(-i\theta_m)$, where $M_n(h_m) = \pm \sqrt{J_n(h_m)^2 + Y_n(h_m)^2}$

and $\theta_m = \arctan \left(\frac{Y_n(h_m)}{J_n(h_m)} \right)$. Then $\frac{H_n^{(1)}(h_m)}{H_n^{(2)}(h_m)} = \exp(2i\theta_m)$, and the pressure may be written as:

$$p_m(r, \omega, z) = E \left[H_0^{(1)} \left(h_m \frac{r}{a} \right) - H_0^{(2)} \left(h_m \frac{r}{a} \right) \exp(2i\theta_m) \right] \exp [i (k_z z - \omega t)] \quad (2.53)$$

Equation 2.53 expresses the solution for pressure in complex notation. To find the actual physical pressure, we replace the Hankel functions with the Bessel and Neuman functions, and the complex exponentials with sine and cosine functions. Expanding the result and taking the real part results in:

$$p_m(r, \omega, z) = E \left\{ J_0 \left(h_m \frac{r}{a} \right) [1 - \cos(2\theta_m)] - Y_0 \left(h_m \frac{r}{a} \right) \sin(2\theta_m) \right\} \{\cos(k_z z - \omega t)\} \quad (2.54)$$

The variable E is seen to be a real, arbitrary pressure amplitude coefficient.

The radial velocity is obtained using Equation 2.19,

$$v_r(r, \omega, z) = \frac{ik_r}{\rho c k} \left[E H_1^{(1)}(k_r r) + F H_1^{(2)}(k_r r) \right] \exp [i (k_z z - \omega t)]$$

Using the expression for F found above, the radial velocity for the m th mode is given by

$$v_{r,m}(r, \omega, z) = \frac{ik_r E}{\rho c k} \left\{ \left[H_1^{(1)} \left(h_m \frac{r}{a} \right) - H_1^{(2)} \left(h_m \frac{r}{a} \right) \exp(2i\theta_m) \right] \exp [i (k_z z - \omega t)] \right\}$$

Expanding and taking the real part, the final expression for the radial velocity is

$$v_{r,m}(r, \omega, z) = \frac{k_r E}{\rho c k} \left\{ J_1 \left(h_m \frac{r}{a} \right) \sin(2\theta_m) - Y_1 \left(h_m \frac{r}{a} \right) [1 + \cos(2\theta_m)] \right\} \{\cos(k_z z - \omega t)\}$$

The axial velocity may be obtained by applying the momentum equation to Equation 2.54 with the result

$$v_{z,m}(r, \omega, z) = \frac{k_z}{\rho c k} p_m(r, \omega, z)$$

The axial velocity is real and in phase with the pressure, which one would expect for a propagating wave.

The equations for the mode shapes of the remaining three cases are identical with those for Case I, but with the appropriate root from the characteristic equation, and with the angle θ_m determined by the boundary conditions.

Thus for Case II (free-fixed), setting $p = 0$ at $r = a$ results in the same value of θ_m as was found for Case I.

The boundary condition for Case III (fixed-free) requires that $p = 0$ at $r = b$ with the result

$$\theta_m = \arctan \left[\frac{Y_0(h_m s)}{J_0(h_m s)} \right]$$

In Case IV (fixed-fixed), setting $v_r = 0$ at $r = a$ yields

$$\theta_m = \arctan \left[\frac{Y_1(h_m)}{J_1(h_m)} \right]$$

Plots of the pressure and radial velocity as a function of the normalized radius ($u = \frac{r}{a}$) for the first three modes for each of the cases studied are presented in Figures 2-23 to 2-26. The radius ratio $s = 10$ for these plots.

The modes in the fluid tube are considerably more complicated than those in a rectangular fluid waveguide or in a fluid cylinder. This is primarily because the boundary conditions for the fluid cylinder are specified at two different physical dimensions, the inner and outer radii (or, equivalently, the inner radius and the radii ratio), whereas the rectangular waveguide and the fluid cylinder are characterized by one physical dimension. In the case of the rectangular waveguide, it is the thickness h , and for the fluid cylinder, the radius a . In the rectangular waveguide, the modes are described by trigonometric functions (sines and cosines), and the peak modal amplitudes are ± 1 for all cases. Also, there is "left-right" symmetry between the free-fixed modes of Case II and the fixed-free modes of Case III. That is, interchanging the boundaries results in a reflection of the mode shapes about the center of the waveguide. This is not the case for the fluid tube.

Mode shapes for the free-free situation of Case I are shown in Figure 2-23. There is no "plane wave" ($m = 0$) mode, unless one considers the trivial case for which the pressure is everywhere zero.

A salient feature of these plots is that the peak modal amplitudes of both pressure and radial velocity vary as functions both of the mode number and the radii ratio, s .

For small values of s , eg $s = 2$, the mode shapes appear almost sinusoidal. As s increases, the mode shapes appear more like the Bessel functions, with large peak amplitudes near the inner radius, and decreasing in amplitude as the outer radius is approached. With increasing s , the node for velocity in mode 1 moves

towards the inner radius a .

The fluid cylinder with both boundaries fixed (Case IV) supports a plane wave mode, unlike the other three cases. This is evident by inspection of the characteristic equation for Case IV, which exhibits a root at $k_r a = 0$. Mode shapes for $m = 1$ to $m = 3$ are shown in Figure 2-24. As s increases, the node for the pressure in mode 1 moves towards the outer radius b .

Cutoff Frequencies

All of the modes for the fluid cylinder (with the exception of the plane wave mode for case IV) will exhibit a cutoff frequency below which propagation will not occur. This cutoff frequency is established by the root of the characteristic equation for the mode, h_m , the inner radius a , and the sound speed c :

$$\omega_c = \frac{h_m c}{a}$$

2.4 External Fluid

2.4.1 Introduction

The final component in any arrangement of concentric cylindrical models is the external medium. In contrast to the other components, which have finite radial boundaries, the external medium is presumed to extend to infinity in the radial direction. This assumption permits the radiation of acoustical energy in the radial as well as in the axial direction.

In this study we restrict our attention to inviscid fluid media, such as air and water. However, solid external media could be incorporated if desired by using

elasticity theory.

A number of authors have discussed the propagation of cylindrical waves, including Morse (1948), Rschevkin (1963), Morse and Ingard (1968), and Junger and Feit (1986).

An especially cogent analysis by Junger (1953) provides an excellent paradigm for the present discussion. In his paper, Junger postulates an infinitely long cylindrical surface which experiences a time harmonic, spatially periodic standing wave excitation in both the circumferential and axial directions. He then constructs solutions to the inhomogeneous wave equation and obtains expressions for the specific acoustic impedance in the external fluid. In a section titled "Physical Interpretation" Junger presents an especially lucid description of cylindrical waves in the fluid medium.

In this section, we analyze the propagation of cylindrical waves in the external medium. The pressure and particle velocity are described at the medium interface and in the field as functions of frequency (acoustic wavenumber) and the axial wavenumber, k_z . The spectral impedance at the interface is also discussed.

2.4.2 Physical Description

Consider an infinite length cylinder of radius a immersed in an inviscid, homogeneous fluid which extends radially to infinity. A travelling harmonic pressure wave of amplitude P_0 , frequency ω , and axial wavenumber k_z is postulated at the surface of the cylinder, as follows:

$$p_n(a, \theta, z, t) = P_0 \cos(n\theta) e^{i(k_z z - \omega t)}$$

The waves in the external fluid medium must decay to zero at $r = \infty$ and also must satisfy the reduced Helmholtz equation,

$$(\nabla^2 + k^2)p(r, \theta, z, t) = 0$$

where

$$\nabla^2 = \frac{\partial^2}{\partial r^2} + \frac{1}{r} \frac{\partial}{\partial r} + \frac{1}{r^2} \frac{\partial^2}{\partial \theta^2} + \frac{\partial^2}{\partial z^2}$$

Assume a field solution of the form

$$p_n(r, \theta, z, t) = \cos n\theta \left[A_n H_n^{(1)}(k_r r) + B_n H_n^{(2)}(k_r r) \right] e^{i(k_z z - \omega t)}$$

For large values of the argument $k_r r$ this may be written as

$$p_n(r, \theta, z, t) = \cos(n\theta) \sqrt{\frac{2}{\pi k_r r}} \left[A_n e^{i(k_r r + k_z z - \omega t - \frac{n\pi}{2} - \frac{\pi}{4})} + B_n e^{i(k_z z - k_r r - \omega t + \frac{n\pi}{2} + \frac{\pi}{4})} \right]$$

The first term within the brackets describes a wave propagating in the positive axial and radial directions, that is, an outgoing conical wave. The second term represents an incoming wave. Since we are interested only in the outgoing wave, we discard the second term, and the B_n coefficients are set equal to zero. Thus the pressure in the field is given by

$$p_n(r, \theta, z, t) = \cos(n\theta) A_n H_n^{(1)}(k_r r) e^{i(k_z z - \omega t)} \quad (2.55)$$

Equating this expression to the excitation pressure wave at $r = a$ enables determination of the coefficients A_n as:

$$A_n = \frac{P_0}{H_n^{(1)}(k_r a)}$$

The velocity in the field is determined using the harmonic form of the momentum equation,

$$\nabla p = i\rho ck \mathbf{v}$$

In cylindrical coordinates this is written

$$\mathbf{v} = \frac{1}{i\rho ck} \left[\mathbf{e}_r \frac{\partial p}{\partial r} + \frac{\mathbf{e}_\theta}{r} \frac{\partial p}{\partial \theta} + \mathbf{e}_z \frac{\partial p}{\partial z} \right] = \mathbf{e}_r v_r + \mathbf{e}_\theta v_\theta + \mathbf{e}_z v_z$$

The three components of velocity thus are:

Radial:

$$v_r = -\frac{ik_r \cos(n\theta) P_0}{\rho ck H_n^{(1)}(k_r a)} \left[\frac{n}{k_r r} H_n^{(1)}(k_r r) - H_{(n+1)}^{(1)}(k_r r) \right] e^{i(k_z z - \omega t)} \quad (2.56)$$

Tangential:

$$v_\theta = \frac{in \sin(n\theta) P_0 H_n^{(1)}(k_r r)}{\rho ck r H_n^{(1)}(k_r a)} e^{i(k_z z - \omega t)}$$

Axial:

$$v_z = \frac{k_z \cos(n\theta) P_0 H_n^{(1)}(k_r r)}{\rho ck H_n^{(1)}(k_r a)} e^{i(k_z z - \omega t)}$$

2.4.3 Wave Propagation

Real Radial Wavenumber For clarity we consider the axisymmetric case, $n = 0$, to investigate the propagation of cylindrical waves in the external medium.

Thus for $n = 0$ the pressure in the field is given by:

$$p(r, z, t) = \frac{P_0 H_0^{(1)}(k_r r)}{H_0^{(1)}(k_r a)} e^{i(k_z z - \omega t)}$$

Since $n = 0$ the tangential particle velocity is zero. The radial particle velocity is given by:

$$v_r = \frac{ik_r P_0 H_1^{(1)}(k_r r)}{\rho c k H_0^{(1)}(k_r a)} e^{i(k_z z - \omega t)}$$

and the axial particle velocity is

$$v_z = \frac{k_z P_0 H_0^{(1)}(k_r r)}{\rho c k H_0^{(1)}(k_r a)} e^{i(k_z z - \omega t)}$$

The Hankel functions may be written in polar form as

$$H_n^{(1)}(z) = M_n(z) e^{i\theta_n(z)}$$

where $M_n(z) = \sqrt{J_n(z)^2 + Y_n(z)^2}$ and $\theta_n(z) = \arctan \frac{Y_n(z)}{J_n(z)}$. With this notation,

$$p(r, z, t) = \frac{P_0 M_0(k_r r) e^{i(\theta_0(k_r r) - \theta_0(k_r a) + k_z z - \omega t)}}{M_0(k_r a)}$$

For large values of the argument $k_r r$, $\theta_0(k_r r) \rightarrow k_r r - \frac{\pi}{4}$ and

$M_0(k_r r) \rightarrow \sqrt{\frac{2}{\pi k_r r}}$ thus the pressure in the limit becomes

$$p(r, z, t) \rightarrow \sqrt{\frac{2}{\pi k_r r}} \frac{P_0}{M_0(k_r a)} e^{i(k_r r + k_z z - \omega t - \phi)}$$

where $\phi = \theta_0(k_r a + \frac{\pi}{4})$ is a fixed phase angle. This describes a traveling wave with wavevector components k_r and k_z . The direction of propagation is indicated by the wavevector $\mathbf{k} = \mathbf{e}_r k_r + \mathbf{e}_z k_z$ which is inclined at an angle $\alpha_k = \arctan \frac{k_r}{k_z}$ with respect to the z axis.

The wavefront (surfaces of constant phase) are conical, symmetrical with respect to the z axis, and perpendicular to the wavevector \mathbf{k} . These relationships are shown in Figure 2-25.

If the axial wavenumber k_z is zero, the radial wavenumber k_r equals the acoustic wavenumber k . This represents a cylindrical wave traveling in the radial direction,

$$\lim_{k_r r \rightarrow \infty} p(r, t) = \sqrt{\frac{2}{\pi k_r r}} \frac{P_0}{M_0(k_r a)} e^{i(k_r r - \omega t - \phi)}$$

Note that the amplitude decays as $\frac{1}{\sqrt{r}}$, which is characteristic of cylindrical waves. This also satisfies the requirement that the wave vanish at $r = \infty$. We may compare this, for instance, with a spherical wave which falls off as $\frac{1}{r}$. The wavefronts are cylinders concentric with the z axis.

Zero Radial Wavenumber As the axial wavenumber approaches the acoustic wavenumber k the radial wavenumber approaches zero and radial phase velocity, $\frac{\omega}{k_r}$, becomes infinite. The result is a purely plane wave propagating in the z direction.

Imaginary Radial Wavenumber When the axial wavenumber exceeds the acoustic wavenumber, the radial wavenumber takes on a purely imaginary value. We will use the notation \bar{k}_r to represent the magnitude of the imaginary radial wavenumber, that is,

$$k_r = i\bar{k}_r = i\sqrt{k_z^2 - k^2}, \quad k_z > k$$

Using the expression for Hankel functions of imaginary argument, $H_n^{(1)}(ix) = \frac{2}{\pi} i^{-(n+1)} K_n(x)$, the expression for the pressure is

$$p(r, z, t) = \frac{P_0 K_0(\bar{k}_r r)}{K_0(\bar{k}_r a)} e^{i(k_z z - \omega t)}$$

For large arguments, $K_n(x) \rightarrow \sqrt{\frac{\pi}{2x}} e^{-x}$ thus for $k_r r$ large, the pressure becomes

$$\lim_{k_r r \rightarrow \infty} p(r, z, t) = \frac{P_0}{K_0(\bar{k}_r a)} \sqrt{\frac{\pi}{2k_r r}} e^{-\bar{k}_r r} e^{i(k_z z - \omega t)}$$

which represents an evanescent wave propagating in the z direction and falling off rapidly in the radial direction as $\sqrt{\frac{\pi}{2k_r r}} e^{-\bar{k}_r r}$.

2.4.4 Radial Spectral Impedance of External Fluid

We wish to study the radial spectral impedance of the external fluid as a function of the axial wavenumber k_r and the acoustic wavenumber k . The general expression for the radial spectral impedance of the external fluid may be obtained by dividing equation 2.55 by equation 2.56, with the result:

$$Z_{r,n} = \frac{i\rho c k H_n^{(1)}(k_r a)}{k_r \left[\frac{n}{k_r r} H_n^{(1)}(k_r r) - H_{(n+1)}^{(1)}(k_r r) \right]}$$

Specializing this to the $n = 0$ case and evaluating at $r = a$ results in

$$Z_a = -i\rho c \left[1 - \left(\frac{k_z}{k} \right)^2 \right]^{-\frac{1}{2}} \frac{H_0^{(1)}(k_r a)}{H_1^{(1)}(k_r a)} \quad (2.57)$$

The nature of Z_a thus depends on the values of k_z and k . Three cases of interest include:

- (I) $k_z = 0$; $k_r = k$ (cylindrical wave)
- (II) $k_z < k$; k_r is real (high frequency case)
- (III) $k_z > k$; k_r is imaginary (low frequency case)

Case I: Cylindrical Wave

When $k_z = 0$, there is no axial propagation and the impedance depends only on

the acoustic wavenumber. In normalized form, it is:

$$\frac{Z_a}{\rho c} = -i \frac{H_0^{(1)}(ka)}{H_1^{(1)}(ka)}$$

This may be separated into a real part, representing radiation resistance, and an imaginary part, representing reactance, as follows:

$$Re \left(\frac{Z_a}{\rho c} \right) = \frac{J_1(ka) Y_0(ka) + J_0(ka) Y_1(ka)}{J_1^2(ka) + Y_1^2(ka)}$$

and

$$Im \left(\frac{Z_a}{\rho c} \right) = \frac{Y_0(ka) Y_1(ka) - J_0(ka) J_1(ka)}{J_1^2(ka) + Y_1^2(ka)}$$

These functions are plotted in Figure 2-26 as functions of the non-dimensional acoustic wavenumber, ka .

The radiation resistance increases from zero at $ka = 0$ and asymptotically approaches unity for large values of the argument. This may be shown by considering

$$\lim_{ka \rightarrow \infty} Z_a = -i\rho c \lim_{ka \rightarrow \infty} \left(\frac{H_0^{(1)}(ka)}{H_1^{(1)}(ka)} \right) = -i\rho c \exp(i\frac{\pi}{2}) = \rho c$$

That is, the radiation resistance approaches the plane wave specific acoustic impedance for large values of ka .

The normalized radiation reactance, Figure 2-26 b, increases from zero at $ka = 0$ to a maximum magnitude of -0.3971 at $ka = 0.4617$, subsequently decreasing monotonically to zero at large values of ka . The negative value of the reactance indicates that physically it is mass-like, representing the accession to inertia of the external fluid.

Case II: High Frequency

When the axial wavenumber k_z is less than the acoustic wavenumber k , the radial wavenumber is real. The real and imaginary components of the normalized spectral impedance are:

$$Re\left(\frac{Z_a}{\rho c}\right) = \left[1 - \left(\frac{k_z}{k}\right)^2\right]^{-\frac{1}{2}} \left[\frac{J_1(ka)Y_0(ka) + J_0(ka)Y_1(ka)}{J_1^2(ka) + Y_1^2(ka)}\right]$$

and

$$Im\left(\frac{Z_a}{\rho c}\right) = \left[1 - \left(\frac{k_z}{k}\right)^2\right]^{-\frac{1}{2}} \left[\frac{Y_0(ka)Y_1(ka) - J_0(ka)J_1(ka)}{J_1^2(ka) + Y_1^2(ka)}\right]$$

Case III: Low Frequency

For $k < k_z$, the normalized impedance is:

$$\frac{Z_a}{\rho c} = -i \left[\left(\frac{k_z}{k}\right)^2 - 1 \right]^{-\frac{1}{2}} \left[\frac{K_0(\bar{k}_r a)}{K_1(\bar{k}_r a)} \right]$$

Since $K_0(\bar{k}_r a)$ and $K_1(\bar{k}_r a)$ are both real, $\frac{Z_a}{\rho c}$ is always imaginary for $k < k_z$.

For very low frequencies, i. e. $k \ll k_z$, $k_r \approx k_z$ and for $\bar{k}_r a \gg 1$, $\frac{K_0(\bar{k}_r a)}{K_1(\bar{k}_r a)} \rightarrow 1$, and

$$\lim_{\substack{k \rightarrow 0 \\ k_z a \gg 1}} Z_a = -i \frac{\rho \omega}{k_z}, \text{ a mass reactance.}$$

The real and imaginary components of the normalized spectral impedance are plotted as a function of ka in Figure 2-27. These curves are plotted for four values of $k_z a$; $\frac{\pi}{2}$, π , $\frac{3\pi}{2}$, and 2π .

The value of $k_z a$ divides the plots into the low frequency ($k < k_z$) and high frequency ($k > k_z$) regions.

In the low frequency region, the real part of Z_a is zero and there is no radiated acoustical energy. The reactance $Im(Z_a)$ increases with frequency. Both the real

and imaginary components become infinite at the cut-off frequency, where $k_r = 0$. This marks the transition between an evanescent radial wave component and a radiating radial wave component.

In the high frequency region the radiation resistance decreases as k increases, asymptotically approaching ρc when $k \gg k_z$, where $k_r \approx k$.

The radiation reactance increases with frequency below the cutoff frequency, and decreases above cutoff, falling to zero at high values of ka .

CHAPTER 3

Elastic Media

3.1 Introduction

A concise review of the historical development of vibration analysis is provided by Soedel (1981). Love (1888) is generally credited with having firmly established the basis for the analysis of vibrations in thin shells. The assumptions made in thin shell theory as described by Junger and Feit (1986) are: that the thickness of the shell is small compared with any length or surface dimension and with the smallest radius of curvature of the shell; that the displacement is small relative to the thickness; that the transverse normal stress acting on planes parallel to the shell middle surface is negligible; and that fibers of the shell normal to the middle surface remain so after deformation and are not subject to elongation. The problem is thus reduced to the determination of the deflection of the middle surface of the shell. Although there is no exact definition of "thinness", Krauss (1967) suggests that a maximum thickness to radius ratio of 1 to 10 defines the limitation of thin shell theory. Herrmann and Mirsky (1956) made a comparison between approximate shell theories with the exact solutions obtained using three dimensional elasticity theory. They concluded that when the wavelength of the vibration in the shell is greater than about thirty times the thickness of the shell, simple membrane shell theory adequately describes the shell behavior. For wavelengths greater than

about eight times the thickness, shell bending theory yields results which are in good agreement with the exact theory.

Since the early work of Love a large number of investigators have developed differing equations of motion for thin cylindrical shells. Leissa (1973) published an extensive monograph in which many of the different thin shell theories are compared in great detail. Leissa's monograph contains over 500 references dealing with circular cylindrical shells. Junger and Feit (1986) emphasize that most of the differences in thin shell theories are related to small differences in the strain-displacement relationships, which do not significantly affect numerical results.

The simplest theory for circular cylindrical shells includes only extensional (membrane) effects, resulting in a system of fourth order partial differential equations in the axial and azimuthal coordinates. When bending effects are included, the resulting equations are of eighth order. The alternative formulations of the "classical" shell theory result from different approximations made in representing the bending effects. When transverse shear and rotary inertia are included, a set of tenth order equations results. This case has been investigated by Naghdi and Cooper (1956) and by Lin and Morgan (1956), using the "strength of materials" approach. These authors obtained the dispersion curves and amplitude ratios for the first three axisymmetric modes of an infinite cylindrical shell. Later Cooper and Naghdi (1957) extended their work to include the non-axisymmetric modes for the first five axial modes with ten circumferential modes.

3.2 Thin Shell Theory

3.2.1 Equations of Motion for Thin Cylindrical Shells

In the current work, we shall employ the simplified equations of motion derived by Donnell (1933) as described by Junger and Feit (1986).

Thus we consider a thin cylindrical shell in a (r, θ, z) coordinate system. The thickness h of the shell is small compared with the mean radius a . The variables w, v , and u represent the radial, circumferential, and axial components of dynamic displacements of the shell midsurface, and are assumed to be small compared with the thickness h . A constant β is defined as

$$\beta^2 = \frac{h^2}{12a^2}$$

Terms proportional to β^2 in the equations of motion are due to the presence of bending stresses. Let Δp represent the differential pressure between the inside and outside surfaces of the shell when fluid loading is present. The Donnell equations then may be written as:

Axial:

$$\frac{\partial^2 u}{\partial z^2} + \frac{(1-\nu)}{2a^2} \frac{\partial^2 u}{\partial \theta^2} + \frac{(1+\nu)}{2a} \frac{\partial^2 v}{\partial z \partial \theta} + \frac{v}{a} \frac{\partial w}{\partial z} - \frac{1}{c_p^2} \frac{\partial^2 u}{\partial t^2} = 0$$

Tangential:

$$\frac{(1+\nu)}{2a} \frac{\partial^2 u}{\partial z \partial \theta} + \frac{(1-\nu)}{2} \frac{\partial^2 v}{\partial z^2} + \frac{1}{a^2} \frac{\partial^2 v}{\partial \theta^2} + \frac{1}{a^2} \frac{\partial w}{\partial \theta} - \frac{1}{c_p^2} \frac{\partial^2 v}{\partial t^2} = 0$$

Radial:

$$\frac{v}{a} \frac{\partial u}{\partial z} + \frac{1}{a^2} \frac{\partial v}{\partial \theta} + \frac{w}{a^2} + \beta^2 \left(a^2 \frac{\partial^4 w}{\partial z^4} + 2 \frac{\partial^4 w}{\partial^2 z^2 \partial \theta} + \frac{1}{a^2} \frac{\partial^4 w}{\partial^4 \theta} \right) + \frac{1}{c_p^2} \frac{\partial^2 w}{\partial t^2} + \Delta p \frac{(1-\nu^2)}{Eh} = 0$$

In these equations E is the Young's modulus of the shell material, ν is Poisson's ratio, and c_p is the low-frequency phase velocity of compressional waves in an elastic plate, given by

$$c_p = \sqrt{\frac{E}{\rho(1-\nu^2)}}$$

in which ρ is the density of the shell material.

3.2.2 Axisymmetric Case

In the present work, we are concerned with the axisymmetric response of the cylinder. With this restriction, all of the partial derivatives with respect to the angular coordinate θ vanish and the equations of motion simplify to:

Axial:

$$\frac{\partial^2 u}{\partial z^2} + \frac{\nu}{a} \frac{\partial w}{\partial z} - \frac{1}{c_p^2} \frac{\partial^2 u}{\partial t^2} = 0 \quad (3.1)$$

Tangential:

$$\frac{(1-\nu)}{2} \frac{\partial^2 v}{\partial z^2} - \frac{1}{c_p^2} \frac{\partial^2 v}{\partial t^2} = 0 \quad (3.2)$$

Radial:

$$\frac{\nu}{a} \frac{\partial u}{\partial z} + \frac{w}{a^2} + \beta^2 a^2 \frac{\partial^4 w}{\partial z^4} + \frac{1}{c_p^2} \frac{\partial^2 w}{\partial t^2} + \Delta p \frac{(1-\nu^2)}{Eh} = 0 \quad (3.3)$$

We note that in this simplified form, the equation for tangential displacement v is uncoupled from the equations for radial and axial motion. The latter two equations are cross-coupled via the Poisson's ratio, in the terms $\frac{\nu}{a} \frac{\partial w}{\partial z}$ and $\frac{\nu}{a} \frac{\partial u}{\partial z}$. It is this cross coupling which is responsible for most of the complications in the behavior of thin elastic shells.

3.3 Transfer Matrix Model of a Thin Shell

To obtain the transfer matrix for a thin shell, we apply the following two-dimensional Fourier transform to the axisymmetric thin shell equations, 3.1 and 3.3.

$$\hat{f}(k_z, \omega) = \iint_{-\infty}^{\infty} f(z, t) e^{-i(k_z z + \omega t)} dz dt$$

Application of this transformation to 3.1 yields:

$$-k_z \hat{u} - ik_z \frac{v}{a} \hat{w} + \frac{\omega^2}{c_p^2} \hat{u} = 0 \quad (3.4)$$

and operation on 3.3 results in:

$$-ik_z \frac{v}{a} \hat{u} + \hat{w} \left[\frac{1}{a^2} + \beta^2 a^2 k_z^4 - \frac{\omega^2}{c_p^2} \right] + \Delta p T = 0 \quad (3.5)$$

where $\hat{u} = \hat{u}(k_z, \omega)$, $\hat{w} = \hat{w}(k_z, \omega)$, and $T = \frac{(1-v^2)}{Eh}$.

Solving for \hat{u} in 3.4, substitution into 3.5, multiplying through by a^2 , and collecting terms results in

$$\hat{w} \left[\frac{k_z^2 v^2}{\left(\frac{\omega^2}{c_p^2} - k_z^2 \right)} + 1 + \beta^2 a^4 k_z^4 - \frac{\omega^2 a^2}{c_p^2} \right] + \Delta p a^2 T = 0 \quad (3.6)$$

Substitution of the non-dimensional frequency $\Omega = \omega a / c_p$ and the non-dimensional axial wavenumber $K_z = k_z a$ into equation 3.6 yields

$$\hat{w} \left[\frac{K_z^2 v^2}{(\Omega^2 - K_z^2)} + 1 + \beta^2 K_z^4 - \Omega^2 \right] + \Delta p a^2 T = 0 \quad (3.7)$$

The Fourier transform of the radial velocity is obtained from the radial displacement, $\hat{V}_r(k_z, \omega) = -i\omega \hat{w}(k_z, \omega)$. Then the radial spectral impedance of the thin shell is calculated as the ratio of differential pressure to radial velocity,

$$Z_s(\Omega, K_z) = \frac{-i\omega_r \rho h}{\Omega} \left[\frac{K_z^2 v^2}{(\Omega^2 - K_z^2)} + 1 + \beta^2 K_z^4 - \Omega^2 \right] \quad (3.8)$$

3.3.1 Two Port Matrix Model

Now let P_1 represent the pressure acting on the inner wall of the shell, and P_2 be the pressure on the exterior surface of the shell. One of the assumptions of thin shell theory is that there is no radial deformation of the shell, so that the radial velocity V_1 at the inner surface is equal to the radial velocity V_2 at the outer surface. The differential pressure across the shell is $\Delta p = P_1 - P_2$, and thus the shell may be represented by the following two port matrix:

$$\begin{bmatrix} P_1 \\ V_1 \end{bmatrix} = \begin{bmatrix} 1 & Z_s \\ 0 & 1 \end{bmatrix} \begin{bmatrix} P_2 \\ V_2 \end{bmatrix} \quad (3.9)$$

3.4 Analysis of Thin Shell in Wavenumber-Frequency Space

The study of free wave propagation in thin cylindrical shells has received the attention of many investigators, including the authors cited in the introduction to this chapter.

Smith (1955) used Kennard's equations of motion (Kennard, 1953) to compute the phase velocities and relative displacement magnitudes for all possible modes of free wave propagation in a thin shell. Naghdi and Cooper (1956) included the effects of transverse shear deformation and rotatory inertia in their model of a thin shell. Herrmann and Mirsky (1956) made a comparison of several thin shell theories with the exact results of elasticity theory. Their analysis determined the range of wall thickness to axial wavelength over which the various approximate theories are acceptable substitutes for the exact analysis. For the range of frequencies of interest in this study, the simplified equations of Donnell (1933) will adequately

describe the behavior of free waves in a thin cylindrical shell.

For this analysis we make use of equations 3.4 and 3.5, with the pressure term in 3.5 set equal to zero. Writing these equations in matrix form, we have:

$$\begin{bmatrix} \left(\frac{\omega^2}{c_p^2} - k_z \right) & -ik_z \frac{v}{a} \\ -ik_z \frac{v}{a} & \left(\frac{1}{a^2} + \beta^2 a^2 k_z^4 - \frac{\omega^2}{c_p^2} \right) \end{bmatrix} \begin{bmatrix} \hat{u} \\ \hat{w} \end{bmatrix} = \begin{bmatrix} 0 \\ 0 \end{bmatrix} \quad (3.10)$$

In order for free wave propagation to occur, the determinant of equation 3.10 must equal zero. This is the dispersion equation, also known as the characteristic equation. Expanding the determinant of 3.10 and substituting the non-dimensional variables Ω and K_z defined earlier results in the following form for the dispersion equation:

$$\Omega^4 - \Omega^2 [1 + K_z^2 + \beta^2 K_z^4] + K_z^2 [(1 - v^2) + \beta^2 K_z^4] = 0 \quad (3.11)$$

We note that equation 3.11 is of fourth order in Ω and sixth order in K_z . The only parameters which influence the behavior of equation 3.11 are Poisson's ratio v and the bending coefficient β . In this study we shall use the values $v = 0.37$ and $\beta = 0.0103$, which represent the experimental tube.

As discussed previously, the Donnell theory is limited in frequency range. Using the Herrmann and Mirsky criterion that the minimum axial wavelength is eight times the shell thickness, we find that the upper limit on the non-dimensional axial wavenumber is $K_z \leq \frac{\pi a}{15h}$, or $K_z \leq \pi/15\beta\sqrt{12}$.

The roots of 3.11 express the frequency as a function of the wavenumber for specified values of Poisson's ratio and β .

$$\Omega = \sqrt{\frac{[1 + K_z^2 + \beta^2 K_z^4] \pm \sqrt{[1 + K_z^2 + \beta^2 K_z^4]^2 - 4K_z^2 [(1 - v^2) + \beta^2 K_z^4]}}{2}} \quad (3.12)$$

The two roots of 3.12 define two branches of the dispersion equation for the $n = 0$ mode of the thin shell. The dispersion curves for the two branches are shown in figure 3-1, in which the frequencies are plotted as a function of the axial wavenumber. The dimensions of the experimental tube were used for these calculations.

Branch 2 is cut off below the "ring" frequency, where $\Omega = K_z$, $f_r = 25.1$ kHz, and $k_z = \frac{1}{a} = 40$ /meter. For wavenumbers far above the "ring" frequency, Branch 2 is not dispersive.

Branch 1 is non-dispersive for very small wavenumbers. If $\beta = 0$, that is, if there is no bending effect, the shell obeys membrane theory. For this situation, branch 1 will cut off slightly below the "ring" frequency. With β finite, the bending terms serve to inhibit the cutoff of branch 1. The wavenumber at which the dispersion curve of branch 1 bends upward varies inversely with β , that is, small values of β delay the upturn to larger wavenumbers.

The phase velocity, defined as $c_\varphi = \frac{2\pi f}{k_z}$, is shown for the two branches in figure 3-2. The phase velocity of branch 2 becomes infinite below the "ring" frequency, and is equal to the plate wavespeed, $c_p = 3939$ meters/second at high wavenumbers. The phase velocity of branch 1 approaches the longitudinal bar velocity, $c_b = c_p \sqrt{1 - v^2} = 3659$ meters/second for very low wavenumbers (Graff, 1975). As the wavenumber increases, the phase velocity of branch 1 decreases to a minimum and

then begins to rise again. The minimum phase velocity for branch 2 is given by $c_{\phi \min} = c_p \sqrt{\frac{h}{a} \sqrt{\frac{1-v^2}{3}}}$, (Herrmann and Mirsky, 1956), and for the experimental tube, $c_{\phi \min} = 544$ meters/second. Lin and Morgan (1956) developed an approximate equation for the frequency of minimum phase velocity. Their result may be put into the form $f_{\min} = f_r \sqrt{2(1-v^2)}$, where f_r represents the ring frequency. For the experimental tube, $f_{\min} = 33$ kHz.

The group velocity is defined as $c_g = \frac{d(2\pi f)}{dk_z}$ and is plotted for the two branches in figure 3-3. The group velocity for branch 2 increases from zero as the branch cuts on at the ring frequency, then levels off at the plate wavespeed c_p at high frequencies. The group velocity for branch 1 is equal to the bar velocity c_b at low wavenumbers and drops rapidly as the "ring" frequency is approached. A minimum of 46 meters/second occurs at $k_z = 121$ /meter, corresponding to a frequency of about 23.3 kHz. From this minimum, the group phase velocity gradually increases with wavenumber and frequency.

Figure 3-4 presents the ratio of radial to axial displacement for each branch as a function of the axial wavenumber. This figure indicates that at low wavenumbers, the displacement for branch 2 is primarily radial, and that at high wavenumbers, the displacement for branch 1 is primarily radial.

3.5 Modes in Harmonically Driven Finite Length Tube

In order to compare the experimental results with those predicted from theory, it is essential to accurately know the value of wave speed in the experimental tube. This problem is discussed in detail in Chapter 5. The most precise method was

based on measurements of the frequency of longitudinal modes when the tube was driven with a continuous sinusoidal excitation. In this section we develop the theory used for the wave speed determination.

Consider, then, a thin cylindrical shell of length L , thickness h , and mean radius a , which is freely suspended and driven radially by an axisymmetric "ring" source at one end. Since the excitation is axisymmetric, the tangential displacement v is uncoupled from the radial displacement w and the axial displacement u . We shall use the axial and radial equations for axisymmetric motion, 3.1 and 3.2. For frequencies at which the axial wavelength λ_z is sufficiently large, that is, $\lambda_z > 30h$, the term involving β^2 may be neglected. This condition is satisfied for the experimental tube for frequencies below the ring frequency, about 25 kilohertz. The resulting equations are identified as those for a thin membrane, viz:

Axial:

$$\frac{\partial^2 u}{\partial z^2} + \frac{v}{a} \frac{\partial w}{\partial z} - \frac{1}{c_p^2} \frac{\partial^2 u}{\partial t^2} = 0 \quad (3.13)$$

Radial:

$$\frac{v}{a} \frac{\partial u}{\partial z} + \frac{w}{a^2} + \frac{1}{c_p^2} \frac{\partial^2 w}{\partial t^2} = 0 \quad (3.14)$$

The "ring" displacement input at $z = 0$ provides one boundary condition, viz

$$w(0, t) = W_0 \cdot \exp(-i\omega t) \quad (3.15)$$

The second boundary condition is found from the requirement that the axial strain, $\frac{\partial u}{\partial z}$, must be zero at the end of the tube, where $z = L$.

Since a harmonic input is assumed, equations 3.13 and 3.14 are reduced to

ordinary differential equations. The axial displacement is described by

$$\frac{d^2u}{dz^2} + \frac{\nu}{a} \frac{dw}{dz} + \left(\frac{\omega}{c_p}\right)^2 u = 0 \quad (3.16)$$

and the radial displacement (with the bending term deleted) is given by

$$\frac{\nu}{a} \frac{du}{dz} + w \left[\frac{1}{a^2} - \left(\frac{\omega}{c_p}\right)^2 \right] = 0 \quad (3.17)$$

Re-arranging equation 3.17 and differentiating with respect to z yields

$$\frac{dw}{dz} = \frac{\nu a}{(\Omega^2 - 1)} \frac{d^2u}{dz^2} \quad (3.18)$$

where the non-dimensional frequency $\Omega = \frac{\omega a}{c_p}$ has been introduced. Substitution of 3.18 into 3.16 results in

$$\frac{d^2u}{dz^2} + \gamma^2 u = 0 \quad (3.19)$$

where

$$\gamma^2 = \frac{\Omega^2 (\Omega^2 - 1)}{a^2 [\Omega^2 - (1 - \nu^2)]} \quad (3.20)$$

Now we assume a standing wave solution to equation 3.19,

$$u(z) = A \cos \gamma z + B \sin \gamma z \quad (3.21)$$

The boundary condition $w = W_0 \cdot \exp(-i\omega t)$ at $z = 0$ determines the coefficient B ,

$$B = \frac{W_0}{\nu \Omega} \left[(\Omega^2 - 1) (\Omega^2 - (1 - \nu^2)) \right]^{\frac{1}{2}}$$

and the boundary condition $\frac{du}{dz} = 0$ at $z = L$ results in

$$A = B \cot \gamma L$$

Using these results, the axial and radial displacements are given by

$$u(z) = \frac{W_0}{\nu\Omega} \left[(\Omega^2 - 1) (\Omega^2 - (1 - \nu^2)) \right]^{\frac{1}{2}} \left[\frac{\cos \gamma (L - z)}{\sin \gamma L} \right] \quad (3.22)$$

and

$$w(z) = W_0 \left[\frac{\sin \gamma (L - z)}{\sin \gamma L} \right] \quad (3.23)$$

Modal resonances will occur for values of γ for which $\sin \gamma L = 0$, or $\gamma = \frac{m\pi}{L}$, $m = 1, 2, 3, \dots$. Note that the axial displacement is zero at $\Omega = 1$, the ring frequency, and also at $\Omega = \sqrt{1 - \nu^2}$, which for brass ($\nu = .37$) is at 0.93 times the ring frequency.

The non-dimensional modal frequencies may be found from the real roots of

$$\Omega^4 - \Omega^2 \left[1 + \left(\frac{m\pi a}{L} \right)^2 \right] + \left(\frac{m\pi a}{L} \right)^2 (1 - \nu^2) = 0$$

or

$$\Omega = \sqrt{\frac{\left[1 + \left(\frac{m\pi a}{L} \right)^2 \right] \pm \sqrt{\left[1 + \left(\frac{m\pi a}{L} \right)^2 \right]^2 - 4 \left(\frac{m\pi a}{L} \right)^2 (1 - \nu^2)}}{2}} \quad (3.24)$$

The expected value of modal frequencies is then calculated for an assumed value of extensional wave speed c_p for the non-dimensional frequencies in equation 3.24 using

$$f_m = \frac{c_p \Omega_m}{2\pi a} \quad (3.25)$$

These are the relationships needed for the wave speed determination described in Chapter 5.

3.6 Membrane Transition Frequencies

It is convenient at this point to develop an aspect of membrane theory which will be of use in the next topic. Thus we consider a harmonically driven, semi-infinite shell which meets the criteria for analysis as a membrane, as discussed previously. As before, the shell is radially driven at $z = 0$ with a harmonic input described by equation 3.15. However, for the present analysis, we shall assume a travelling wave solution for the axial displacement u of the form:

$$u(z, t) = A \exp[-i(\gamma z + \omega t)] + B \exp[i(\gamma z - \omega t)] \quad (3.26)$$

Since we have assumed a semi-infinite tube extending in the positive z direction, there can be no wave travelling in the negative z direction, and therefore $A = 0$. The radial displacement w is given by

$$w(z, t) = \frac{va}{(\Omega^2 - 1)} i\gamma B \exp[i(\gamma z - \omega t)] \quad (3.27)$$

Substituting 3.15 into 3.27 and evaluating at $z = 0$ determines B ,

$$B = \frac{W_0(\Omega^2 - 1)}{iva\gamma}$$

Thus the equations of motion for this case are:

$$u(z, t) = \frac{W_0(\Omega^2 - 1)}{iva\gamma} \exp[i(\gamma z - \omega t)] \quad (3.28)$$

and

$$w(z, t) = W_0 \exp[i(\gamma z - \omega t)]$$

Replacing γ in the denominator of equation 3.28 with the expression in equation 3.20 and simplifying results in

$$u(z, t) = \frac{W_0 \sqrt{(\Omega^2 - 1)(\Omega^2 - (1 - v^2))}}{i v \Omega} \exp[i(\gamma z - \omega t)] \quad (3.29)$$

Equation 3.29 implies that the horizontal displacement u will vanish for two values of the non-dimensional frequency, Ω . These are $\Omega = 1$, which is the well known ring frequency, and $\Omega = \sqrt{1 - v^2}$, which we shall refer to as the "lower transition frequency." For free waves propagating in an infinite membrane shell, this lower transition frequency corresponds to the cutoff of the flexural branch (identified as "Branch 1" earlier). The ring frequency, or upper transition frequency, corresponds to the onset of propagation in the longitudinal mode.

Now consider the wave number γ for the present case. From equation 3.20,

$$\gamma = \frac{\Omega}{a} \sqrt{\frac{\Omega^2 - 1}{\Omega^2 - (1 - v^2)}} \quad (3.30)$$

If there were no Poisson coupling, that is, $v = 0$, then $\gamma = \Omega/a = \omega/c_p$, which is identified as an ordinary wave number for a non-dispersive wave. For values of $\Omega < \sqrt{1 - v^2}$ and for $\Omega > 1$, the expression under the radical in equation 3.30 is positive, and γ is real. For $\sqrt{1 - v^2} < \Omega < 1$, the expression is negative, and γ is imaginary. Thus, γ "jumps" from a real number to an imaginary number at the lower transition frequency, and back to a real number at the upper transition (or "ring") frequency. For the brass tube used in this study, the lower transition frequency is 23.338 kilohertz, and the upper transition frequency is 25.121 kilohertz. Also note that γ has a pole at $\Omega = \sqrt{1 - v^2}$, and a zero at $\Omega = 1$.

3.7 Transient Response of Thin Shell

3.7.1 Previous Work on Transient Response

In 1948, R. M. Davies published an 82 page paper titled "A Critical Study of the Hopkinson Pressure Bar." (The Hopkinson pressure bar is an apparatus which was used to study the propagation of stress pulses; a concise description is given by Kolsky (1963)). Davies used the exact equations of motion of a circular elastic cylinder developed by Pochhammer (1876) and Chree (1889), as presented by Love (1944) to compute the dispersion curves (phase and group velocity versus wavenumber) for the first three modes of vibration of an infinite length bar. He used the method of stationary phase to predict the displacements and stresses in a free bar excited by an impulse applied one end. The group velocity curves of the first two modes exhibit a "valley" which is also a characteristic of the flexural mode of an axisymmetric thin shell.

Using a very ingenious physical argument, Skalak (1957) constructed an integral solution for the propagation of the pulse resulting from the longitudinal impact of two semi-infinite rods. The integral was evaluated via the asymptotic saddle-point method for large values of time. The resulting pulse is described by Airy integrals and is characterized by a smooth rise from zero to a maximum value, followed by a decaying oscillation about the level which is predicted from the elementary (non-dispersive) theory using the one dimensional wave equation.

Berkowitz (1963) analyzed the response of a semi-infinite cylindrical shell moving at constant velocity which impacts a rigid surface. The impact provides an

axisymmetric step function velocity input in the longitudinal direction. He formulated the problem in terms of the Laplace transformed (in time) axisymmetric membrane equations for the radial and longitudinal displacements, and the axial and circumferential stresses.

The resulting inversion integrals cannot be evaluated in closed form, so the method of stationary phase was used to obtain approximate asymptotic solutions for large values of non-dimensional time. The solution is characterized by an initial disturbance which propagates at the plate wavespeed, c_p , followed by a steep wavefront travelling at the bar velocity, c_o . This is followed by a damped oscillation which is described by the Airy integral.

An excellent discussion of these and other investigators of transient phenomena is presented by Graff (1975).

3.7.2 Synopsis of Approach

The objective of the present study is to compute the predicted response of the experimental cylindrical shell to an axisymmetric radial impulse input applied at the origin of the axial coordinate, $z = 0$. A detailed description of the experiment is presented in Chapter 5.

The axisymmetric equations of motion for the radial and axial displacements (Equations 3.1 and 3.3) are Fourier transformed in time and Laplace transformed in the axial coordinate z . The resulting transformed equations are algebraic in the transform variables k_p and s where $k_p = \omega/c_p$ is a frequency dependent wavenumber, and s is a complex spatial wavenumber, $s = \sigma + ik_z$, where k_z is the real

valued axial wavenumber. An axisymmetric radial delta function input is applied to the system at the origin, $z = 0$. The inverse Laplace transform of the result is then computed by contour integration, which yields two equations in (k_p, z) space. These equations are essentially transfer functions which describe the radial and longitudinal displacements at axial location z as a function of frequency ω , that is, $u(\omega, z)$ and $w(\omega, z)$. When these functions are multiplied by the Fourier transform of an input at $z = 0$, and the inverse Fourier transform is applied to the product, the result is the response as a function of time at the axial position specified; that is, $u(t, z_o)$ and $w(t, z_o)$ where z_o is a particular observation point.

3.7.3 Transformed Equations of Motion

A double transform comprising a Fourier transform on the time variable, and a Laplace transform on the axial variable z defined as:

$$\hat{f}(k_p, s) = \int_{-\infty}^{\infty} e^{ik_p t} \int_0^{\infty} f(t, z) e^{-sz} dz dt$$

is applied to the axisymmetric equations of radial and longitudinal motion, 3.1 and 3.3. The resulting transformed equations of motion are:

Axial:

$$\hat{u}(s^2 + k_p^2) + \hat{w}(s \frac{v}{a}) = 0 \quad (3.31)$$

Radial:

$$\hat{u}(s \frac{v}{a}) + \hat{w}(\frac{1}{a^2} + s^4 \beta^2 a^2 - k_p^2) = \hat{P}(\omega, s) \quad (3.32)$$

where $\hat{P}(\omega, s)$ is the transform of the input,

$$\hat{P}(\omega, s) = \int_{-\infty}^{\infty} e^{i\omega t} \int_0^{\infty} P(t, z) e^{-sz} dz dt$$

The mechanical input for the experiment is provided by a piezoelectric disk which is bonded to the end of the brass tube. For transient measurements, a short rectangular pulse of voltage is applied to the disk. This results in a radial expansion of the disk, which in turn applies an axisymmetric radial displacement to the tube. We may approximate this input as $P_o \delta(t) \delta(z)$, that is, a delta function of time and axial position, in which P_o has the dimensions of inverse length. Applying the double transform above to this input yields:

$$\hat{P}(\omega, s) = P_o$$

Substitution of this input into equation 3.32 and solving for \hat{u} and \hat{w} results in

$$\hat{u}(k_p, s) = -\frac{svP_o}{aD} \quad (3.33)$$

and

$$\hat{w}(k_p, s) = \frac{(s^2 + k_p^2) P_o}{D} \quad (3.34)$$

In equations 3.33 and 3.34, D represents the dispersion equation, which is a polynomial of sixth order in s and fourth order in k_p , as indicated below:

$$D = s^6(\beta a)^2 + s^4(\beta a k_p)^2 + s^2 \left[\frac{(1 - v^2)}{a^2} - k_p^2 \right] + k_p^2 \left(\frac{1}{a^2} - k_p^2 \right) \quad (3.35)$$

3.7.4 Response in Spatial and Frequency Domain

To obtain the radial and longitudinal displacements as functions of axial position z and frequency (or wavenumber, k_p), we apply the complex inversion integral (Spiegel, 1971) to equations 3.33 and 3.34,

$$g(z) = \frac{1}{2\pi i} \int_{c-i\infty}^{c+i\infty} e^{sz} G(s) ds, \quad z > 0$$

This is accomplished by contour integration, using the Cauchy residue theorem (Hildebrand, 1962), that is,

$$\oint_C e^{sz} G(s) ds = 2\pi i \sum_{k=1}^n R(a_k) \quad (3.36)$$

where $R(a_k)$ is the k th residue. The residues are evaluated at the singularities of $G(s)$.

We note that $\hat{u}(k_p, s)$ and $\hat{w}(k_p, s)$ share the same singularities, namely, the roots of equation 3.35.

Location of Roots

Consider the expression for D , equation 3.35. Although D is of sixth order in s , it is a cubic in s^2 . Now let $q = s^2$; so that D may be written as

$$D = q^3(\beta a)^2 + q^2(\beta a k_p)^2 + q \left[\frac{(1-v^2)}{a^2} - k_p^2 \right] + k_p^2 \left(\frac{1}{a^2} - k_p^2 \right) \quad (3.37)$$

Equation 3.37 will have three roots. The roots will either be all real, or one real and one complex conjugate pair, depending on the discriminant of 3.37. (Spiegel, 1968) Denoting the roots of 3.37 as Q_n , $n = 1, 2, 3$, the six roots of equation 3.35 are given by:

$$S_j = \pm \sqrt{Q_n}, \quad j = 1, \dots, 6 \quad (3.38)$$

The values of S may be real, imaginary, or complex, depending on the values of Q . All of these roots will be functions of frequency due to the variable $k_p = \omega/c_p$ in equations 3.35 and 3.37. Although exact literal expressions for the values of the roots S may be written, the results are so cumbersome algebraically that little insight into the behavior of the roots as a function of frequency is achieved. Thus in this study we pursue a numerical evaluation using the following values of the parameters appropriate for the experimental tube:

Mean radius, meters: $a = .0249555$

Thickness, meters: $h = .000889$

Poisson's ratio: $\nu = 0.37$

Plate wave speed, meters/second: $c_p = 3939$

The value of c_p was determined experimentally, as discussed in Chapter 5. The frequency range of interest in this study is from 0 to 100 kilohertz, about four times the "ring" frequency, $f_r = c_p/2\pi a$, which is 25.12 kHz for the experimental tube.

Variation of roots Q_n with Frequency:

We consider the nature of the roots Q_n of equation 3.37 in three frequency regimes: (1) far below the lower transition frequency; (2) far above the upper transition frequency; and (3) in the range between the transition frequencies. The real and imaginary components of the three roots are shown in figure 3-5 for the frequency range from 10 kilohertz to 40 kilohertz.

(1) Below lower transition frequency: Below the lower transition frequency, roots Q_1 and Q_2 are a complex conjugate pair. Root Q_3 is negative and real.

(2) Above the upper transition frequency: Far above the "ring" frequency, Q_1 and Q_3 are negative and real, and Q_2 is positive and real.

(3) Between the transition frequencies: In this range, the behavior of the roots becomes very complicated. Figure 3-6 presents the frequency dependence of the roots in the region between the transition frequencies. Root Q_1 , which is complex with a positive imaginary component at low frequencies, experiences an increase in the real component slightly below the first transition frequency. The imaginary component, which has been decreasing with increasing frequency, suddenly drops to zero at the lower transition frequency. The real part of Q_1 jumps from a positive to a negative value, and continues to become more negative at higher frequencies. Root Q_2 is complex with a negative imaginary component at low frequencies. The imaginary component jumps to a positive value at the lower transition frequency, then decreases to zero. The positive component of Q_2 continually increases with frequency.

Root Q_3 is negative and real at low frequencies, becoming more negative as the lower transition frequency is approached, at which point it becomes complex for a small range of frequencies. The real component jumps to a positive value at the lower transition frequency and remains positive up to the upper transition frequency. We shall find shortly that the bending term β has an important effect

on these roots in the transition region.

Figure 3-7 shows the behavior of the magnitude of all three roots in the region between the transition frequencies. Below the lower transition frequency, roots Q_1 and Q_2 are equal in magnitude and are decreasing. Root Q_3 (dashed line) is increasing. All three roots meet at the lower transition frequency, 23.338 kHz. At this frequency, root Q_1 becomes real and negative, increasing in magnitude with frequency. Roots Q_2 and Q_3 now form a complex conjugate pair until a second branch point is reached at 23.606 kHz. At the second branch point, Q_2 becomes real and positive, increasing in magnitude with frequency. Root Q_3 becomes real and positive, decreasing rapidly with frequency until the "ring", or upper transition, frequency, where it vanishes. Above the "ring" frequency, Q_3 is real and negative, increasing in magnitude with frequency. The branch points just described are illustrated in figure 3-8, where the path of the Q roots is plotted in the neighborhood of the lower transition frequency.

Roots of Dispersion Equation

The six roots of equation 3.37 in the complex wavenumber (s) plane are found from the values of Q_n , as indicated in equation 3.38. Negative real values of the roots Q_n give rise to imaginary values of S_j . The six roots in s occur in conjugate pairs, from taking both the positive and negative values of $\sqrt{Q_n}$. The relationship between the Q roots and the S roots is shown qualitatively in figure 3-9. Here the relative positions of the roots are shown in the complex Q and S planes. The arrows indicate the path followed by the roots as the frequency is increased. In

figures 3-9 (a & b) the paths of the roots are shown for frequencies below the lower transition frequency. Figures 3-9 (c & d) present the relationships for frequencies above the upper transition frequency.

Variation of Roots S_n With Frequency: For brevity, we shall focus on a description of the behavior of the S roots which arise from the positive square root of the Q roots. A similar argument is easily constructed for the image roots.

Below the lower transition frequency, roots S_1 and S_2 are a complex conjugate pair with positive real part. The magnitude of these roots decreases as the frequency increases. Root S_3 derives from root Q_3 , which is negative and real in this frequency regime. Therefore, S_3 is positive and imaginary below the lower transition frequency. Root S_3 increases with frequency.

Above the upper transition frequency, roots S_1 and S_3 are both positive and imaginary. These roots increase with frequency. Root S_2 is positive, real, and also increases with frequency.

In the region between the lower and upper transition frequencies, the magnitudes of the S roots vary in a fashion similar to the behavior of the Q roots described above. This is shown in figure 3-10. The changes in the root S_3 are of special interest and will be analyzed further.

Figure 3-11 (a) is a plot of the real and imaginary components of S_3 in the transition zone. Note that this root acquires a real component in this frequency range. This is the only part of the entire spectrum for which root S_3 has a real part. The imaginary part of S_3 is positive below the lower transition frequency

(identified by the symbol "f1" on figure 3-11 (a)), where it "jumps" to a negative value. It remains negative until the second branch point (symbol "f2") at 23.606 kHz, where it vanishes. The imaginary component continues to be zero until the "ring" frequency (symbol "f3"). At this frequency, the real component of S_3 vanishes, and the imaginary component returns, becoming positive and increasing with frequency.

The rather unusual behavior of the S roots in the transition zone is related to the bending term β in the governing equation for the radial displacement, equation 3.3. This will be demonstrated by plotting the components of S_3 in the transition zone for several values of β .

Figures 3-11 (b), 3-11 (c), and 3-11 (d) present the components of root S_3 for values of $\beta = .1$, $.001$, and $.0001$, respectively. We see that as β decreases, the second branch frequency moves towards the lower transition frequency. In addition, the magnitude of S_3 increases substantially at the lower transition frequency. In the limit as $\beta \rightarrow 0$, the real part of S_3 and the second branch frequency both vanish. This limit represents the transition to shell membrane theory, for which there will only be two roots.

Specification of Contour

In order to apply the Cauchy residue method indicated in equation 3.36, the contour of integration must be specified. Since we are interested in wave propagation in the positive z direction, we choose a Bromwich contour which includes the imaginary axis, and a semi-circle of infinite radius in the left half of the complex

s plane. This contour is shown in figure 3-12 for the pole locations in the low frequency regime (3-12 (a)) and for the high frequencies (3-12 (b)). We include the poles which derive from the negative roots of Q_n , that is, S_4, S_5 , and S_6 . Note that the poles which are excluded represent waves travelling in the negative z direction.

Evaluation of Residues

We now express equations 3.33 and 3.34 in terms of the poles which are to be included, viz.

$$\hat{u}(k_p, s) = -\frac{svP_0}{a(s - S_4)(s - S_5)(s - S_6)} \quad (3.39)$$

and

$$\hat{w}(k_p, s) = \frac{(s^2 + k_p^2) P_0}{(s - S_4)(s - S_5)(s - S_6)} \quad (3.40)$$

Each of equations 3.39 and 3.40 will have three residues, which we shall designate as $UR1, UR2, UR3$ and $WR1, WR2, WR3$, respectively. Now if the function $G(s)$ in equation 3.36 has a simple pole at $s = a_k$, for instance, the k th residue is found as:

$$R(k) = \lim_{s \rightarrow a_k} [(s - a_k) G(s) e^{sz}] \quad (3.41)$$

Applying equation 3.41 to 3.39 and 3.40, we have:

$$UR1 = \frac{v P_0 S_4 e^{S_4 z}}{a(S_4 - S_5)(S_4 - S_6)} \quad (3.42)$$

$$UR2 = \frac{v P_0 S_5 e^{S_5 z}}{a(S_5 - S_4)(S_5 - S_6)} \quad (3.43)$$

$$UR3 = \frac{v P_0 S_6 e^{S_6 z}}{a(S_6 - S_4)(S_6 - S_5)} \quad (3.44)$$

and

$$WR1 = \frac{P_0 (S_4^2 + k_p^2) e^{S_4 z}}{(S_4 - S_5)(S_4 - S_6)} \quad (3.45)$$

$$WR2 = \frac{P_0 (S_5^2 + k_p^2) e^{S_5 z}}{(S_5 - S_4)(S_5 - S_6)} \quad (3.46)$$

$$WR3 = \frac{P_0 (S_6^2 + k_p^2) e^{S_6 z}}{(S_6 - S_4)(S_6 - S_5)} \quad (3.47)$$

Equations 3.42 to 3.47 are essentially transfer functions which describe the frequency dependence of the three components of longitudinal displacement u and the three components of radial displacement w as functions of the axial position, z . The net displacements are obtained by summing the components, viz.

$$w(k_p, z) = WR1 + WR2 + WR3 \quad (3.48)$$

$$u(k_p, z) = UR1 + UR2 + UR3 \quad (3.49)$$

3.8 Discussion of $w(f, z)$ and $u(f, z)$ Transfer Functions

We now consider the transfer functions for the radial and longitudinal displacements in the spatial (z) and frequency ($f = c_p k_p / 2\pi$) domains. Figures 3-13 to 3-16 present three dimensional surface plots of the magnitude (absolute value) of

the displacement functions $w(f, z)$ and $u(f, z)$ for frequencies ranging from 0 to 50 kilohertz, and two ranges of axial distance, 0 to 5 cm, and 1 to 50 cm. Plots with a logarithmic scale for the functions are also included. The logarithmic plots enhance low amplitude characteristics which are not obvious on a linear scale. A small offset (.001) is added to the magnitude of the functions to provide a "floor" for the logarithmic plots.

The far-field topography of $w(f, z)$ is emphasized in figure 3-13 (a), which exhibits a plateau above the "ring" frequency, a steep cliff in the transition region, and a rather flat plain below the lower transition frequency. There is a ripple near the edge of the plateau which indicates a variation in the magnitude of the spectral components with axial distance. The logarithmic plot of this function (figure 3-13 (b)) shows a smooth rise from the plain to the plateau. The ripples at the edge of the plateau are suppressed in this presentation. The "wall" at $z = 0$ cm is due to the near field.

The predominant feature in the far field of the longitudinal displacement $u(f, z)$, figure 3-14 (a), is a jagged ridge which is parallel to the z (distance) axis. This ridge is located in the transition region in frequency space.. The function falls off smoothly at lower frequencies. The logarithmic plot, figure 3-14 (b), shows a number of smaller ridges which radiate away from the primary ridge above the transition region. These minor ridges follow a curved trajectory in (f, z) space.

Figures 3-15 and 3-16 focus on the near field. The "wall" parallel to the frequency axis at $z = 0$ in figure 3-15 (a) reflects the fact that the temporal input

to the model is a delta function in the time domain, which has a uniform spectral density in the frequency domain. The presence of evanescent near field frequency components is evident near the origin of figure 3-15 (a). The near field structure of $w(f, z)$ is more visible in the logarithmic plot, figure 3-15 (b).

The near field of $u(f, z)$ is shown in figures 3-16 (a) and 3-16 (b). The amplitude of $u(f, z)$ is zero for all frequencies at $u = 0$, since the axial strain, $\frac{\partial u}{\partial z}$ is zero at this location. The formation of the ridge in the transition zone as the axial distance increases is clearly shown in this figure. The minor ridges which radiate in (f, z) space are visible in the logarithmic plot, figure 3-16 (b).

The detailed structure of $w(f, z)$ and $u(f, z)$ is studied by taking "slices" of these functions at selected values of f and z . Figure 3-17 (a) is a plot of the magnitude of $w(f, z)$ as a function of frequency at four axial positions in the near field. At $z = .01$ cm, the spectrum is nearly flat. This is the upper edge of the "wall" seen in figure 3-15 (a). As the distance increases, the lower frequencies diminish, whereas the high frequencies persist. The transition zone "ridge" is evident in this figure, at $z = .11$ and $z = .21$ cm. Figure 3-17 (b) shows the frequency spectrum at $z = .91$, $.41$, and 2.01 cm, indicating the formation of the "plain" and "plateau" regions as the far field is approached. In figure 3-17 (c), the frequency spectrum is plotted for $.2$, $.4$, $.6$, and 50 cm. The far field structure is indicated by the spectrum at $z = 50$ cm.

The development of the topography of $u(f, z)$ is illustrated in figure 3-18. Figures 3-18 (a) and 3-18 (b) show the growth of the ridge in the transition zone

of $u(f, z)$. The spectrum at $z = 50$ cm in figure 3-18 (c) indicates the formation of the minor ridges in frequency space.

The magnitudes of $w(f, z)$ and $u(f, z)$ as a function of axial distance is plotted in figures 3-19 to 3-22 for several frequencies of interest. The near field plots, figures 3-19 and 3-20 show the decay of the low frequency components at 10 and 22 kilohertz as the far field is approached.

Figures 3-21 and 3-22 emphasize the far field characteristics of $w(f, z)$ and $u(f, z)$ at 10, 22, 23.6, 25.1, and 50 kilohertz. The 10 kilohertz component attenuates rapidly with distance, whereas components at the lower and upper transition frequencies do not reach steady state until about 6 centimeters, or about 2.5 times the mean radius of the tube. These figures also demonstrate the stable spatial periodicity of the high frequency spectral components.

3.9 Transformation to the Time Domain

The next step in the analysis is to obtain the transient response of the tube as a function of distance by application of the inverse Fourier transform to the transfer functions, $w(f, z)$ and $u(f, z)$. Formally this is defined by:

$$g(t, z) = 2\pi \int_{-\infty}^{\infty} g(f, z) e^{i2\pi ft} df \quad (3.50)$$

We will perform the inversion numerically on the transfer functions by means of the Inverse Fast Fourier Transform (IFFT), which is a widely implemented version of the discrete Fourier transform (DFT). The theory and application of numerical versions of the Fourier transform has been extensively studied by many

authors, including, for instance, Bracewell (1965), Papoulis (1977), Burdic (1984), Oppenheim and Schaffer (1989), Jackson (1986, 1991), and Strum and Kirk (1995).

Certain restrictions apply when using numerical tools such as the Fast Fourier Transform for the evaluation of integrals such as equation 3.50. First of all, the DFT uses a discrete infinite sum as an approximation to the continuous function implied in 3.50. Thus the differential df in the integral formulation is replaced by an increment Δf in the discrete version. This limits the resolution which may be attained with the discrete approximation. Nyquist (1928) proved that if a continuous time function $g(t)$ is sampled at a frequency f_s , then the upper limit in frequency space for spectral components of the Fourier transform of $g(t)$ is at best equal to $f_s/2$, that is, one half of the sampling frequency. This is known as the Nyquist frequency, f_N . In most practical applications, the bandwidth is restricted to slightly below the Nyquist frequency. The infinite DFT may be viewed as a Fourier series representation of a frequency function defined over a finite interval. This series will also represent the same function replicated at integral multiples of the sampling frequency. If the original time function is not band limited in frequency, artificial frequency components will appear in the DFT spectrum. This phenomenon is known as aliasing.

A second constraint results as a consequence of replacing the infinite sum of the DFT with a finite sum of N terms as is the case with the FFT. The spectrum obtained with the finite FFT represents a function which is replicated in the time domain. Thus the period T of a time function obtained with the IFFT is limited

to $T \leq 1/\Delta f$. The temporal resolution of the time function is $\Delta t = T/N$, and therefore $\Delta f \Delta t \leq 1/N$.

An additional constraint applies to the present analysis due to the limitations of the Donnell shell theory as described in the analysis of the thin shell in wavenumber-frequency space, that is, the transfer functions $w(f, z)$ and $u(f, z)$ must be band-limited in frequency to the region for which the thin shell theory is a valid model.

We recall that the analysis which resulted in the transfer functions for w and u was predicated on a temporal input which is a delta function of time. A delta function in time transforms to an infinite spectrum in frequency space. Before applying the inverse transform to the transfer functions, we shall band limit the spectrum by multiplying each transfer function by an appropriate weighting function $H(f)$ chosen so as to assure that the desired constraints are realized. Thus the inversion integral 3.50 will take the form

$$g(t, z) = 2\pi \int_{-\infty}^{\infty} g(f, z) H(f) e^{i2\pi ft} df \quad (3.51)$$

where $g(f, z)$ represents the transfer functions, and $H(f)$ is a weighting function to be determined.

3.9.1 Development of Weighting Function

The characteristics required of the weighting function $H(f)$ are:

- (1) A uniform ("flat") spectral density from zero to some upper band limit, F_c
- (2) A rapid and smooth transition to zero spectral density for frequencies above

F_c .

The first requirement stems from the need to simulate the spectrum of a delta function within the frequency range of interest. A function which meets this requirement is the rectangular, or "boxcar" function, which is defined as:

$$H_1(f) = \begin{cases} 1 & \text{for } 0 \leq f \leq F_c \\ 0 & \text{for } f > F_c \end{cases} \quad (3.52)$$

Unfortunately the Fourier transform of $H_1(f)$ does not meet the second requirement. The abrupt discontinuity at the corner frequency, $f = F_c$, will produce the so-called "Gibbs' Phenomenon" (Strum and Kirk, 1995), which consists of overshoot and ripples in the transform (time) domain.

One function which does meet the second criterion is the Gaussian waveform (Burdic, 1984, Bracewell, 1965). The Gaussian function may be expressed as

$$H_2(f) = \exp -\sigma^2 \left[\frac{f}{F_c} - 1 \right]^2 \quad (3.53)$$

Equation 3.53 describes a Gaussian frequency distribution centered at F_c . The parameter σ controls the rate at which this function falls off on either side of the cutoff frequency F_c .

The desired weighting function is synthesized from a combination of 3.52 and 3.53:

$$H(f) = \begin{cases} H_1(f) & \text{for } 0 \leq f < F_c \\ H_2(f) & \text{for } f \geq F_c \end{cases} \quad (3.54)$$

3.9.2 Weighted Transfer Functions

Examples of the weighted transfer functions are shown in figures 3-23 and 3-24 for axial position $z = 6$ cm. The weighting function $H(f)$ (multiplied by $\frac{1}{2}$ for

greater visibility) is also included in the plot of $w(f)$ in figure 3-23. The weighted transfer function is labeled $H(f) * w(f)$ in this figure. We note that the weighted transfer functions make a gracefully smooth transition to zero in frequency space. Thus we have satisfied the requirement discussed earlier that the spectrum of the transfer functions must be band-limited before inversion to the time domain using the IFFT. Also note that the amplitude of $u(f)$ is much lower than the amplitude of $w(f)$ at this axial position.

3.9.3 Time Domain Response

Application of the IFFT to the weighted transfer functions shown in figures 3-23 and 3-24 yields the radial and axial displacements as functions of time at the selected location, $z = 6$ cm. This result is shown in figures 3-25 and 3-26. The effects of dispersion on the propagation of waves in the tube is clearly evident in these plots. The high frequency components of the transient disturbance arrive first. These are followed by a long decaying "tail" in which the frequency gradually decreases. The frequency components in this "tail" are in the transition zone discussed earlier. The amplitude of the radial displacement $w(t)$ is about 50 times that of the axial displacement $u(t)$.

The resolution in the time domain is determined by the number of points N and the frequency increment Δf , as mentioned above. The frequency increment must be large enough so that period T of the IFFT includes the transient of interest. With these parameters established, the minimum number of points N_{\min} depends on the desired value of time resolution, Δt , thus $N_{\min} = 1/(\Delta f \Delta t) = T/\Delta t$.

3.10 Joint Time-Frequency Distributions

The fundamental premise which supports the theory of Fourier transforms is that the process which generates the function in the time domain is stationary, that is, the statistical properties of the process are invariant in time. The Fourier integral itself is evaluated formally over an infinite time interval. In analyzing real physical data, of course, the sample space is of necessity finite. Real signals are limited both in bandwidth and in time. However, for many problems of interest, the spectral content of the process is sufficiently stable over the time span of the measurement that the conditions for the existence and validity of the Fourier transform are satisfied.

However, there are many processes for which the spectral content varies significantly during the time sample of interest. Common examples include human speech, bird calls and other biological sounds, music, gravity waves in large bodies of water, and transients in dispersive systems, as is the case in the present study. A useful construction in understanding such phenomena is the concept of a joint time-frequency distribution, in which the energy or intensity of a signal is represented simultaneously in time and in frequency.

The topic of joint time-frequency distributions has received intense investigation by the signal processing community in recent years. An excellent review of the subject has been published by Cohen (1989). A study of joint time-frequency distributions usually begins with a discussion of the Wigner-Ville Distribution Function (WVDF). Wigner (1932) devised a distribution function to facilitate his study of

quantum statistical mechanics. Ville (1948) applied the same type of distribution function to signal analysis.

Janse and Kaizer (1983) give the following formulation for generalized time-frequency distributions:

$$C_f(t, \omega, \Phi) = \frac{1}{2\pi} \iiint_{-\infty}^{\infty} e^{i(\xi t - \tau \omega - \xi u)} \Phi(\xi, \tau) f(u + \frac{\tau}{2}) f^*(u - \frac{\tau}{2}) du d\tau d\xi \quad (3.55)$$

in equation 3.55, $f(u)$ is the time signal, $f^*(u)$ is the complex conjugate of the time signal, and $\Phi(\xi, \tau)$ is a kernel function which determines the nature of the distribution function. The WVDF is obtained by setting $\Phi(\xi, \tau) = 1$ in equation 3.55. Claasen and Mecklenbrauker (1980) established that all time-frequency distribution functions may be obtained by convolution of the Wigner distribution with some window function.

In the present study, the short term Fourier transform, or spectrogram, will be used for analysis of the transient response of the tube in time-frequency space. The spectrogram is a well known tool used in acoustical studies of speech, music, and biological events. Authors differ in their definition of the spectrogram. Cohen (1989), Claasen and Mecklenbrauker (1980), and Janse and Kaizer (1983) define the spectrogram as the square of the magnitude of the short term Fourier transform (SFT). This definition emphasizes the power spectral density of the signal. Oppenheim and Schaffer (1989) and Rabiner and Schaffer (1978) define the spectrogram as the magnitude of the SFT. We shall use the latter definition in the present study.

The short-time Fourier transform is given by (Claasen and Mecklenbrauker,

1980):

$$F_t(\omega) = \int_{-\infty}^{\infty} e^{-i\omega\tau} f(\tau) h(\tau - t) d\tau \quad (3.56)$$

in which $h(\tau - t)$ is a window function centered at time t , and $f(\tau)$ is the signal. Then the spectrogram is $S_f(t, \omega) = |F_t(\omega)|^2$. In this study we shall employ an algorithm for the spectrogram which is implemented in the MATLAB (1994) system for numerical analysis. The spectrogram is developed by sliding a window along the time axis. At each discrete position of the window, the SFT is computed. The result is a matrix in which each column represents the spectrum at a particular instant of time. The rows in the matrix contain the complex values of the spectrogram at specific frequencies.

The Uncertainty Problem There is an inherent fundamental limitation in the application of time-frequency distributions, namely, the duration of a signal and its bandwidth are reciprocally related. This is often referred to the "uncertainty principle," in analogy to the famous Heisenberg uncertainty principle in quantum mechanics. As generally expressed, the uncertainty principle states that the duration of a signal and the spectral bandwidth of its Fourier transform are bounded by

$$(\Delta T)(\Delta F) \geq \frac{1}{4\pi} \quad (3.57)$$

where ΔT is the length of the signal in seconds, and ΔF is the spectral bandwidth in hertz.

Proof of this may be found in Papoulis (1977), Claasen and Mecklenbrauker (1984) and Elmore and Heald (1985). Cohen (1989) offers the following quotation

from Skolnik (1980): "The use of the word 'uncertainty' is a misnomer, for there is nothing uncertain about the 'uncertainty relation.' . . . It states the well-known mathematical fact that a narrow waveform yields a wide spectrum and a wide waveform yields a narrow spectrum and both the time waveform and the frequency spectrum cannot be made arbitrarily small simultaneously." Applications of joint time-frequency distributions are described by Yen (1987), Janse and Kaizer (1983), Rossano, Shin, and Hamilton (1990), and Rao, Taylor, and Harrison (1990).

The uncertainty relation enters into the computation of the time domain response in terms of the cutoff frequency of the weighting function, $H(f)$. If the effective bandwidth of the weighting function is F_c , then the minimum signal length in the time domain is given by $\Delta T = 1/(4\pi F_c)$.

Spectrogram Parameters: We now consider some of the factors which enter into the computation of the spectrogram of discrete, finite time series. In the experimental study of time-dependent phenomena, measurements may be made as a continuous function of time with an analog device, such as a conventional tape recorder, or as a discrete function of time using a digital device such as an analog to digital (A/D) converter. In the first case, the temporal resolution is determined by the bandwidth of the measurement device. In the digital case, the limitations are set by the sampling frequency F_s (Hertz) and the maximum number of data points which may be recorded with the instrument, N . The bandwidth in the discrete case must be limited by anti-aliasing filters to a value less than the Nyquist frequency, $F_s/2$.

The sampling interval Δt is the reciprocal of the sampling frequency, $\Delta t = 1/F_s$, and the record length, or maximum signal duration, is $T_{\max} = N \cdot \Delta t$. (But note that for a signal that is bounded in time, such as a transient, the effective signal duration may be artificially extended by adding zeros to the time series, a technique known as "zero padding"). The uncertainty relation states that the minimum bandwidth of the Fourier transform is

$$\Delta F \geq \frac{1}{4\pi N \Delta t} = \frac{F_s}{4\pi N}$$

There is an inherent trade-off between the frequency and time resolution in a spectrogram. The frequency resolution Δf of the spectrum of the entire time series of N points is given by $\Delta f = \frac{1}{N \Delta t} = \frac{F_s}{N}$. However, in the algorithm employed for the computation of the spectrograms, the original time series of N data points is divided into sections of length N_{fft} , and then each section is multiplied by a window function. (The Hanning window is used in this study.) The frequency resolution of the spectrogram is determined by the length of the original sampling interval and the length of the section, thus $\Delta f_{sp} = 1/N_{fft} \Delta t$. Thus the frequency resolution is reduced in the spectrogram in the ratio N/N_{fft} . Put another way, spectral lines which were narrow in the spectrum of the whole time series will be broadened or smeared in the spectrogram. On the other hand, the time domain resolution is approximately determined by the same ratio, N/N_{fft} which determines the number of points in time at which the FFT is computed. This problem is endemic to all joint time-frequency distributions (Classen and Mecklenbrauker, 1980, 1984). Thus a judicious compromise must be made in selecting N_{fft} for the spectrogram.

Another factor which influences the appearance of spectrograms is known as "overlap." It is customary to include a certain amount of overlap between contiguous sections of the subdivided time series. If the number of overlap samples is N_{ol} , then the number of discrete time points in the spectrogram is given by the integer part of $(N - N_{ol}) / (N_{fft} - N_{ol})$. Generally the overlap is set to $N_{fft}/2$, so that half of the samples of the J th section are included in the $(J + 1)$ th section. For this case the number of time points is the integer part of $\frac{2N}{N_{fft}} - 1$.

Spectrograms of the waveforms displayed in figures 3-25 and 3-26 are presented as contour plots in figures 3-27 and 3-28 respectively. In this representation, the absolute value of the FFT results in the spectrogram matrix are normalized to the global maximum. Contour lines connect points of equal magnitude. The spectrograms are shaped somewhat like a boomerang, with a steep ridge parallel to the frequency axis occurring early in time. The long tail parallel to the time axis represents the low frequency components. The spectrogram results agree with the description of these waveforms earlier in the section "Time Domain Response." The longer tail in the spectrogram of the axial component reflects the increased relative amplitude of the low frequencies evident in figure 3-26.

Figures 3-29 and 3-30 are three dimensional contour plots of the spectrograms. In the three dimensional plots, contour planes of equal amplitude are drawn parallel to the time-frequency plane. The dispersive nature of the wave propagation is clearly evident in the contour plots.

CHAPTER 4

Composite Systems

4.1 Introduction

The models developed in Chapters 2 and 3 are brought together here to formulate the description of various composite systems of interest. This will include models comprised of all fluid components, and systems in which elastic media are incorporated. The transfer matrix approach described in Chapter 1 will be used for this study.

4.2 Fluid Systems

4.2.1 Parameters for Two Fluid Systems: The behavior of a system which includes two different fluids will depend on the density and sound speed in the fluids as well as the frequency and wavenumber of the excitation. Analysis of such systems is simplified by defining several non-dimensional ratios of various physical parameters. For a two fluid system, the subscript 1 will denote the inner fluid, and subscript 2 will represent the outer fluid. We now define the following ratios:

Ratio of sound speeds:

$$R_c = \frac{c_2}{c_1}$$

Ratio of densities:

$$R_\rho = \frac{\rho_2}{\rho_1}$$

Ratio of specific acoustic impedances:

$$R_z = \frac{\rho_2 c_2}{\rho_1 c_1} = R_c R_\rho$$

Table 4-1, Parameter Matrix for Two-Fluid Problems

Sound Speed	$c_1 < c_2$	$c_1 = c_2$	$c_1 > c_2$
Wavenumber	$k_1 > k_2$	$k_1 = k_2$	$k_1 < k_2$
Density			
$\rho_1 < \rho_2$	$R_z, R_\rho, R_c > 1$	$R_z, R_\rho > 1, R_c = 1$	$R_z = ?, R_\rho > 1, R_c < 1$
$\rho_1 = \rho_2$	$R_z > 1, R_\rho = 1, R_c > 1$	$R_z, R_\rho, R_c = 1$	$R_z < 1, R_\rho = 1, R_c < 1$
$\rho_1 > \rho_2$	$R_z = ?, R_\rho < 1, R_c > 1$	$R_z, R_\rho < 1, R_c = 1$	$R_z > 1, R_\rho, R_c < 1$

Table 4-1, "Parameter Matrix for Two-Fluid Problems", indicates that there are nine combinations of fluid density and sound speed which must be considered in two fluid problems. The relative magnitudes of the three ratios defined above are also indicated in Table 4-1.

There will be two acoustic wavenumbers, $k_1 = \omega/c_1$, and $k_2 = \omega/c_2$, and two radial wavenumbers, $k_{r1}^2 = k_1^2 - k_z^2$, and $k_{r2}^2 = k_2^2 - k_z^2$. When the frequency and axial wavenumber are both independent, we may define a variable $c_z = \omega/k_z$ which represents the speed at which a wave propagates in the z direction. (This is sometimes called the "trace velocity"). We now define the ratio of radial wavenumbers

as:

$$R_{kr} = \frac{k_{r2}}{k_{r1}} = \frac{\sqrt{\frac{1}{c_2^2} - \frac{1}{c_z^2}}}{\sqrt{\frac{1}{c_1^2} - \frac{1}{c_z^2}}}$$

For propagation to occur in both fluids, k_{r2} and k_{r1} must be real. This will be true if both c_1 and c_2 are less than c_z . For a system driven at the inner boundary of fluid 1, if $c_1 < c_z$ and $c_2 > c_z$, propagation will occur in fluid 1, but not in fluid 2. If $c_1 > c_z$, propagation will not occur in either fluid.

4.2.2 Fluid Tube in External Fluid: The first case consists of a fluid tube driven at its inner surface and imbedded in an external fluid. The external medium has a real component of radiation impedance, enabling the radiation of energy.

Consider, then, a fluid tube of inner radius a_1 and outer radius a_2 , with fluid density ρ_1 , sound speed c_1 , and wavenumber $k_1 = \frac{\omega}{c_1}$. The fluid tube is in intimate contact with the external fluid of density ρ_2 and sound speed c_2 at the boundary, $r = a_2$. The wavenumber in the external fluid is $k_2 = \frac{\omega}{c_2}$. The input to the system is a traveling wave of pressure or velocity of the form $P_o \exp i(k_z z - \omega t)$, where P_o is an amplitude coefficient, k_z is an arbitrary axial wavenumber, and ω is the angular frequency.

This model could represent, for example, a cylindrical transducer or towed array in which a ceramic cylinder or array of cylinders is enclosed in a soft elastomer (with a negligible shear modulus), immersed in sea water.

The boundary conditions which must be satisfied at the interface $r = a_2$ are:

(1) continuity of the state variables of pressure and radial velocity, and (2) waves in the fluid tube and in the external fluid must have the same axial wavenumber

k_z if propagation is to occur.

The pressure and radial velocity at $r = a_2$ are related by the spectral impedance of the external fluid; that is, $P_{a_2} = Z_2 V_{a_2}$, where

$$Z_2 = \frac{-i\rho_2 c_2 k_2 H_0^{(1)}(k_{r_2} a_2)}{k_{r_2} H_1^{(1)}(k_{r_2} a_2)}$$

Using the equations for a fluid tube,

$$\left[\frac{P_{a_2}}{V_{a_2}} \right] = [M_{ab}] \left[\frac{P_{a_1}}{V_{a_1}} \right]$$

where

$$[M_{ab}] = \begin{bmatrix} A_1 & B_1 \\ C_1 & D_1 \end{bmatrix}$$

and A_1, B_1, C_1, D_1 are the ABCD parameters for the fluid tube as defined in Chapter 2.

Solving for V_{a_1} we find

$$V_{a_1} = P_{a_1} \frac{(A_1 - C_1 Z_2)}{(D_1 Z_2 - B_1)}$$

and the pressure at $r = a_2$ is

$$P_{a_2} = P_{a_1} \left[A_1 + \frac{B_1 (A_1 - C_1 Z_2)}{(D_1 Z_2 - B_1)} \right]$$

thus, all of the state variables are determined from either the applied pressure P_{a_1} or velocity V_{a_1} , the fluid tube dimensions a_1 and a_2 , and the acoustic properties of both media.

The ABCD parameters for the fluid tube are given by

$$A_1 = \frac{\pi}{2} k_{r_1} a_1 Q_{10}(k_{r_1})$$

$$B_1 = i \frac{\pi}{2} k_{r_1} a_1 Q_{00}(k_{r_1}) Z_1$$

$$C_1 = i \frac{\pi}{2} \frac{k_{r_1} a_1}{Z_1} Q_{11}(k_{r_1})$$

$$D_1 = -\frac{\pi}{2} k_{r_1} a_1 Q_{10}(k_{r_1})$$

where $Z_1 = \frac{\rho_1 c_1 k_1}{k_{r_1}}$.

Now consider the spectral impedance at boundary a_1 ,

$$Z_{a_1} = \frac{P_{a_1}}{V_{a_1}} = \frac{D_1 Z_2 - B_1}{A_1 - C_1 Z_2} \quad (4.1)$$

Substituting the explicit expressions into 4.1 and simplifying yields

$$Z_{a_1} = i Z_1 \frac{\left[\frac{\rho_2 c_2 k_2}{Z_1 k_{r_2}} Q_{01}(k_{r_1}) \frac{H_0^{(1)}(k_{r_2} a_2)}{H_1^{(1)}(k_{r_2} a_2)} - Q_{00}(k_{r_1}) \right]}{\left[Q_{10}(k_{r_1}) - \frac{\rho_2 c_2 k_2}{Z_1 k_{r_2}} \frac{H_0^{(1)}(k_{r_2} a_2)}{H_1^{(1)}(k_{r_2} a_2)} \right]} \quad (4.2)$$

For convenience we define the following ratios:

Ratio of Hankel functions:

$$H_{rat}(x) = \frac{H_0^{(1)}(x)}{H_1^{(1)}(x)}$$

Ratio of radii:

$$s = \frac{a_2}{a_1}$$

Note that $\frac{k_1}{k_2} = R_c$, and also $\frac{\rho_2 c_2}{Z_1} = R_c$.

Substituting these quantities into 4.2 yields

$$Z_{a_1} = i Z_1 \frac{\left[R_{\rho \frac{k_{r_1}}{k_{r_2}}} Q_{01}(k_{r_1}) H_{rat}(k_{r_2} s a) - Q_{00}(k_{r_1}) \right]}{\left[Q_{10}(k_{r_1}) - R_{\rho \frac{k_{r_1}}{k_{r_2}}} Q_{11}(k_{r_1}) H_{rat}(k_{r_2} s a) \right]} \quad (4.3)$$

The response of this system to a specific excitation will depend on the wavenumber and frequency of the excitation (k_z and ω), as well as the acoustical properties

of the fluid tube and the external medium. Several limiting cases of interest will be studied using equation 4.3.

Case I - Zero Axial Wavenumber The simplest case is that for which there is no axial wave propagation, that is, $k_z = 0$. The excitation at $r = a_1$ is a pressure or velocity which is uniform in amplitude along the z axis, varying harmonically at frequency ω .

For this case, $k_{r1} = k_1$, $k_{r2} = k_2$, and $\frac{k_{r1}}{k_{r2}} = R_c$; also, $Z_1 = \rho_1 c_1$. The spectral impedance at $r = a_1$ (normalized to the specific acoustic impedance of medium 1, $\rho_1 c_1$), is found from 4.3 as

$$\frac{Z_{a1}}{\rho_1 c_1} = i \frac{\left[R_z Q_{01}(k_1) H_{rat}\left(\frac{k_1 s a}{R_c}\right) - Q_{00}(k_1) \right]}{\left[Q_{10}(k_1) - R_z Q_{11}(k_1) H_{rat}\left(\frac{k_1 s a}{R_c}\right) \right]} \quad (4.4)$$

The variables for this special case are the non-dimensional wavenumber in the fluid tube, $k_1 a_1$, the ratio of specific acoustic impedances R_z , the ratio of sound speeds R_c , and the ratio of radii, s .

Now for large values of the arguments in equation 4.4, that is, $k_1 a_1$, $k_1 a_2$, and $k_2 a_2$ are all greater than 2π , substitution of the asymptotic expressions developed in Chapter 2 leads to the following approximation:

$$\lim_{k_1 a_1 \rightarrow \infty} \left(\frac{Z_{a1}}{\rho_1 c_1} \right) = \frac{R_z - i \tan[k_1(a_2 - a_1)]}{1 - i R_z \tan[k_1(a_2 - a_1)]} \quad (4.5)$$

With these simplifications, the spectral impedance at the inner surface of the fluid tube is determined by R_z , the ratio of acoustic impedances, and the argument

of the tangent function, $k_1(a_2 - a_1)$, the product of the wavenumber in fluid 1 and the thickness of the tube. Two limiting cases of interest will be discussed.

(1) Tube thickness an integral number of half-wavelengths: If the tube thickness $a_2 - a_1$ is an integral number of half-wavelengths, that is,

$$a_2 - a_1 = \frac{n\pi}{k_1}, \quad n = 1, 2, 3 \dots$$

then $Z_{a_1} \rightarrow \rho_2 c_2$, the characteristic impedance of the external fluid.

(2) Tube thickness an odd number of quarter-wavelengths: If

$$a_2 - a_1 = \frac{(2n + 1)\pi}{4k_1}, \quad n = 1, 2, 3 \dots \quad (4.6)$$

then $Z_{a_1} \rightarrow \frac{\rho_1 c_1}{R_z} = \frac{(\rho_1 c_1)^2}{\rho_2 c_2}$. This relationship suggests an interesting method for "matching" the impedance of a source, such as a ceramic ring, to the specific acoustic impedance of the external fluid. If Z_{a_1} represents the impedance of the source, the fluid in the tube would be chosen such that

$$\rho_1 c_1 = \sqrt{Z_{a_1} \rho_2 c_2}$$

Of course, the assumptions made in obtaining equation 4.5 must hold, and exact "matching" will occur only at frequencies satisfying equation 4.6. For other combinations of frequency and tube thickness, the impedance Z_{a_1} will be complex.

In rectangular components, this may be expressed as

$$\lim_{k_1 a_1 \rightarrow \infty} \left(\frac{Z_{a_1}}{\rho_1 c_1} \right) = \frac{R_z + \tan^2 [k_1 (a_2 - a_1)]}{1 + R_z^2 \tan^2 [k_1 (a_2 - a_1)]} + i \frac{(R_z - 1) \tan [k_1 (a_2 - a_1)]}{1 + R_z^2 \tan^2 [k_1 (a_2 - a_1)]}$$

Returning to the general case described by equation 4.4, we will discuss the behavior of the normalized specific acoustic impedance as a function of the non-dimensional wavenumber $k_1 a_1$ for various combinations of the parameters R_c, R_z , and s .

(1) Variation with tube thickness, $a_1(s - 1)$: For this case, we assume a sound speed ratio of $R_c = 2$, and an impedance ratio $R_z = 2$. Figure 4-1 presents the variation in impedance as a function of $k_1 a_1$ for three values of the radius ratio, $s = 1, 2$, and 4. The magnitude, phase angle, and rectangular components of the impedance are shown.

The degenerate case $s = 1$, shown as a solid line, represents the impedance of the external medium alone, as discussed in Chapter 2. (For this case, there is no fluid tube in the system). For large values of the argument, the spectral impedance approaches the specific acoustic impedance of the external medium, $\rho_2 c_2$. For $s = 2$ (dotted line) and $s = 4$ (dashed line) the impedance functions exhibit cyclic behavior as a function of acoustic wavenumber (or frequency). The period of the fluctuations decreases with increasing tube thickness, in a fashion similar to that discussed for the fluid tube in Chapter 2. The impedance magnitude varies from R_z to $1/R_z$, as in the simplified case described above. The imaginary component of impedance is skewed in a triangular fashion. The real component waveform is less than unity for a greater part of the cycle, and exceeds unity for the remainder of the cycle. At large values of the argument, a steady-state condition is reached for the amplitude of the impedance variations.

(2) Variation with acoustic impedance ratio, R_z : In figure 4-2, a sound speed variation of two to one is assumed ($R_c = 2$), and the fluid tube thickness is twice the inner radius ($s = 2$). The spectral impedance is shown for three values of the impedance ratio, $R_z = \frac{1}{2}, 1$, and 2. Since the sound speed ratio is fixed at 2, the impedance ratio R_z is determined by the fluid density in each medium. Thus for $R_z = 1$, $\rho_2 = \frac{\rho_1}{2}$, etc.

Again, a cyclic variation of spectral impedance with wavenumber is observed. The phase of the variation is determined by the magnitude of the impedance ratio. (Compare, for example, the solid curves for $R_z = \frac{1}{2}$ with the dashed curves for $R_z = 2$.) The magnitude of the variation also depends on the value of R_z , being lowest for $R_z = 1$, and increasing for both larger and smaller values of the impedance ratio. The same comments regarding the waveforms of the real and imaginary components as made in the preceding case apply to the present analysis.

(3) Variation with sound speed ratio, R_c : For this example, the impedance ratio is fixed at 1.5, and the ratio of radii is again 2. Figure 4-3 presents the spectral impedance versus frequency for $R_c = \frac{1}{10}, 1$, and 10. When the sound speed in the external fluid exceeds that in the fluid tube (dashed line), the impedance variation is greatest at small values of $k_1 a_1$, decreasing with increasing wavenumber until a steady state is reached. The reverse is true for $c_1 > c_2$, where the impedance variation builds up to a steady state value as the frequency increases. The same asymmetry previously noted in the real and imaginary components is apparent for this case.

In summary, there are three parameters which affect the normalized spectral impedance of the fluid tube - external fluid system. The tube radius ratio s controls the periodicity of the cyclic impedance variations, with the period decreasing as s increases. The fluid impedance ratio R_z and sound speed ratio R_c primarily influence the magnitude of the cyclic impedance variations. In all cases, the cyclic variations reach a steady state for $k_1 a_1 \gg 2\pi$.

Case II - Finite Axial Wavenumber: The more general case in which the axial wavenumber is finite will include both propagating waves as described earlier, and standing waves in which the excitation may be of the form $P_o(\cos k_z z)(\cos \omega t)$. The conditions for the existence of a standing or a propagating wave in the fluid tube were described earlier, that is, $k_1 > k_z$. The radial spectral impedance at $r = a_1$ will be given by equation 4.3. The behavior of the impedance will be similar to that described for Case I when both radial wavenumbers k_{r1} and k_{r2} are real. When $k_1 < k_z$ an evanescent wave will occupy the fluid tube. This may "leak" into the external medium if the fluid tube is sufficiently thin.

4.2.3 Multiple Concentric Fluid Tubes: We now consider a system comprised of any number N of concentric fluid tubes immersed in an external fluid, as illustrated in Figure 1-1. The first fluid tube extends radially from $r = a_1$ to $r = a_2$ and contains a fluid of density ρ_1 and sound speed c_1 . The j th tube is bounded by the inner radius a_j and outer radius a_{j+1} , with fluid of characteristic impedance $\rho_j c_j$. The outermost fluid tube extends from radius a_{N-1} to a_N , where a_N is the radius

of the interface between the N th tube and the external fluid.

Now let P_1 and V_1 be the state variables of pressure and radial velocity applied to the innermost fluid tube at $r = a_1$. The pressure and radial velocity at the interface $r = a_2$ are given by

$$\begin{bmatrix} P_2 \\ V_2 \end{bmatrix} = \begin{bmatrix} A_1 & B_1 \\ C_1 & D_1 \end{bmatrix} \begin{bmatrix} P_1 \\ V_1 \end{bmatrix} \quad (4.7)$$

The values of P_2 and V_2 from equation 4.7 become the input for the second fluid tube of inner radius a_2 , so that the transfer function from a_1 to a_3 may be expressed as

$$\begin{bmatrix} P_3 \\ V_3 \end{bmatrix} = \begin{bmatrix} A_2 & B_2 \\ C_2 & D_2 \end{bmatrix} \begin{bmatrix} A_1 & B_1 \\ C_1 & D_1 \end{bmatrix} \begin{bmatrix} P_1 \\ V_1 \end{bmatrix}$$

This process is repeated for each fluid tube in the system, with the result

$$\begin{bmatrix} P_N \\ V_N \end{bmatrix} = \begin{bmatrix} A_T & B_T \\ C_T & D_T \end{bmatrix} \begin{bmatrix} P_1 \\ V_1 \end{bmatrix}$$

where P_N and V_N are the state variables at $r = a_N$, the interface with the external fluid, and $P_N = V_N Z_N$, in which Z_N is the spectral impedance of the external fluid, equation 2.57.

The overall transfer matrix is obtained by cascading the matrices for each component, viz

$$\begin{bmatrix} A_T & B_T \\ C_T & D_T \end{bmatrix} = \begin{bmatrix} A_{N-1} & B_{N-1} \\ C_{N-1} & D_{N-1} \end{bmatrix} \begin{bmatrix} \dots \end{bmatrix} \begin{bmatrix} A_j & B_j \\ C_j & D_j \end{bmatrix} \begin{bmatrix} \dots \end{bmatrix} \begin{bmatrix} A_1 & B_1 \\ C_1 & D_1 \end{bmatrix}$$

Care must be taken when using this model that the correct $ABCD$ expressions are used in each component, depending on whether the radial wavenumber k_j is

real or imaginary. The conditions discussed earlier in the section "Parameters for Two Fluid Systems" must be evaluated at each radial interface to determine whether propagating or evanescent waves will exist in the succeeding fluid tube.

4.2.4 Systems Including a Fluid Cylinder: When a composite cylindrical system includes a fluid cylinder, this component may exert a major influence on wave propagation. When the radial wavenumber in the fluid cylinder is real, equation 2.14 and Figure 2.3 show that the spectral impedance of the cylinder will cycle from zero to infinity as a function of the argument $k_{rc}a$ where k_{rc} is the radial wavenumber and a is the radius of the cylinder. This establishes the range of boundary conditions at the cylinder surface, ranging from zero velocity ("blocked" pressure) to zero pressure ("free" surface).

When the axial wavenumber k_z is much greater than the acoustic wavenumber in the fluid cylinder, equation 2.17 predicts a mass-like spectral impedance which increases with frequency and decreases with axial wavenumber.

Fluid Cylinder within Fluid Tube: We now consider a fluid cylinder of radius a_1 and specific acoustic impedance $\rho_1 c_1$ which is concentric with a fluid tube of outer radius a_2 and filled with a fluid of impedance $\rho_2 c_2$. This system is driven by a wave of frequency ω and wavenumber k_z applied at the outer radius. The transfer matrix for the fluid tube is

$$\begin{bmatrix} P_1 \\ V_1 \end{bmatrix} = \begin{bmatrix} A_{21} & B_{21} \\ C_{21} & D_{21} \end{bmatrix} \begin{bmatrix} P_2 \\ V_2 \end{bmatrix}$$

where the $ABCD$ functions are as defined by equations 2.37 to 2.40. The

pressure and velocity at $r = a_1$ are related by $P_1/V_1 = Z_{fc}$, the spectral impedance of the fluid cylinder. Solving for the spectral impedance at the input, $r = a_2$, we have

$$\frac{P_2}{V_2} = Z_2 = \frac{D_{21}Z_{fc} - B_{21}}{A_{21} - C_{21}Z_{fc}} \quad (4.8)$$

When the impedance of the fluid cylinder is zero, Z_2 is given by

$$Z_2|_{Z_{fc} \rightarrow 0} = -\frac{B_{21}}{A_{21}} = -i \frac{\rho_2 \omega [J_0(k_{r2}a_2)Y_0(k_{r2}a_1) - J_0(k_{r2}a_1)Y_0(k_{r2}a_2)]}{k_{r2} [J_1(k_{r2}a_2)Y_0(k_{r2}a_1) - J_0(k_{r2}a_1)Y_1(k_{r2}a_2)]}$$

Similarly, when the impedance of the fluid cylinder is infinite, Z_2 is

$$Z_2|_{Z_{fc} \rightarrow \infty} = -\frac{D_{21}}{C_{21}} = i \frac{\rho_2 \omega [J_1(k_{r2}a_1)Y_0(k_{r2}a_2) - J_0(k_{r2}a_2)Y_1(k_{r2}a_1)]}{k_{r2} [J_1(k_{r2}a_2)Y_1(k_{r2}a_1) - J_1(k_{r2}a_1)Y_1(k_{r2}a_2)]}$$

The impedance Z_2 is always reactive, since there is no dissipation or energy radiation in the system. The magnitude and phase of the spectral impedance will vary with the dimensions a_1 and a_2 , as well as the frequency and wavenumber of the excitation.

4.3 Fluid Loaded Elastic Shells

One of the most widely studied topics in the area of structural acoustics is that of fluid loaded elastic shells. The preponderance of work has been concerned with cylindrical elastic shells, first, because of the multitude of practical problems which may be described by this configuration (several examples were cited in Chapter 1), and second, because the separability of the wave equation in cylindrical coordinates renders such problems analytically tractable.

Junger and Feit (1986) devote substantial attention to both finite and infinite fluid loaded cylindrical shells, including sound radiation by driven shells and the

scattering of incident sound by elastic cylinders. Their book "Sound, Structures and Their Interaction" is an excellent starting point for the study of this topic. Most authors use thin shell theories, such as described in Chapter 3, to represent the elastic cylinder in their analyses of fluid loaded shells. One exception is Greenspan (1960) who used elasticity theory in his study of an elastic shell with fluid loading on both surfaces and driven by a spatially arbitrary, time harmonic pressure applied to the inner surface. A more recent example is Pathak (1993) who applied elasticity theory to study the radiated pressure from an infinite length thick cylindrical shell harmonically driven by a ring force. The present discussion will employ the axisymmetric thin shell model developed in Chapter 3.

4.3.1 Elastic Shell in Fluid System: Now consider a system with a fluid tube of inner radius a_1 and outer radius a_2 , with an elastic shell at this outer radius. Since the thickness of the elastic shell is very small compared to its radius, we may neglect it when computing fluid impedances. A second fluid tube extends radially from a_2 to a_3 where it meets the external fluid. The specific acoustic impedance of the first fluid is $\rho_1 c_1$, the second fluid is $\rho_2 c_2$, and the external fluid is $\rho_3 c_3$. This model could represent, for example, a sonar transducer comprising a piezoelectric ceramic cylinder surrounded by a coupling fluid, such as castor oil or isoper, a thin metal casing, and a protective outer elastomeric jacket of a material with negligible shear modulus. The external fluid in this case would be water. The system input at $r = a_1$ would be provided by the piezoelectric ceramic cylinder.

Following the method described under "Multiple Concentric Fluid Tubes," the

model for such a system is:

$$\begin{bmatrix} P_4 \\ V_4 \end{bmatrix} = \begin{bmatrix} A_3 & B_3 \\ C_3 & D_3 \end{bmatrix} \begin{bmatrix} 1 & Z_s \\ 0 & 1 \end{bmatrix} \begin{bmatrix} A_1 & B_1 \\ C_1 & D_1 \end{bmatrix} \begin{bmatrix} P_1 \\ V_1 \end{bmatrix}$$

in which P_1 and V_1 are the pressure and radial velocity at the interface between the ceramic cylinder and the first fluid tube; $A_1 B_1 C_1 D_1$ represent the first fluid tube, $A_3 B_3 C_3 D_3$ represent the second fluid tube, and Z_s is the spectral impedance of the shell, from Eq. 3.8. The pressure and radial velocity at $r = a_3$ are related by the spectral impedance of the external fluid, $P_4 = Z_4 V_4$, where Z_4 is computed by substitution of the characteristics of the external fluid into Eq. 2.57. Thus the state and field variables of the entire system may be determined.

A generalized discussion of this system is not feasible due to the large number of parameters involved (three radii, three fluids, and the shell characteristics). However, a specific design problem is easily approached following the methods described in this and earlier chapters.

4.3.2 Elastic Shell With Fluid Cylinder: The problem of wave propagation in a fluid filled elastic shell has been approached by many authors, including Thomson (1953), Skalak (1956), White and Sawley (1972), Kumar (1966,1972). Merkulov, Prikhod'ko and Tyutekin (1978), Fuller (1981, 1988), Ujihashi et al (1987), Fuller and Fahy (1982), and more recently, Brévar and Fuller (1994). The great interest in this problem stems from practical considerations such as noise (e.g. "water hammer") in piping systems and the reduction of noise from the exhaust of internal combustion engines.

The propagation of free waves in a fluid filled thin elastic cylinder was studied by Fuller and Fahy. They computed the dispersion curves for circumferential modes of order $n = 0, 1$ and 2 for steel and hard rubber shells filled with water. The coupling of the fluid to the shell complicates the solution for the complex roots of the characteristic equation because the roots are embedded in the argument of the Bessel functions which represent the fluid loading term (that is, the argument $k_r a$ in Eq. 2.14 of this study). This requires that the roots be determined by numerical analysis.

Brévar and Fuller computed the response of an infinite fluid filled elastic shell to a radial impulse defined as a delta function in both time and space. The axisymmetric description of this system may be constructed using Eqs. 2.14 and 3.8 as follows:

$$\widehat{V}_w(\Omega, K_z) = \frac{\widehat{P}_o}{\frac{i\omega_r \rho_s h}{\Omega} \left[\frac{K_z^2 v^2}{(\Omega^2 - K_z^2)} + 1 + \beta^2 K_z^4 - \Omega^2 \right] + \frac{i\rho_f \Omega c_p}{K_r} \frac{J_0(K_r)}{J_1(K_r)}} \quad (4.9)$$

where $\widehat{V}_w(\Omega, K_z)$ is the double Fourier transform of the radial velocity in frequency-wavenumber space, ρ_s is the density of the shell material, ρ_f is the density of the fluid, c_p is the extensional wave speed of the shell, $K_r = \sqrt{\left(\Omega \frac{c_p}{c_f}\right)^2 - K_z^2}$ is the non-dimensional radial wavenumber for the fluid cylinder, and \widehat{P}_o is the Fourier transform of the input ring force function, $P_o \delta(t) \delta(z)$. The authors obtained the time domain response by numerical inversion of the three dimensional version of Eq. 4.9. The inversion in wavenumber space was computed by summing the residues of the transfer receptance, as previously described by Fuller (1983). This required knowledge of the location of the poles of the transfer mo-

bility, which occur at the zeros of the characteristic equation for free vibrations of the fluid loaded cylinder. The earlier paper by Fuller and Fahy (1982) provided this information.

4.3.3 Elastic Shell with External Fluid: The response of an infinite cylindrical shell with external fluid loading to harmonic excitation from a ring force has been studied by Photiadis (1990). In contrast with the internal fluid problem, where all radial impedances are purely reactive and energy flow is confined to the axial direction in the shell and fluid, the propagation of waves outward in the external fluid complicates the analysis of this case.

In terms of the present study, the problem discussed by Photiadis may be expressed as

$$\widehat{V}_w(\Omega, K_z) = \frac{\widehat{P}_o(\Omega)}{\frac{i\omega_r \rho_s h}{\Omega} \left[\frac{K_z^2 v^2}{(\Omega^2 - K_z^2)} + 1 + \beta^2 K_z^4 - \Omega^2 \right] + \frac{i\rho_f \Omega c_p}{K_r} \frac{H_0^{(1)}(K_r)}{H_1^{(1)}(K_r)}} \quad (4.10)$$

in which $\widehat{P}_0(\Omega)$ is the spatial Fourier transform of the harmonic input, $P_o(\Omega)\delta(t)$, and the Bessel functions representing the fluid cylinder impedance in Eq. 4.9 have been replaced with the Hankel functions to represent the external medium, as written in Eq. 2.57. The other quantities in Eq. 4.10 are as defined above.

Photiadis constructs a Green's function solution for the radial velocity as a function of axial distance by inverse Fourier transformation of the denominator of Eq. 4.10, that is,

$$V_w(\Omega, z) = P_o(\Omega)G(z)$$

where

$$G(z) = \frac{1}{2\pi} \int_{-\infty}^{\infty} \frac{e^{iK_z \frac{z}{a}} dK_z}{\frac{i\omega_r \rho_s h}{\Omega} \left[\frac{K_z^2 v^2}{(\Omega^2 - K_z^2)} + 1 + \beta^2 K_z^4 - \Omega^2 \right] + \frac{i\rho_f \Omega c_p}{K_r} \frac{H_0^{(1)}(K_r)}{H_1^{(1)}(K_r)}}$$

The inversion integral is evaluated by contour integration in the complex K_z plane. The analysis is fairly recondite and will not be pursued at length here. Essentially, Photiadis evaluates the integral at the various poles by introducing simplifying approximations based on physical reasoning. The approximate analytical results compare favorably with the exact values computed numerically.

CHAPTER 5

Experimental Work

5.1 Introduction

In this chapter we discuss an experiment which was conducted to study the propagation of transients in a thin cylindrical shell for comparison with the theoretical predictions described in Chapter 3. We begin with a description of the experimental apparatus and the considerations which affected the design of the experiment. This is followed by a discussion of the measurements obtained. Results of the experimental work are compared with the predicted values.

5.2 Design of Experiment

5.2.1 Description of Experiment

The experimental apparatus comprised a thin brass tube which was freely suspended on very compliant supports (bungee cords) at two axial locations. The tube was mechanically driven by a piezoelectric disk which was bonded to one end. The disk was driven from an electronic function generator, thus various waveforms of interest (such as sinusoidal, triangular, or rectangular) could be applied to the tube. The radial displacement of the tube was measured with gages made from poly-vinylidene fluoride film applied circumferentially to the exterior wall of the tube at various locations of interest. Electrical output from the displacement gages was amplified, filtered, and displayed on a digital oscilloscope. The oscillo-

scope has a transient capture capability and a digital recorder. Raw data obtained with the digital oscilloscope was saved on computer data storage disks for off-line processing. A sketch of the apparatus is shown in figure 5-1.

5.2.2 Selection of Tube

The important factors involved in the selection of a tube for the experiment include the tube material, the length, the diameter, the wall thickness, the availability, and the cost. The most significant factor in the selection of the material is the wave speed. For a finite length tube, a low wave speed maximizes the time in which transients may be observed before echoes occur. Unfortunately the materials with the lowest wave speeds, such as plastics and lead, are also lossy. For a given material, the diameter will determine the ring frequency. This should be chosen so as to be within the bandwidth of the available instrumentation. The wall thickness should be selected to meet the criteria for a "thin" shell, as indicated by the analytical models.

The criteria of cost and availability limited the choices to aluminum, brass, copper, and steel. Brass was selected since it has the lowest wave speed of the four choices (a dilatational wave speed of 4700 meters per second, compared with 6300 m/s for aluminum, 5000 m/s for copper, and 6100 m/s for steel) and is readily available. Standard brass tube is available in 12 foot (3.61 meter) lengths, and this would conveniently fit in the available laboratory space. A diameter of 2 inches (5 cm) was selected, which places the ring frequency at approximately 25 kilohertz. The wall thickness of the experimental tube is 0.035 inches (.89 millimeters), so

the thickness to mean radius ratio is 0.036.

5.2.3 Displacement Gages

In order to observe wave propagation and dispersion in the experimental tube, it is necessary to measure the components of displacement at various axial positions along the length of the tube. Since axisymmetric radial excitation is employed, only radial and axial displacements are expected. An ideal displacement gage would have the following attributes: high sensitivity, low noise, minimum interference with the signal, and dimensions which are small compared with the wavelength of the stress waves to be measured. For measurement of the radial displacement, a gage which wraps around the circumference of the tube will provide spatial integration of any non-axisymmetric signal components.

Graff (1975) describes several methods which have been employed for the experimental investigation of stress waves. These include the electrical-resistance strain gage, capacitance gages, inductance effects, piezoelectric devices, and photoelasticity. More recently, laser velocimeters have been employed by a number of investigators.

For the present application, a relatively new plastic piezoelectric material, polarized poly-vinylidene fluoride film (PVDF), offered several advantages. This film is produced by stretching extruded PVDF film to induce a phase transition from the non-polar alpha phase, to the polar beta phase. The beta phase film is then polarized by exposure to a high electrostatic field at elevated temperature. The resulting permanent alignment of molecular dipoles in the film produces the

piezoelectric activity. Electrodes are applied to the film either by sputtering or by silk-screening using conductive silver ink. Electrodes may be produced in any desired pattern.

The area density of thin ($52 \cdot 10^{-6}$ meters) PVDF film is about 93 grams per square meter, which represents a negligible mass load when applied to the experimental tube. The Young's modulus of PVDF is also very low, $2 \cdot 10^9$ Newtons per square meter, so that a thin strip will have a negligible stiffness effect when bonded to the tube. The film is easily attached either with cement or double sided plastic tape.

The electrical and mechanical properties of piezoelectric film are categorized in terms of a 1, 2, 3 rectangular coordinate system. The axes are oriented such that 1 corresponds to length (the direction in which the film is stretched), 2 corresponds to the width, and 3 to the thickness, which is the direction of polarization. The film is anisotropic, so that the piezoelectric constants are greatest in the 3,1 and 3,3 directions, and minimum in the 3,2 direction. For example, the g_{31} constant is about 11 times greater than g_{32} , which means that the voltage produced by a given stress in the length (1) direction is over 20 dB greater than the voltage resulting from the same stress in the width (2) direction. This is advantageous in the current application, as it discriminates against displacements which are orthogonal to the desired displacement.

Sensitivity of PVDF Gages: The PVDF gages are applied circumferentially to the exterior surface of the brass tube. The active length of the gages is 155 millimeters,

about 5 mm less than the circumference of the tube. Since the Young's modulus of the tube is about 50 times that of the PVDF gages, we may assume that the strain in the gages is the same as that of the tube. The stress in the gage is the product of the strain and the Young's modulus of the gage, and the electric field E_3 is g_{31} times the stress. The voltage developed is the product of the electric field times the thickness of the gage. Thus the voltage V resulting from a given strain ϵ is given by $V = (Y_g t_g g_{31}) \cdot \epsilon$, where Y_g is the Young's modulus of the PVDF and t_g is the thickness of the PVDF film. Evaluation of this expression using the values for the circumferential gages results in $V/\epsilon = 22.46 \cdot 10^3$ (volts/unit strain). A typical strain gage has a sensitivity of about 5 volts/unit strain, thus the PVDF film is about 73 dB more sensitive than a strain gage. The radial displacement w is $\epsilon L_g / 2\pi$, since the length of the gage L_g is approximately equal to the circumference of the tube. Thus the radial sensitivity of the gage is $w/V = 1.112 \cdot 10^{-6}$ meters per volt, or -119 dB re 1 meter/volt.

5.2.4 Piezoelectric Disk Driver

Mechanical input to the experimental tube was generated with a lead zirconate titanate (PZT) ceramic disk which was bonded to one end of the tube with epoxy cement. The disk is 5.08 cm in diameter and 2.57 mm thick. Circular silver electrodes 4.85 cm in diameter are provided on the flat faces of the disk. When a voltage is applied to the electrodes, the 3,1 mode coupling in the disk produces an axisymmetric radial strain, which is communicated to the brass tube. The static radial displacement of a free thin piezoelectric ceramic disk is given by: (Vernitron,

1984)

$$\Delta r = 2d_{3,1}V\frac{r}{t}$$

where $d_{3,1}$ is the piezoelectric strain constant for the 3,1 mode, V is the applied voltage, r is the radius of the disk, and t is the thickness. For the disk used in this experiment, $d_{3,1} = -109 \cdot 10^{-12}$ meters/volt and the ratio of radial displacement to applied voltage is $\Delta r/V = 2.2 \cdot 10^{-6}$ millimeters per volt.

The piezoelectric disk will have an infinite number of radial and thickness vibrational modes. Since the disk is almost completely silvered on both flat surfaces, only the $n = 0$ (axisymmetric) radial modes will be excited. Since the radius of the disk is approximately 10 times the thickness, the lower order radial modes will be independent from the thickness modes. The thickness mode frequencies are given by

$$f_m = \frac{m c_t^D}{2t}, \quad m = 1, 2, 3, \dots$$

(Mason, 1964) where c_t^D is the wave speed in the 3,3 direction at constant electric displacement D , and m is the mode number. Using the value $c_t^D = 4300$ meters/second (Berlincourt and Krueger, 1964) yields the value $f_1 = 838$ kilohertz for the first thickness mode of the disk.

The frequencies of the axisymmetric radial modes are found from the roots of

$$\eta J_0(\eta) = (1 - \nu^E) J_1(\eta) \quad (5.1)$$

(Meitzler, O'Bryan, and Tiersten, 1973) where $\nu^E = -(s_{12}^E/s_{11}^E) = .315$ is a planar Poisson's ratio, and the argument $\eta = 2\pi f a/c^p$. The quantity c^p in η is a

planar wave speed,

$$(c^p)^2 = \frac{s_{11}^E}{\rho [(s_{11}^E)^2 - (s_{12}^E)^2]}$$

in which ρ is the density of the ceramic material, and s_{11}^E and s_{12}^E are the elastic compliance constants at constant electric field E . For the disk used in this experiment, $c^p = 3464$ meters/second. Solving 5.1 the frequencies of the first seven radial modes are found as 44.61, 117, 186.1, 254.7, 323.1, 391.4 and 459.7 kilohertz, respectively.

Measurements made on the piezoelectric disk prior to installation are shown on figures 5-2, 5-3, and 5-4. Figures 5-2 and 5-3 present the magnitude of the electrical admittance of the disk as a function of frequency, plotted on logarithmic axes. The peak of the admittance magnitude on figure 5-2 at 44.61 kilohertz identifies the frequency of the first radial mode. The admittance minimum at 51.33 kilohertz occurs at the antiresonant frequency for the first radial mode. From these frequencies, the planar coupling factor was determined to be $k_p = .55$. (IEEE 1984) Radial modes two through seven are easily identified on figure 5-3, occurring at 117.0, 184.4, 250.0, 311.3, 368.6, and 420.0 kilohertz, respectively. The magnitude of the ratio of maximum to minimum admittance at a specific mode decreases as the mode number increases, thus it is difficult to identify modes above the seventh on the plot of figure 5-3. The measured frequencies agree closely with those calculated above, especially for the first four modes. Note that the difference between the predicted and measured nodal frequencies increased with mode number. This may be due to the fact that the diameter of the electrodes is 23 millimeters less than

the diameter of the disk. This creates a ring of inactive ceramic at the outer edge of the disk. The mass of this inactive ring will tend to lower the modal frequencies, becoming more significant at the higher frequencies.

The first thickness mode appears at 808 kilohertz on figure 5-3. The rapid fluctuations in admittance near and above this resonance may be due to modal interaction with higher order radial modes. For example, the computed values for modes 12 to 14 are 800.9, 869.1, and 937.3 kilohertz, respectively.

The complex admittance locus (susceptance versus conductance) for the first radial mode of the disk is shown in figure 5-4. The mechanical "Q", or quality factor, of the disk is determined from this plot as:

$$Q = \frac{f_r}{(f_2 - f_1)} \quad (5.2)$$

in which f_r is the mechanical resonance frequency, the frequency at which the conductance is a maximum, and f_1 and f_2 are the quadrantal frequencies, where the conductance is half of the maximum value. The Q for the experimental disk computed with equation 5.2 is 816, which indicates that the free disk has very low losses.

5.2.5 Development of Dummy Load

Initial measurements on the apparatus with a 2 microsecond rectangular pulse input applied to the piezoelectric disk revealed the presence of strong spectral components at frequencies near those of the first three radial modes of the free piezoelectric disk. Figure 5-5 presents the spectrum of the radial displacement at gage C-1, located approximately 7 cm from the piezoelectric disk. Since it is

desireable to have a relatively flat spectrum in the mechanical input to the tube, various means for achieving this end were explored.

The measurements on the free piezoelectric disk, before it was attached to the tube, were made with an impedance analyzer which applies a continuous harmonic excitation to the test specimen. However, driving the attached disk with a continuous signal was not feasible due to the multiple resonant modes which were excited in the tube. Instead, the disk was driven with a tone burst comprised of a gated sinusoidal voltage signal at the first radial mode, about 44 kHz. The Q of the system was then estimated from the rise time of the current in the disk. With this method, the tone burst must be long enough to encompass the initial and final transients in the system response.

Tone burst measurements indicated that the Q of the system at the first radial mode was approximately 50. One simple way to reduce the Q of a system is to increase the damping by adding resistive losses. Various lossy materials, such as a mastic material, and plastic tape, were applied to the free face of the piezoelectric disk, and the free end of the tube. The lowest value of Q which could be achieved with these methods was about 15, which was still too high for the planned measurements.

A more sophisticated approach to increasing the bandwidth of piezoelectric transducers is by the use of an electrical "dummy load." With this method, a second piezoelectric element is mechanically coupled to the driven device. The electrical output of the second, or "dummy," element is connected to a suitable

electrical network, which is designed to maximize the bandwidth of the system. Application of this method to ultrasonic transducers has been described by Gazallet, Houze, et al (1988). For the present application, the dummy element comprises a piezoelectric disk which is identical to the driven disk. The dummy disc is cemented to the driven disk, with appropriate means for connection to an external electrical network.

The first step in the development of the dummy load was to prepare a test setup comprising two piezoelectric disks which were bonded together, but not attached to the tube. This enabled the dummy load system to be optimized independent of the additional load imposed when the brass tube is driven. Initial measurements were made on the two disks to determine their free characteristics, then the disks were cemented together to form a prototype dummy load system.

For frequencies in the vicinity of the first radial mode, the electromechanical characteristics of the piezoelectric disk may be represented by a lumped analogous electrical network, shown in figure 5-6 (a) (Mason, 1964; Kinsler, Frey et al, 1982). In figure 5-6 (a) we employ the impedance analogy, in which electrical voltage is analogous to force, and electrical current is analogous to velocity (Beranek, 1954). The mechanical elements (mass, compliance, and loss resistance) have been converted into equivalent electrical circuit elements (inductance L_{me} , capacitance C_{me} , and resistance R_{me}) using the electromechanical transformation factor, N . The input electrical voltage E and current I are also indicated on figure 5-6 (a). The capacitor C_{01} represents the "blocked" capacitance of the disk, that is, the

capacitance which one would measure if the disk was physically restrained from any mechanical motion. The mechanical variables, force and velocity, are shown as F/N and $U \cdot N$. All of the elements shown in figure 5-6 (a) may be determined from the results of two terminal measurements of a "free" (that is, mechanically unloaded) disk. Since air has a very low specific acoustic impedance, the mechanical terminals of figure 5-6 (a) are effectively "short circuited" for air measurements, resulting in the equivalent circuit of figure 5-6 (b). First, the capacitance of the disk is measured at a frequency far below resonance. This "free" capacitance is equal to the parallel combination of C_0 and C_{me} , which in turn may now be computed using the measured capacitance and the planar coupling factor, k_p . The remaining elements, L_{me} and R_{me} are found using the complex admittance locus, such as shown in figure 5-4. The mechanical resonance frequency f_r is the frequency at maximum conductance, G_{max} . The inductance $L_{me} = 1/C_{me}(2\pi f_r)^2$, and the resistance $R_{me} = 1/G_{max}$. These quantities were determined from measurements of several disks to implement the next stage in the dummy load design.

Figure 5-6 (c) represents the equivalent circuit of the dummy load system. The driven disk is represented by the elements with subscript 1, and the dummy disk by elements with subscript 2. The blocks Z_{me1} and Z_{me2} comprise the series mechanical branch of each disk. The dummy disk is connected to a circuit comprising a resistor R_d in parallel with an inductor L_d . When the dummy load system is connected to a mechanical load, such as the experimental brass tube, a load impedance Z_{le} would appear at terminals a-a' in figure 5-6 (c).

A mathematical model was made of the equivalent circuit of figure 5-6 (c) using average values for the circuit elements from the measurements described above. The model enabled prediction of the response of the dummy load system as function of the electrical dummy load resistor and inductor. By extensive exercise of the model it was determined that a Q of 2.1 could be achieved with the proper values of R_d and L_d . Using these results, input admittance measurements were made on the prototype dummy load system with various combinations of R_d and L_d . The lowest Q obtained experimentally on the prototype system was 4, determined from analysis of the complex admittance locus.

The next effort was focused on the application of the dummy load to the experimental apparatus. A dummy load disk was bonded to the primary driving disk with epoxy cement. A thin (0.2 millimeter) circular disk of expanded metal was placed between the piezoelectric disks to facilitate the electrical connection to the common silver interfaces of the disks. The dummy load disk was then connected to the electrical dummy load which had been developed previously using the prototype dummy load system.

Addition of the dummy load produced a dramatic improvement in the operation of the experimental system. This is illustrated in figure 5-7, which compares the system response with the dummy load "off," that is, electrically disconnected, with that when the electrical dummy load was connected to the dummy load disk. The primary disk was driven with a 3.3 microsecond, 30 volt rectangular pulse for these measurements. The output was taken as the voltage developed across the

dummy load disk, which is proportional to the radial displacement.

Figure 5-7 (a) displays the dummy disk voltage with the dummy load "off." The system "rings" for about 800 microseconds with this input. The spectrum of this waveform is shown in figure 5-7 (c), in which a logarithmic scale is used on the ordinate. The major peak in the response occurs at 47.8 kilohertz, and the Q as determined from the frequencies at which the response has decreased by 3 dB is about 28.

When the dummy load is connected (figure 5-7 (b)), the response decays to zero in less than 100 microseconds. The spectrum, in figure 5-7 (d), peaks at 43 kilohertz. The Q has dropped to 2.7, a ten to one improvement over the first case. Figure 5-7 (d) also shows that the spectrum from 100 to 200 kilohertz has been elevated about 20 dB, indicating that the dummy load also improves the high frequency response of the system.

5.2.6 Determination of Wave Speed

In order to insure an accurate comparison of the results of experimental measurements with those predicted by theory, it is necessary to know the exact value of the wave speed in the experimental brass tube. Five independent methods were investigated for this purpose. First, a review was made of published values for brass. The second approach was a calculation from the material properties published for the type of brass used. Then three experimental methods were considered: (1) Time of Flight measurement; (2) Ring Mode Resonance; and (3) Extrapolation from free longitudinal modal resonances. The most accurate result was attained

with the last method.

Review of Published Data: The results of a review of three texts Fahy (1985), Elmore and Heald (1985), and Kinsler and Frey, et. al. (1982)) and tables from a commercial source (Metrotek (1982)) are presented in Table 5-1. The entry labeled "Cartridge Brass," which is the type of brass for the experimental tube, was computed from values of Young's modulus and density from Hoyt (1954). The table lists the source, the value of Young's Modulus E , in Newtons per square meter; the density ρ , in kilograms per cubic meter; Poisson's ratio ν ; the longitudinal wave speed (also known as the "bulk wave speed" and the "dilatational wave speed") c_d ; the "thin plate" (or "extensional") wave speed c_p ; the "thin bar" wave speed c_b ; the shear wave speed c_s ; (all wave speeds are in units of meters per second); the shear modulus of elasticity G in Newtons per square meter (this is also the Lamé' coefficient μ); the bulk modulus B in Newtons per square meter; and the Lamé' coefficient λ , Newtons per square meter.

None of the sources reviewed published all of the properties listed in each row of Table 5-1. Any missing values were calculated from those published, using one or more of the equations listed below.

Dilatational (longitudinal) wave speed:

$$c_d = \sqrt{\frac{\beta}{\rho}} = \sqrt{\frac{E(1-\nu)}{\rho(1+\nu)(1-2\nu)}} = \sqrt{\frac{\lambda+2\mu}{\rho}}$$

Extensional (thin plate) wave speed:

$$c_p = \sqrt{\frac{E}{\rho(1-\nu^2)}} = \sqrt{\frac{4\mu(\lambda+\mu)}{\rho(\lambda+2\mu)}}$$

Thin bar wave speed:

$$c_b = \sqrt{\frac{E}{\rho}} = \sqrt{\frac{\mu(3\lambda + 2\mu)}{\rho(\lambda + \mu)}}$$

Shear wave speed:

$$c_s = \sqrt{\frac{E}{2\rho(1 + \nu)}} = \sqrt{\frac{\mu}{\rho}}$$

Bulk modulus of elasticity:

$$\beta = \lambda + \frac{2}{3}\mu$$

Young's modulus of elasticity:

$$E = 2\mu(1 + \nu) = \frac{\mu(3\lambda + 2\mu)}{\lambda + \mu}$$

Poisson's ratio:

$$\nu = \frac{\lambda}{2(\lambda + \mu)}$$

The mean and standard deviation of the published data are shown in the table.

The deviation expressed as a percentage of the mean is also included. The large variation in the published data on brass may be due to the fact that brass is an alloy of copper and zinc, with trace quantities of lead and iron. Hoyt (1954) lists over 13 different types of brass. The copper content varies from 60% to 80%, and the lead from .07% to 2%. The iron content ranges from .05% to .15%. The balance of the alloy is zinc. The mean value of Young's modulus for these alloys is 10.65×10^{10} Newtons/square meter, with a standard deviation of 5.76%, and the mean value of density is 8.47×10^3 kg/cubic meter, with a standard deviation of 1.16%. These values compare closely with those in Table 5-1. Unfortunately,

Hoyt does not list the values of Poisson's ratio. The composition of the brass tube used in the experiment is: copper, 68.5% minimum, 71.5% maximum; lead, 0.07%, iron, 0.05%, and the remainder is zinc. This composition fits the description of cartridge brass in Hoyt.

Time of Flight Measurement: In the time of flight method, the wave speed is measured by determination of the time required for a transient wave, such as an impulse or short rectangular pulse, to traverse a known distance. For a non-dispersive system (such as a string, or long thin bar), this method yields accurate results. With a dispersive system, such as the experimental tube, distortion of the input pulse with distance makes it difficult to identify the precise time of arrival of the signal. Nine measurements on the experimental tube gave values of c_p ranging from 3696 to 4507 meters per second. The average value was 3959 meters per second, with a standard deviation of 244 meters per second. These results indicated the need for a more precise method for the determination of wave speed.

Ring Mode Resonance: Another potential method for determining c_p is based on harmonic excitation of the so-called "ring" frequency of the tube. With an axisymmetric ($n = 0$ mode) excitation, a strong resonance should occur at the "ring" frequency, where the axial wavelength is equal to the mean circumference of the tube. The extensional wave speed may then be computed from the relation $c_p = 2\pi f_r a$, where f_r is the measured ring frequency, and a is the mean radius of the tube. This measurement was attempted by applying continuous sinusoidal

excitation to the piezoelectric driver disk and monitoring the radial displacement of the tube on the circumferential PVDF gages. Using the estimated value of $c_p = 3872$ meters/sec from Table W-1, the ring frequency should occur at 24.69 kilohertz.

The problem with this approach is that since a finite length tube is used, many longitudinal modes are excited when a continuous harmonic excitation is applied. Modes were found at 24.431 kHz, 24.652 kHz, and 25.811 kHz. The dilemma in this approach is in separating the true ring frequency from the longitudinal modal frequencies. This difficulty, in fact, suggested that the low frequency longitudinal modes might be used to more accurately assess the wave speed of the tube.

Longitudinal Modal Resonance: This method is based on an analysis of a finite length tube driven at frequencies far below the "ring" frequency, so that bending stresses may be neglected. The experimentally determined modal frequencies, which depend on the tube dimensions and the wave speed, are compared with those predicted by the model developed in Chapter 3. The value of wave speed in the model is adjusted until close agreement between the predicted and measured modal frequencies is achieved.

The modal resonance frequencies were measured on the experimental tube for the first eight longitudinal modes. The piezoelectric disk was driven with a continuous sinusoidal waveform from a frequency synthesizer which could be controlled in increments of 0.1 Hertz. The radial and longitudinal displacements were monitored on four PVDF gages. The approximate location of the modal frequencies was de-

terminated with equation 3.25 using the value of $c_p = 3872$ meters/second calculated for cartridge brass. For a particular mode, the frequency synthesizer was set to the calculated frequency for that mode. The frequency was then adjusted until a maximum (peak displacement) was observed on one of the four gages. (Due to the sinusoidal nature of the mode shapes, a particular gage may be at a displacement node for some of the modes.)

The measured modal frequencies are shown in Table 5-2, which also includes the modal frequencies computed from the model. Table 5-2 also includes for comparison a list of modal frequencies computed for a free-free bar of the same length and material as the experimental tube. Such a bar would be non-dispersive, with modal frequencies given by

$$f_{ndm} = \frac{m \cdot c_p \sqrt{1 - \nu^2}}{2 \cdot L}$$

where $c_p \sqrt{1 - \nu^2} = c_b = \sqrt{\frac{E}{\rho}}$ is the thin bar wave speed.

The best estimate for the extensional wave speed was determined by an iterative process in which a range of values were assumed. For each assumed value, the modal frequencies were computed for the membrane model, and also for the free-free bar model. Then the difference between the measured and calculated modal frequencies was obtained for the first eight modes. A typical plot of the difference frequency as a function of mode number is shown in figure 5-8. A positive value for the difference indicates that the calculated modal frequency exceeds the measured modal frequency for that mode.

Then the mean and standard deviation was computed for each set of differ-

ence frequencies. The standard deviation is plotted in figure 5-9 as a function of the assumed values of extensional wave speed. Figure 5-9 indicates a minimum standard deviation of 2 Hertz for the membrane model at a wave speed of 3939 meters/second. Thus this value was chosen as being the most likely from a statistical viewpoint.

Figure 5-10 presents the difference between the computed and measured modal frequencies expressed as a percentage of the measured frequency, using the final value of 3939 meters/second. The maximum deviation is in the order of 0.2%.

5.3 Transient Measurements

As indicated earlier, transient waves were applied to the experimental tube by exciting the piezoelectric disk with appropriate electrical waveforms, such as a short rectangular pulse. Circumferential PVDF gages were placed at axial locations 3.3 (Gage C-3), 7.3 (Gage C-1), 19.6 (Gage C-2), and 151 (Gage C-2) centimeters. Gage outputs were applied directly to adjustable gain, high impedance instrumentation amplifiers. Filtered outputs from the amplifiers were observed with a digital oscilloscope which had an 8 bit, 20 megahertz analog to digital converter. Captured signals were stored in a 2 by 4096 memory, from which they could be output to a computer via an RS-232 interface. The digital oscilloscope placed two constraints on the quality and quantity of data which could be measured. The 8 bit A/D converter limits the resolution, and the memory length of 4096 points limits the length of record which may be stored. A variety of electronic signal generators were used to generate input to the system.

The finite length of the tube, approximately 361 centimeters, meant that multiple echos would be present in long records. The fastest wave components travel at 0.3939 cm/microsecond, so the first echo at a particular gage may be expected at $t_e = (722 - L_g)/(.3939)$ microseconds, where L_g is the distance from the input disk to the gage. Thus for gage C-2, at 151 cm, the echo appears about 1450 microseconds after the first arrival at gage C-2.

A large number of measurements were made over the course of the study. One such series will be described to illustrate the results obtained. In this set of tests, the input disk was driven with a rectangular pulse about 3.3 microseconds in length.

The waveforms observed at the four gages are reproduced in figure 5-11. The effects of dispersion are evident in this figure, as the length of the transient increases at greater axial distances. The structure of the waveforms is similar to those which were computed, especially for the first two signals, exhibiting a burst of high frequency energy followed by a long tail of long period waves. Echos are evident on gages C-4, at 19.6 cm, and C-2, at 151 cm. The echo on gage C-2 is compressed in amplitude and extended in time compared to the direct arrival. The time scale for figure 5-11 is in milliseconds.

The frequency spectra for the waveforms in figure 5-11 are shown in figure 5-12, in which the magnitude of the FFT (normalized to the level of the largest component) is plotted as a function of frequency in kilohertz. The spectrum for gage C-3 at 3.3 cm is similar to that discussed earlier for the dummy load disk.

At gage C-1 (7.3 cm), the spectrum is more complex, as the transient moves down the tube. The echos arriving at gages C-4 (19.6 cm) and C-2 (151 cm) produce rapid fluctuations in the spectra, figures 5-12 (c) and 5-12 (d).

The effects of dispersion are clearly evident in the spectrograms, figures 5-13 to 5-16. At gage C-3 (fig 5-13)) we see the lag in the wave components near the ring frequency beginning to form as a little "nub." By the time the wave reaches gage C-1 (figure 5-14) a well developed "tail" of low frequency energy is evident.

Echos complicate the spectrograms at gages C-4 and C-2. Figure 5-15 clearly shows dispersion on the first arrival, and the presence of the echo at 2 milliseconds. The lack of a "tail" on the echo is due to the limited length of the time series (see fig 5-11 (c)) which has truncated the echo. The echo and the first arrival are closer in time for gage C-2 (figure 5-11 (d)) and thus more of the echo energy appears in the spectrogram, figure 5-16.. The "boomerang" shape of the joint distribution is clearly evident on this figure. The echo also displays the increased spreading in both frequency and time as a consequence of the transient travelling a greater distance than the first arrival.

Further insight is provided by the three dimensional contour plots of figures 5-17 to 5-20. In particular, the magnitude of the components of the joint distribution is more apparent in the 3 D contours. The peaks in the frequency domain correlate well with the maximum in the spectra of figure 5-12. The growth of the ring frequency "tail" is evident in figures 5-17 and 5-18. The structure of the first arrival and the echo at gages C-4 and C-2 is evident in figures 5-19 and 5-20.

5.3.1 Comparison of Measured and Computed Results

The theoretical results presented in Chapter 3 were obtained with an idealized band-limited frequency spectrum. In order to apply the analysis to the experimental situation, it is first necessary to simulate the spectrum of the test input. A first-order approximation to the experimental input spectrum shown in figure 5-7 (d) is given by the Gaussian frequency distribution described in equation 3.53 using a cutoff frequency F_c of 45 kilohertz and a standard deviation of 1.7. The predicted waveform of the radial displacement at gage C-1, located at 7.3 cm., is shown in figure 5.21. The measured displacement is presented in figure 5-11 (b). The two waveforms are similar in general aspects. The spectrogram for the computed waveform shown in figure 5-22 may be compared with the experimental spectrogram at gage C-1, figure 5-14. The tip of the trailing "tail" occurs at 23.4 kHz in the calculated spectrogram, and at 23.75 kHz on the experimental plot. Both figures indicated a concentration of energy at 38 kHz, and around 55 kHz. The maximum frequency component occurs at 89 kHz in figure 5-22, versus 83.6 kHz for the experiment.

The major difference is in the overall width in time. The computed spectrogram is about 0.4 milloseconds in width, whereas the experimental spectrogram shows a 1 millisecond duration. The discrepancy is probably due to the approximate nature of the Gaussian simulation to the experimental spectrum.

CHAPTER 6

Conclusions

6.1 Transfer Matrix Method

The transfer matrix method is a simple and straightforward approach to the solution of wave propagation problems for concentric cylindrical systems with fluid and elastic components. Models were developed for a fluid cylinder, a fluid tube, a thin elastic cylinder, and the external fluid. These models are easily combined to represent a complex system comprised of any number of components.

Practical applications of this method include: (1) Analysis of cylindrical sonar transducers, (2) Study of the effects of turbulent boundary layer noise on the performance of towed arrays, (3) Analysis of sound transmission and noise reduction in aircraft, submarines, piping systems, and other structures which may be approximated by elastic cylinders.

The fluid models developed in this work were studied to examine the propagation of free waves in the fluid cylinder, the fluid tube, and the external fluid for fixed and free boundary conditions. These limiting values are useful in understanding the effects of fluid density, sound speed, and the characteristics of external excitation (frequency and axial wavenumber) in multicomponent systems.

Several examples of composite systems are described in Chapter 4, which begins with a discussion of the parameters for two fluid problems and the conditions under which wave propagation may occur. A detailed study of a fluid tube in an

external fluid illustrates the application of the transfer matrix method, and calculations and plots of the radial spectral impedance at the inner surface of the fluid tube are shown for various combinations of fluid tube thickness and the characteristics of the two fluids. A practical application in which a fluid tube is used to match the impedance of a source to that of the external fluid is described.

The special case of a system which includes a fluid cylinder is described. It is shown that the fluid cylinder has a major influence on the radial spectral impedance of the system.

Two examples of systems including elastic shells are described briefly.

6.2 Elastic Media

An extensive study of the response of a semi-infinite thin elastic cylinder to axisymmetric harmonic and transient excitation is presented. Significant results include the transfer matrix model for a thin shell, an accurate method for the determination of extensional wave speed in a harmonically driven finite length shell, the effect of shell thickness on the roots of the dispersion equation, and the dispersion of transient waves in a thin shell. Joint time-frequency distributions are shown to be of value in understanding the propagation of transient waves in dispersive media.

6.2.1 Thin Shell Model

The transfer matrix model of a thin shell is developed for use in modeling multicomponent cylindrical systems. This model is valid for shells which satisfy the

assumptions made in the formulation of the Donnell shell equations. The radial spectral impedance of a thin shell is shown to be a function of the excitation frequency, the axial wavenumber, the shell thickness and radius, and the density, elastic modulus and Poisson's ratio of the shell material. The radial spectral impedance, that is, the ratio of the differential pressure across the shell to the shell radial velocity, is the principal term in the two-port transfer matrix for the thin shell.

6.2.2 Determination of Wave Speed

A very accurate method was developed for the determination of the extensional wave speed in a thin elastic shell. In this approach, the longitudinal resonant frequencies are measured for the lower order modes of the finite length shell. The wave speed is computed from these frequencies using a model based on membrane theory, which is accurate for modal frequencies which are below the ring frequency. The extensional wave speed for the experimental shell was 3939 meters/second, with a maximum estimated error in the order of 0.2%.

6.2.3 Effect of Shell Thickness on the Dispersion Equation

The dispersion equation for a thin shell includes a bending term, β , which is proportional to the ratio of shell thickness to radius. When β is zero, the shell is characterized by membrane theory and there are two real roots in the solution of the dispersion equation. These roots define a lower transition frequency, at which free wave propagation of flexural waves in a membrane is cut off, and an upper transition frequency, at which longitudinal wave propagation cuts on. The upper

transition frequency is shown to be the traditional "ring" frequency of the shell. The separation of the transition frequencies depends solely on the Poisson's ratio for the material.

When β is finite, the dispersion equation is of sixth order in terms of the axial wavenumber. The bending term causes the dispersion curve of the flexural branch to dip to a minimum and then to increase indefinitely (a more sophisticated theory which includes rotatory inertia and shear effects is required to correctly predict the flattening of the dispersion curve at very high frequencies). The bending effects are responsible for the propagation of very slow waves for frequencies in the transition zone.

6.2.4 Transfer Functions in Frequency and Spatial Domains

Using Fourier and Laplace transform methods, two dimensional transfer functions for the radial and axial displacements were constructed with frequency and axial distance as arguments. These transfer functions are studied to provide understanding of the propagation of waves resulting from arbitrary axysymmetric inputs to the shell. The near field and far field behavior of these shell displacements are inferred from two and three dimensional representations of the transfer functions.

6.2.5 Time and Frequency Domain Response of the Thin Shell

The radial and axial displacement responses of the shell as functions of time and frequency at arbitrary axial positions are evaluated by inverse Fourier transformation of the transfer functions on the frequency variable. A weighting function technique is introduced to band limit the transfer functions in frequency. This is

shown to be required to prevent aliasing when using discrete versions of the inverse Fourier transform, and also due to limitations on the bandwidth of the transfer functions which are imposed by the simplifications inherent in the formulation of the Donnell thin shell theory. The weighting function may also be tailored to represent the spectra of various special temporal inputs, such as discrete frequency components.

Plots of the radial and axial displacements as functions of time clearly show the dispersive nature of the waves propagating in a thin shell. Typically, the high frequency components arrive first, followed by a long "tail" of slower components at frequencies in the transition zone. The length of the transient increases at greater axial distances, due to the spatial separation of the fast and slow components of the transient wave. A beating effect is evident in the displacements due to constructive and destructive interference between nearby frequency components in the transition zone.

The temporal variation of the spectral components of the transient displacements are clearly shown by two and three dimensional contour plots of the joint time-frequency distribution obtained by application of the spectrogram to the time waveform. The spectrograms are shaped like a boomerang in the $t - f$ plane, with a long tail parallel to the time axis representing the slow, low frequency components.

6.3 Experimental Work

Chapter 5 describes an apparatus constructed to generate and observe transient wave propagation in a thin cylindrical shell. Gages made from polarized

poly-vinylidene fluoride film (PVDF) were found to be an excellent means for the measurement of radial displacement. These gages have high sensitivity and do not provide a significant mechanical load on the metallic cylinder.

Mechanical input to the shell was provided by an electrically driven piezoelectric ceramic disk. An electro-mechanical driver has several advantages over strictly mechanical devices (such as blows from an instrumented hammer, explosive charges, or the impact from projectiles). Precise, repetitive inputs of arbitrary waveform are easily obtained from an electronic function generator. This approach enables a large volume of experimental data to be obtained in a relatively short time span. The ability to accurately repeat the test stimuli enhances the reliability of the results as compared to the less controllable mechanical sources.

The initial test system had very low losses, which limited the available bandwidth. This was corrected by use of an electromechanical dummy load technique, in which a second, identical piezoelectric ceramic disk was bonded to the electrically driven disk. The second disk was connected to an electrical network which provided overall damping to the system. The result was a ten fold increase in system bandwidth.

Extensive measurements of transient wave propagation were made with the experimental apparatus. The results are in good agreement with those predicted by the theory. The joint time-frequency distribution analysis was shown to be an effective tool in understanding wave propagation in dispersive systems.

ILLUSTRATIONS

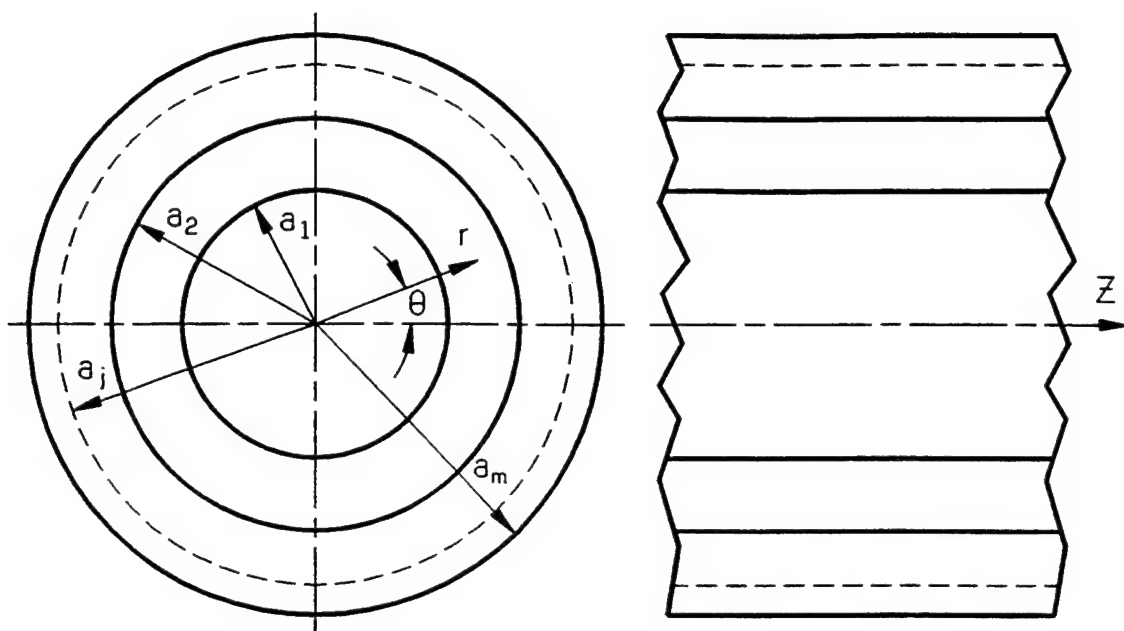


Fig. 1-2 General Cylindrical System

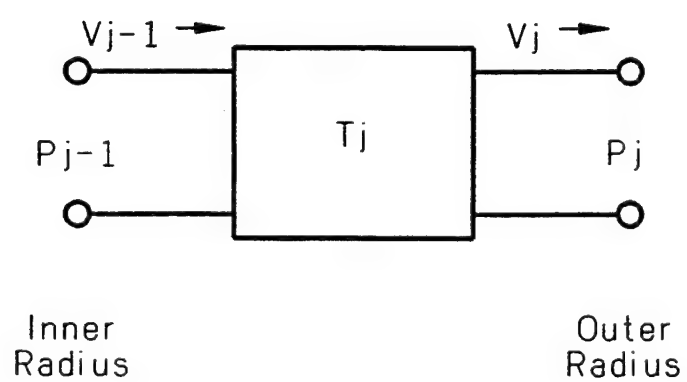


Fig. 1-3 Transfer Matrix for Fluid Tube

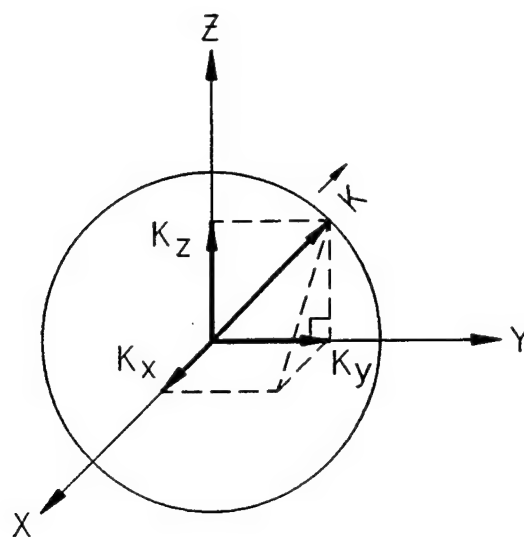


Fig. 1-4 Wavevector Domain

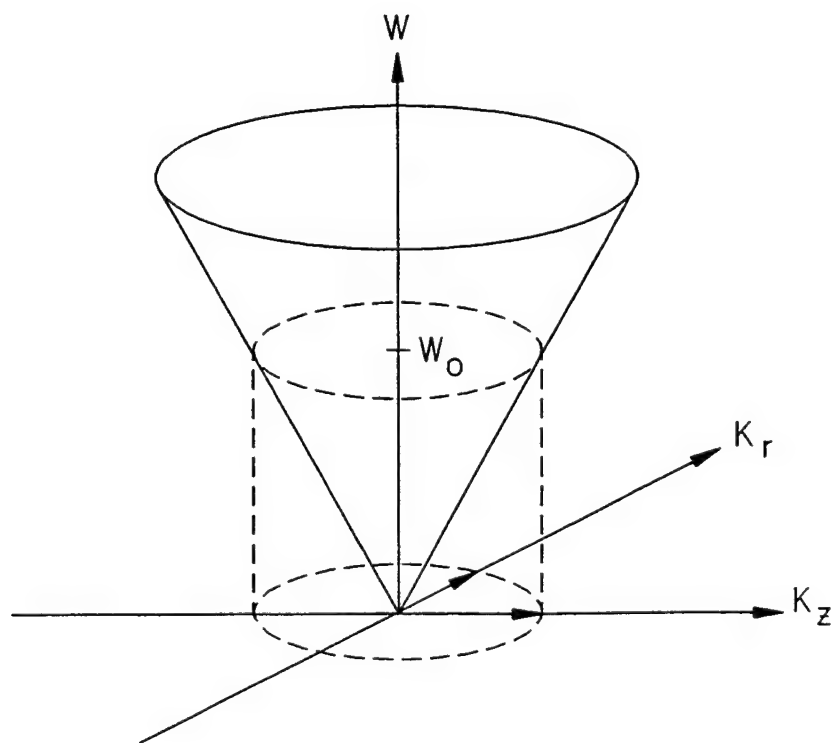


Fig. 1-5 Wavevector-Frequency Space

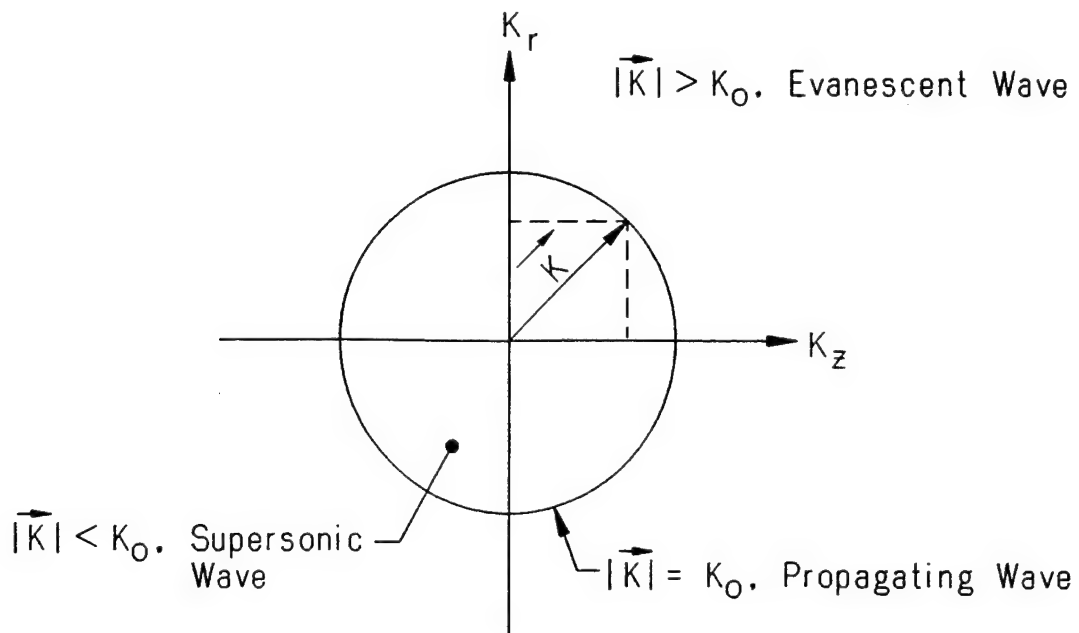


Fig. 1-6 Wavevector in Cylindrical Coordinates

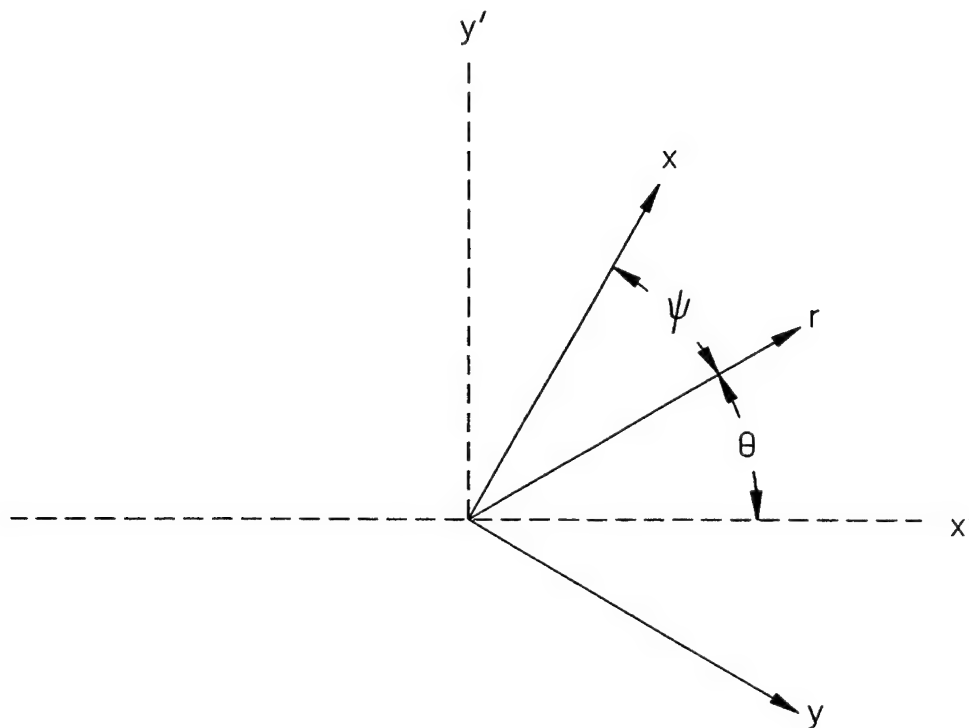


Fig. 1-7 Geometry for Synthesis of Cylindrical Wave

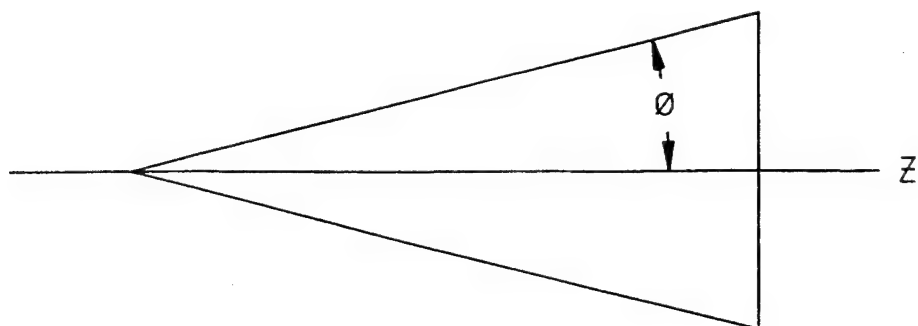


Fig. 1-8 Diverging Cylindrical Wave

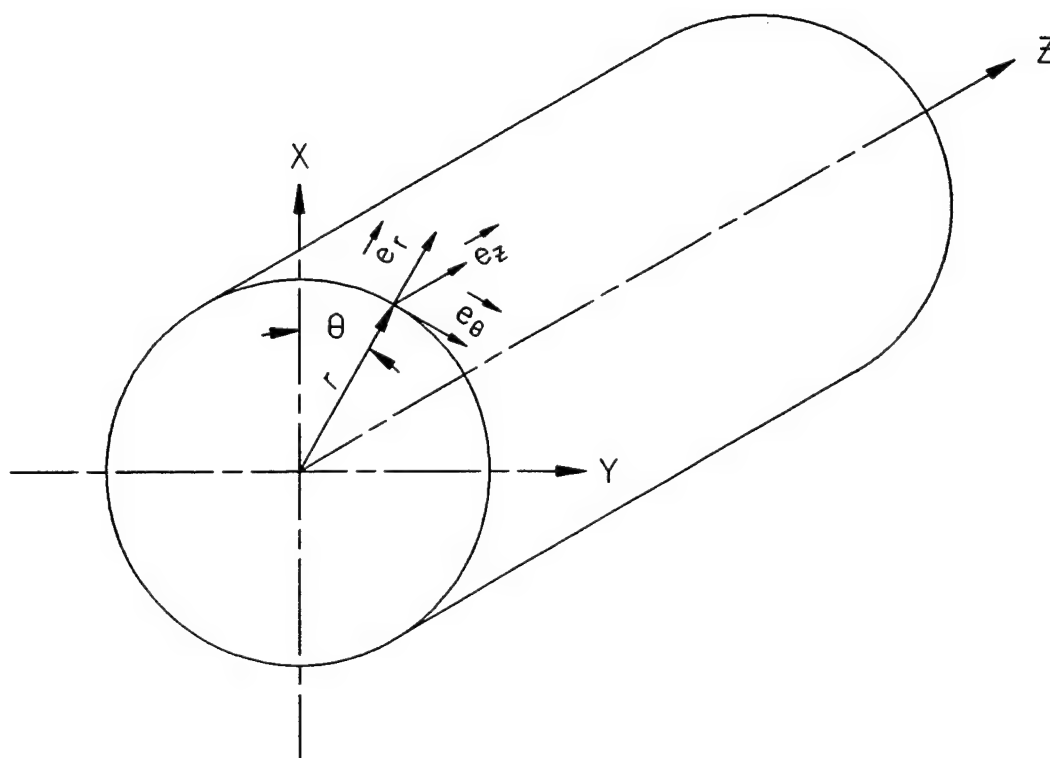


Fig. 2-1 Cylindrical Coordinate System

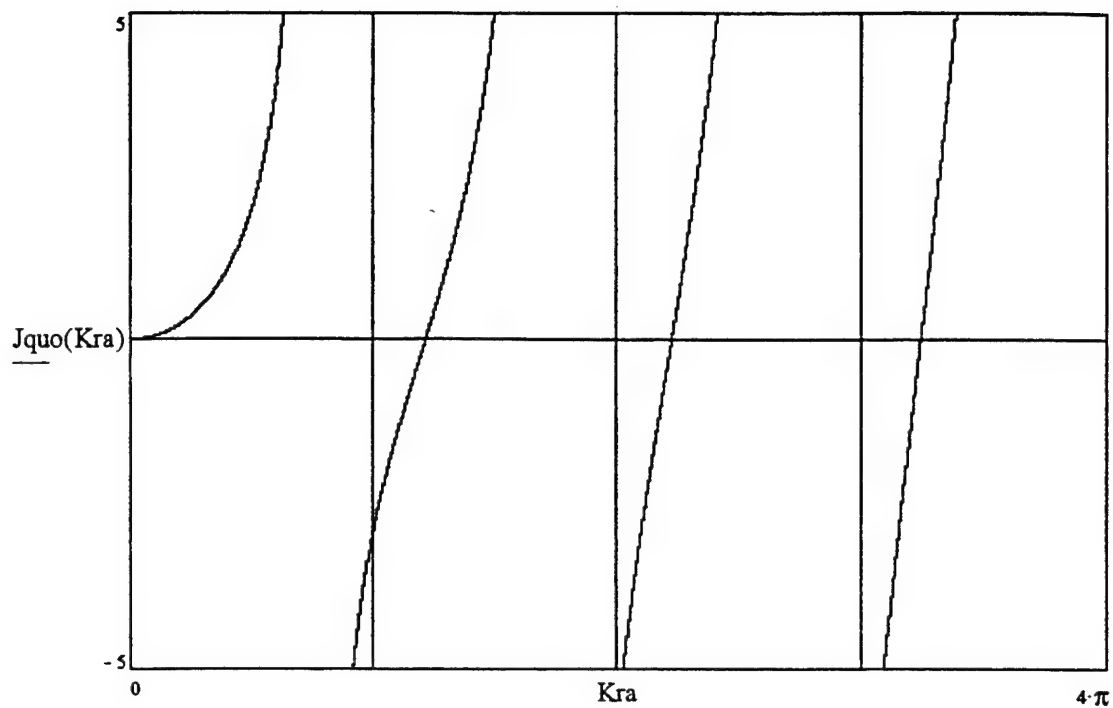


Fig. 2-2 Modified Quotient of Bessel Functions vs. non-dimensional radial wavenumber, Kra

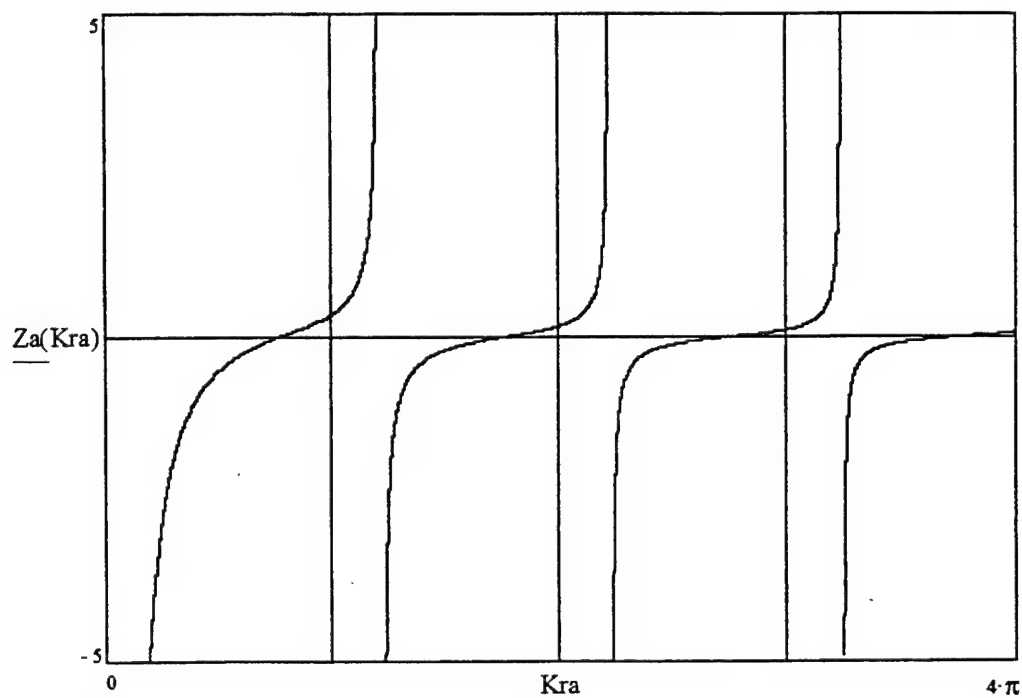


Fig. 2-3 Spectral Impedance of Fluid Cylinder vs Kra , computed for $Ka = 1$.

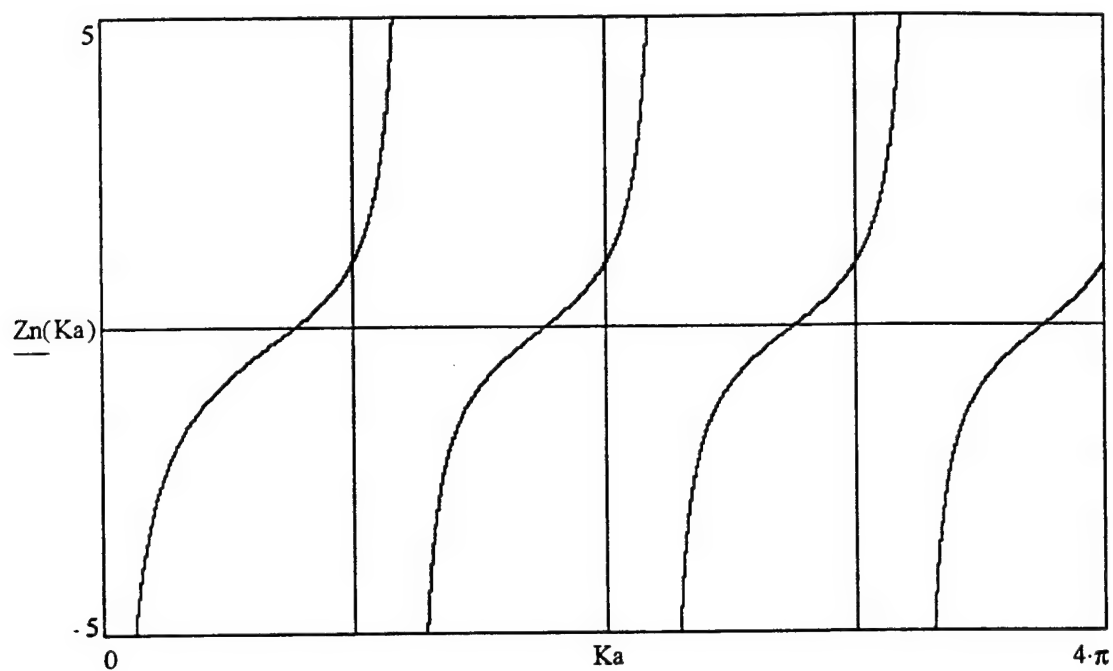
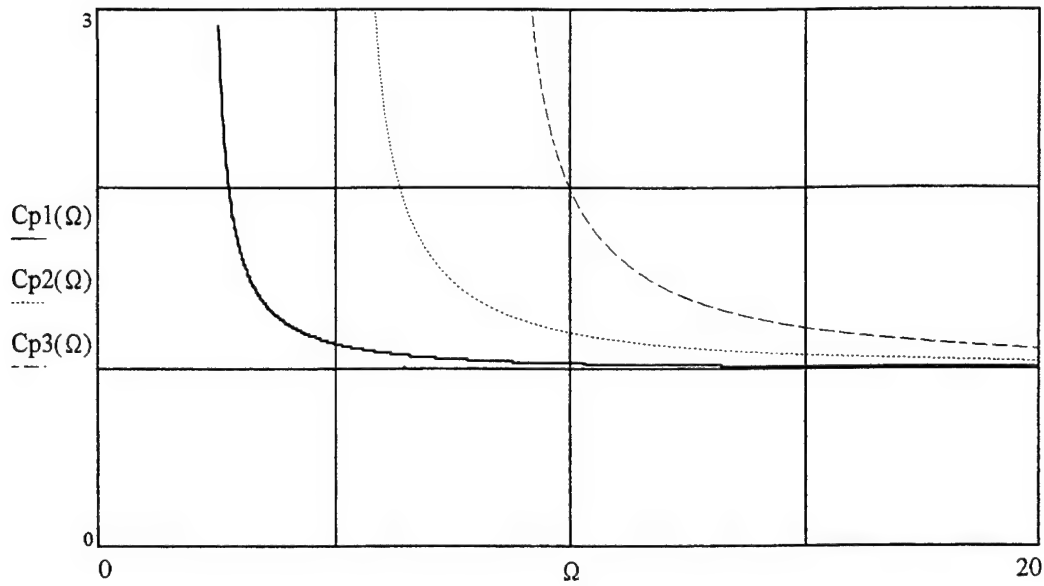
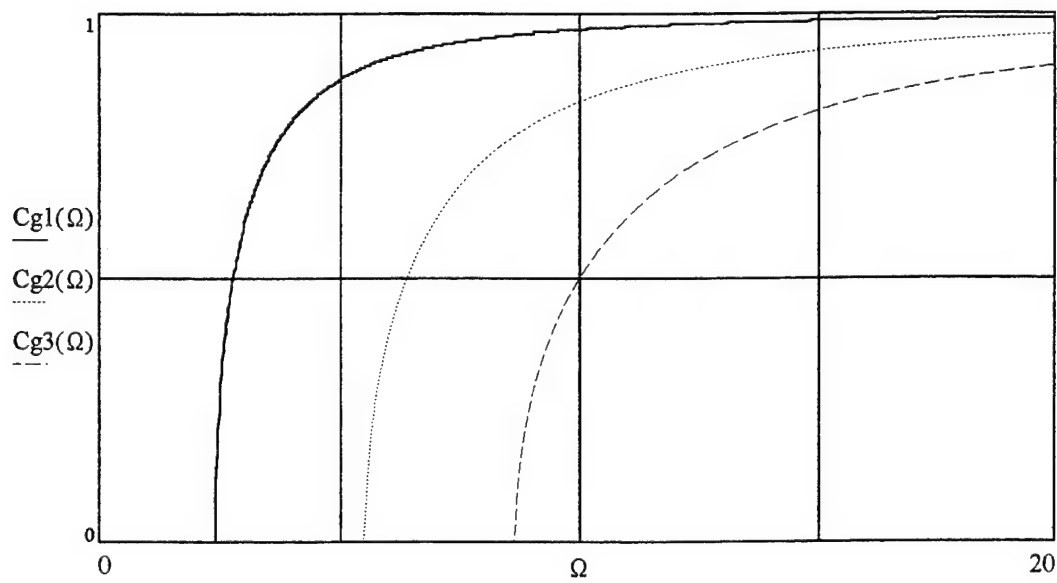


Fig. 2-4 Normalized spectral impedance of fluid cylinder
as a function of non-dimensional wavenumber Ka , for $K_z = 0$



(a) Phase Velocity



(b) Group Velocity

Fig. 2-5 Normalized phase and group velocities vs non-dimensional frequency for a fluid cylinder with free radial boundary, modes 1, 2, and 3

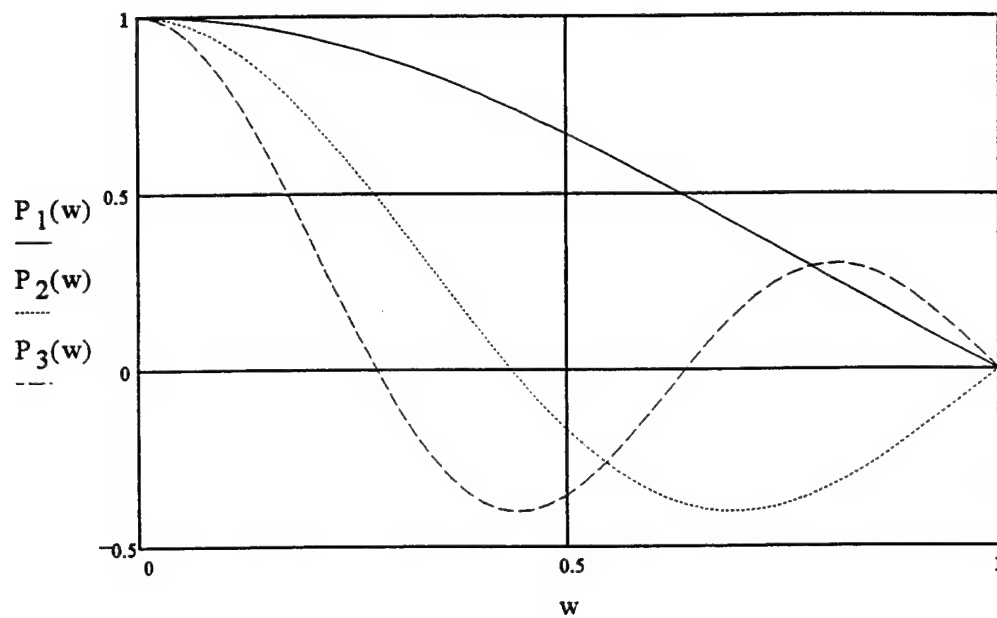
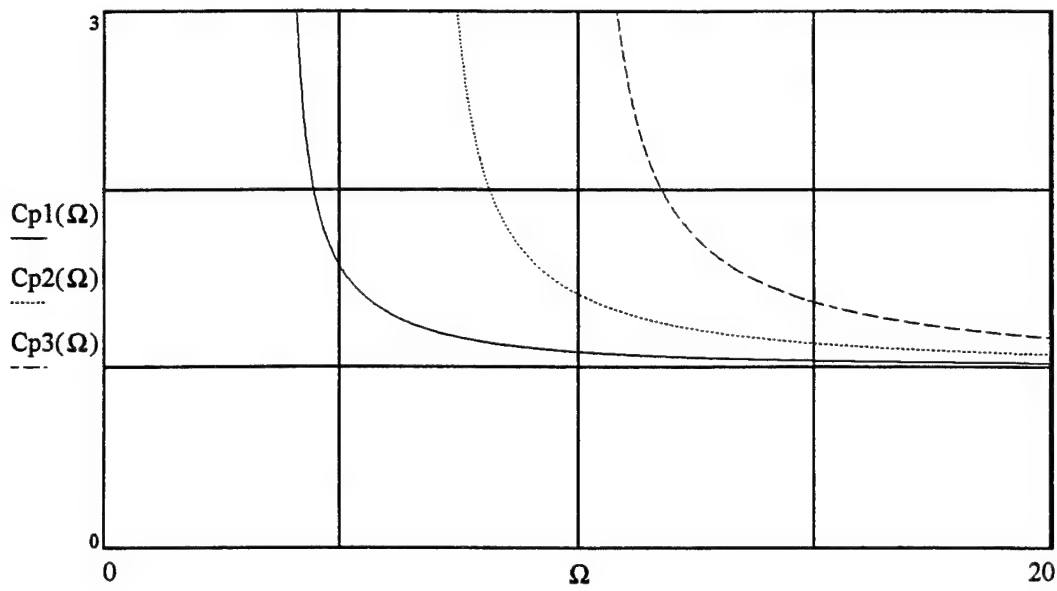
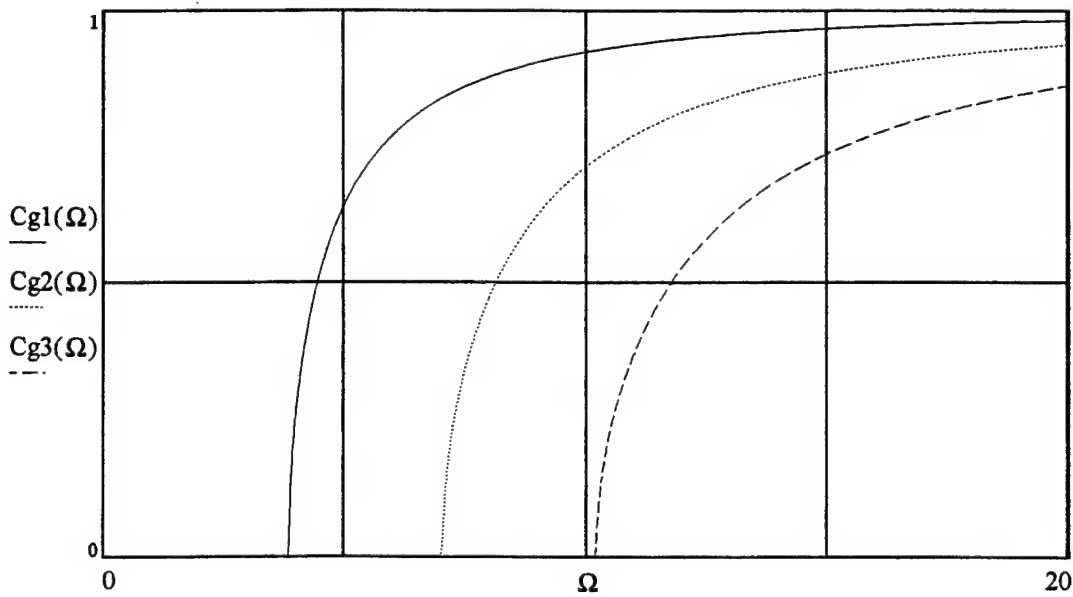


Fig. 2-6. Normalized pressure vs non-dimensional radius for a fluid cylinder with free radial boundary.



(a) Phase Velocity



(b) Group Velocity

Fig. 2-7. Normalized phase and group velocities vs non-dimensional frequency for a fluid cylinder with fixed radial boundary, modes 1, 2, and 3.

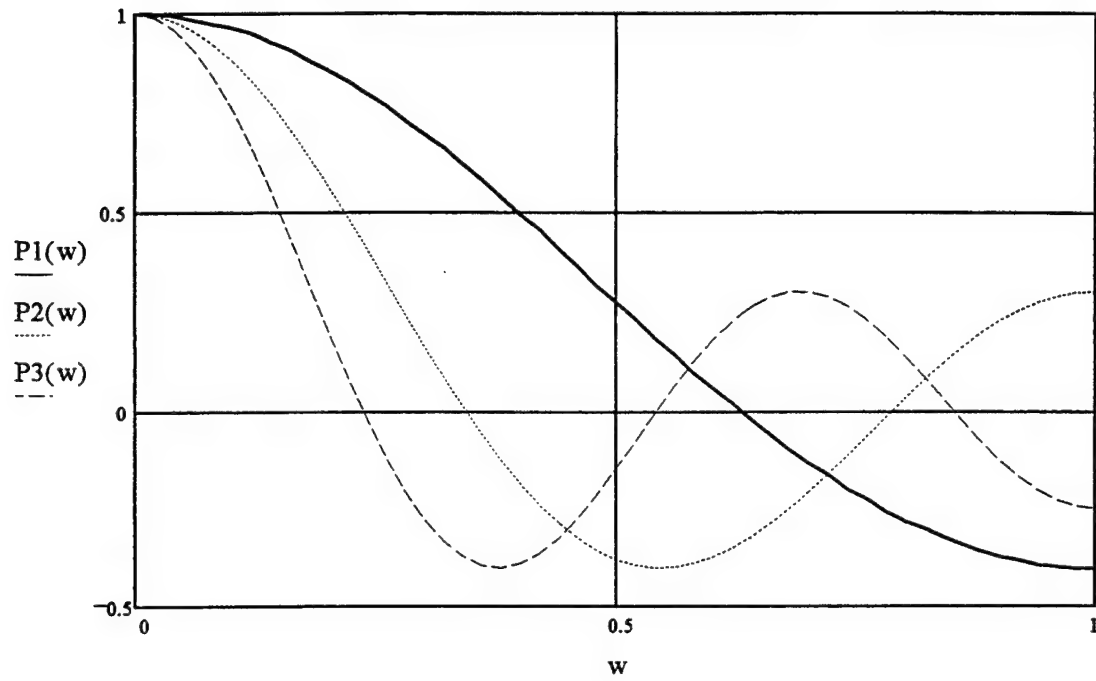


Fig. 2-8 Normalized pressure vs non-dimensional radius for a fluid cylinder with fixed radial boundary.

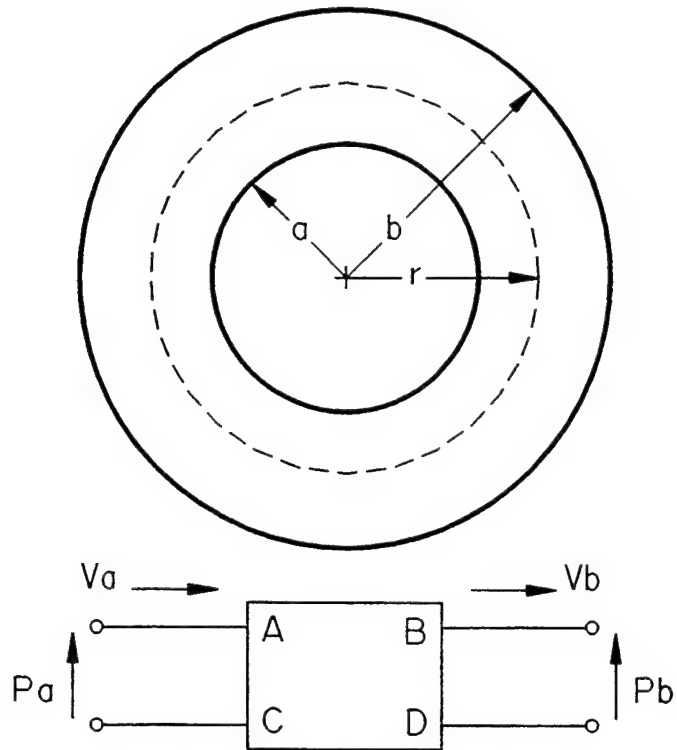


Fig. 2-9 Fluid Tube Model

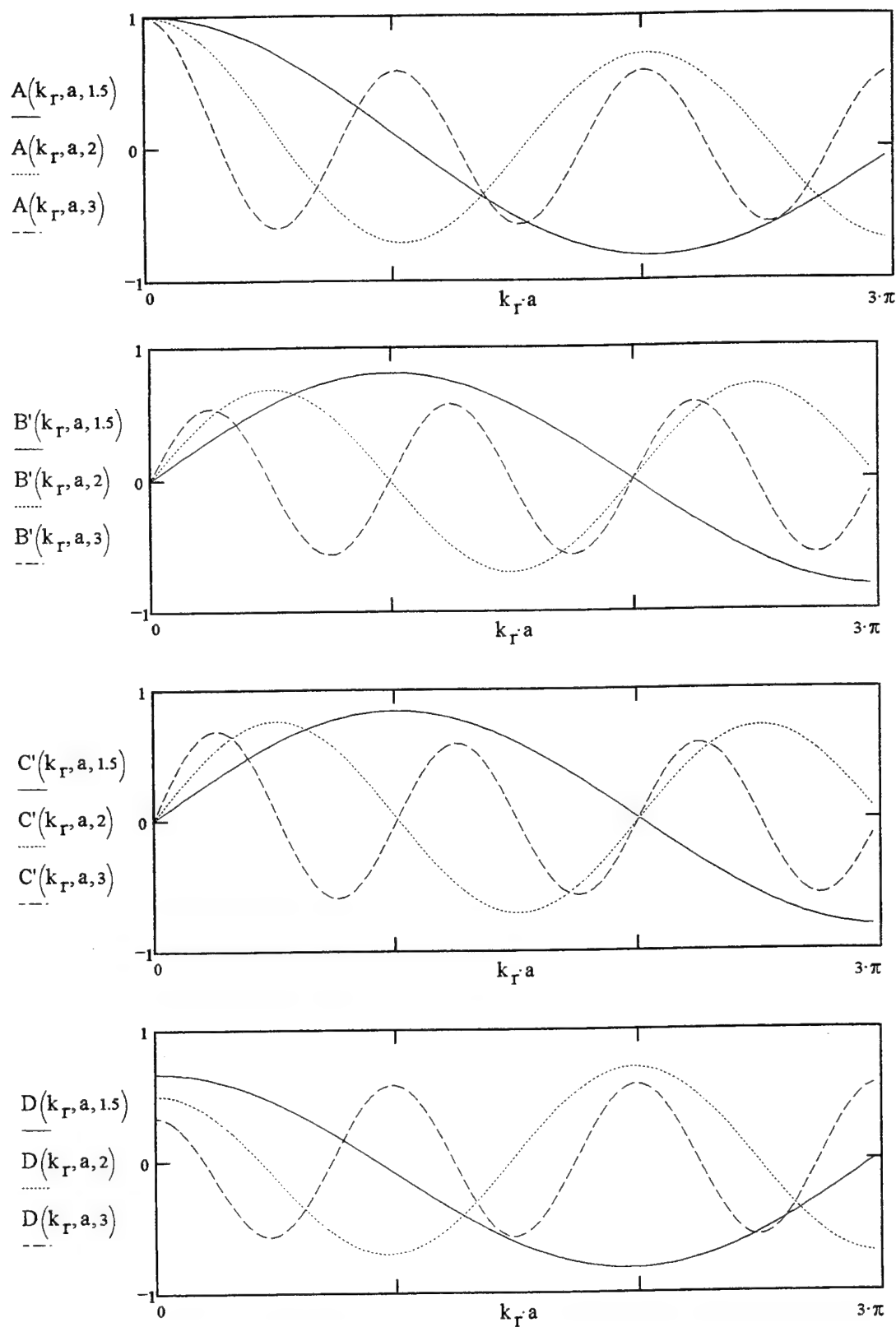


Fig. 2-10 ABCD parameters as a function of non-dimensional radial wavenumber $Kr \cdot a$ for $S = 1.5, 2$, and 3 .

Fig. 2-11, Surface Plot of Parameter A

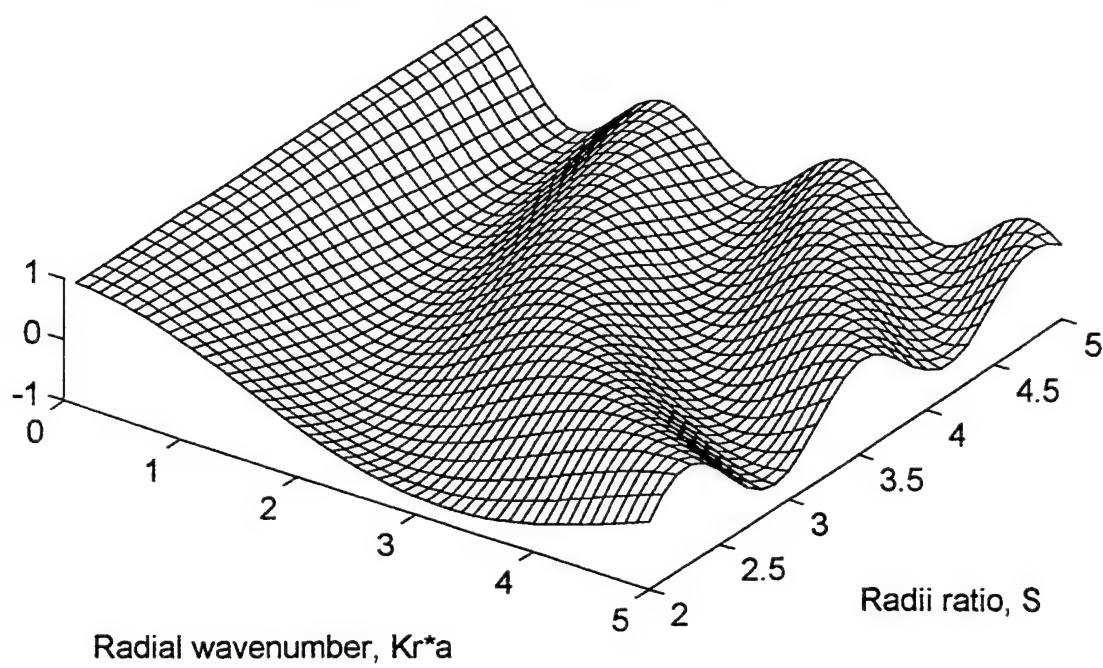


Fig. 2-12, Surface Plot of Parameter B

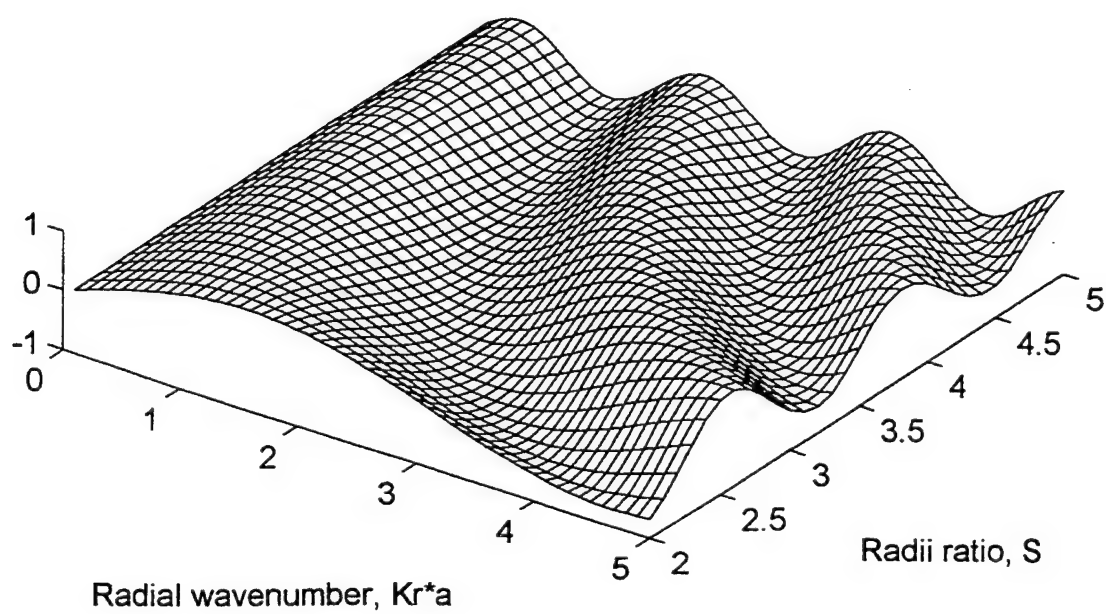


Fig. 2-13, Surface Plot of Parameter C

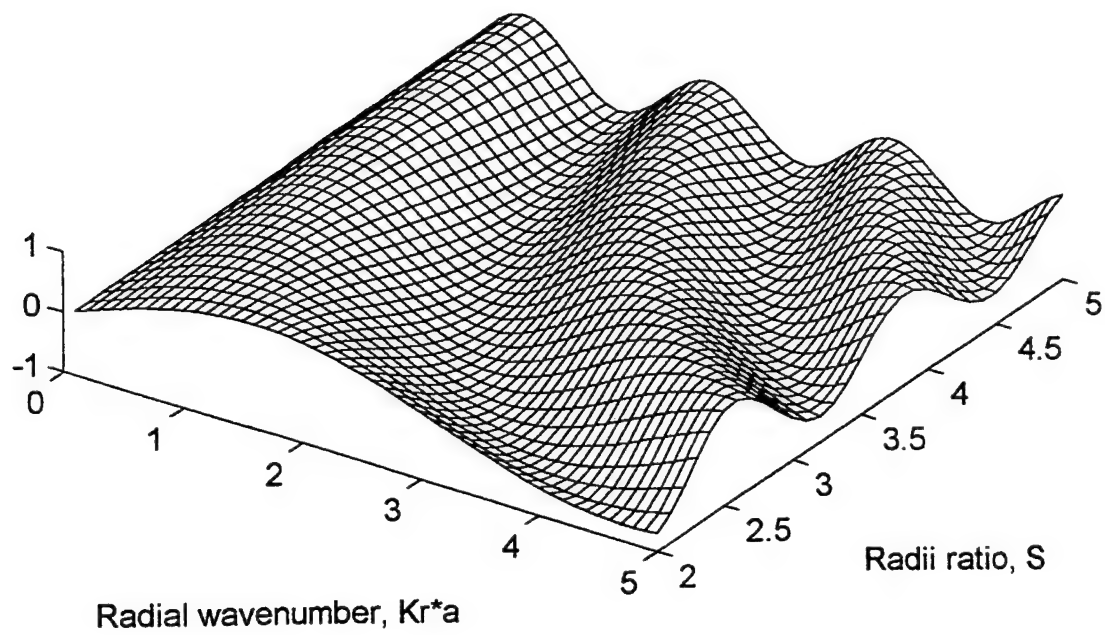


Fig. 2-14, Surface Plot of Parameter D

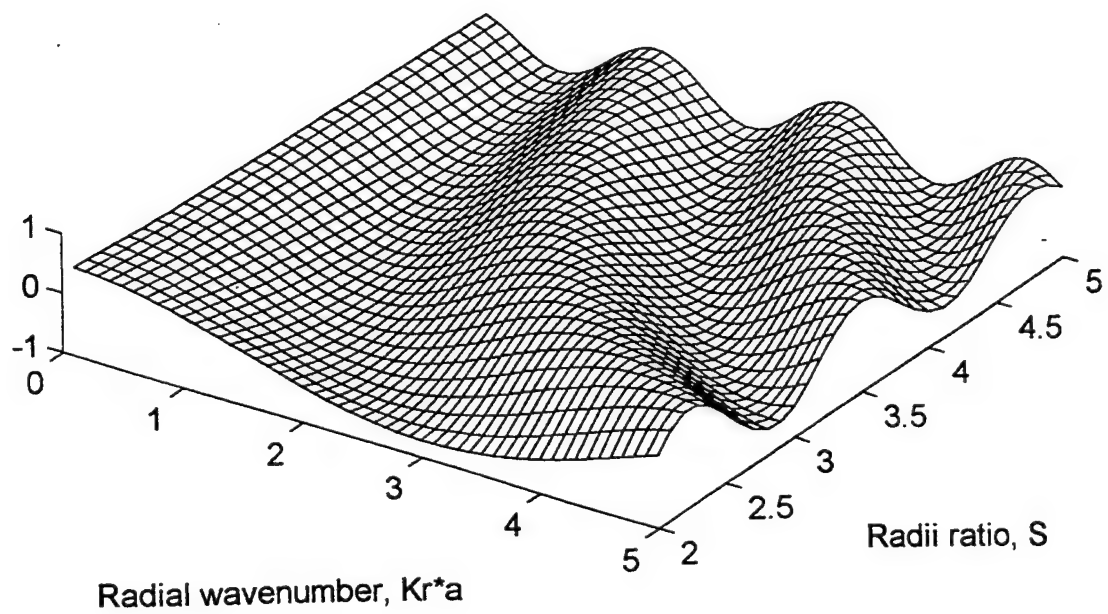


Fig. 2-15 Percent error in the asymptotic expression for the roots of the free-free mode in a fluid tube vs mode number.

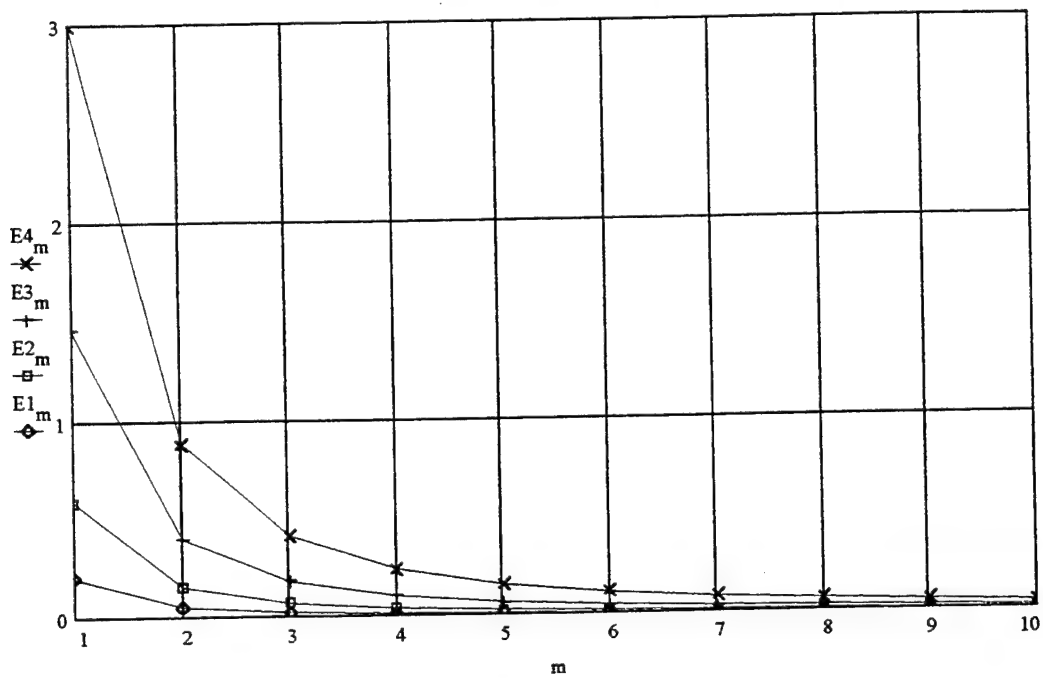


Fig. 2-16 Percent error in the asymptotic expression for the roots of the fixed-free modes in a fluid tube vs mode number.

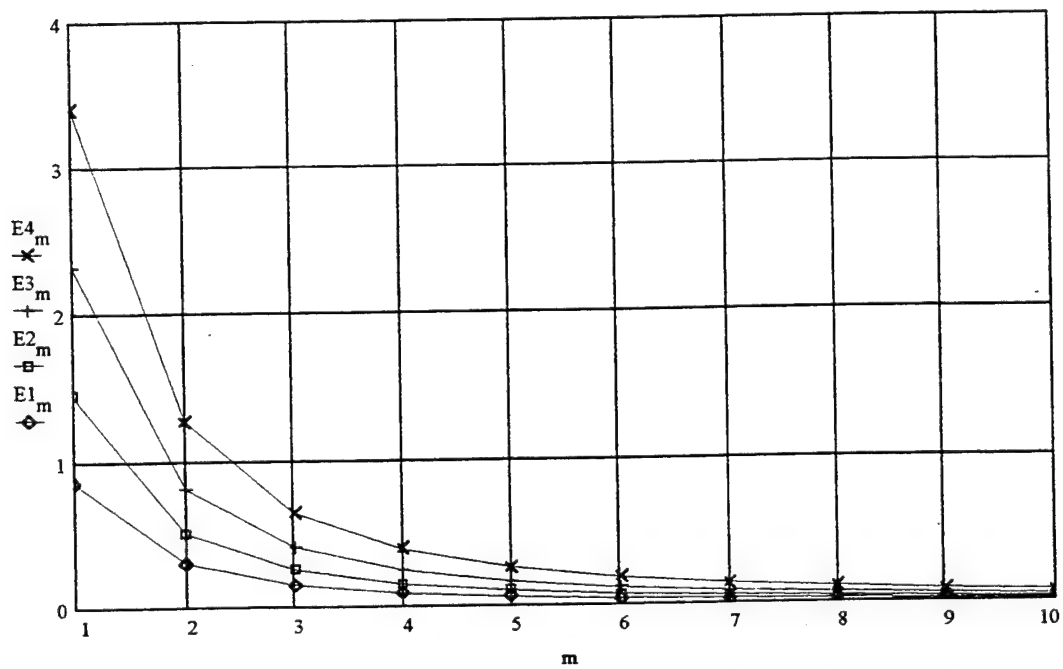


Fig. 2-17 Percent error in the asymptotic expression for the roots of the fixed-free modes in a fluid tube vs mode number.

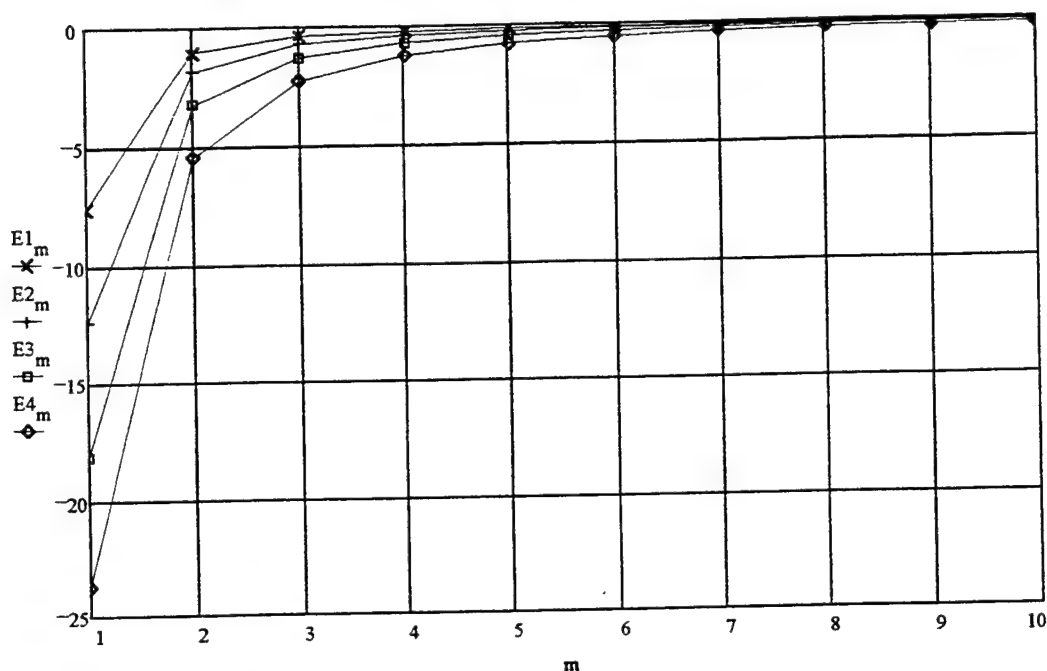


Fig. 2-18 Percent error in the asymptotic expression for the roots of the fixed-fixed modes in a fluid tube vs mode number.

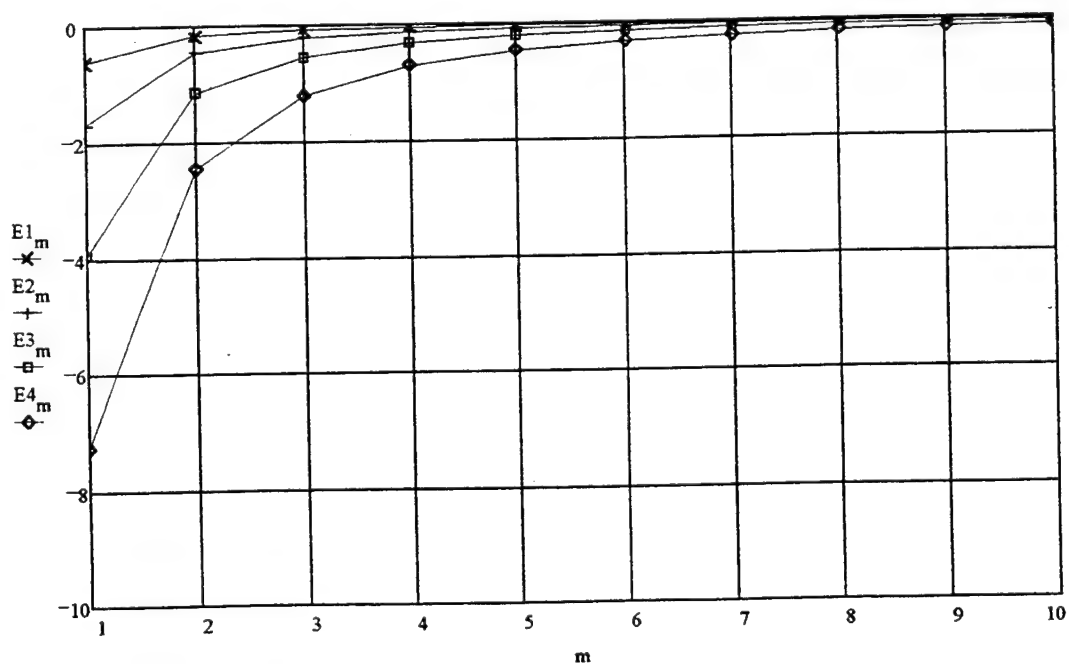
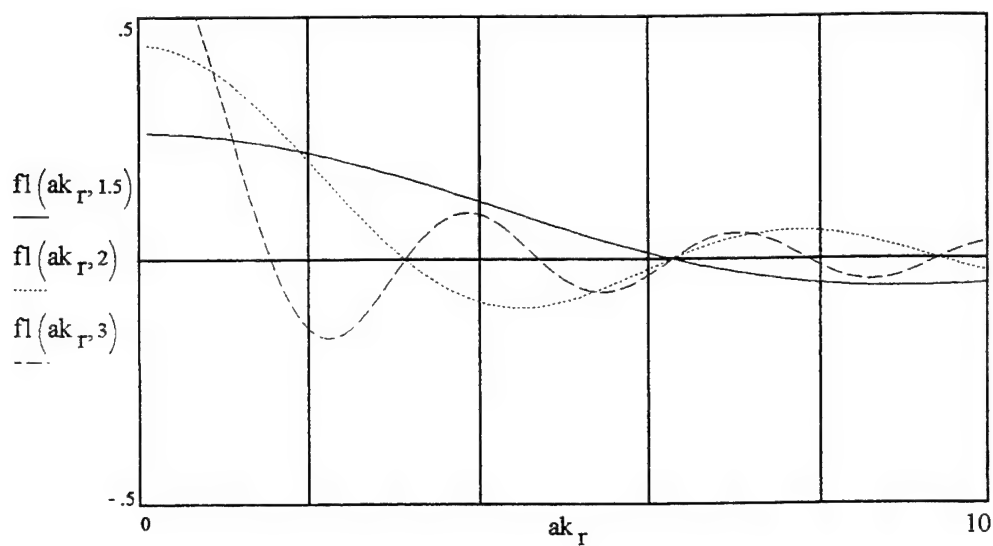
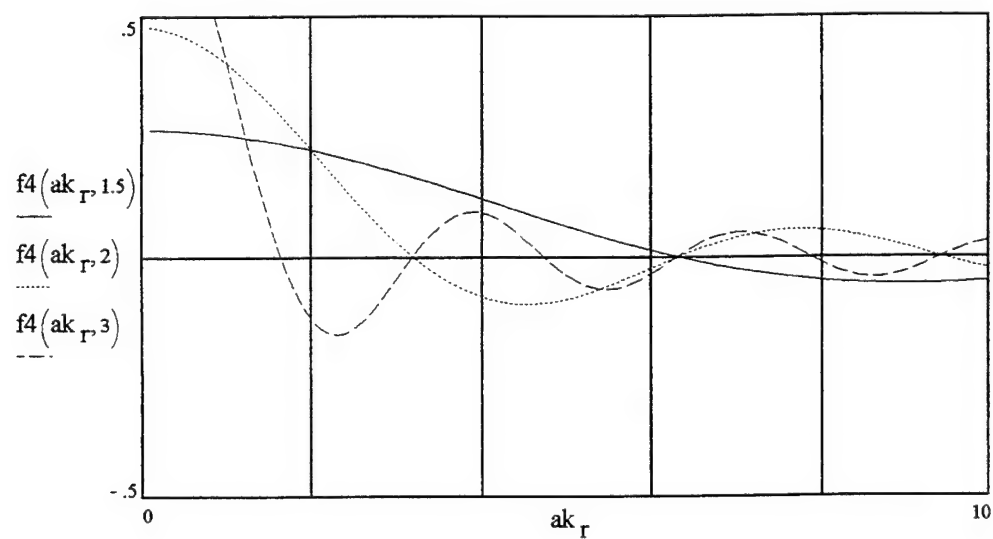


Fig. 2-19 Characteristic equations for free-free and fixed-fixed modes of a fluid tube for radii ratios $s = 1.5, 2$, and 3

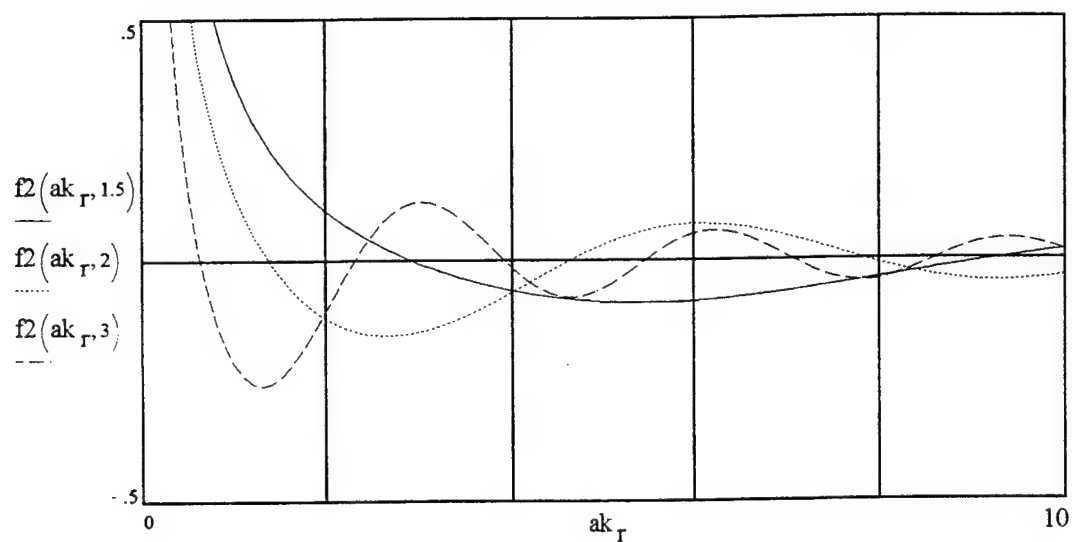


(a) Free-Free

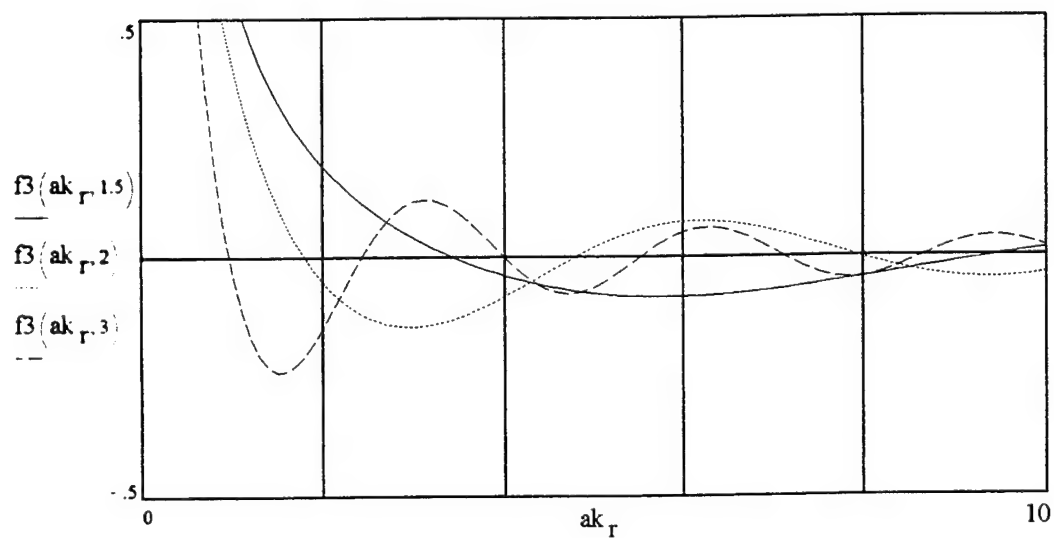


(b) Fixed-fixed

Fig. 2-20 Characteristic equations for free-fixed and fixed-free modes of a fluid tube for radii ratios $s = 1.5, 2$, and 3

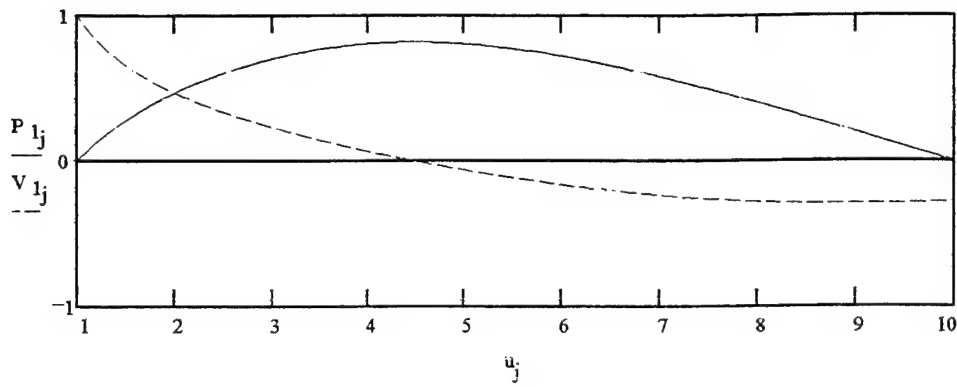


(a) Free-fixed

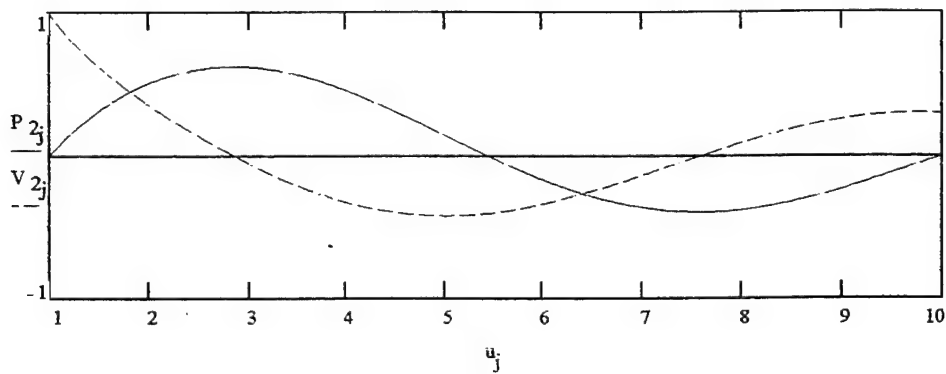


(b) Fixed-Free

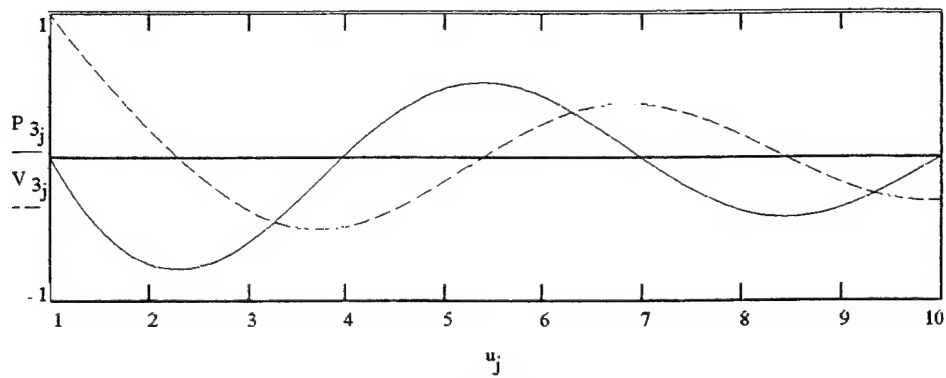
Fig 2-21 Pressure and radial velocity vs non-dimensional radius for the first three free-free modes in a fluid tube. Solid line = pressure; dashed line = velocity



Mode 1

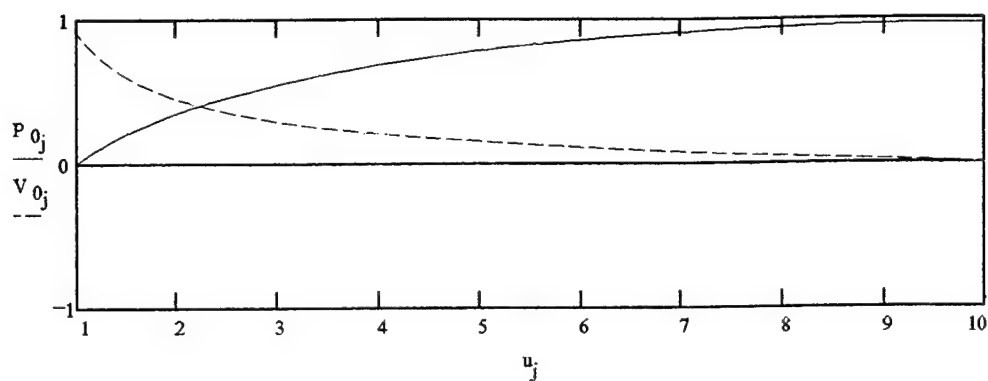


Mode 2

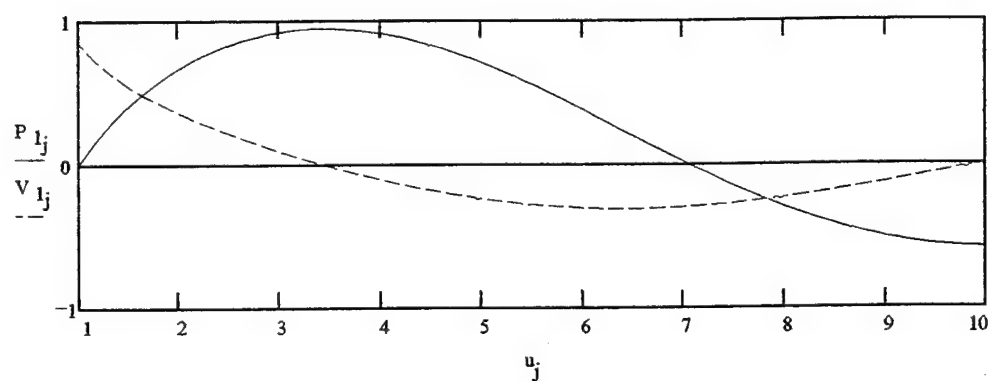


Mode 3

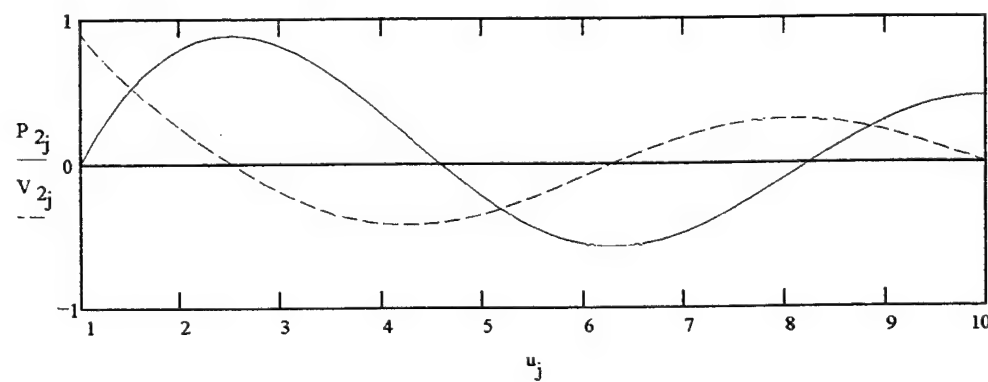
Fig 2-22 Pressure and radial velocity vs non-dimensional radius for the first three free-fixed modes in a fluid tube. Solid line = pressure, dashed line = velocity.



Mode 0

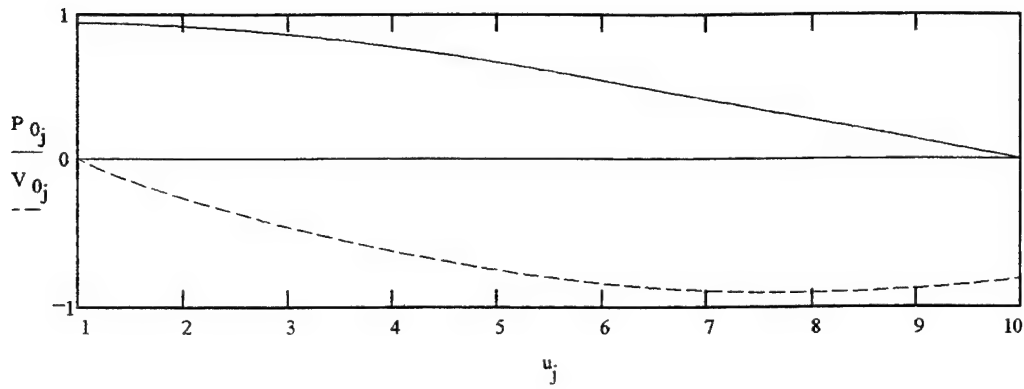


Mode 1

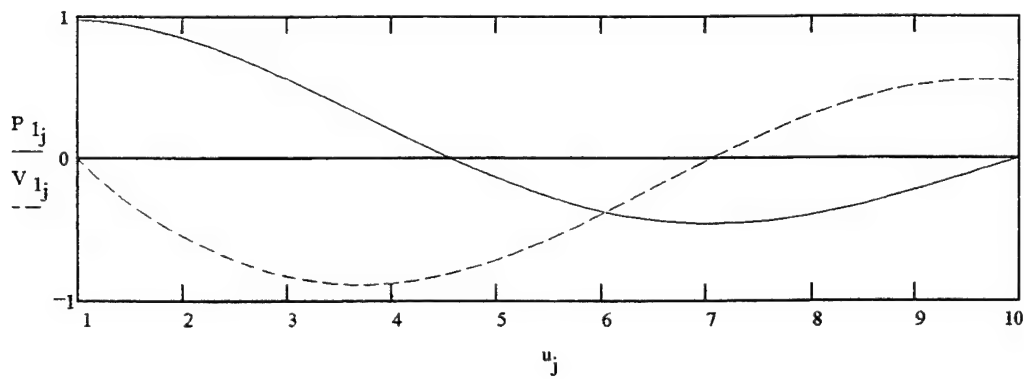


Mode 2

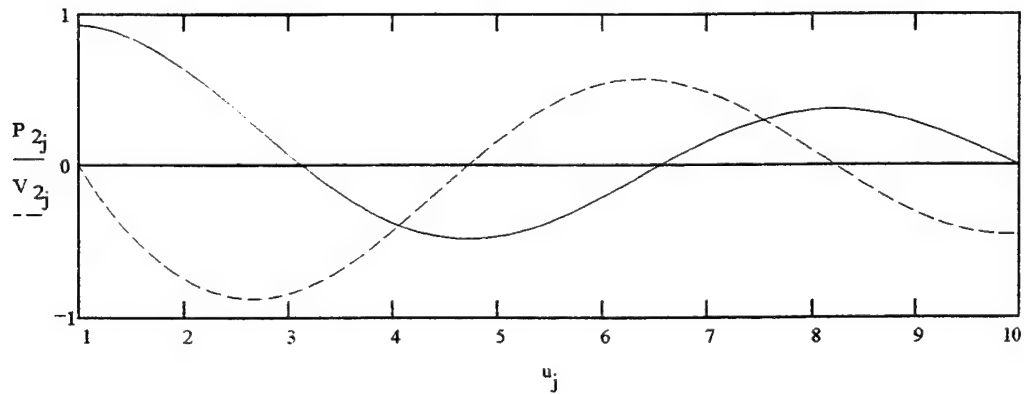
Fig 2-23 Pressure and radial velocity vs non-dimensional radius for the first three fixed-free modes in a fluid tube. Solid line = pressure, dashed line = velocity.



Mode 0

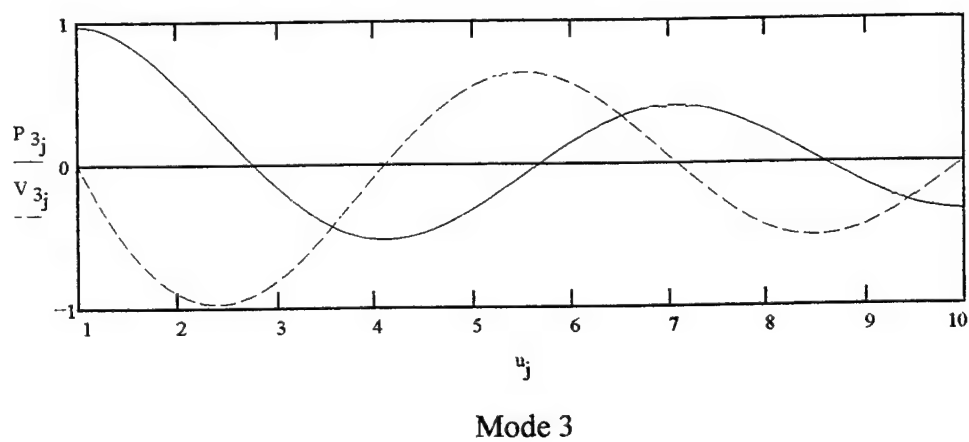
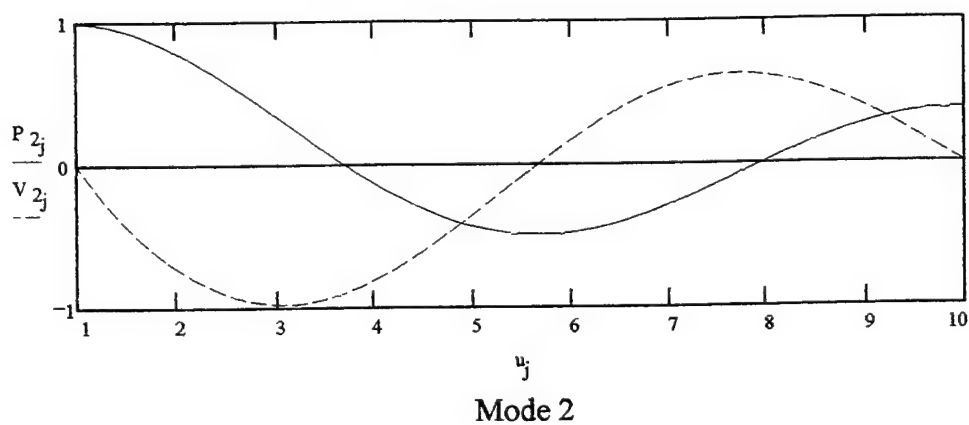
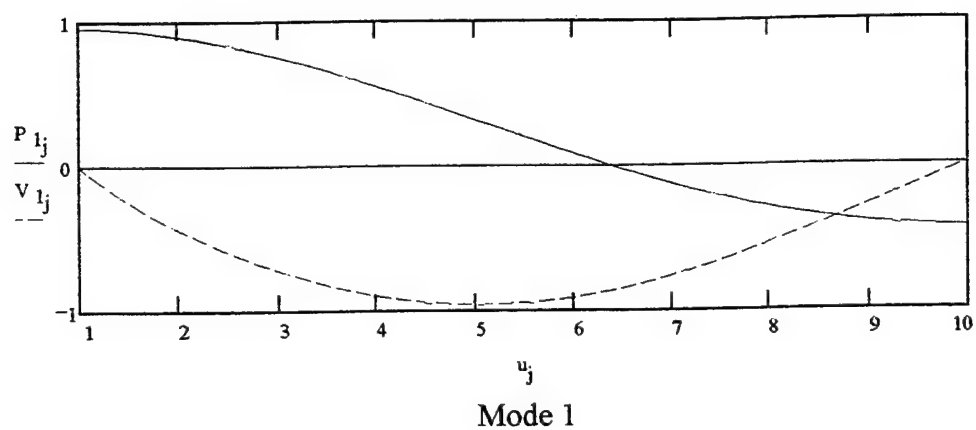


Mode 1



Mode 2

Fig 2-24 Pressure and radial velocity vs non-dimensional radius for fixed-fixed modes in a fluid tube. Plane wave mode not shown. Solid line = pressure, dashed line = velocity.



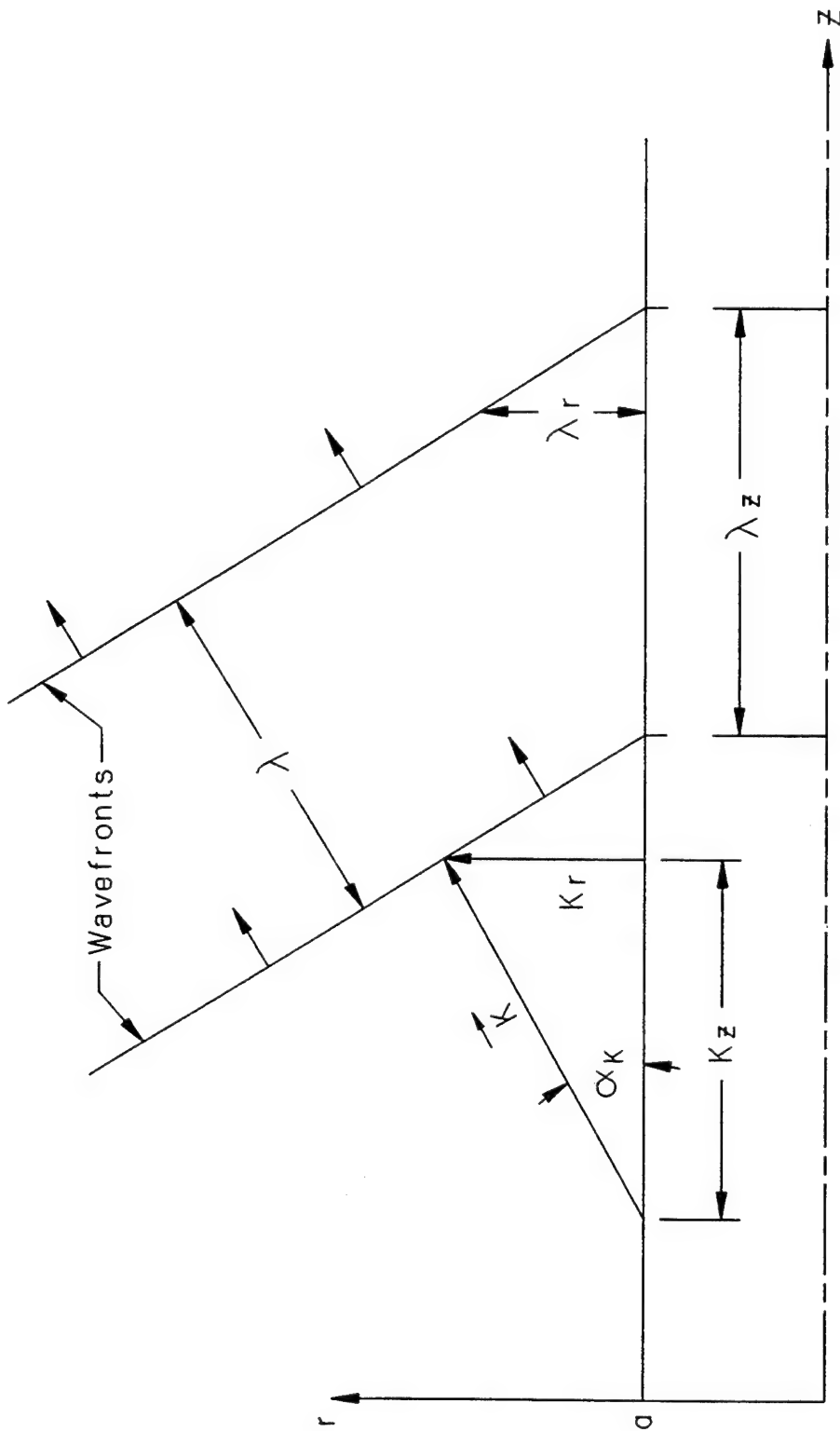
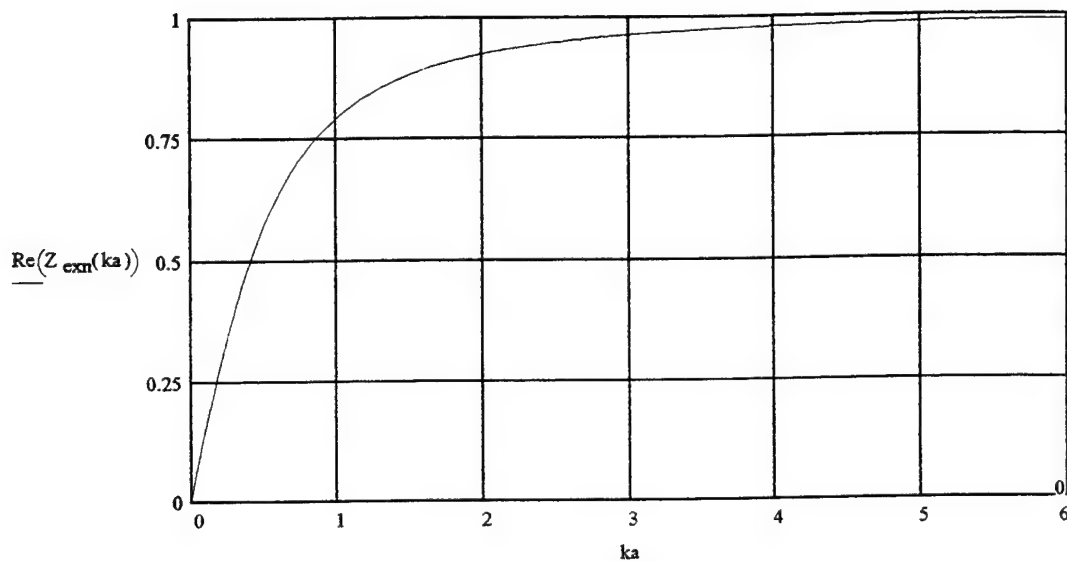
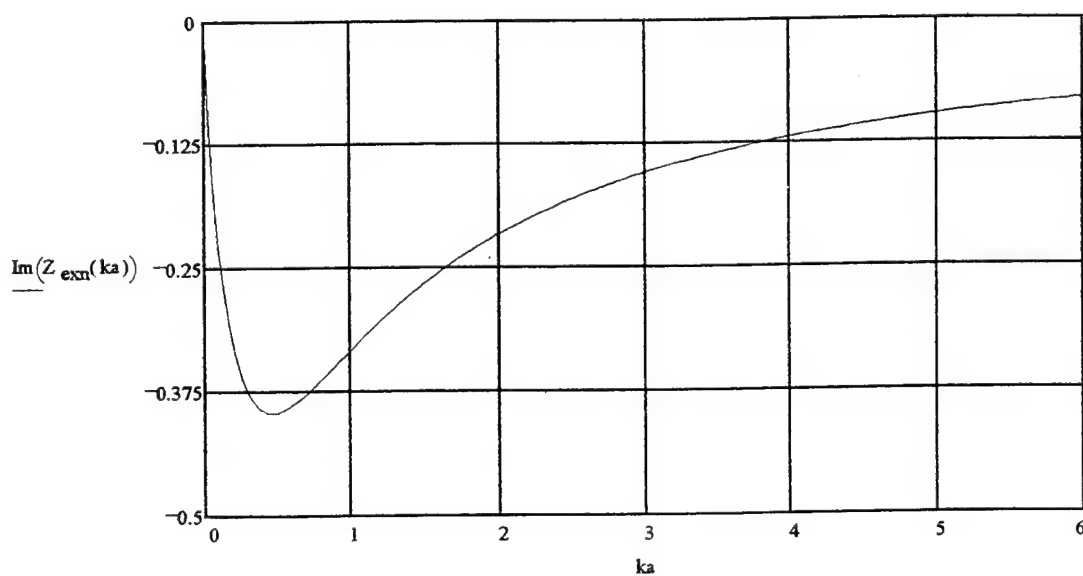


Fig. 2-25 Wavevectors and Wavefronts in External Fluid

Fig. 2-26 Normalized specific acoustic impedance of external fluid as a function of non-dimensional frequency ka for zero axial wavenumber kz .



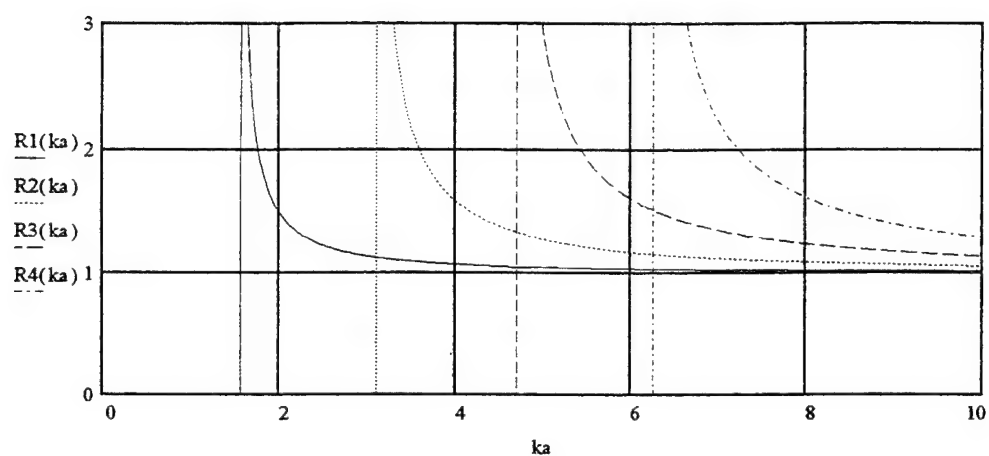
(a) Real component (radiation resistance) of normalized external impedance



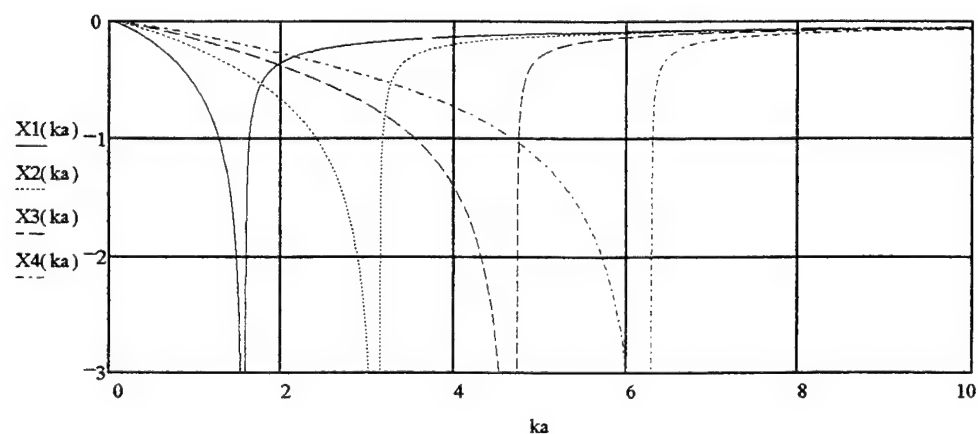
(b) Reactive component of normalized external impedance

Figure 2-27 Normalized specific acoustic impedance of external fluid as a function of non-dimensional frequency for four values of axial wavenumber.

$$k_z \cdot a := \frac{\pi}{2}, \pi, \frac{\pi}{2}, 2 \cdot \pi$$



(a) Real component of normalized external impedance



(b) Imaginary component of normalized external impedance

Fig. 3-1 Branch 1 (solid line) and Branch 2 (dashed line) frequencies for thin elastic shell as functions of axial wavenumber. Frequencies in kilohertz, wavenumber in 1/meters

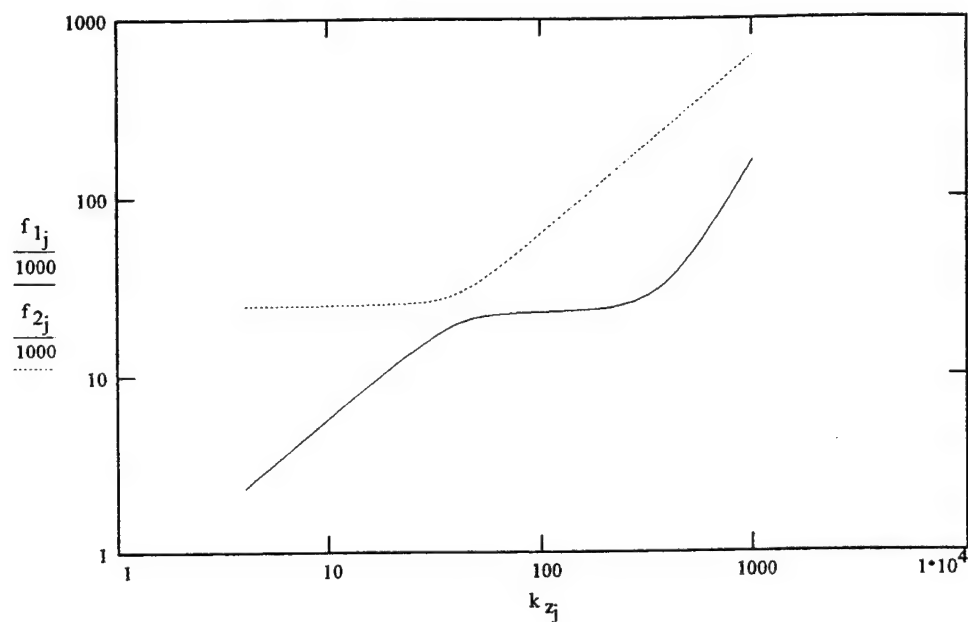


Fig. 3-2 Phase velocity of Branch 1 (solid line) and Branch 2 (dashed line) for thin elastic shell as functions of axial wavenumber. Velocities in meters/second, wavenumber in 1/meters

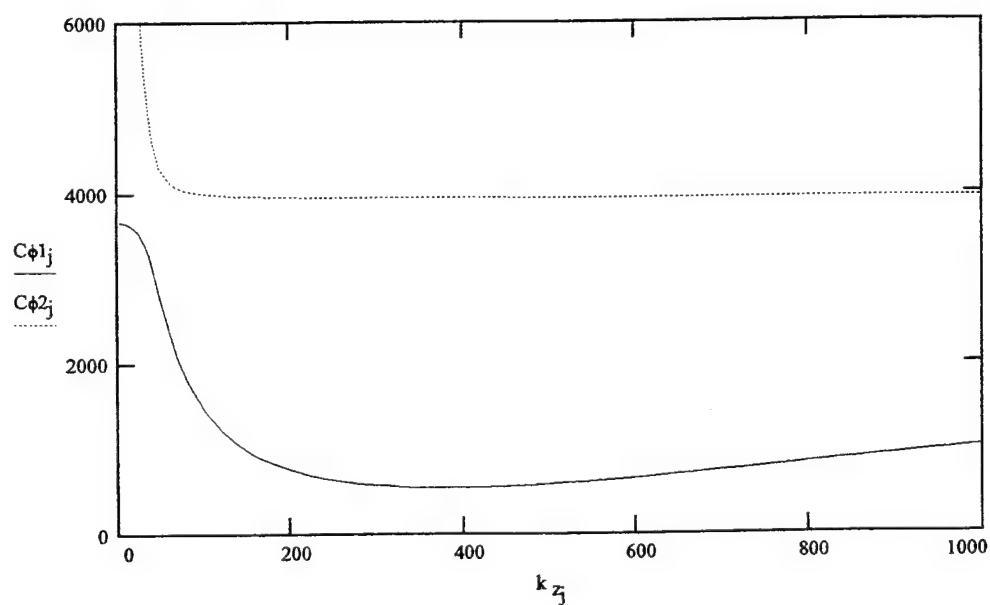


Fig. 3-3 Group velocity of Branch 1 (solid line) and Branch 2 (dashed line) for thin elastic shell as functions of axial wavenumber. Velocities in meters/second, wavenumber in 1/meters

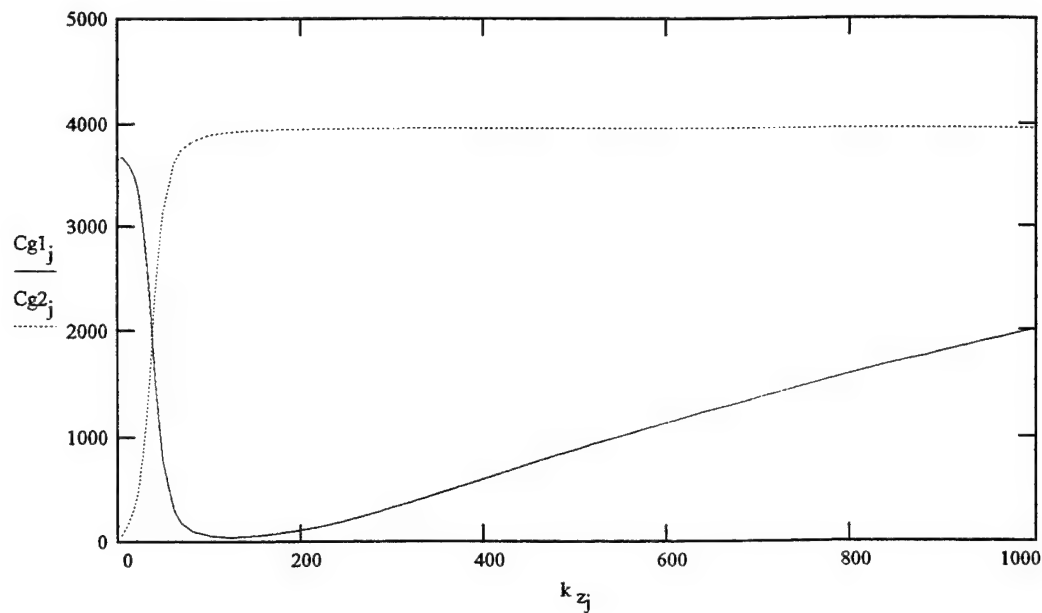
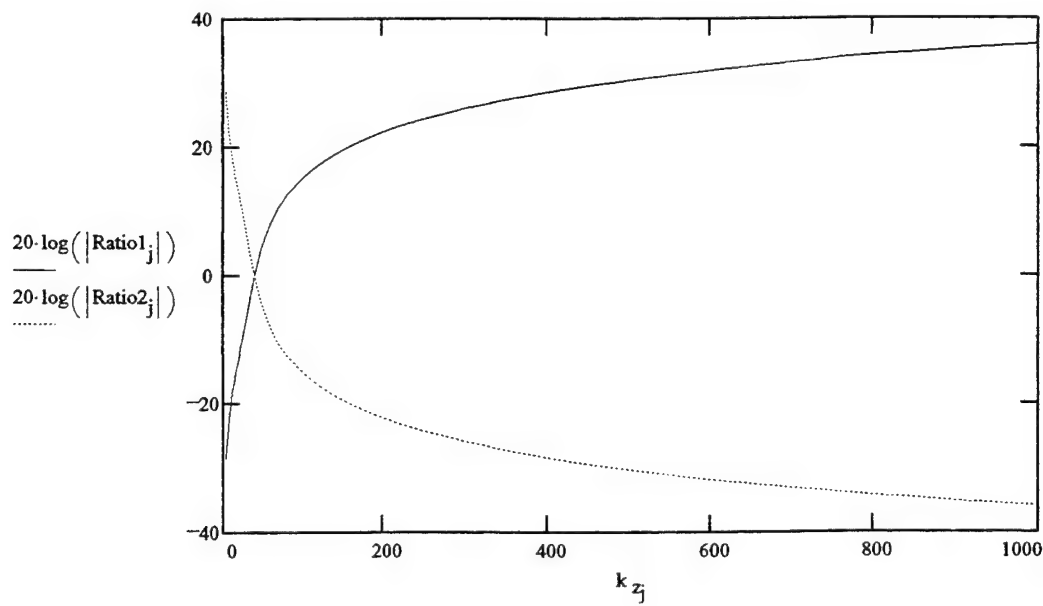


Fig. 3-4 Ratio of radial to axial displacements for Branch 1 (solid line) and Branch 2 (dashed line) for thin elastic shell as functions of axial wavenumber.



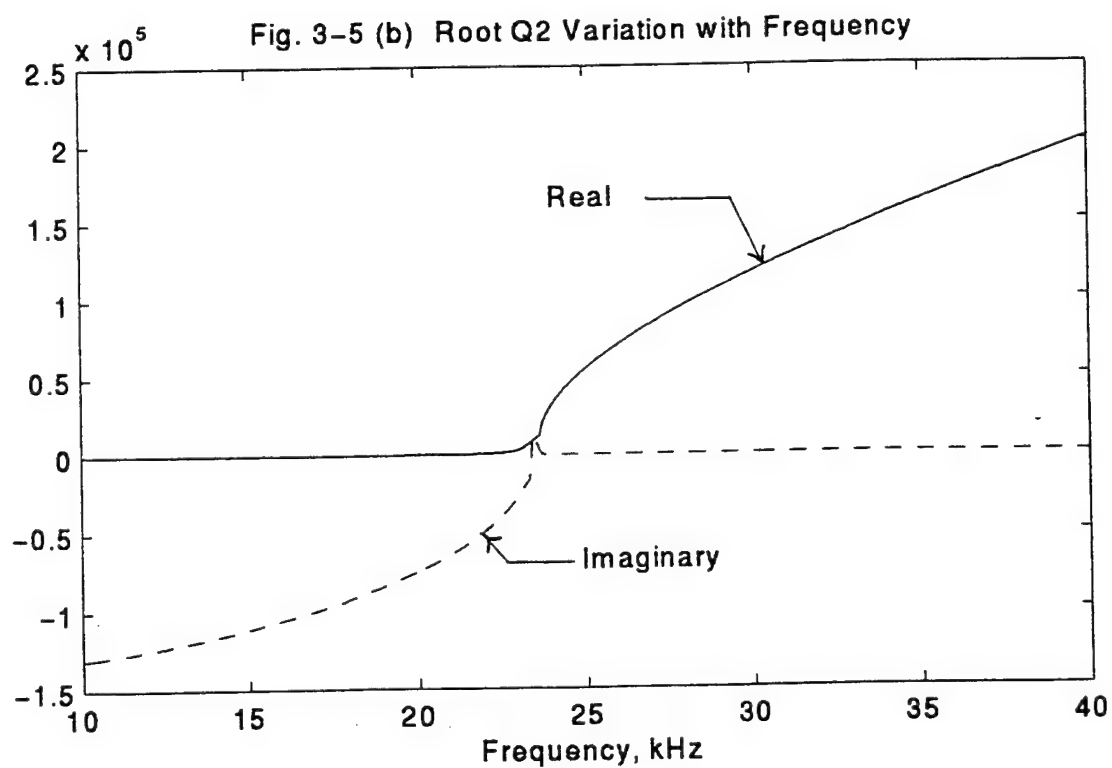
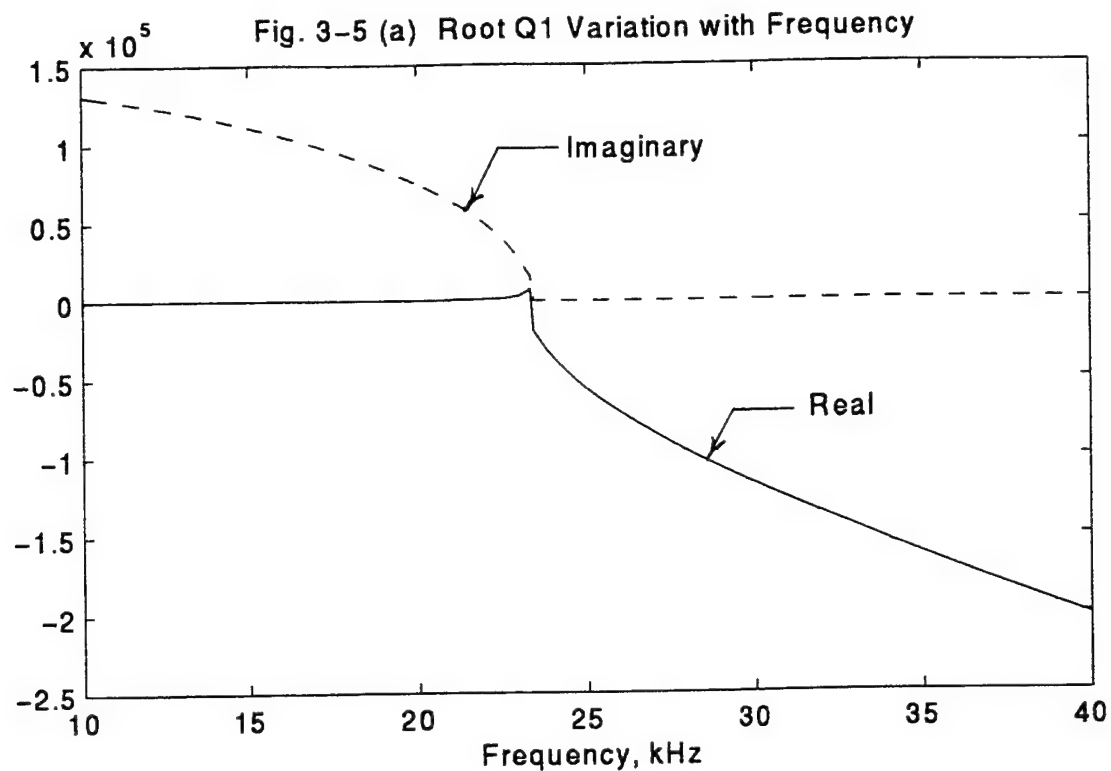


Fig. 3-5 (c) Root Q3 Variation with Frequency

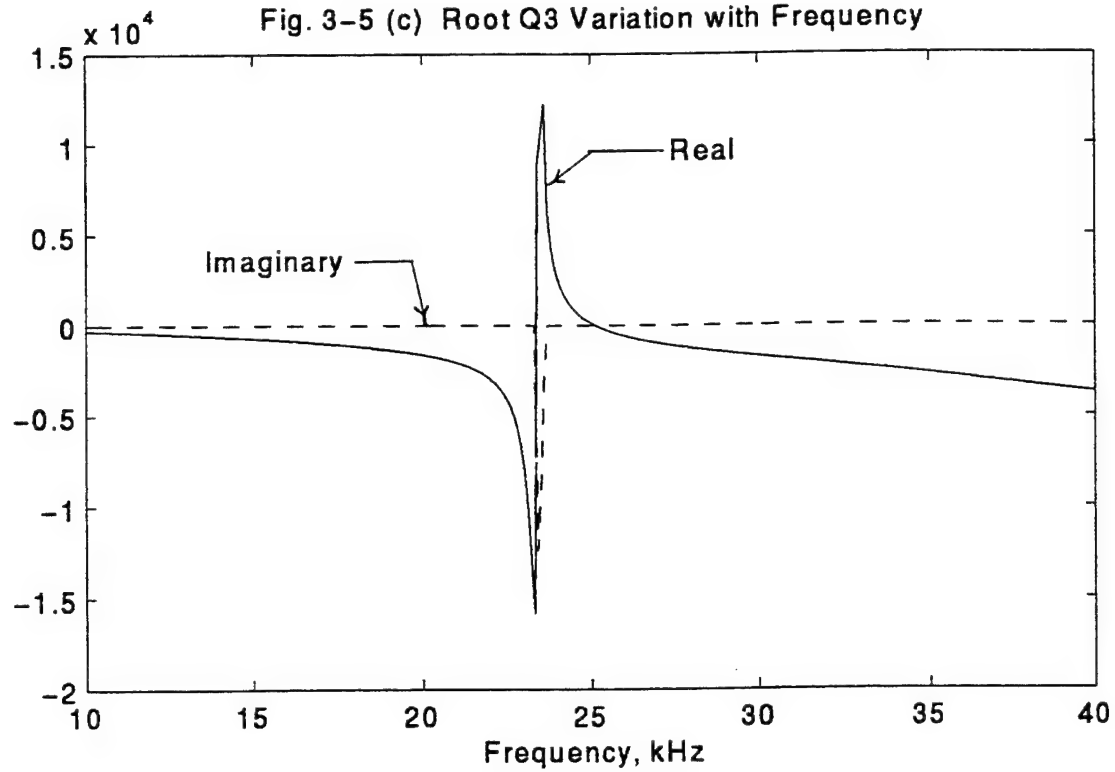
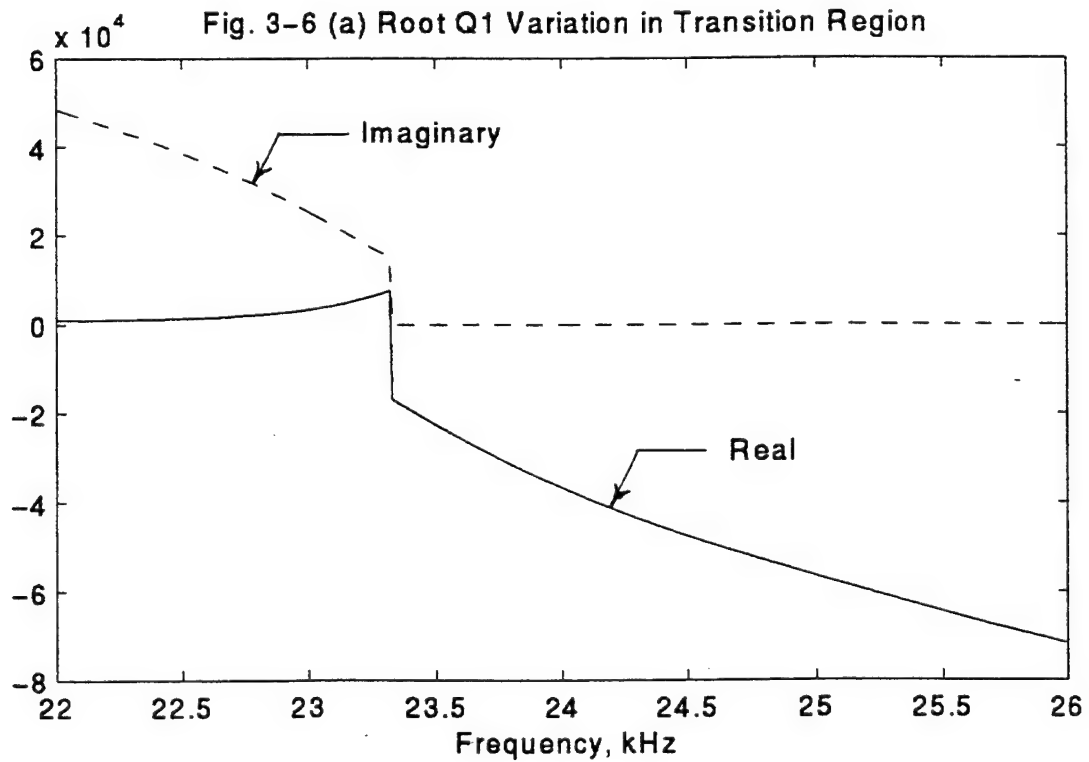


Fig. 3-6 (a) Root Q1 Variation in Transition Region



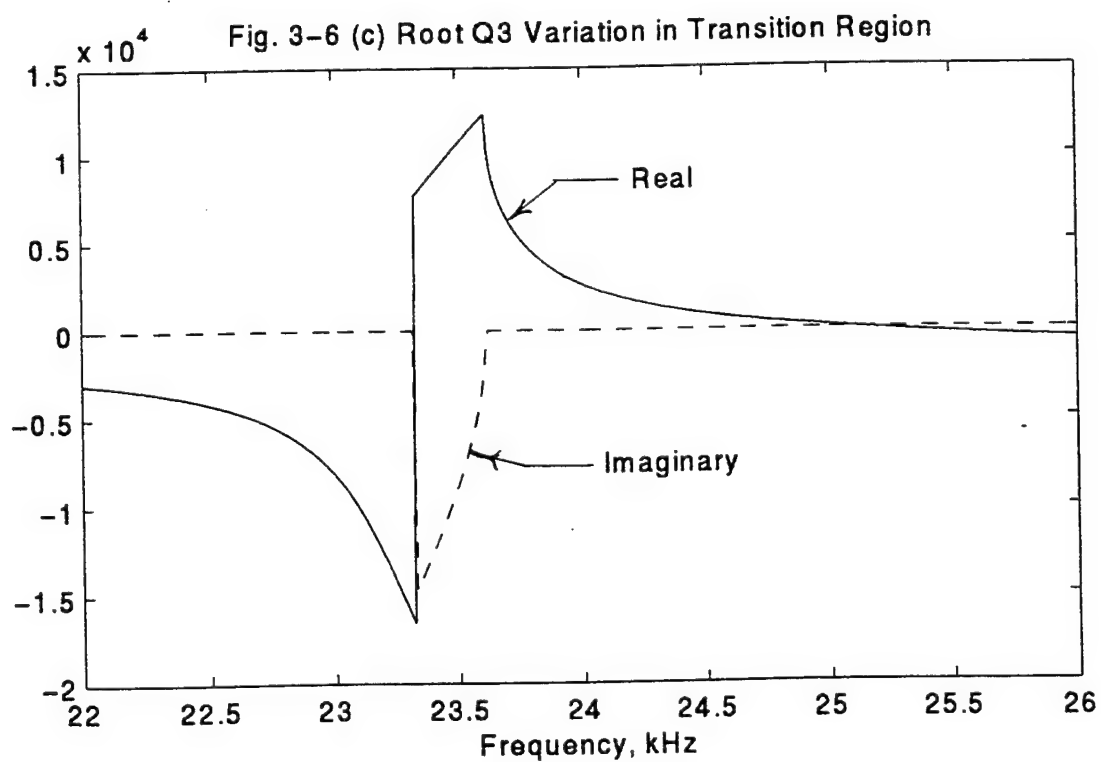
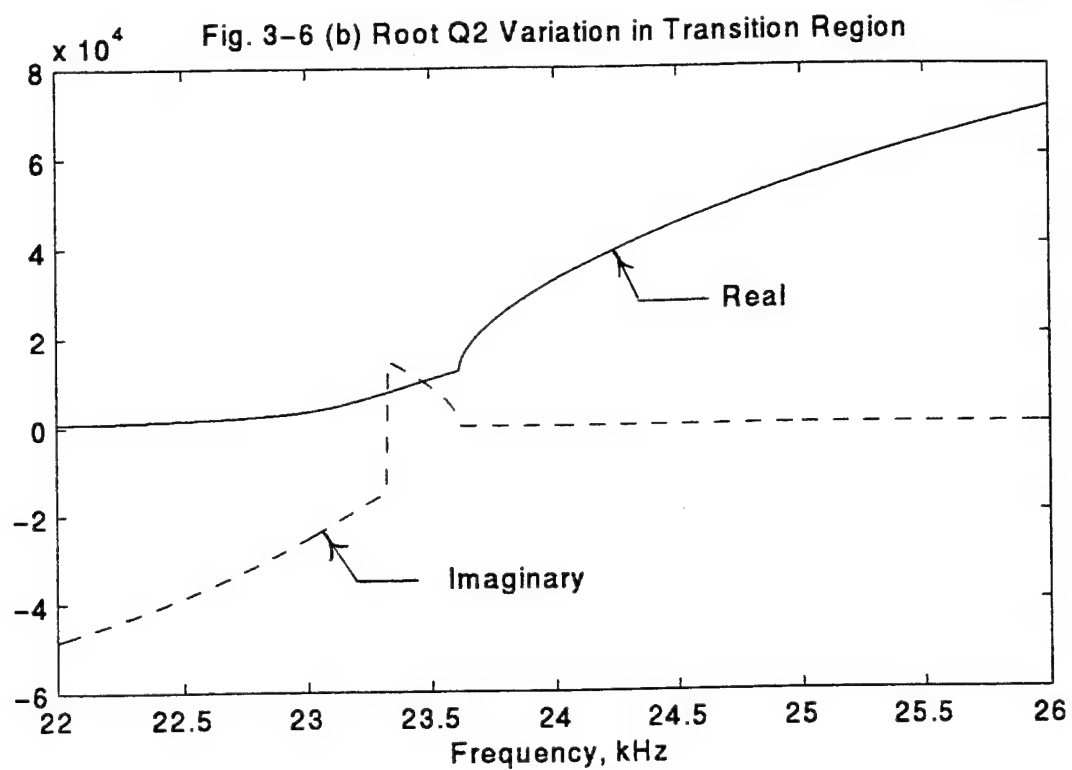
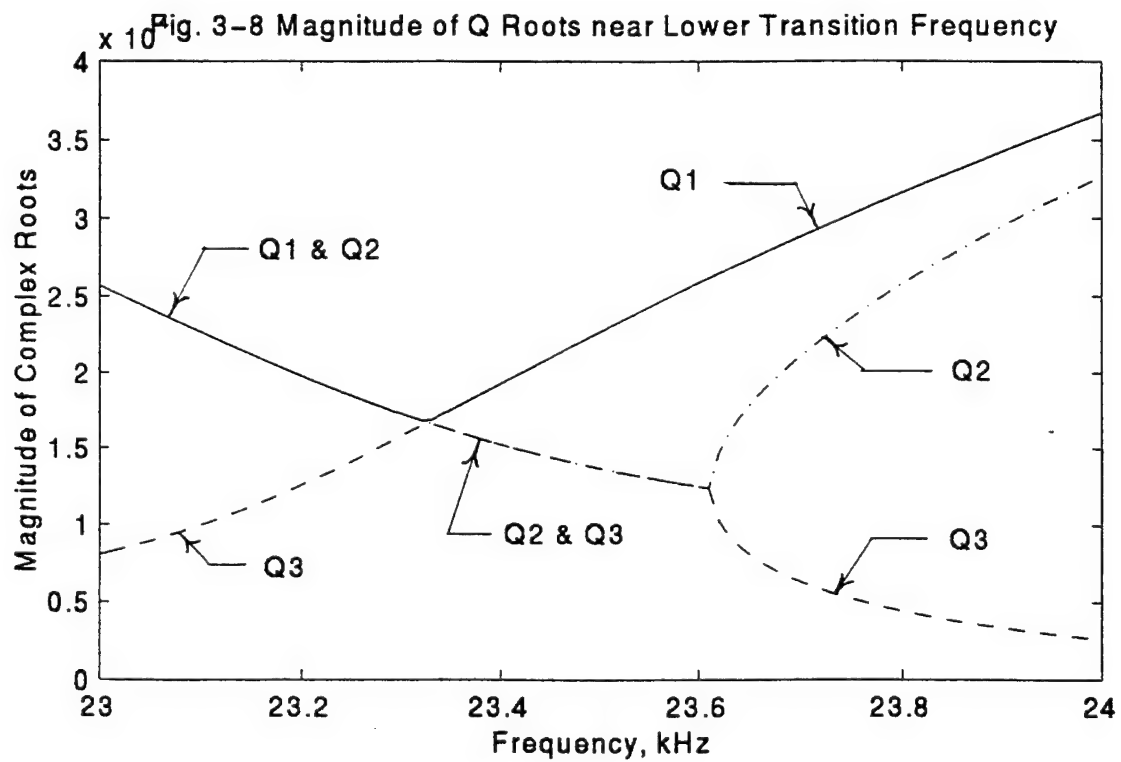
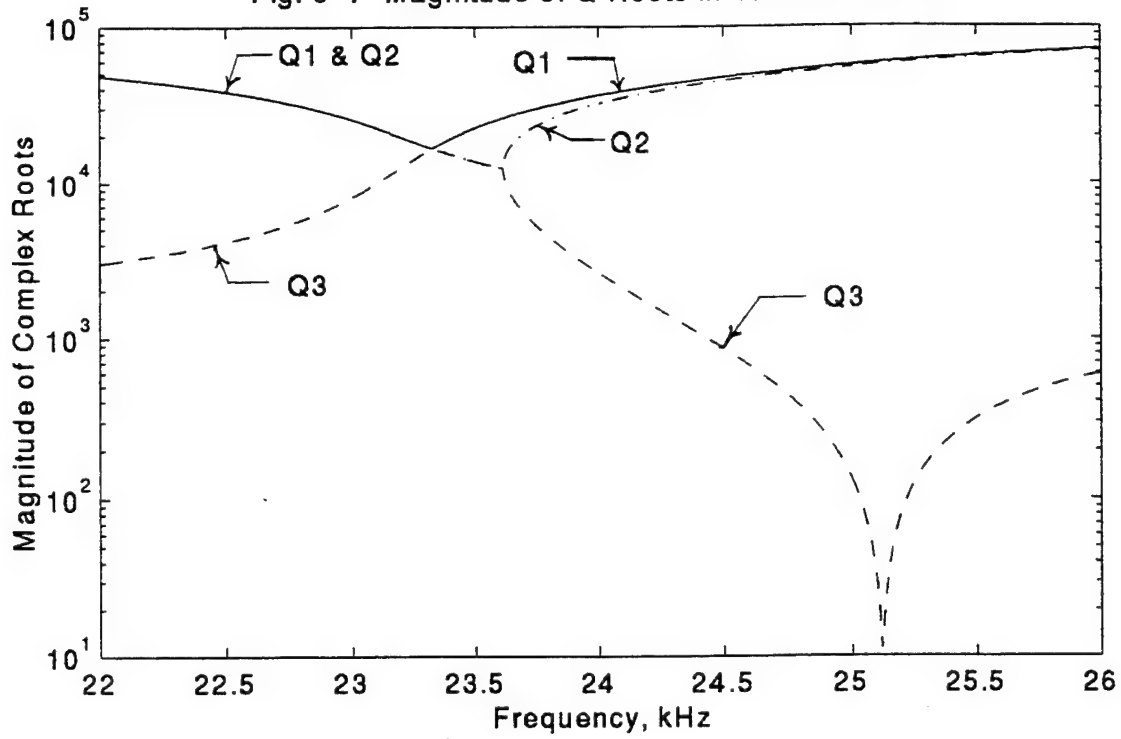


Fig. 3-7 Magnitude of Q Roots in Transition Zone



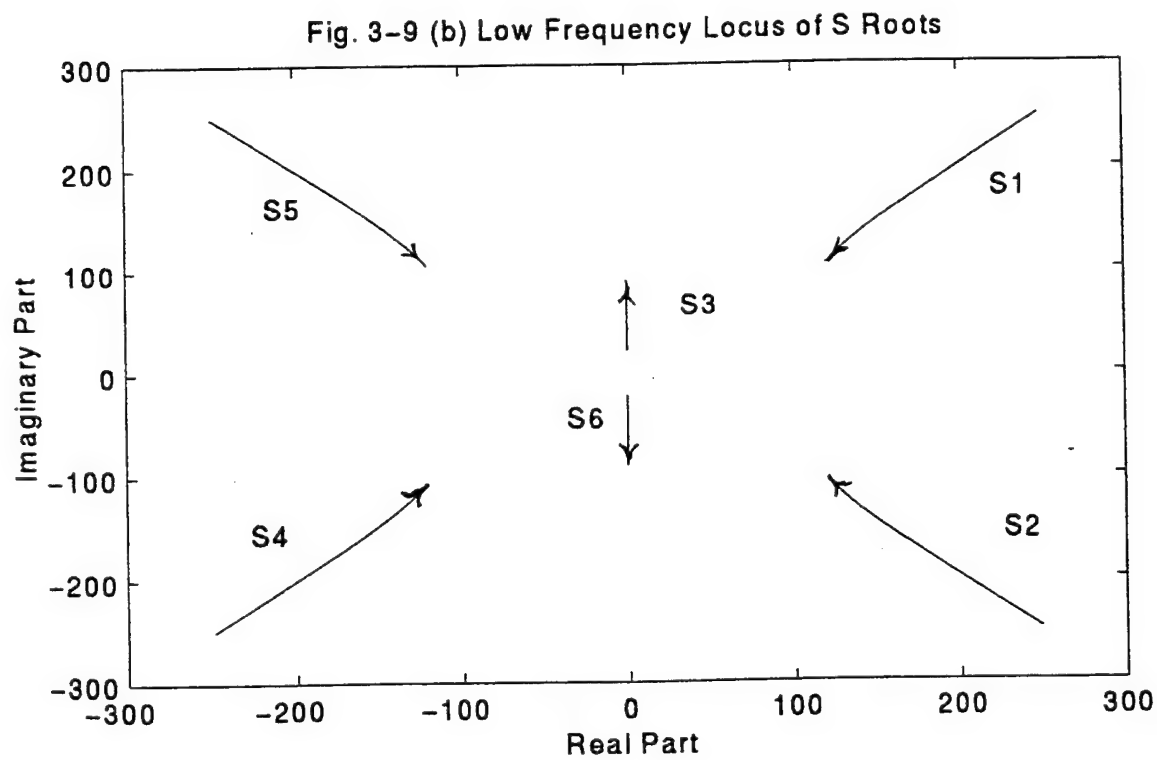
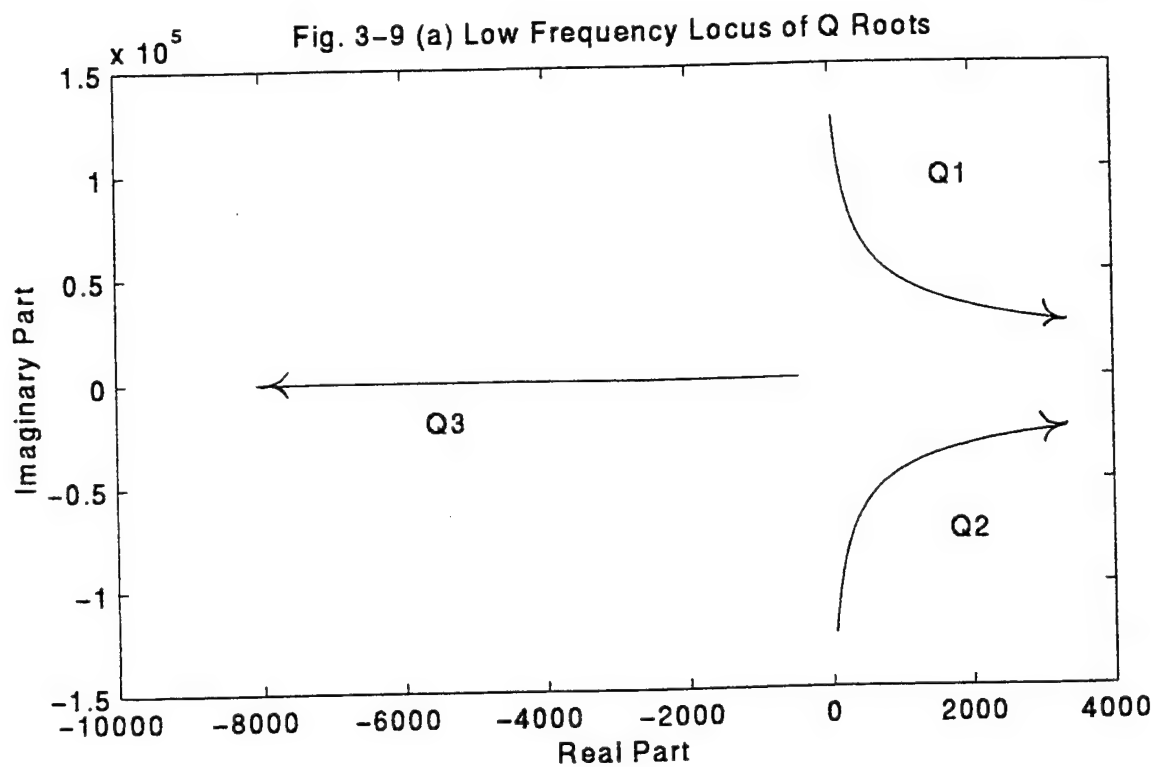


Fig. 3-9 (c) High Frequency Locus of Q Roots

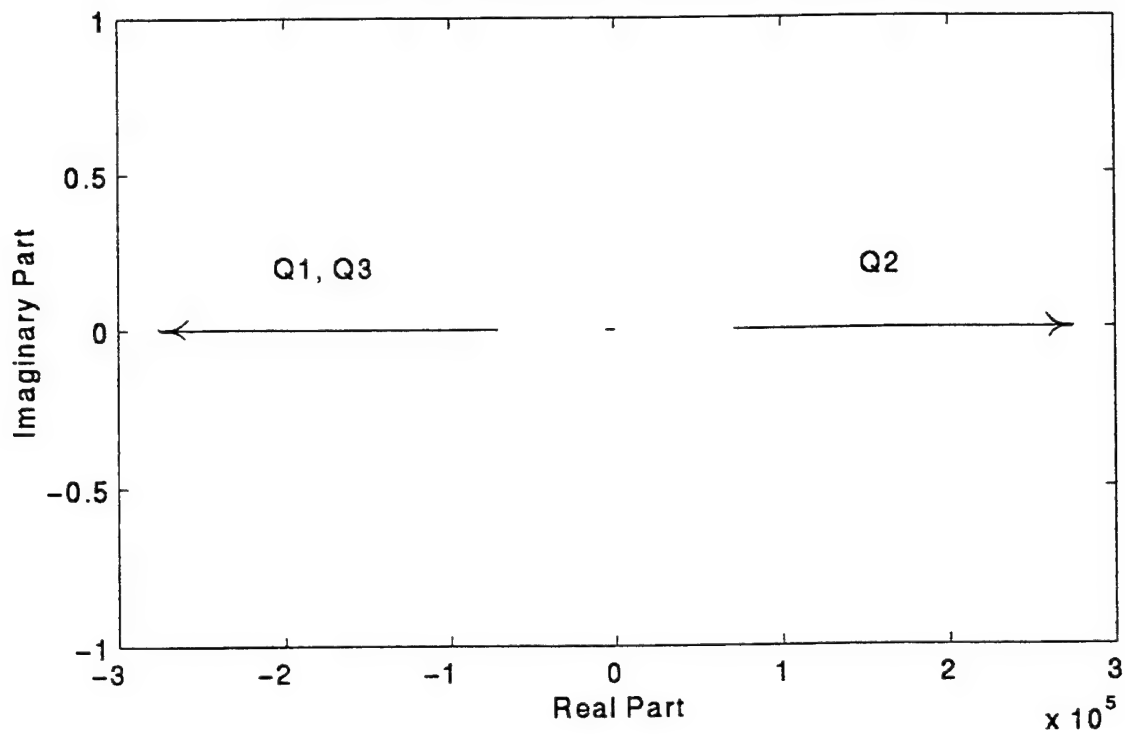


Fig. 3-9 (d) High Frequency Locus of S Roots

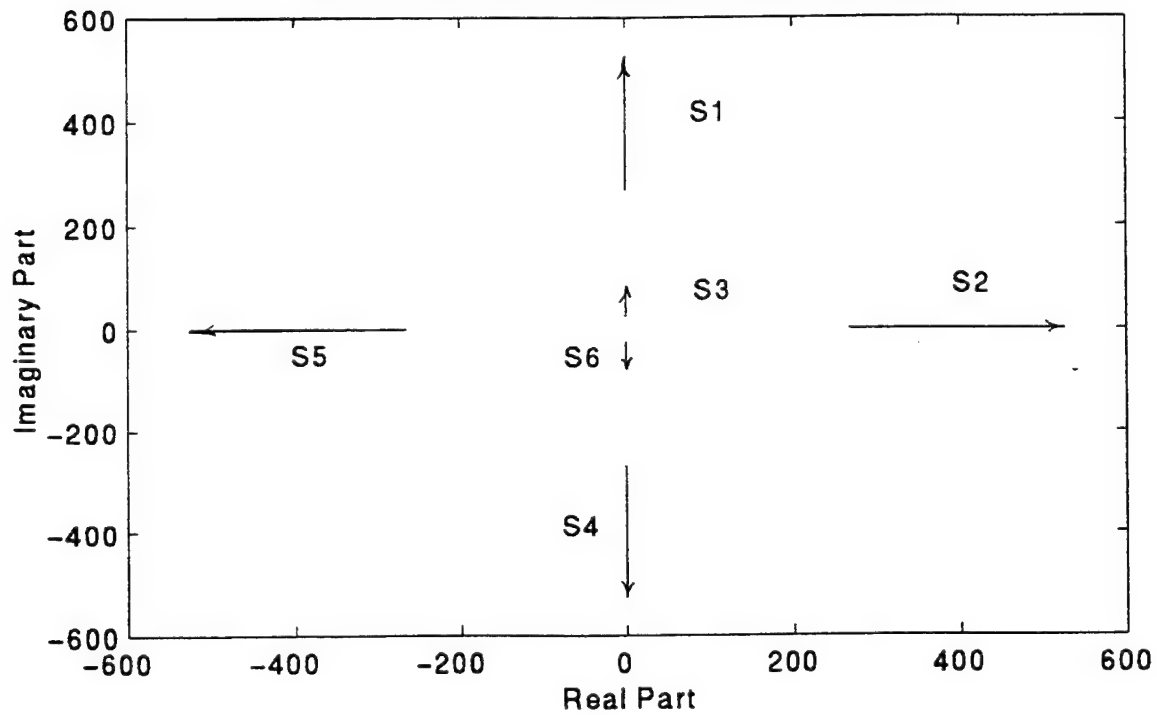


Fig 3-10 Magnitude of S Roots in Transition Zone

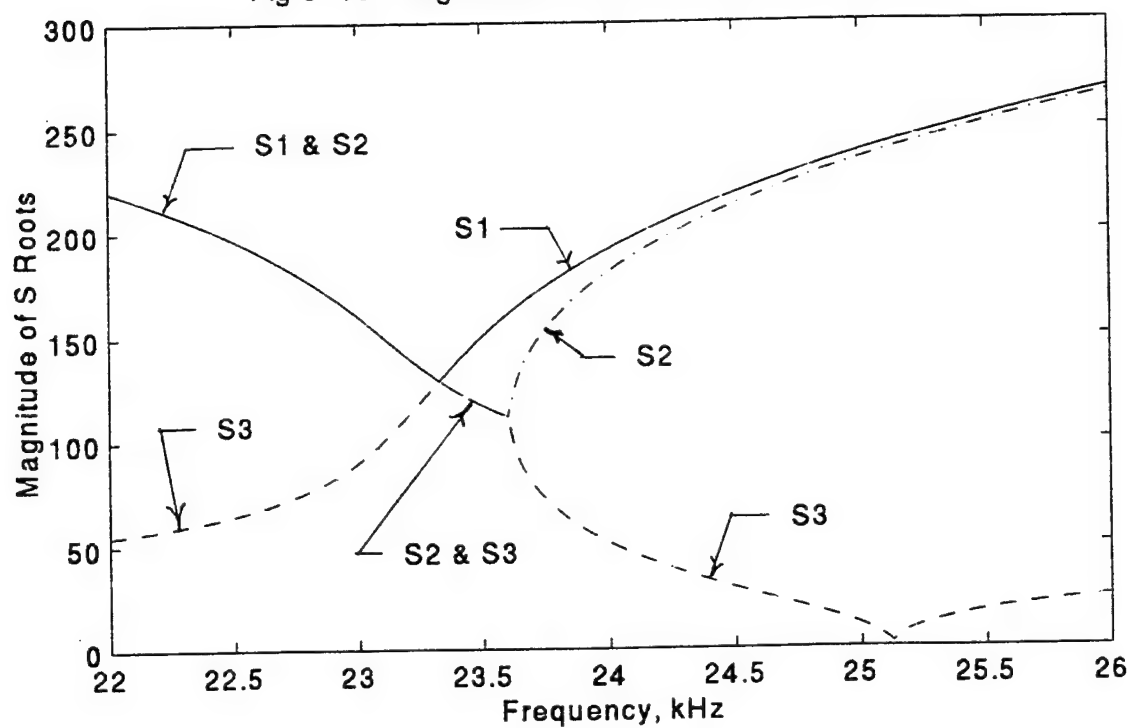


Fig 3-11 (a) Components of S3 in Transition Zone, Beta = .0103

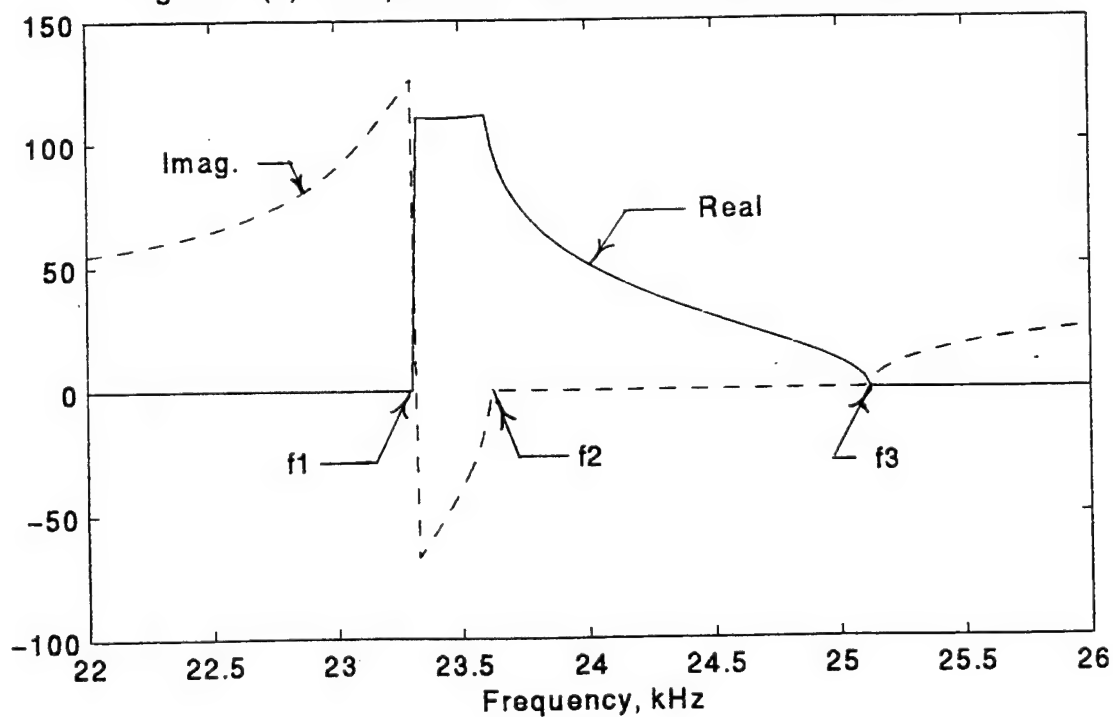


Fig 3-11 (b) Components of S3 in Transition Zone, Beta = 0.1

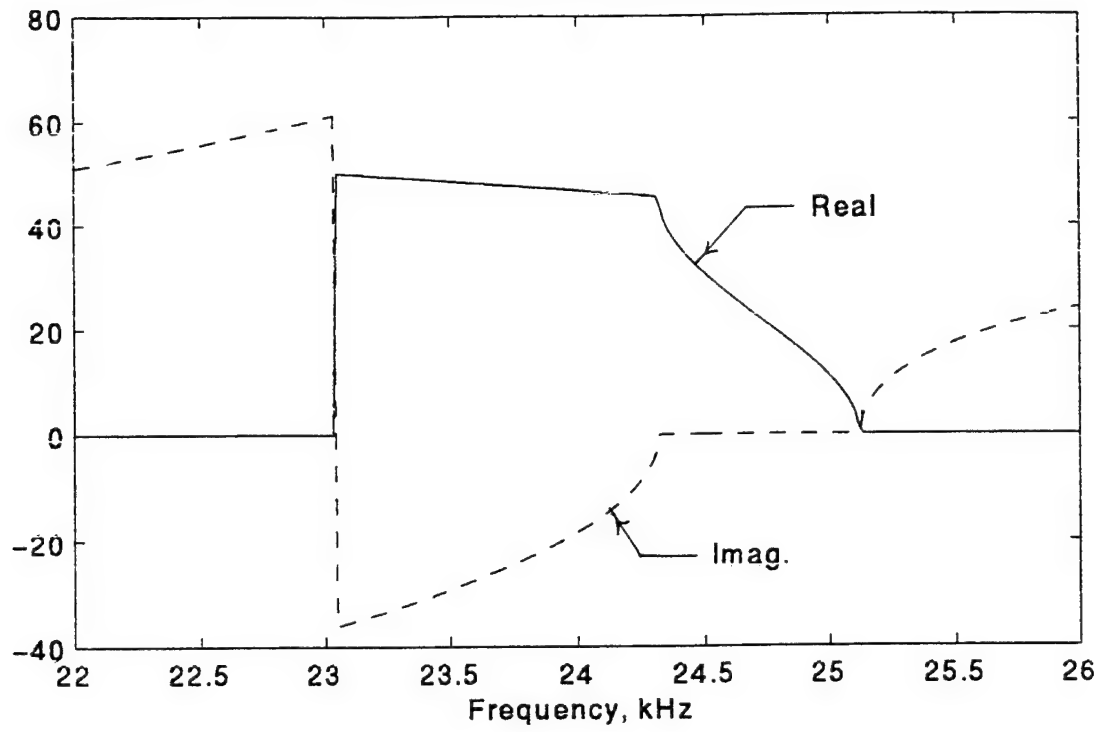


Fig 3-11 (c) Components of S3 in Transition Zone, Beta = 0.001

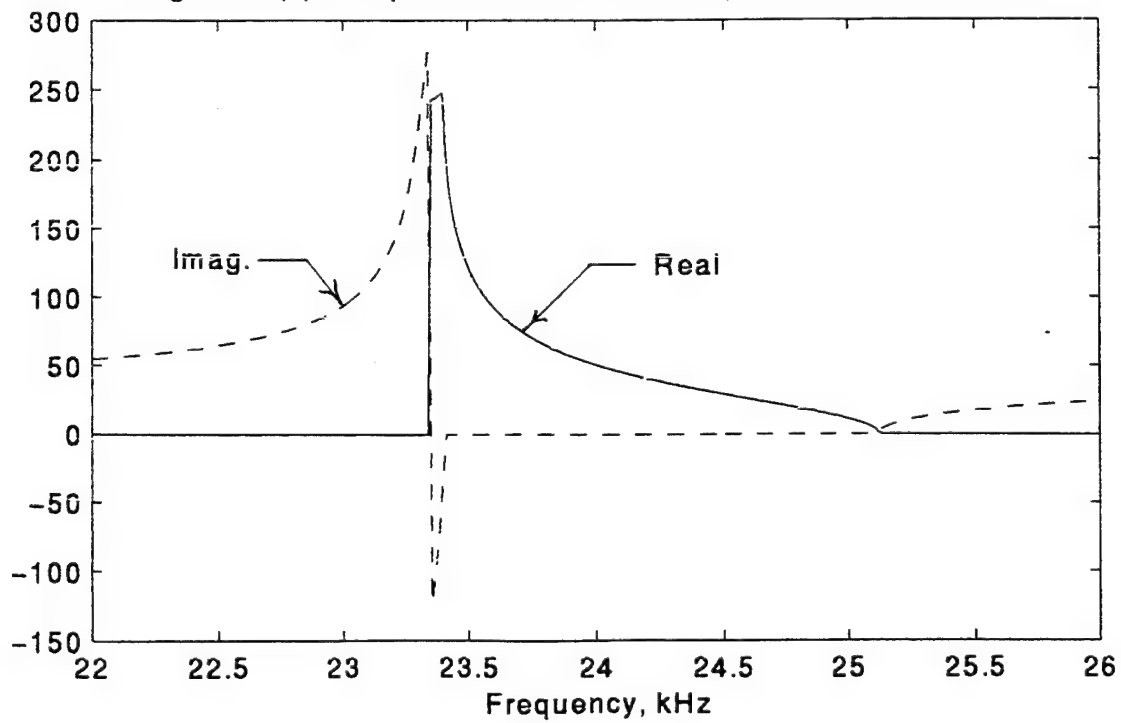
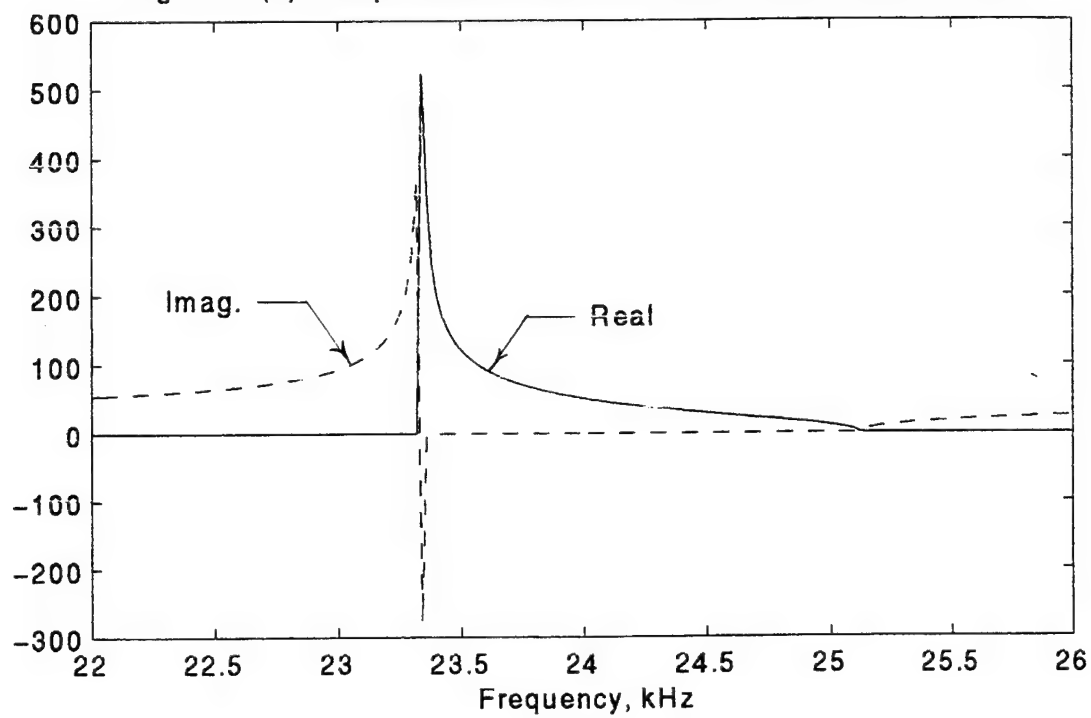


Fig 3-11 (d) Components of S3 in Transition Zone, Beta = 0.0001



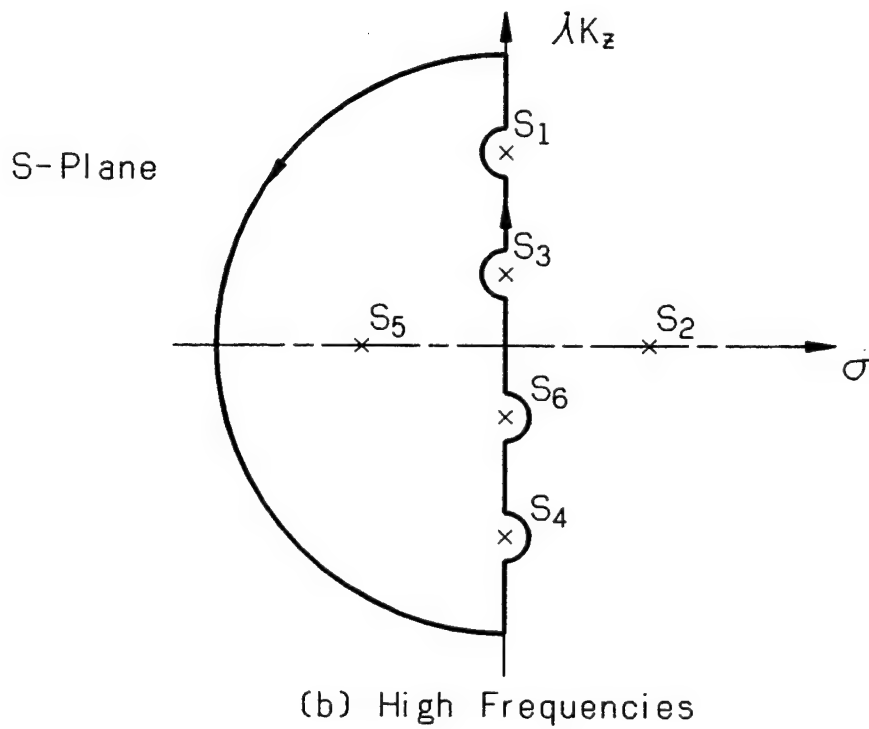
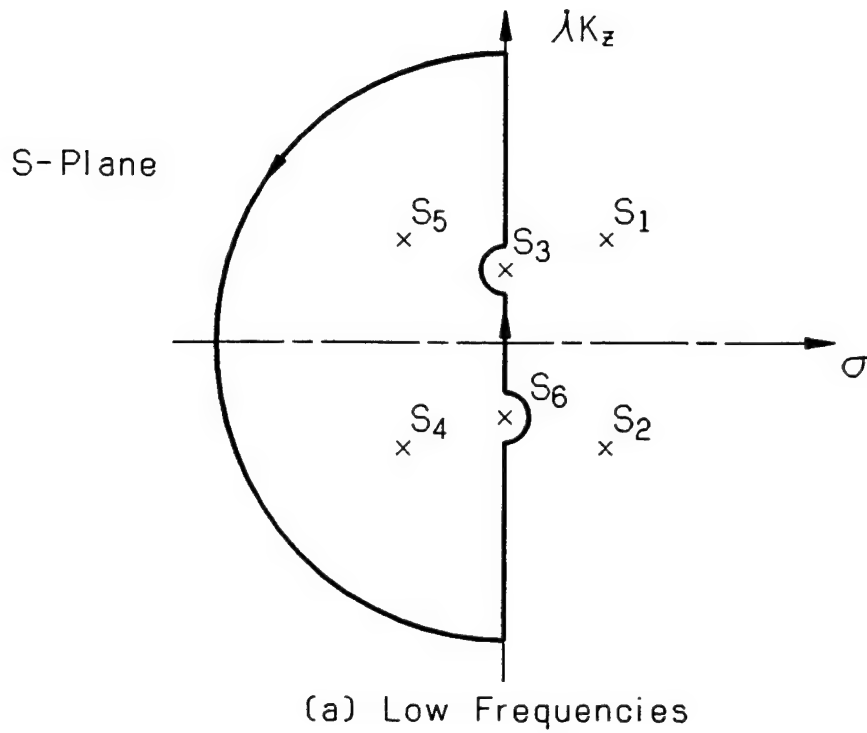


Fig. 3-12 Contour for LaPlace Transform Inversion

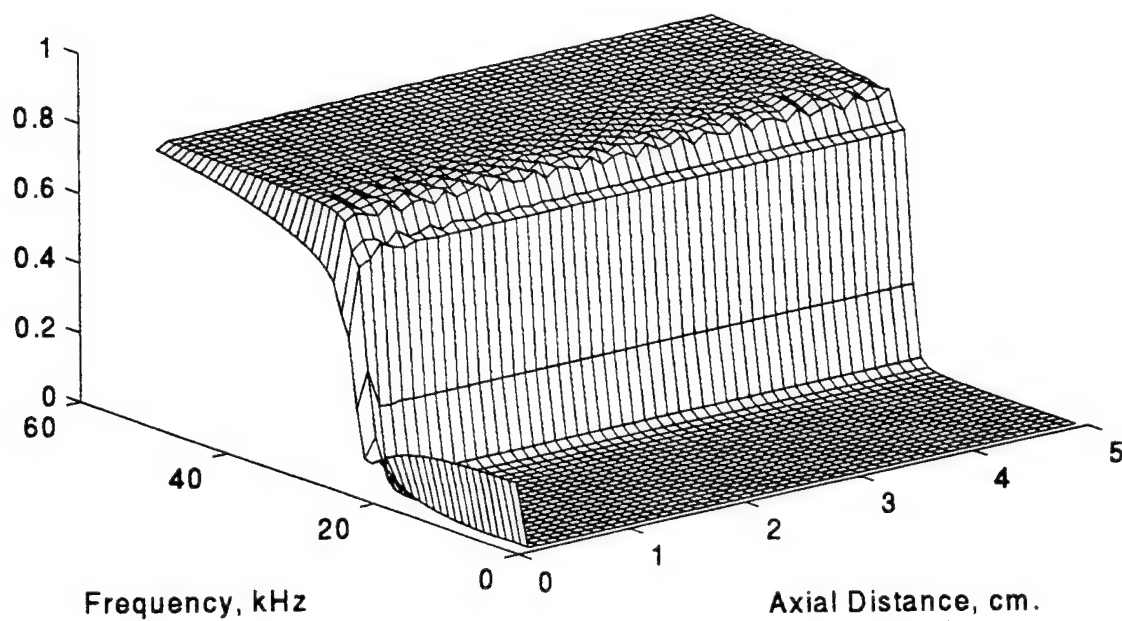
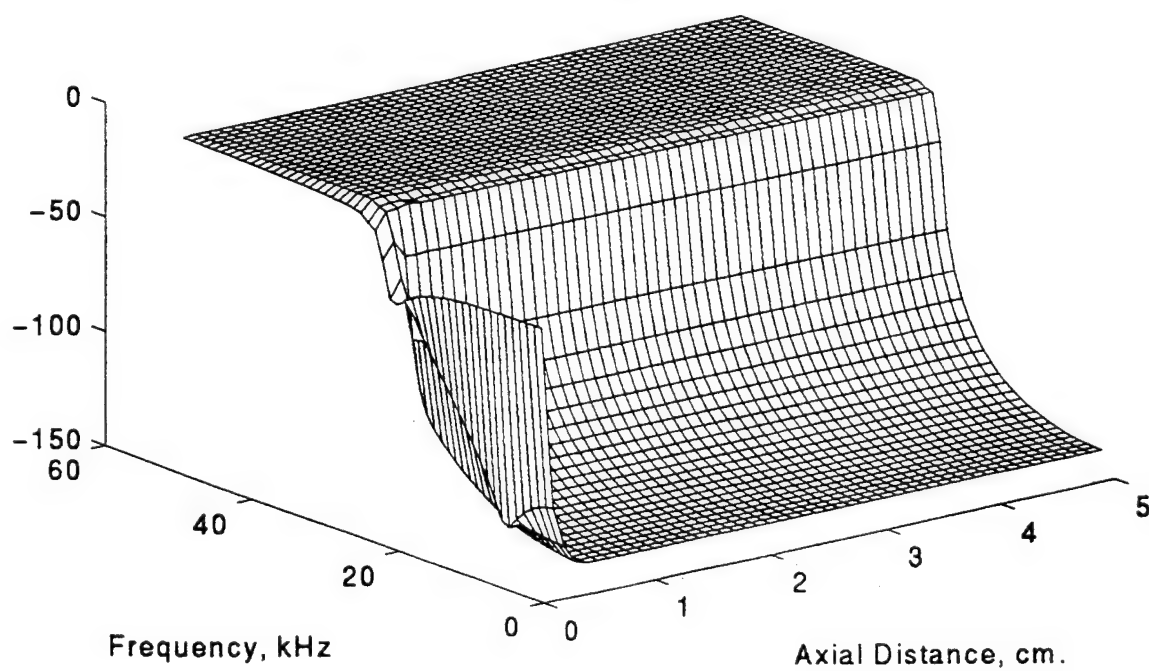
Fig 3-13 (a) Magnitude of $W(f,z)$ vs Distance and FrequencyFig 3-13 (b) $20 \cdot \log$ Magnitude of $W(f,z)$ vs Distance and Frequency

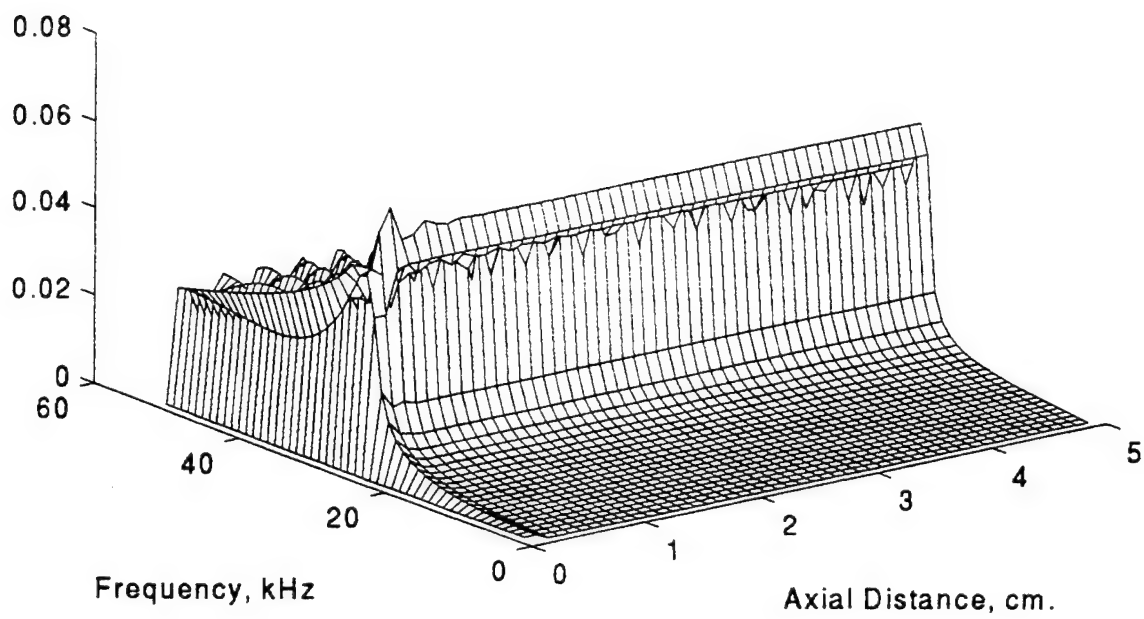
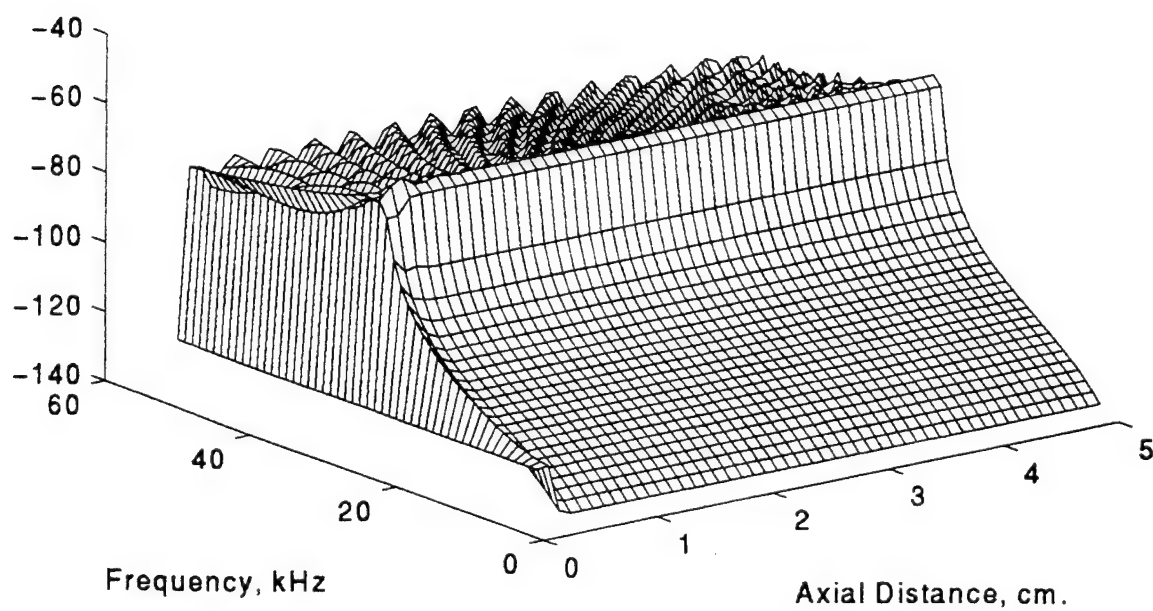
Fig 3-14 (a) Magnitude of $U(f,z)$ vs Distance and FrequencyFig 3-14 (b) $20 \cdot \log$ Magnitude of $U(f,z)$ vs Distance and Frequency

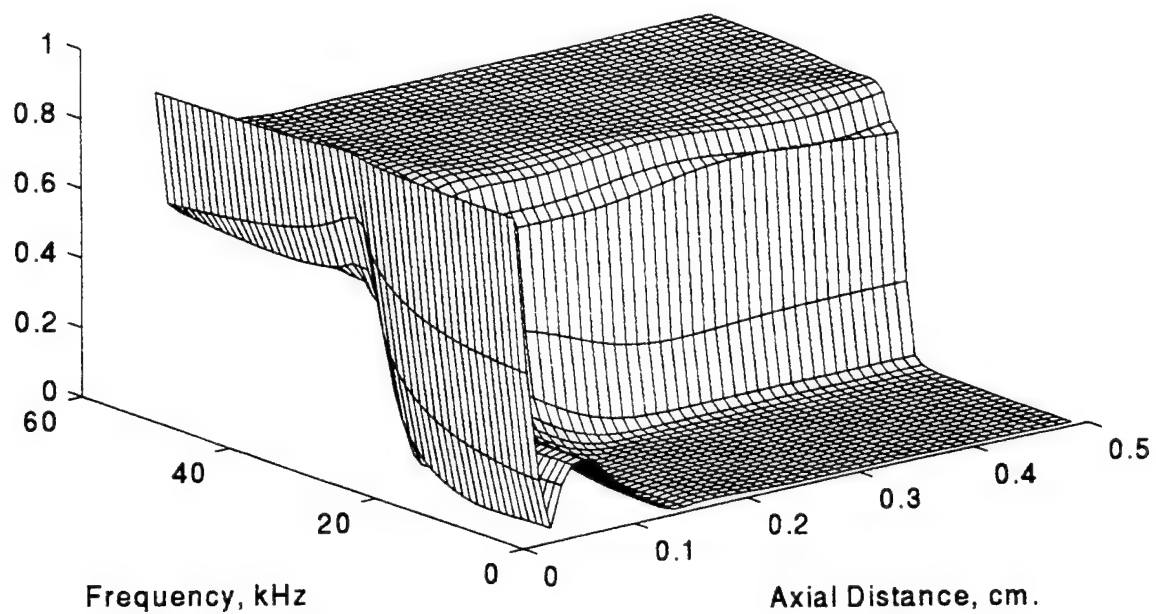
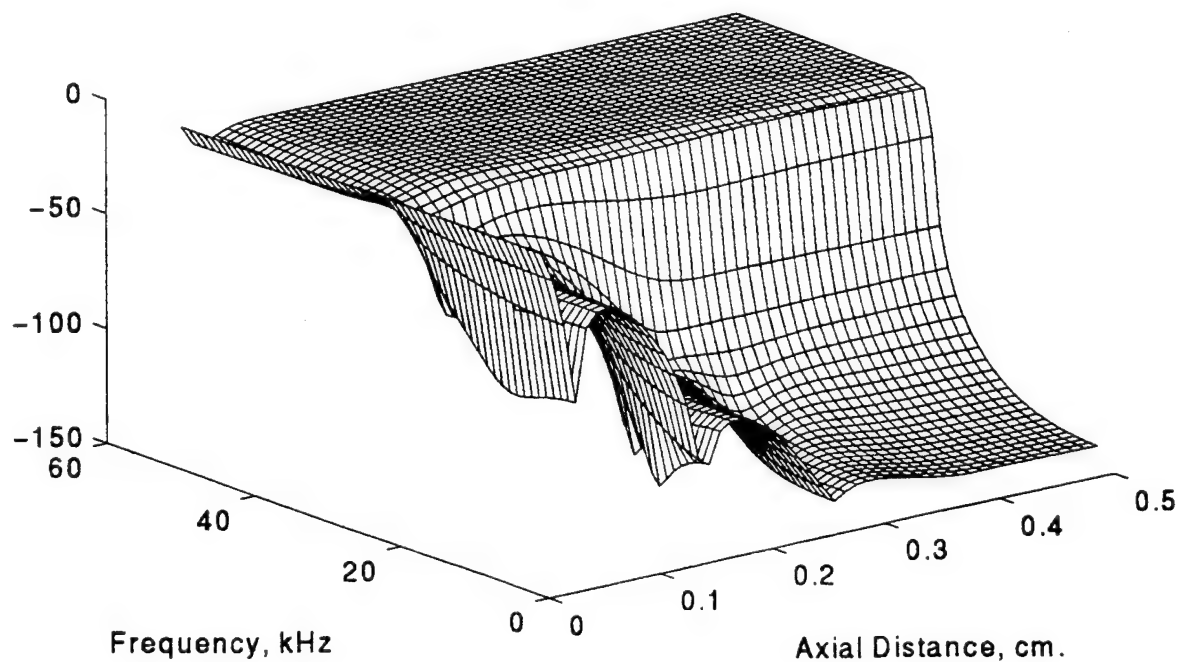
Fig 3-15 (a) Magnitude of $W(f,z)$ vs Distance and FrequencyFig 3-15 (b) $20 \cdot \log$ Magnitude of $W(f,z)$ vs Distance and Frequency

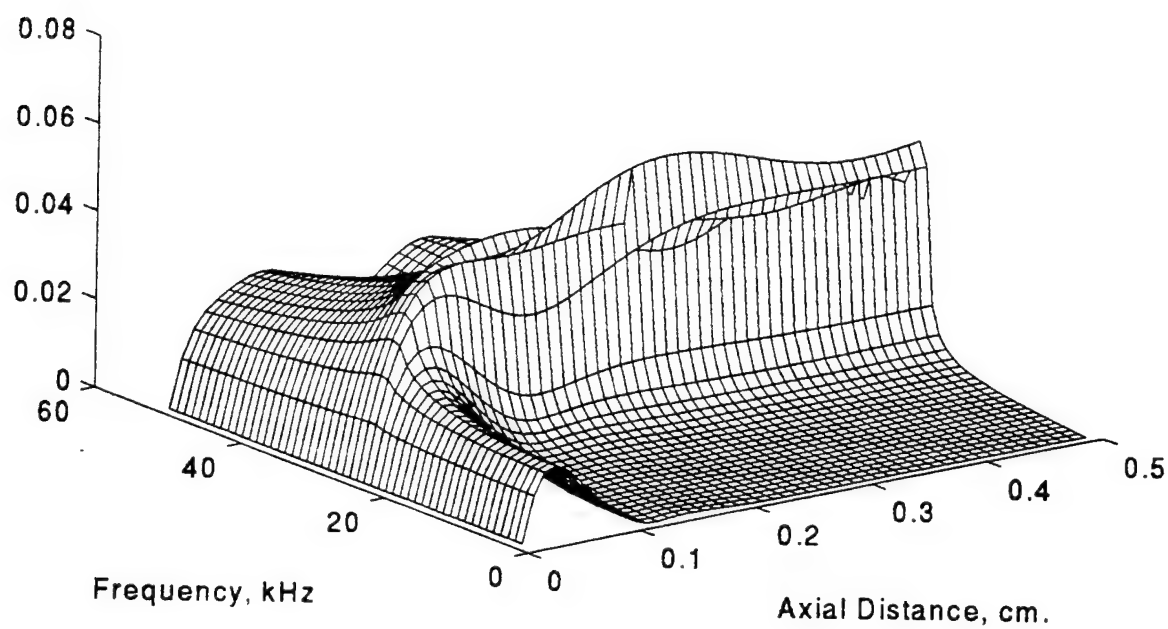
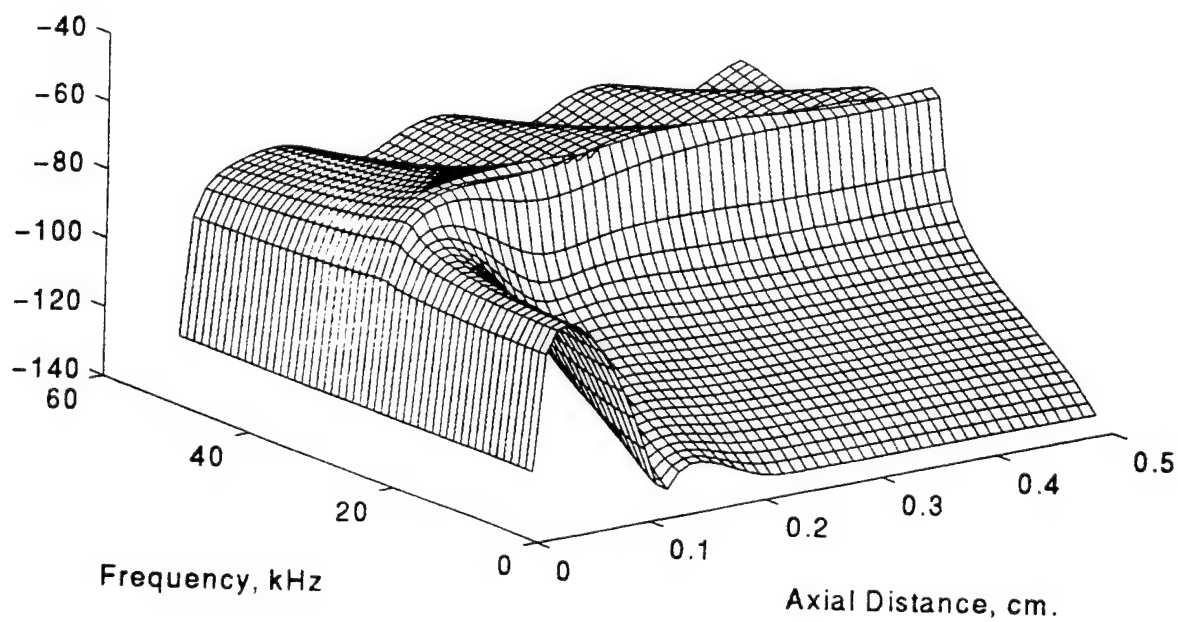
Fig 3-16 (a) Magnitude of $U(f,z)$ vs Distance and FrequencyFig 3-16 (b) Magnitude of $U(f,z)$ vs Distance and Frequency

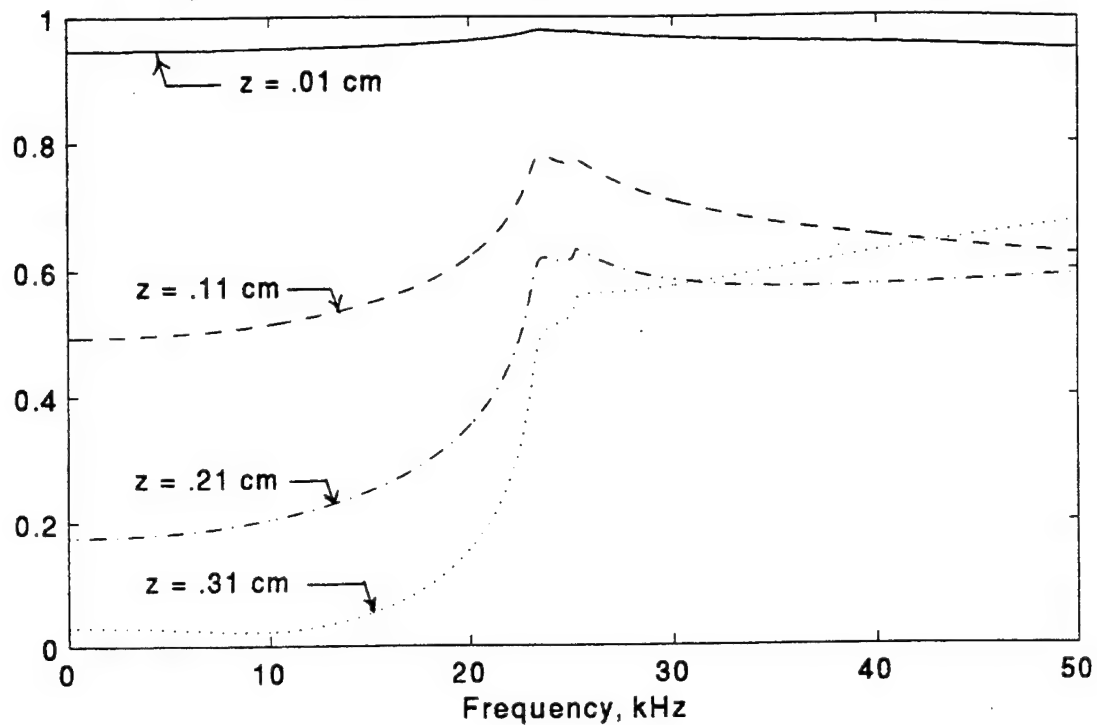
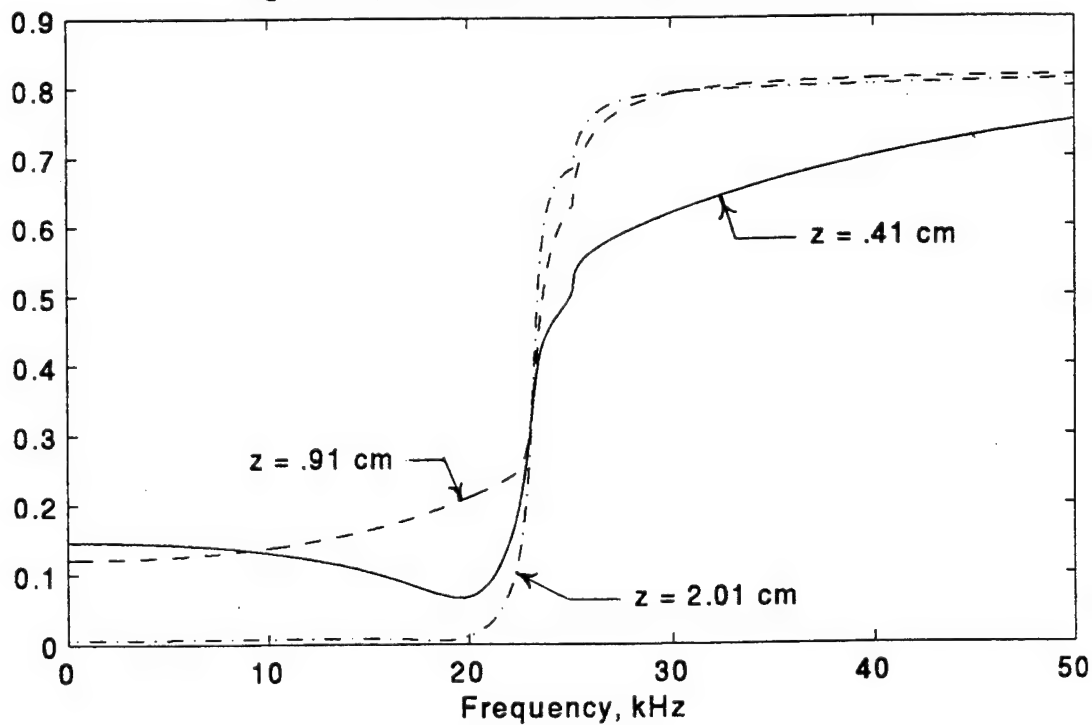
Fig 3-17 (a) Magnitude of $W(f,z)$ vs Frequency (near field)Fig 3-17 (b) Magnitude of $W(f,z)$ vs Frequency

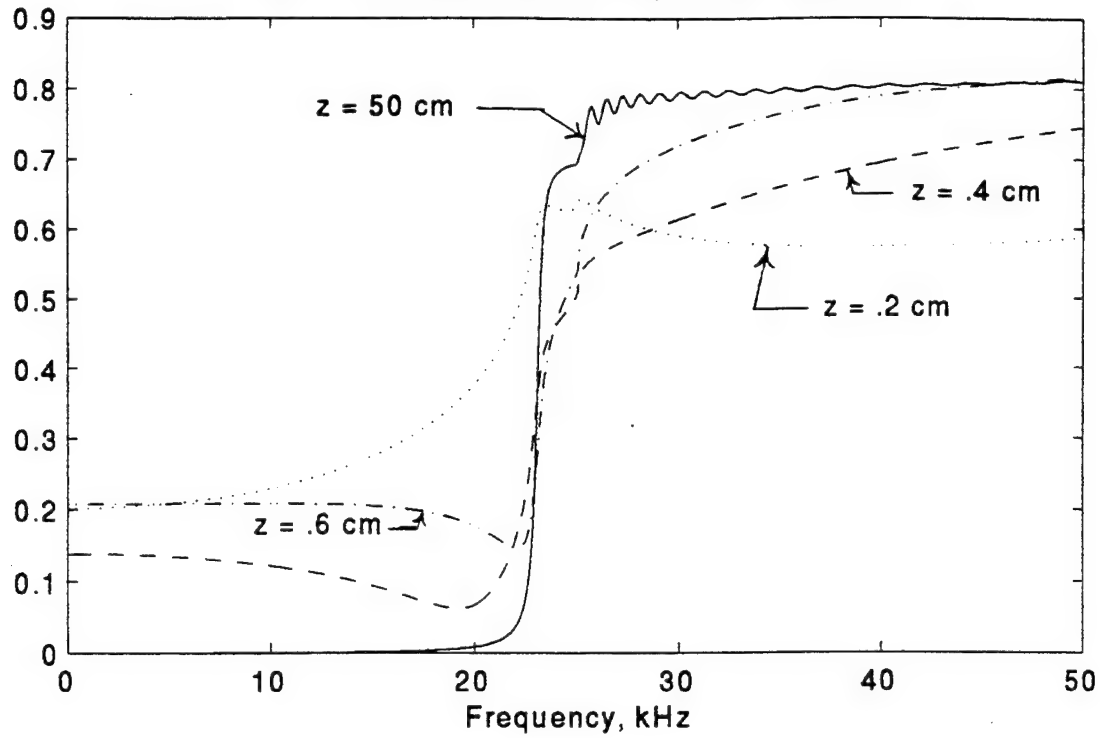
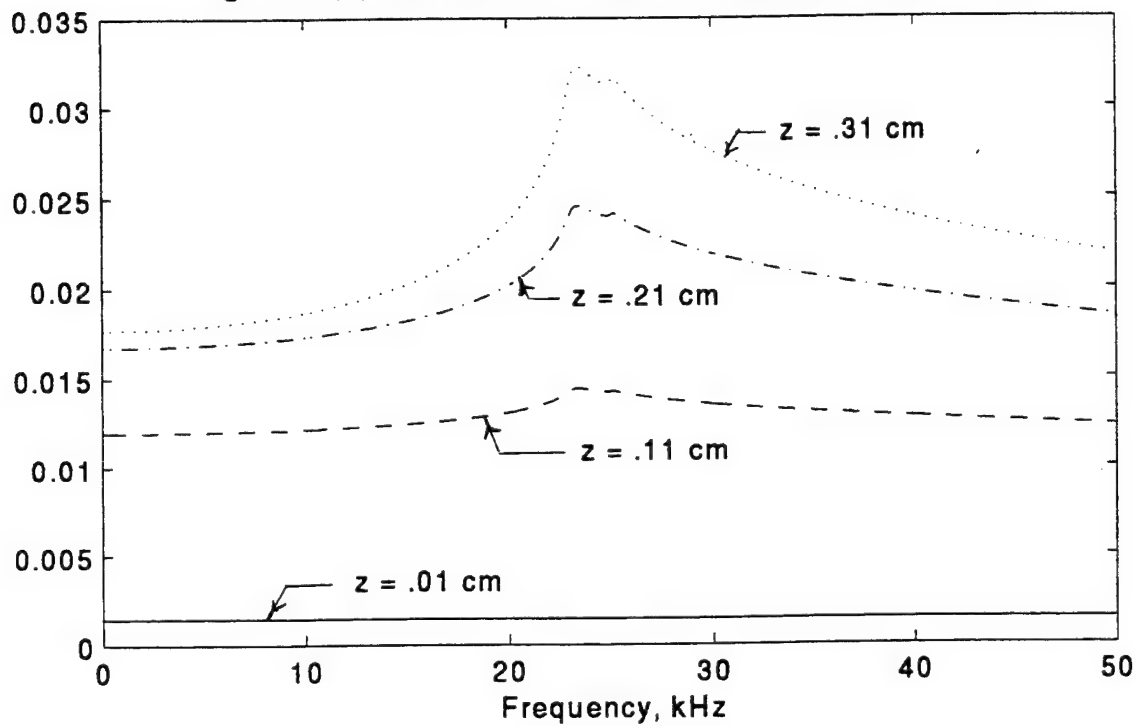
Fig 3-17 (c) Magnitude of $W(f,z)$ vs FrequencyFig 3-18 (a) Magnitude of $U(f,z)$ vs Frequency (near field)

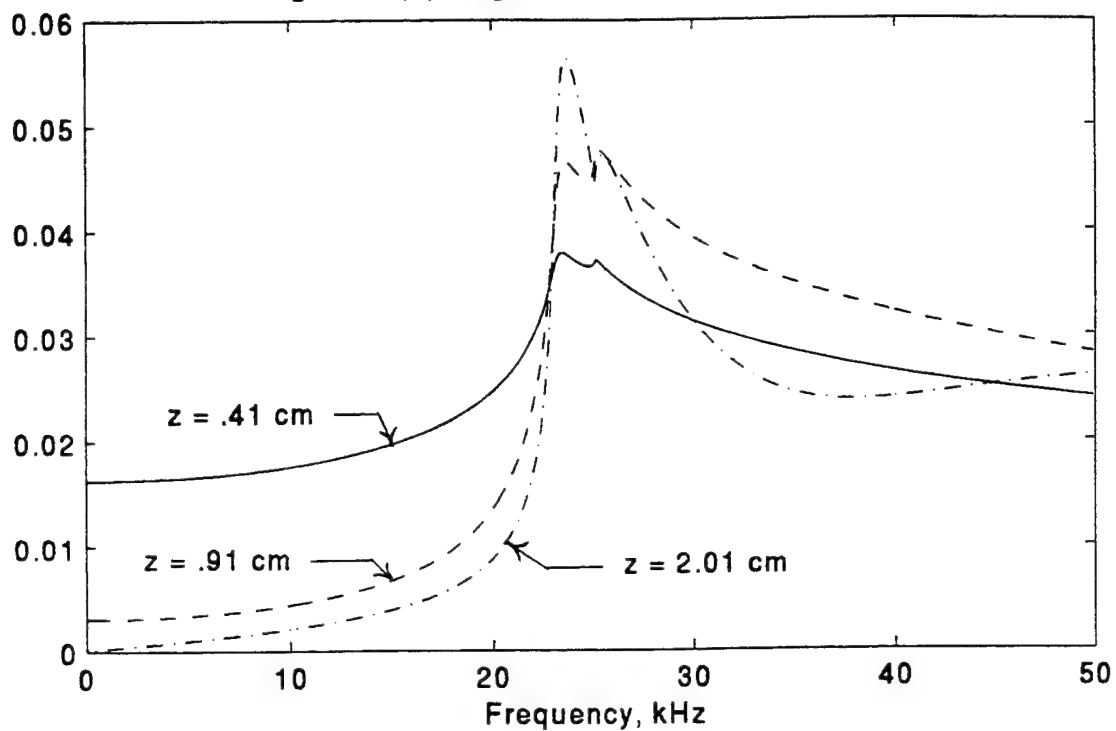
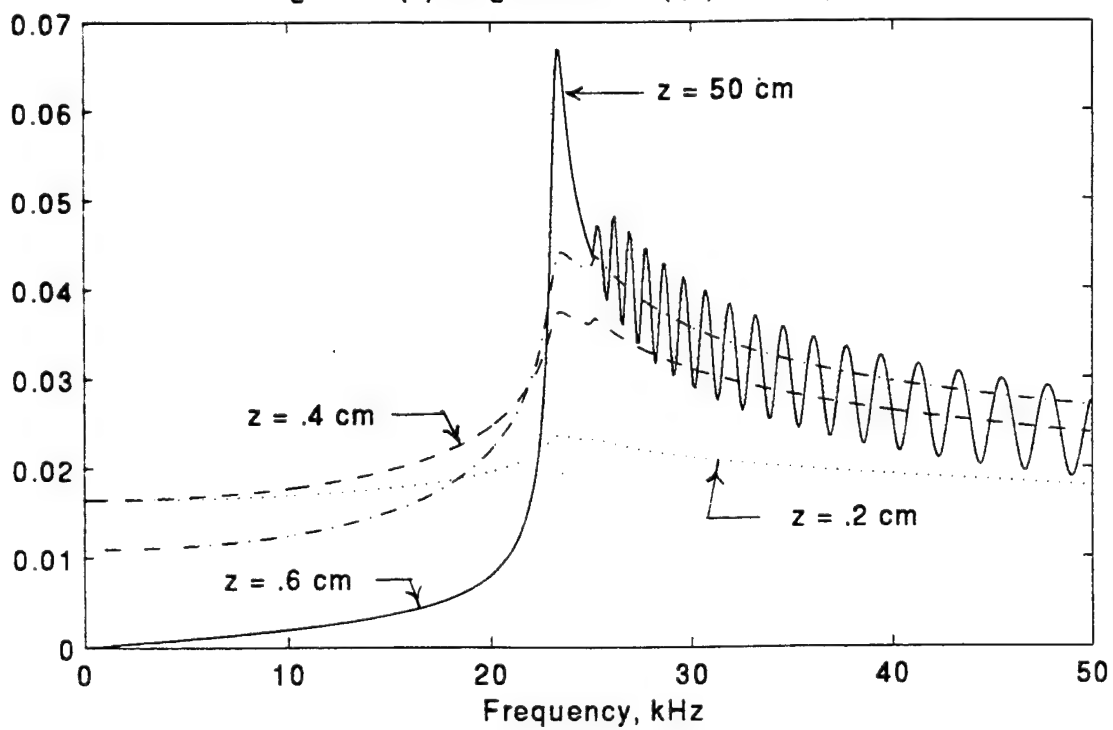
Fig 3-18 (b) Magnitude of $U(f,z)$ vs FrequencyFig 3-18 (c) Magnitude of $U(f,z)$ vs Frequency

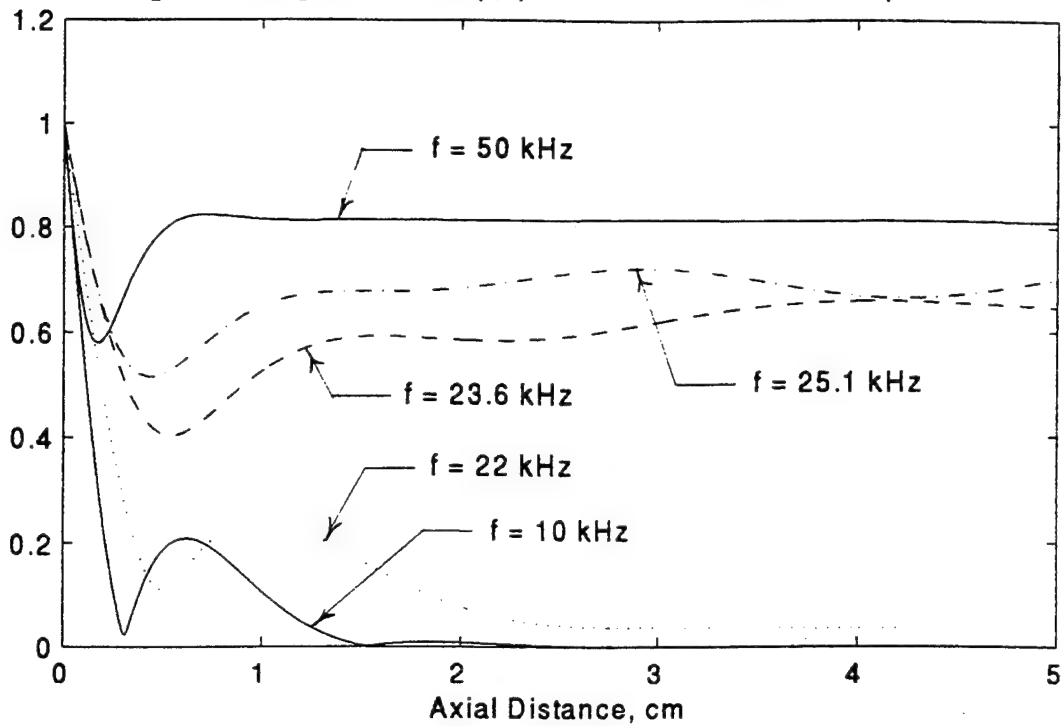
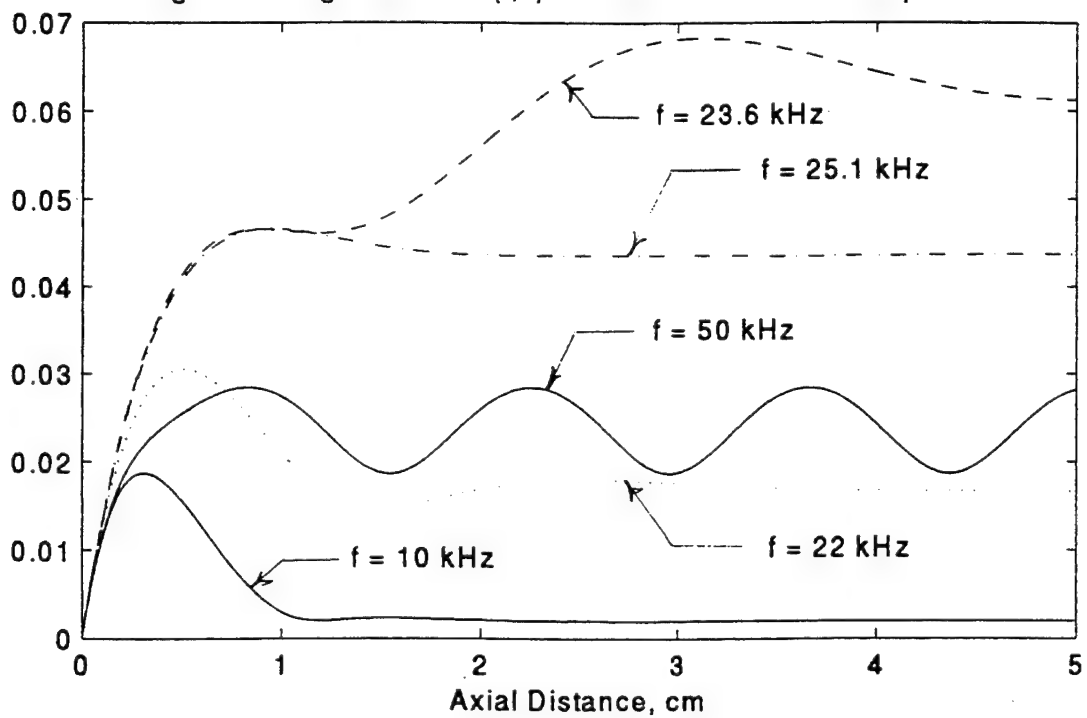
Fig 3-19 Magnitude of $W(f,z)$ vs Distance at Fixed FrequenciesFig 3-20 Magnitude of $U(f,z)$ vs Distance at Fixed Frequencies

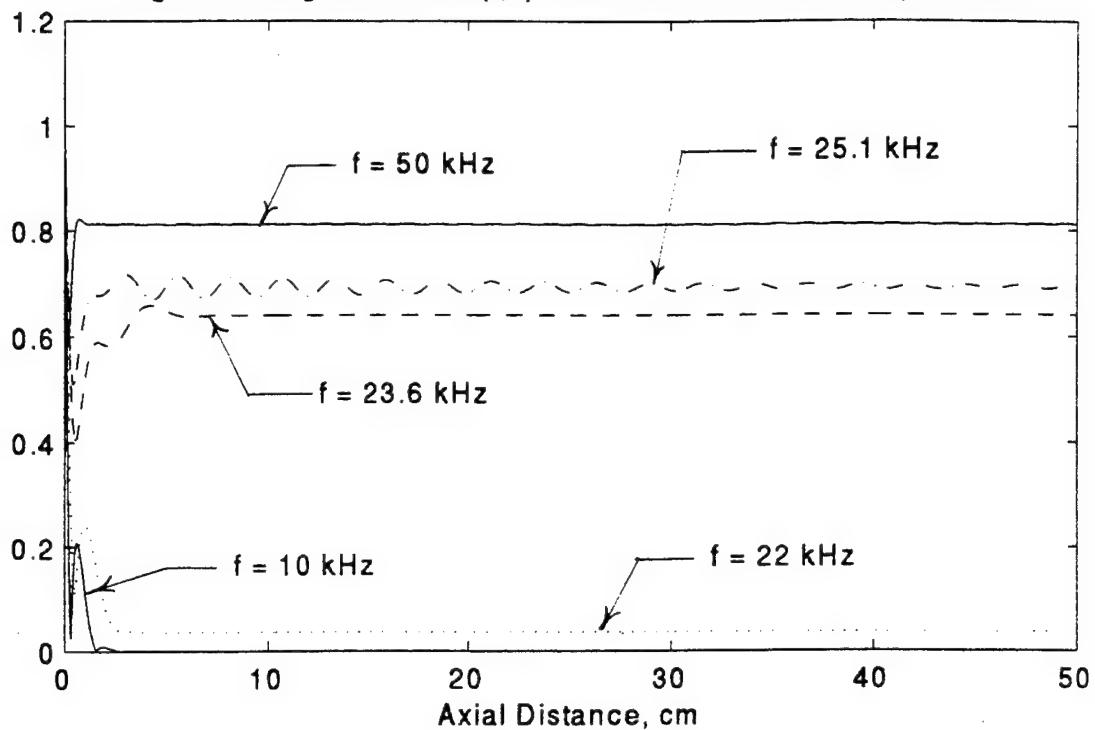
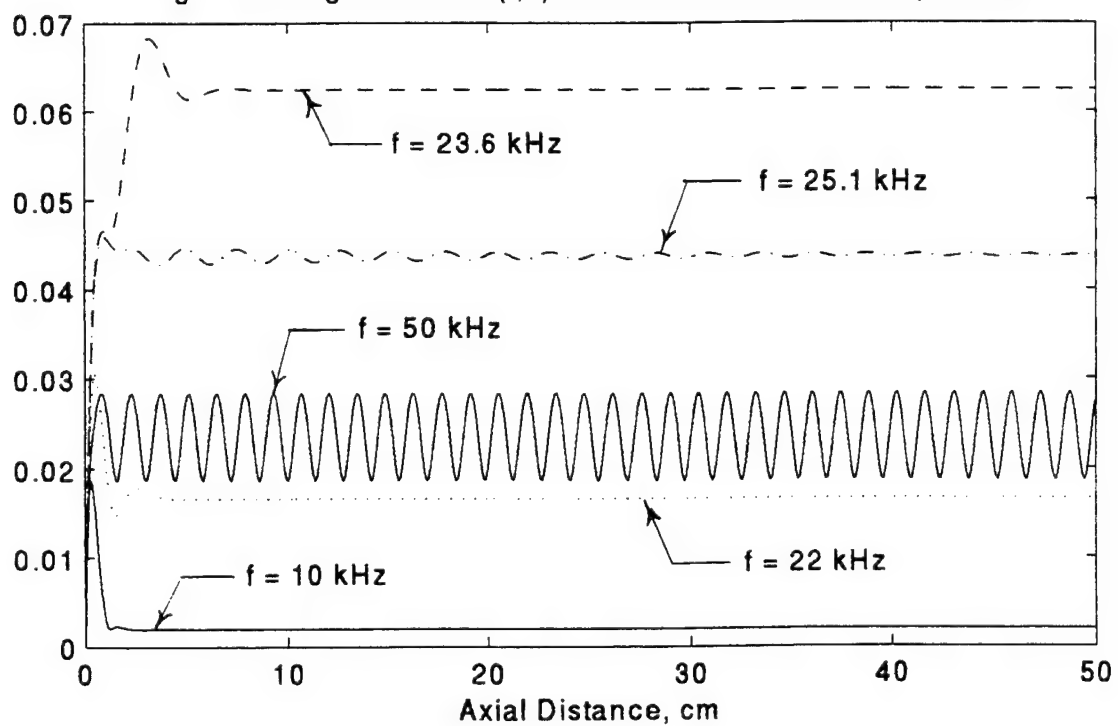
Fig 3-21 Magnitude of $W(f,z)$ vs Distance at Fixed FrequenciesFig 3-22 Magnitude of $U(f,z)$ vs Distance at Fixed Frequencies

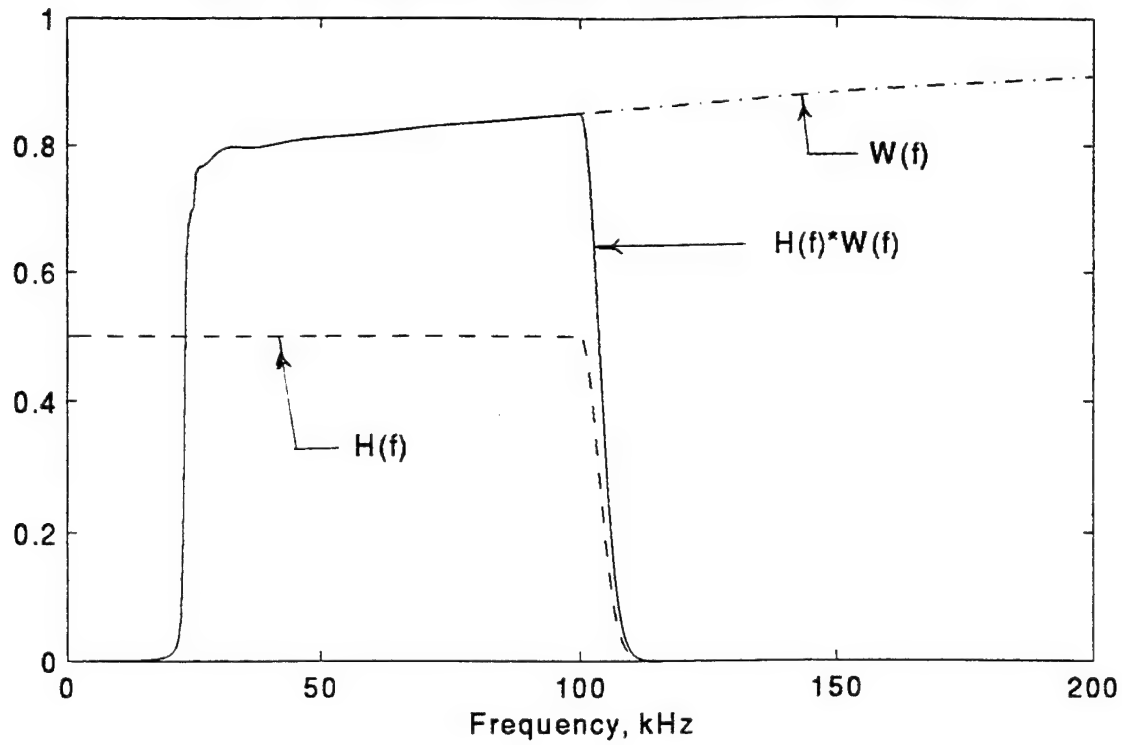
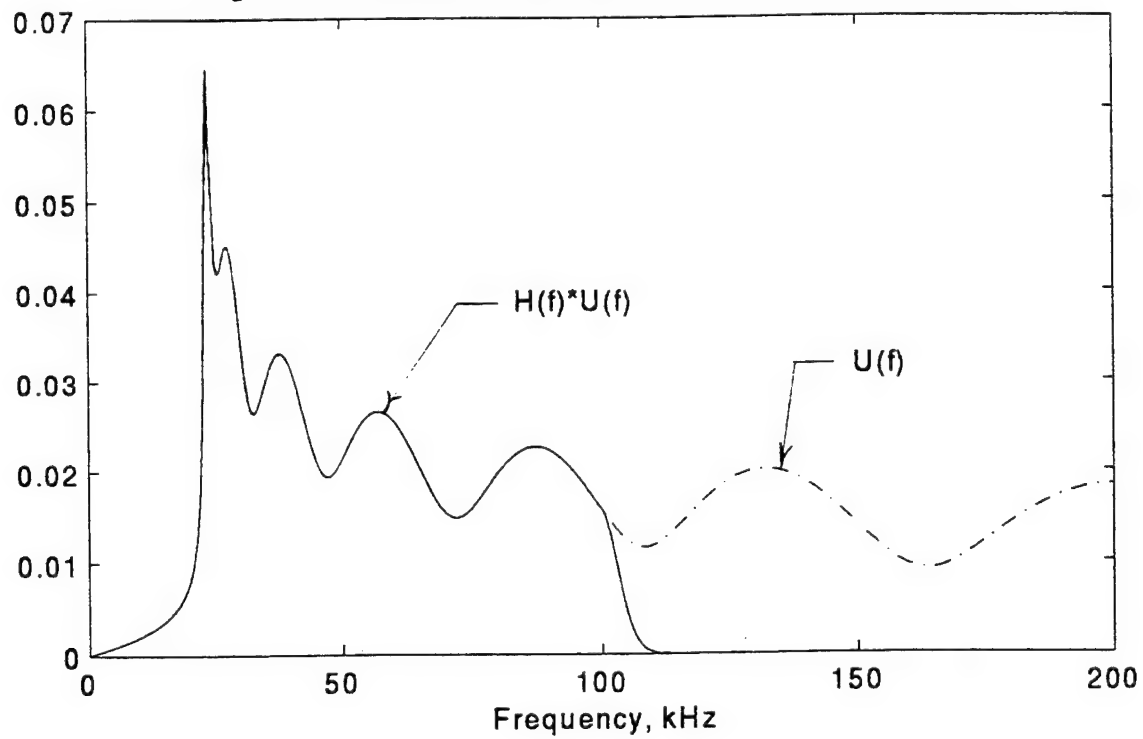
Fig. 3-23 Weighted Transfer Function $W(f)$ at $Z = 6$ cmFig. 3-24 Weighted Transfer Function $U(f)$ at $Z = 6$ cm

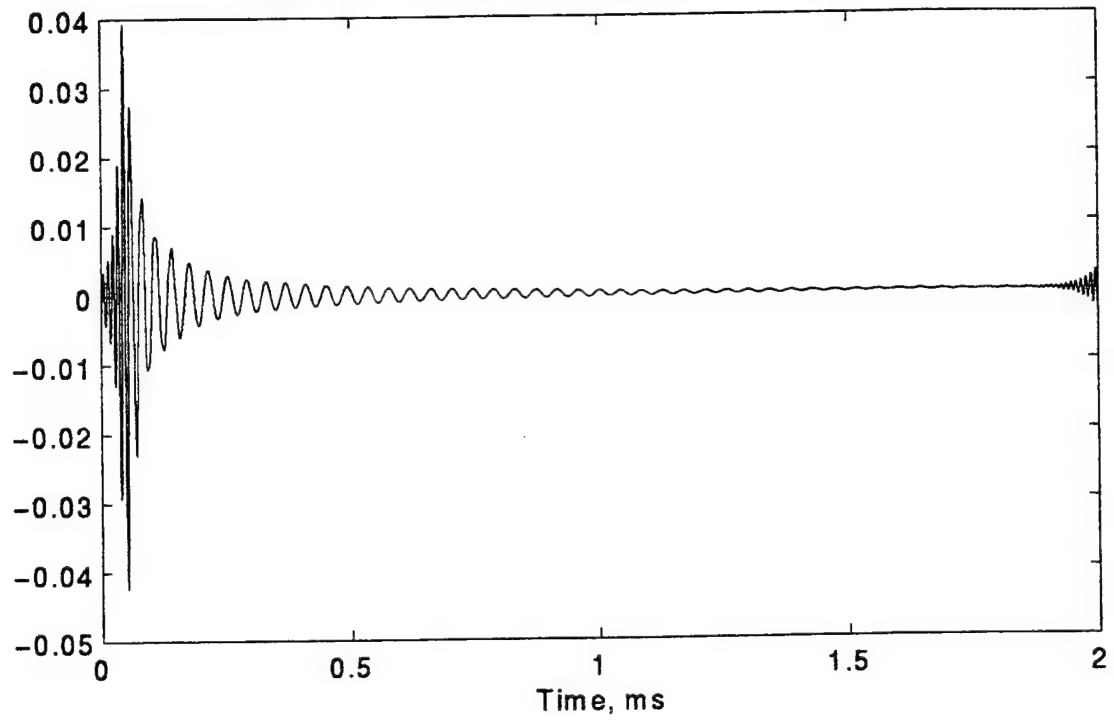
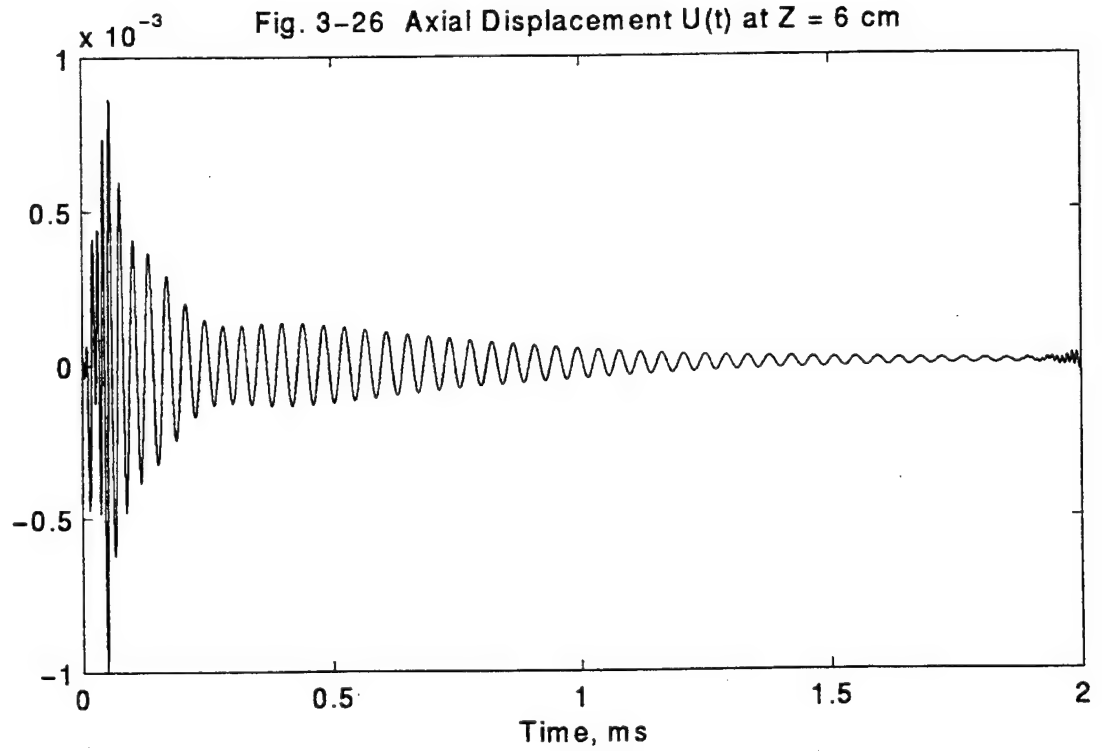
Fig. 3-25 Radial Displacement $W(t)$ at $Z = 6$ cmFig. 3-26 Axial Displacement $U(t)$ at $Z = 6$ cm

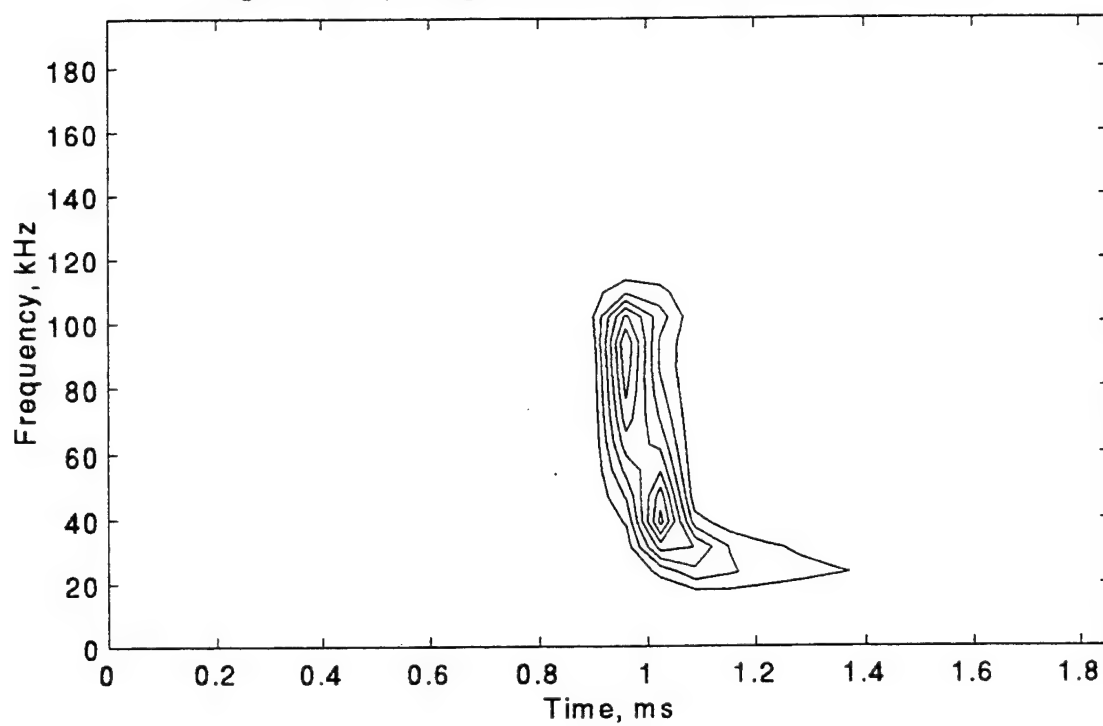
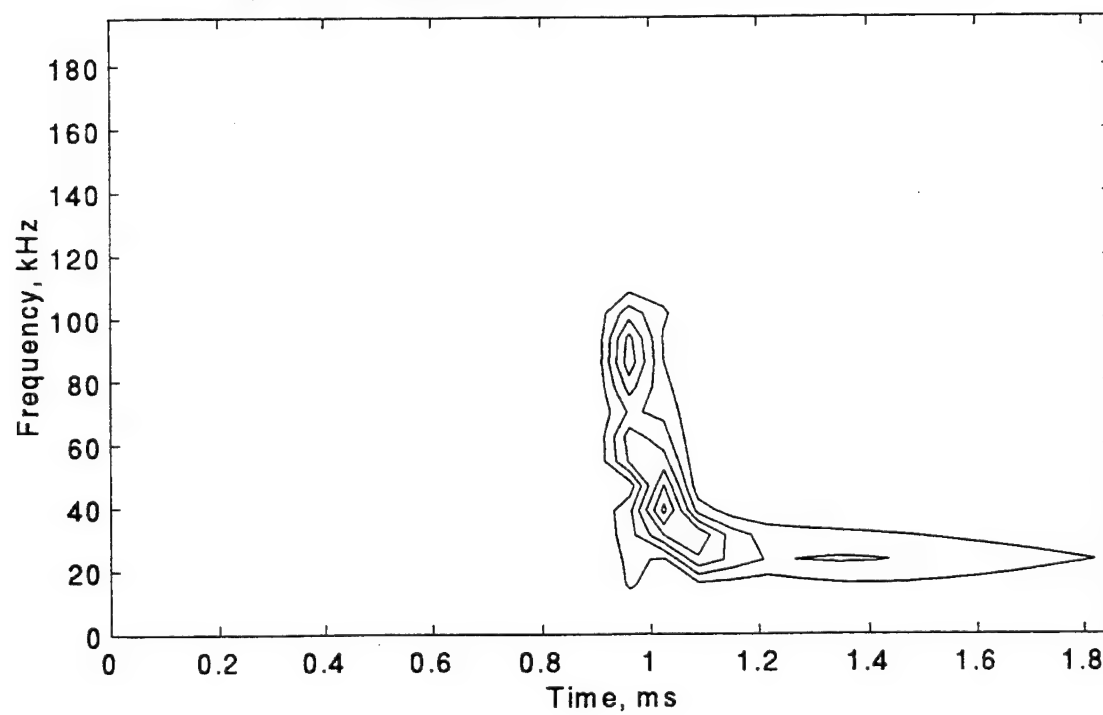
Fig. 3-27 Spectrogram countour plot of $W(t)$ at $Z = 6$ cmFig. 3-28 Spectrogram countour plot of $U(t)$ at $Z = 6$ cm

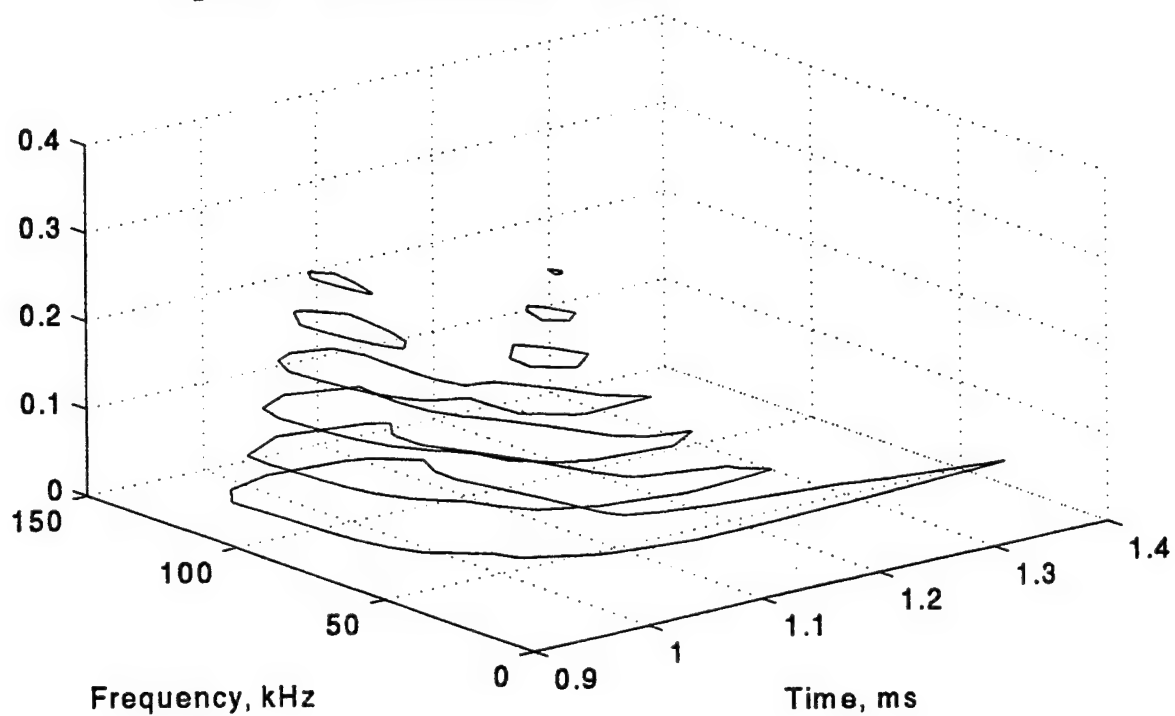
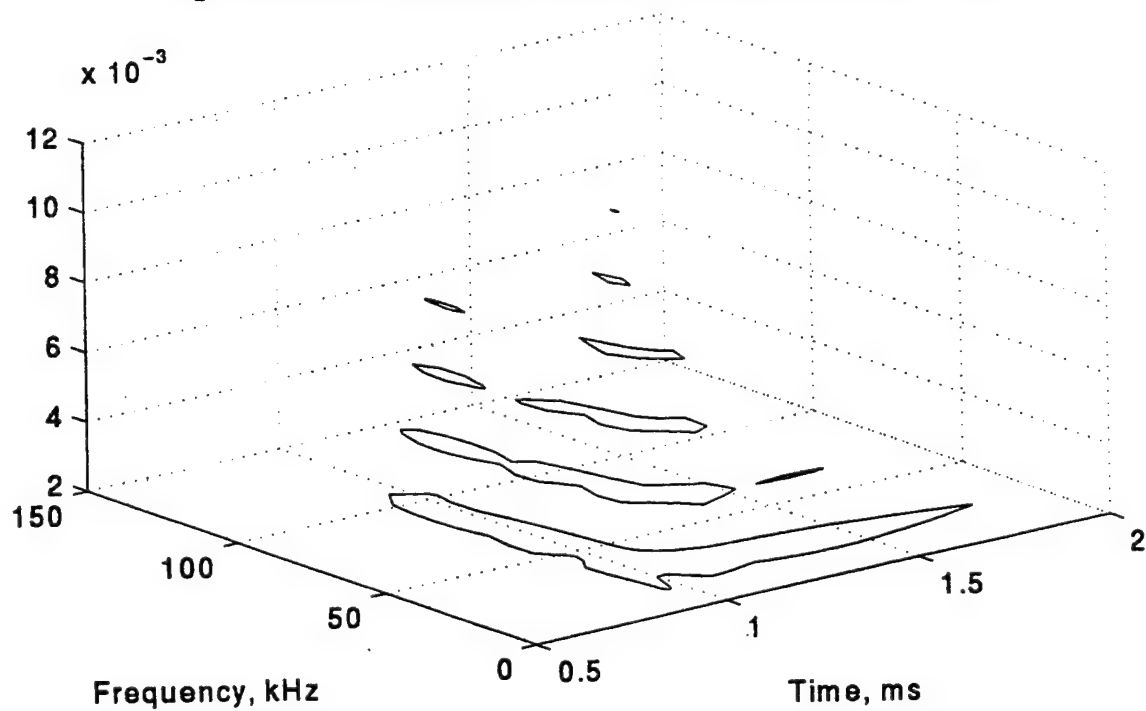
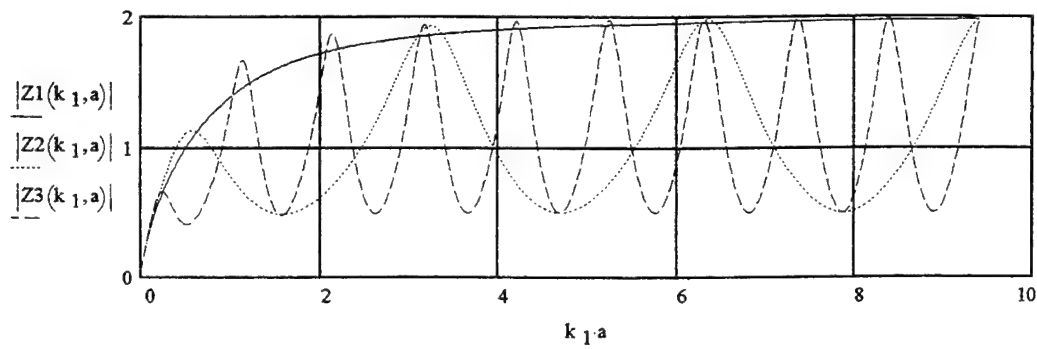
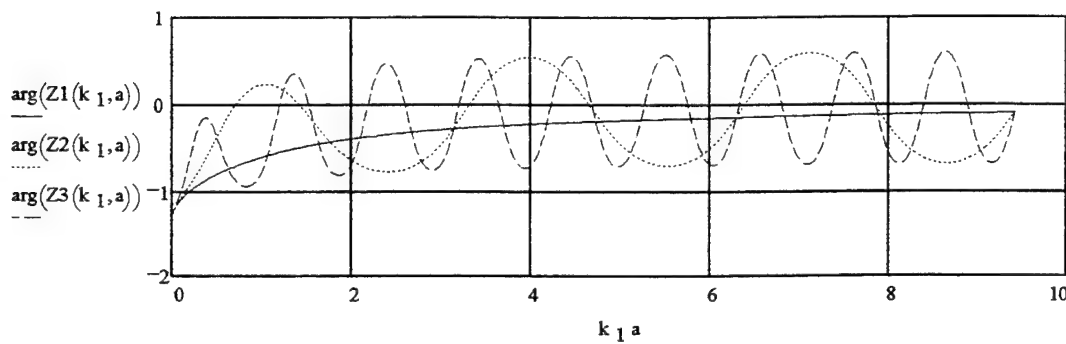
Fig. 3-29 3-D Spectrogram Contour Plot of $W(t)$ at $Z = 6$ cmFig. 3-30 3-D Spectrogram Contour Plot of $U(t)$ at $Z = 6$ cm

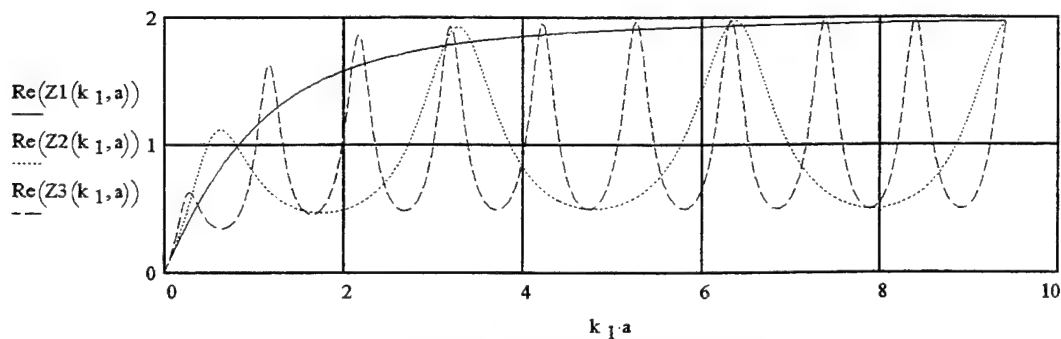
Figure 4-1 Normalized Spectral Impedance of a Fluid Tube in an External Fluid. Impedance vs Wavenumber for radius ratio $s = 1$ (solid curve), 2 (dotted curve) and 4 (dashed curve). Sound Speed Ratio $R_c = 2$; Fluid impedance ratio $R_z = 2$



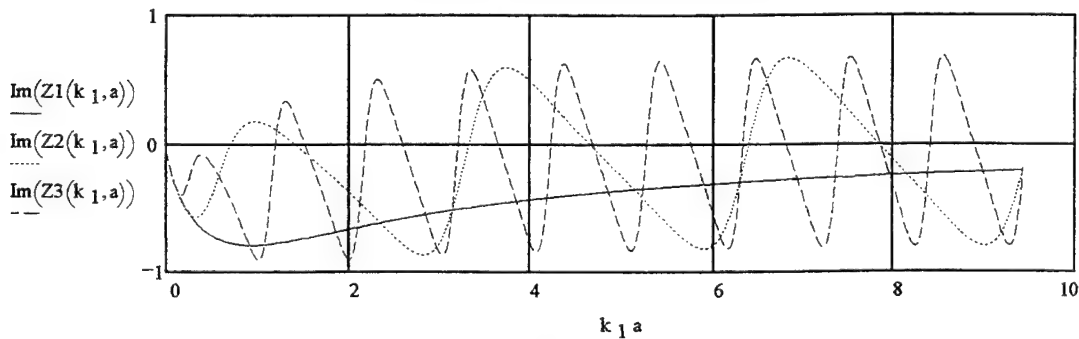
(a) Impedance Magnitude



(b) Impedance Phase Angle (radians)

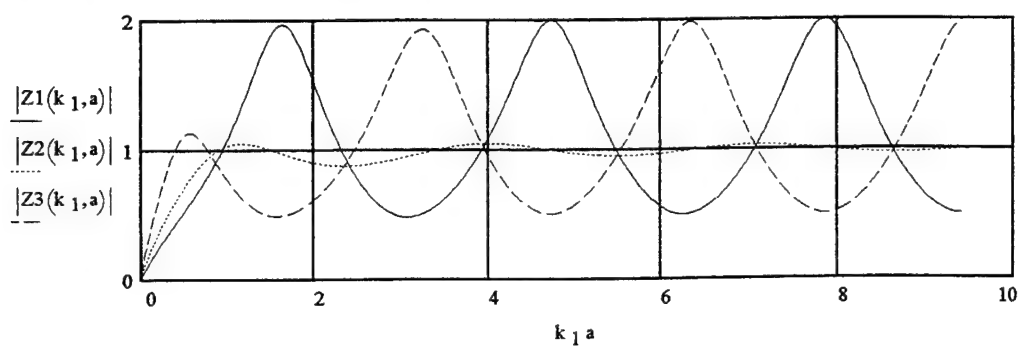


(c) Real Component of Impedance

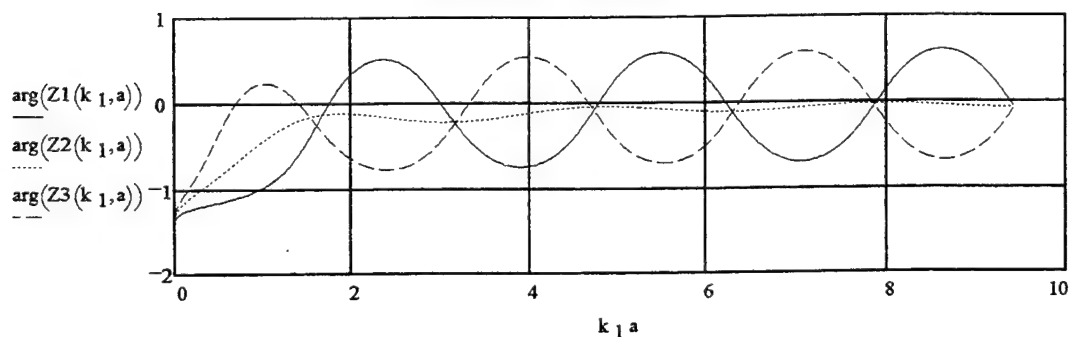


(d) Imaginary Component of Impedance

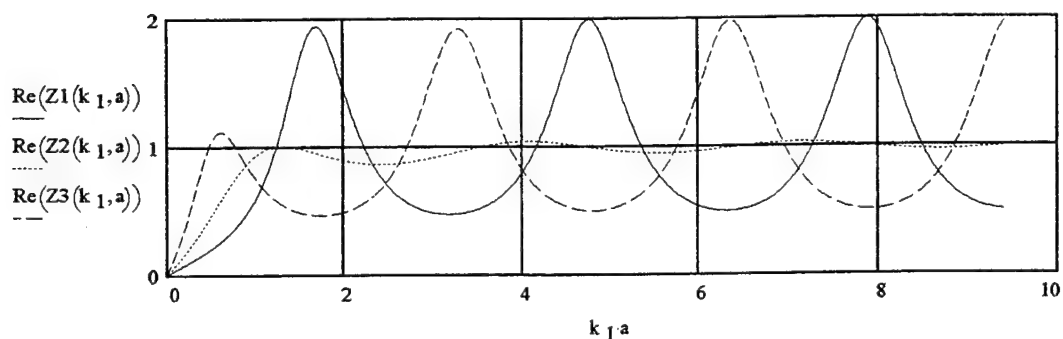
Figure 4-2 Normalized Spectral Impedance of a Fluid Tube in an External Fluid Impedance vs Wavenumber for fluid impedance ratios $R_z = .5$ (solid curve), 1 (dotted curve) and 2 (dashed curve). Sound speed ratio $R_c = 2$; ratio of radii: $s = 2$



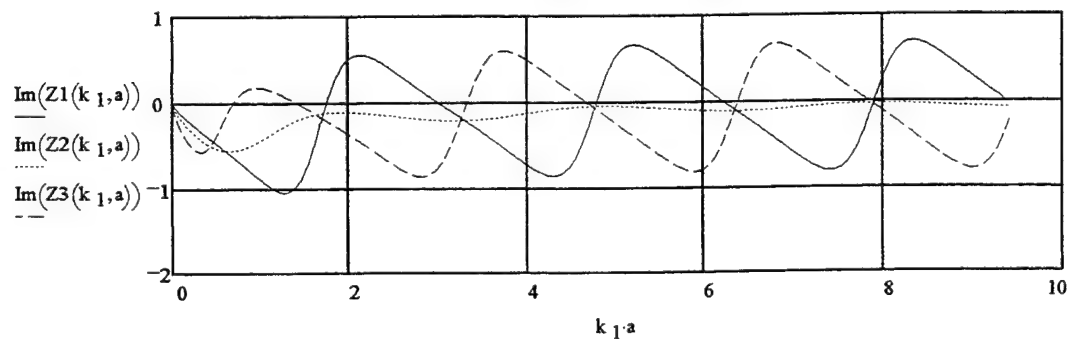
(a) Impedance Magnitude



(b) Impedance Phase Angle (radians)

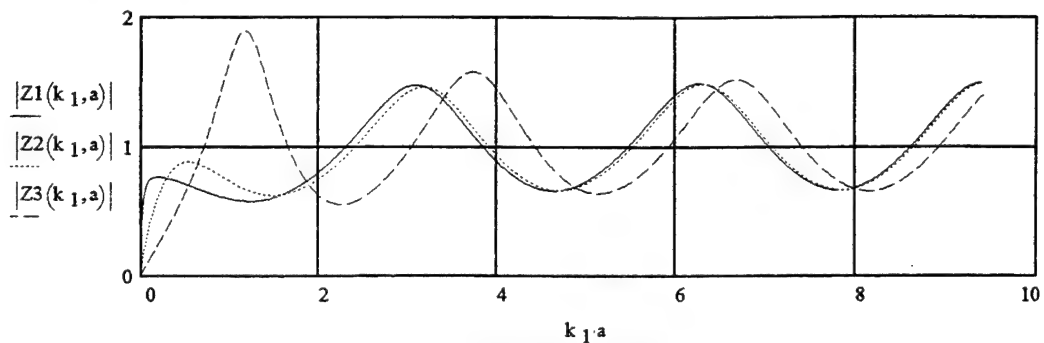


(c) Real Component of Impedance

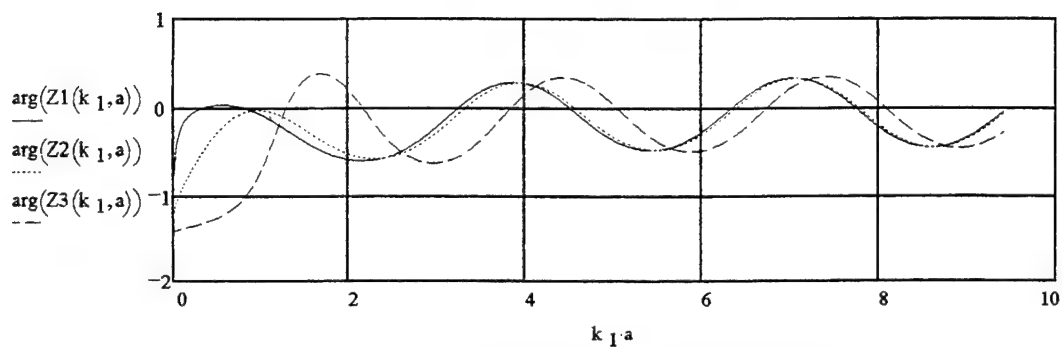


(d) Imaginary Component of Impedance

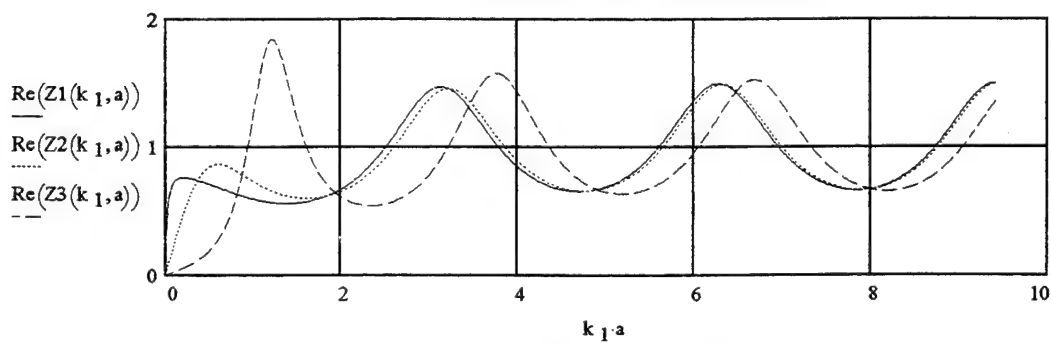
Figure 4-3 Normalized Spectral Impedance of a Fluid Tube in an External Fluid. Impedance vs Wavenumber for sound speed ratios $R_c = 0.1$ (solid curve), 1 (dotted curve) and 10 (dashed curve). Ratio of fluid impedance: $R_z = 1.5$; ratio of radii: $s = 2$.



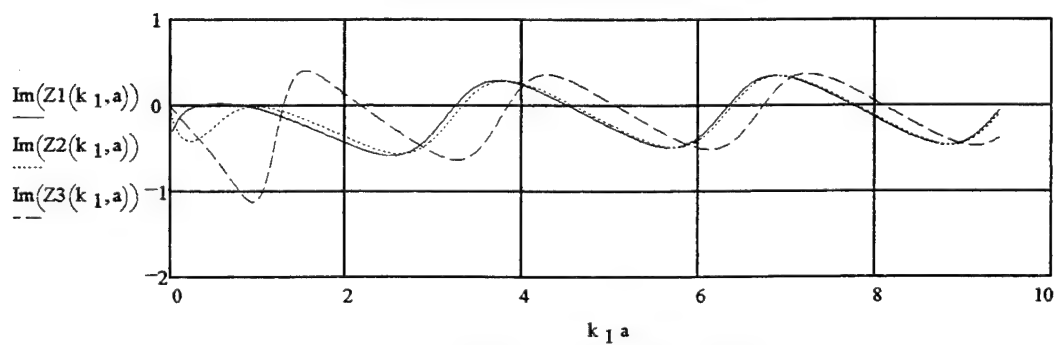
(a) Impedance Magnitude



(b) Impedance Phase Angle (radians)



(c) Real Component of Impedance



(d) Imaginary Component of Impedance

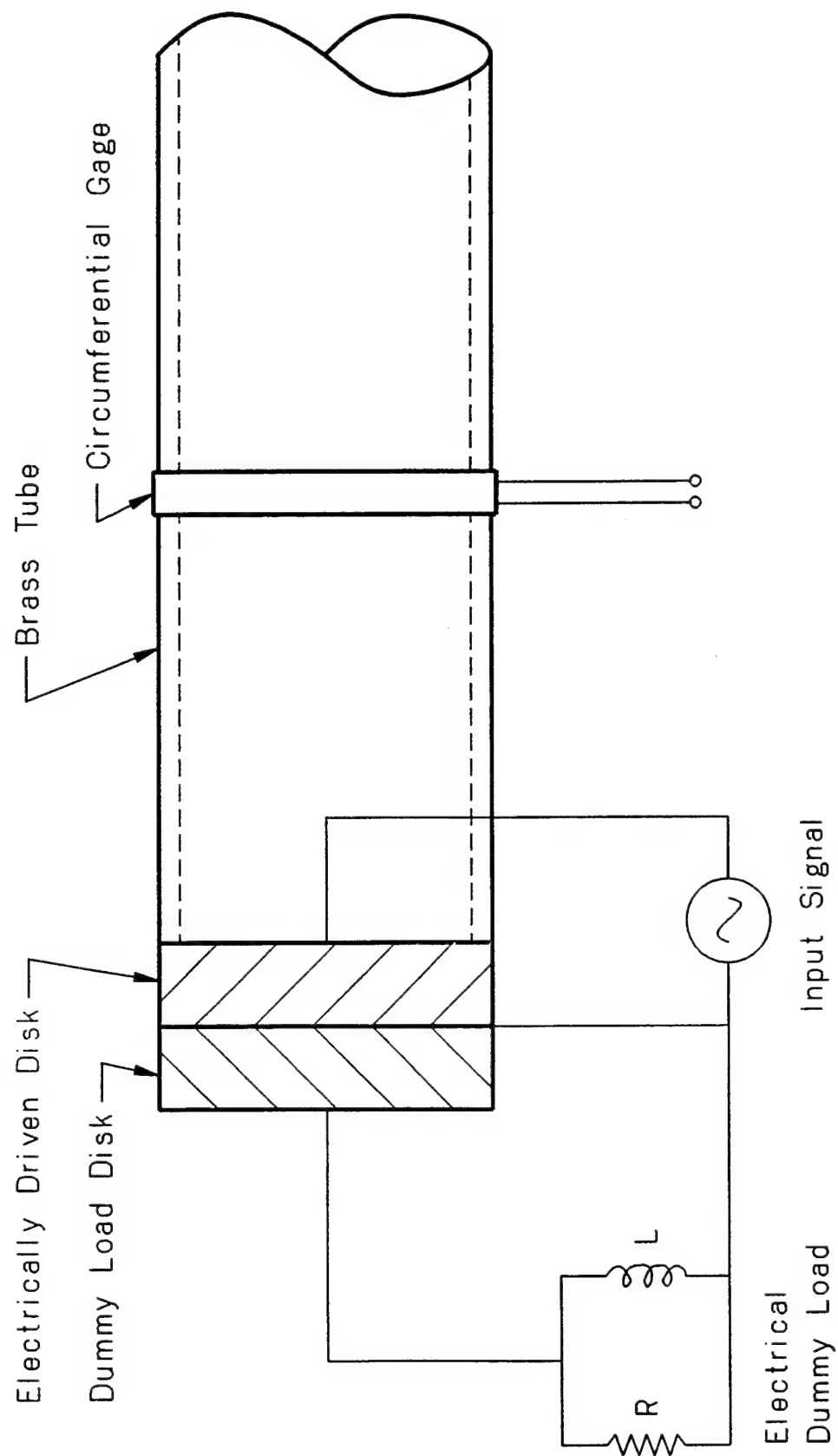


Fig. 5-1 Experimental Apparatus

Fig. 5-2 Admittance of Disk Near First Radial Mode

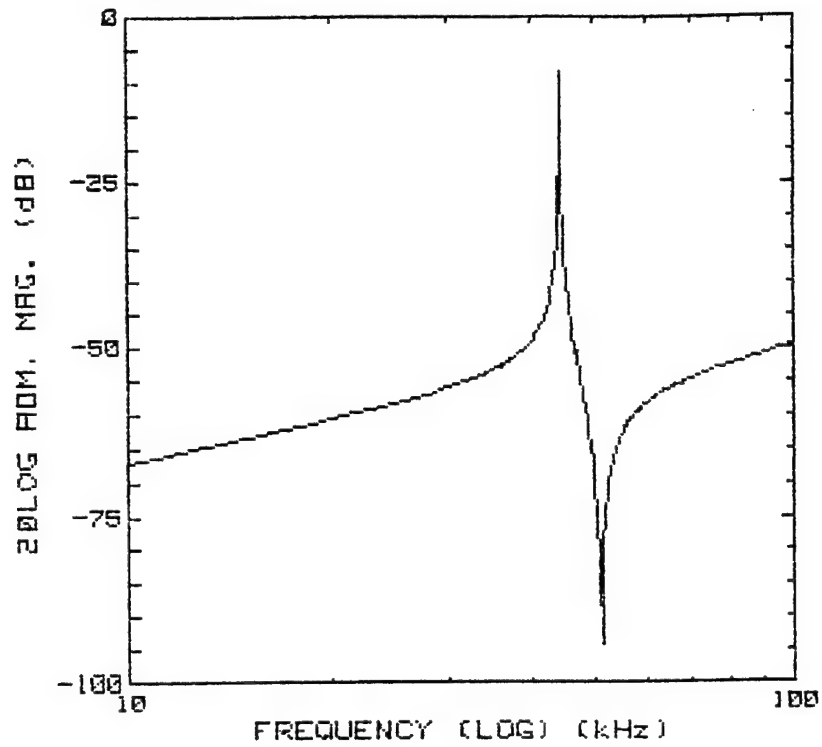


Fig. 5-3 Admittance of Disk vs Frequency

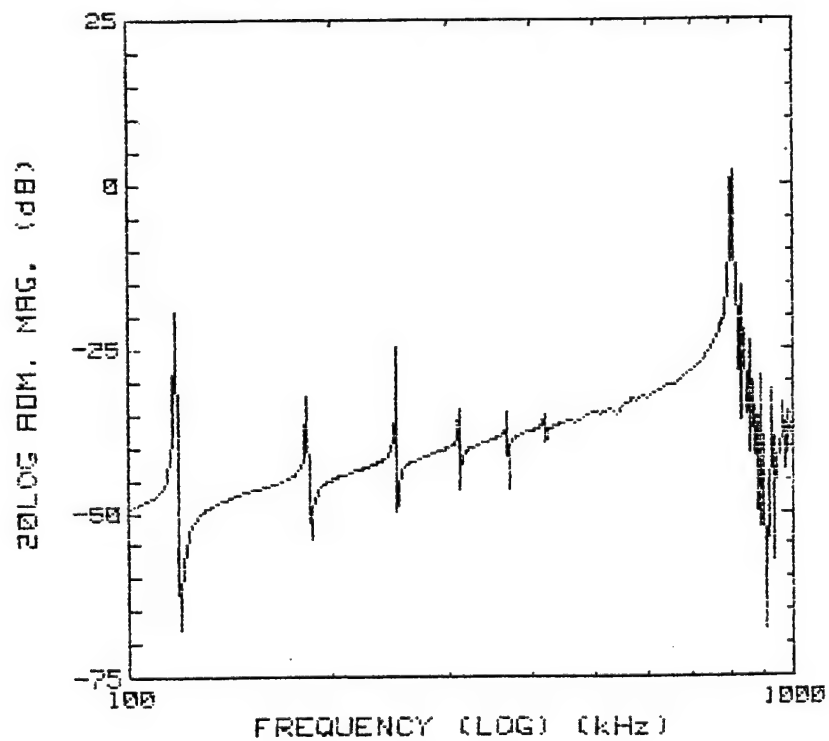


Fig. 5-4 Complex Admittance Locus of PZT Disk

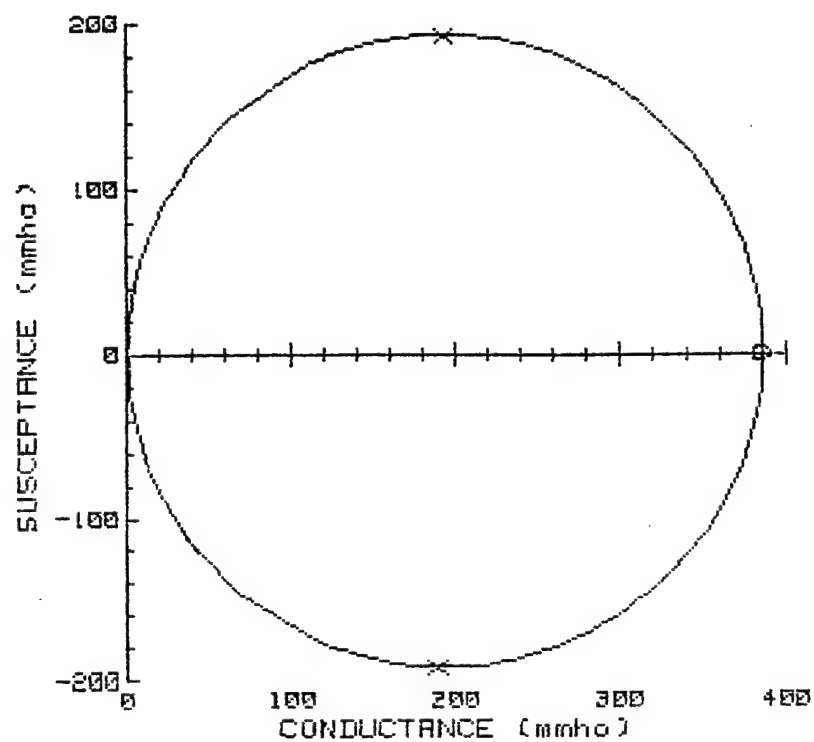
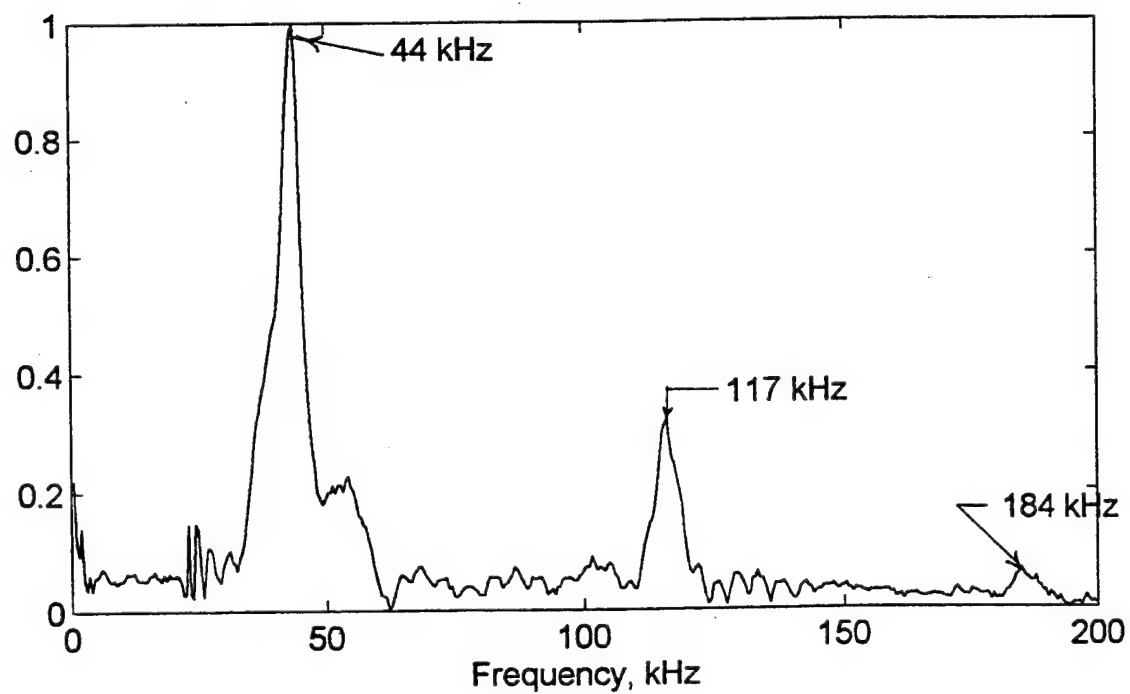


Fig. 5-5 Early Spectrum at Gage C-1



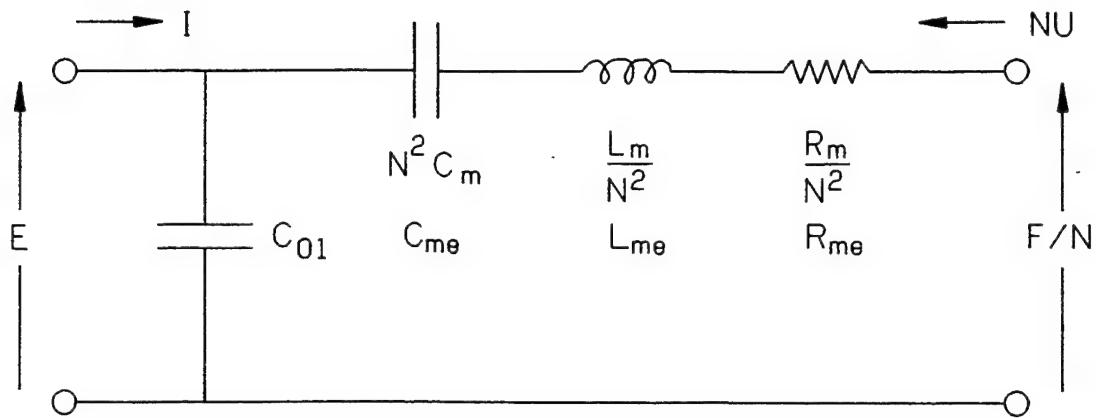


Fig. 5-6(a) Equivalent Electrical Circuit for Piezoelectric Disk

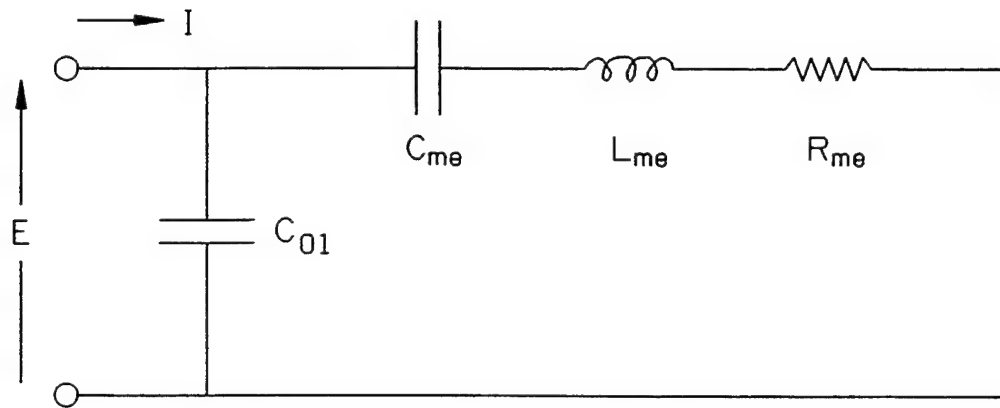


Fig. 5-6(b) Equivalent Circuit for Measurements in Air

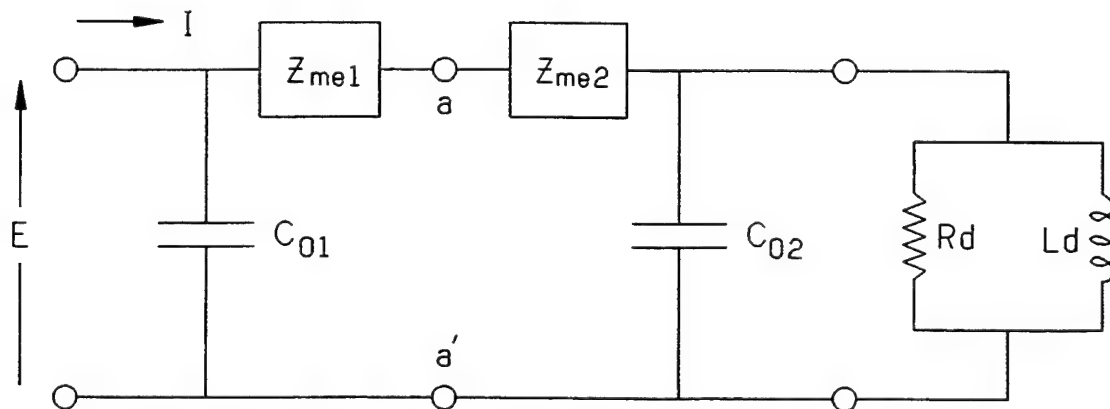
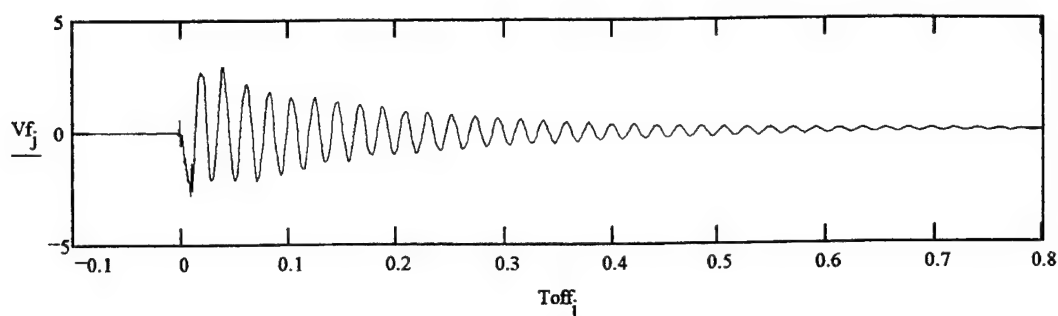
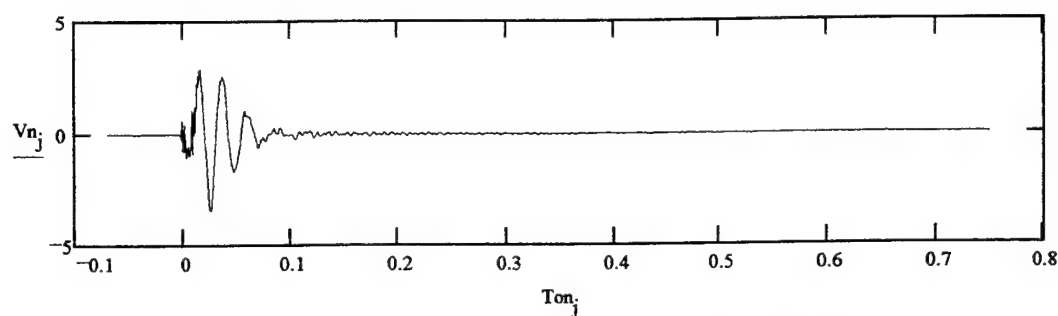


Fig. 5-6(c) Equivalent Circuit for Dummy Load

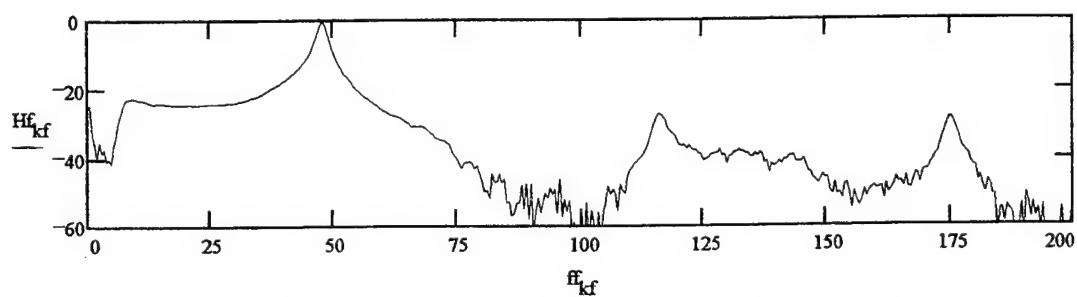
Fig. 5-7 Performance Improvement with Dummy Load



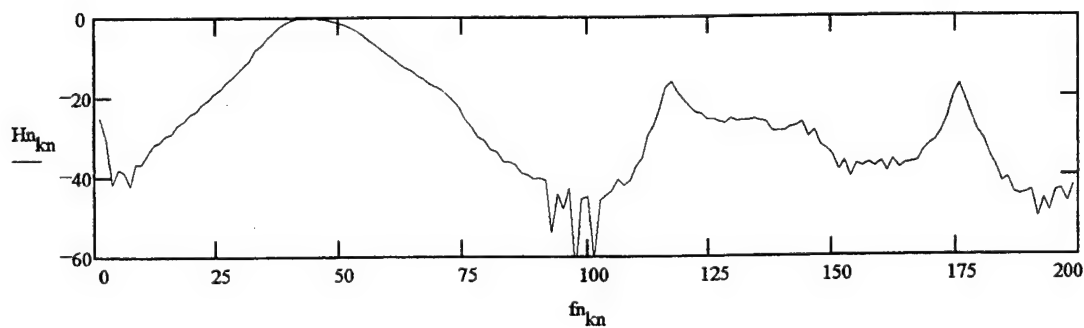
(a) Dummy disk voltage vs time (milliseconds), dummy load "off"



(b) Dummy disk voltage vs time (milliseconds), dummy load "on"



(c) Spectral level of dummy disk voltage (dB) vs frequency (kHz), dummy load "off"



(d) Spectral level of dummy disk voltage (dB) vs frequency (kHz), dummy load "on"

Fig. 5-8 Difference between computed and measured modal frequencies (in kHz) vs mode number for the first eight modes. Solid curve from the membrane model, dashed curve represents a free-free bar. Calculated values based on wave speed of 3939 meters/second.

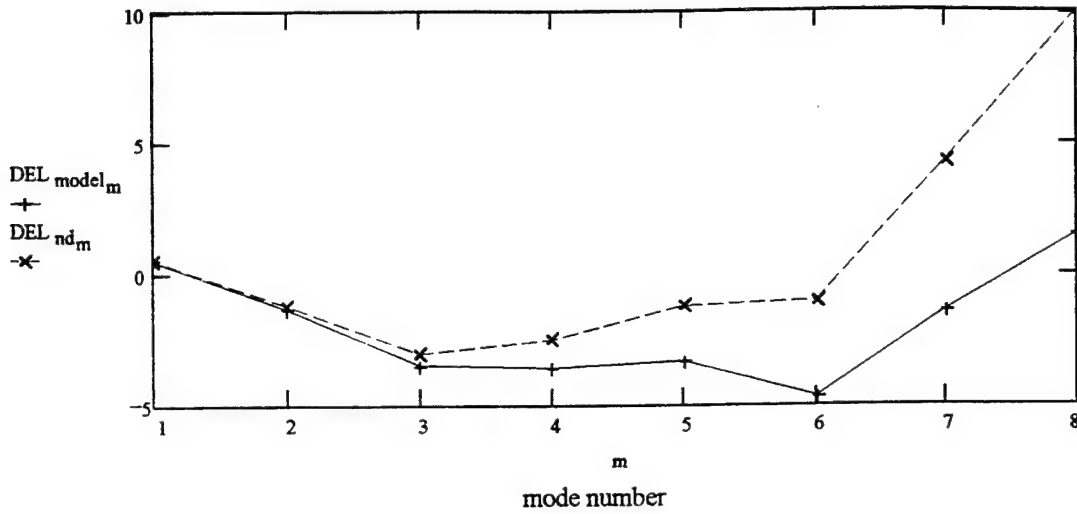


Fig. 5-9 Standard deviation of the difference between measured and computed modal frequencies (in Hz) as a function of assumed wave speed. Solid curve is model, dashed curve is free-free bar.

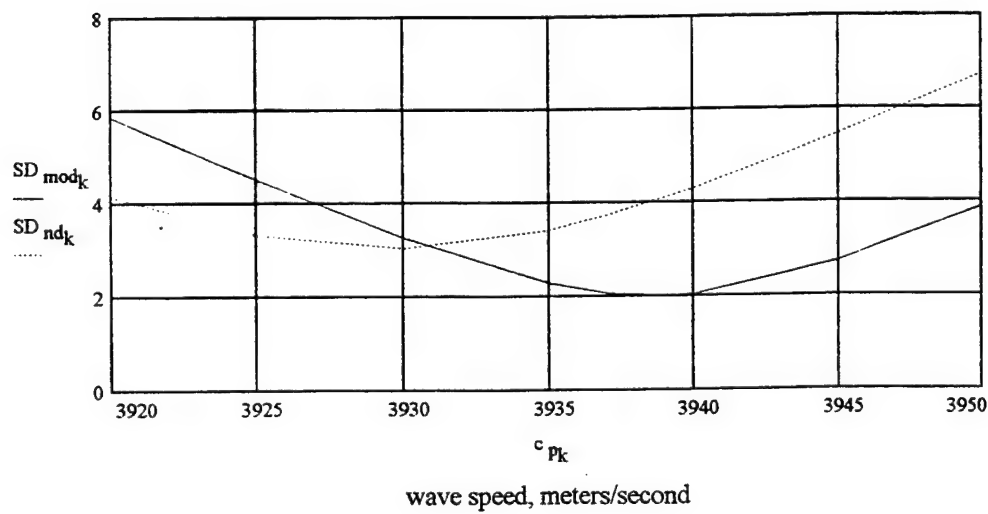


Fig. 5-10 Difference between computed and measured modal frequencies vs mode number expressed as a percentage of the measured frequency. Model results indicated by "x", free-free bar by "+".

Calculated modal frequencies based on extensional wave speed of 3939 meters/second

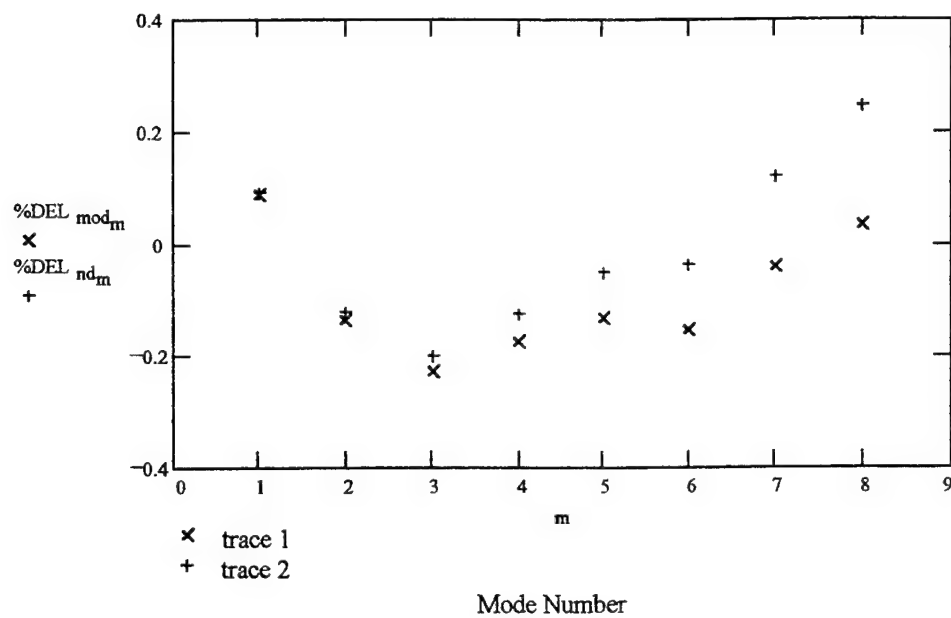
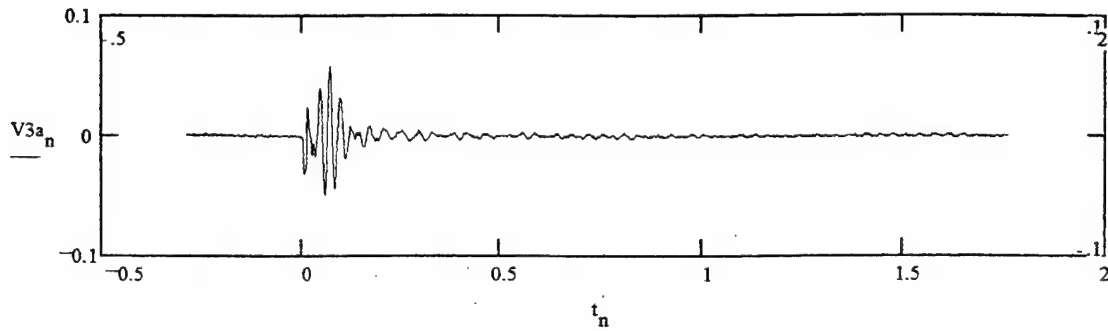
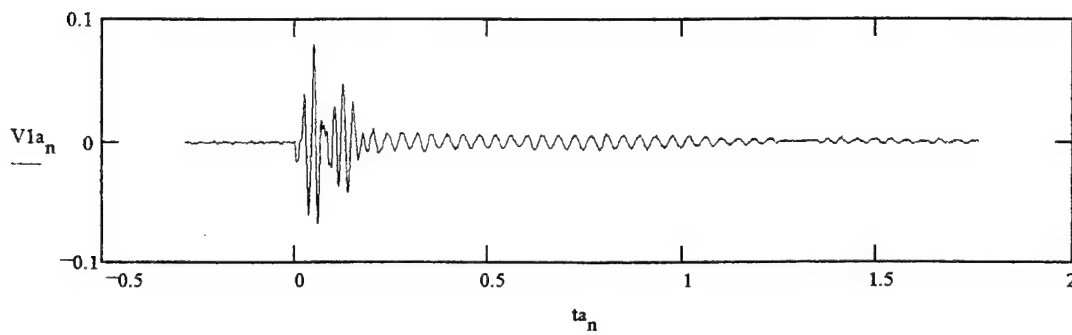


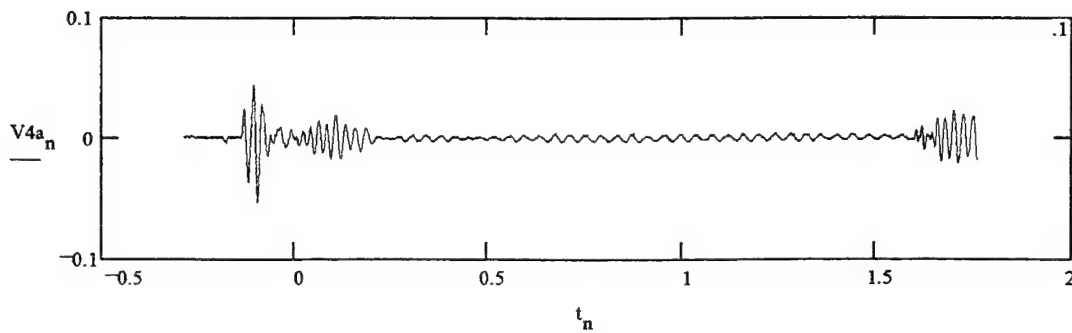
Fig. 5-11 Radial displacements as functions of time at four axial locations. Plots show amplified outputs of circumferential gages (volts) vs time (ms).



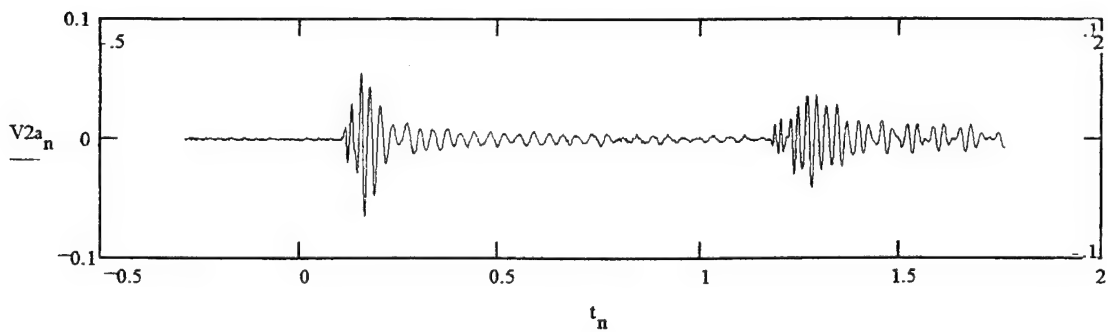
(a) Output at gage C-3, at $Z = 3.3$ cm



(b) Output at gage C-1, at $Z = 7.3$ cm

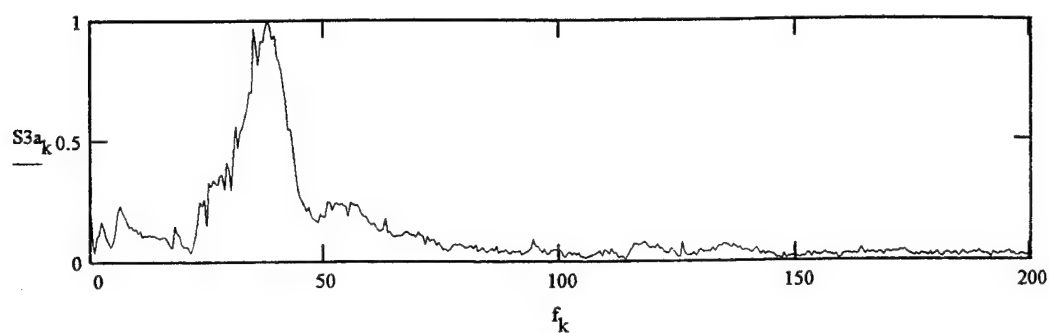


(c) Output at gage C-4, at $Z = 19.6$ cm

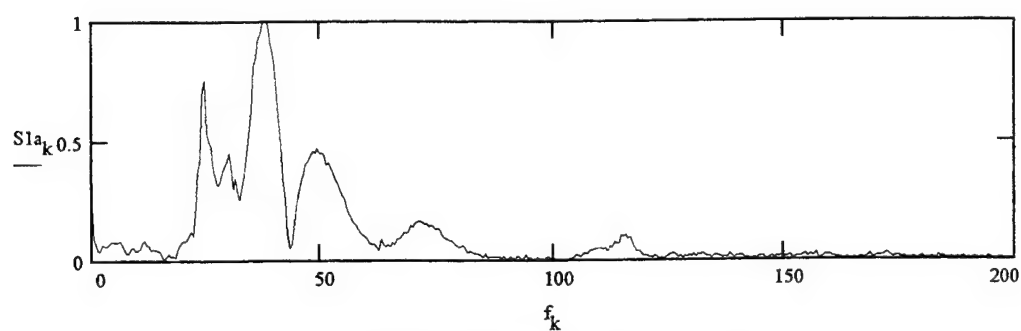


(d) Output at gage C-2, at $Z = 151$ cm

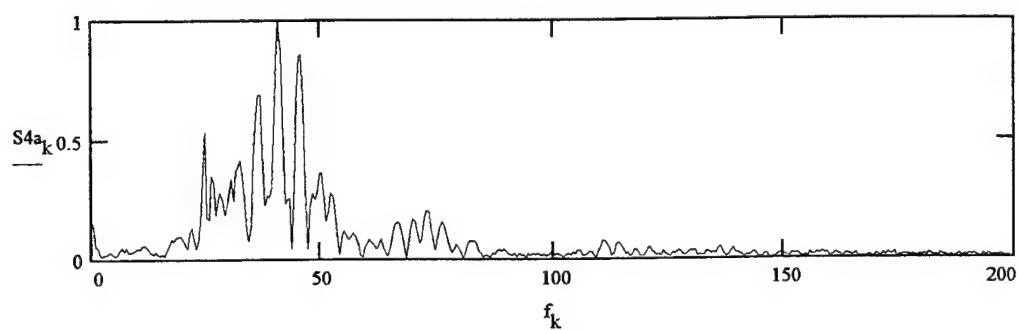
Fig. 5-12 Spectra of radial displacements at four distances. Frequencies in kilohertz



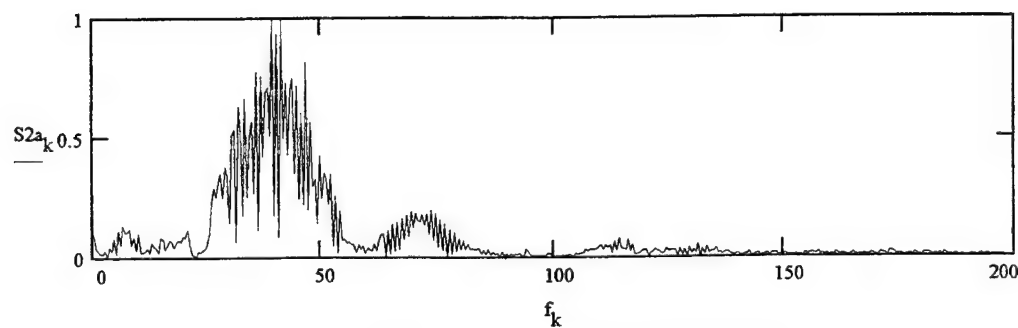
(a) Spectrum at gage C-3, at $Z = 3.3$ cm



(b) Spectrum at gage C-1, at $Z = 7.3$ cm



(c) Spectrum at gage C-4, at $Z = 19.6$ cm



(d) Spectrum at gage C-2, at $Z = 151$ cm

Fig. 5-13 Spectrogram contour plot of waveform at gage C-3

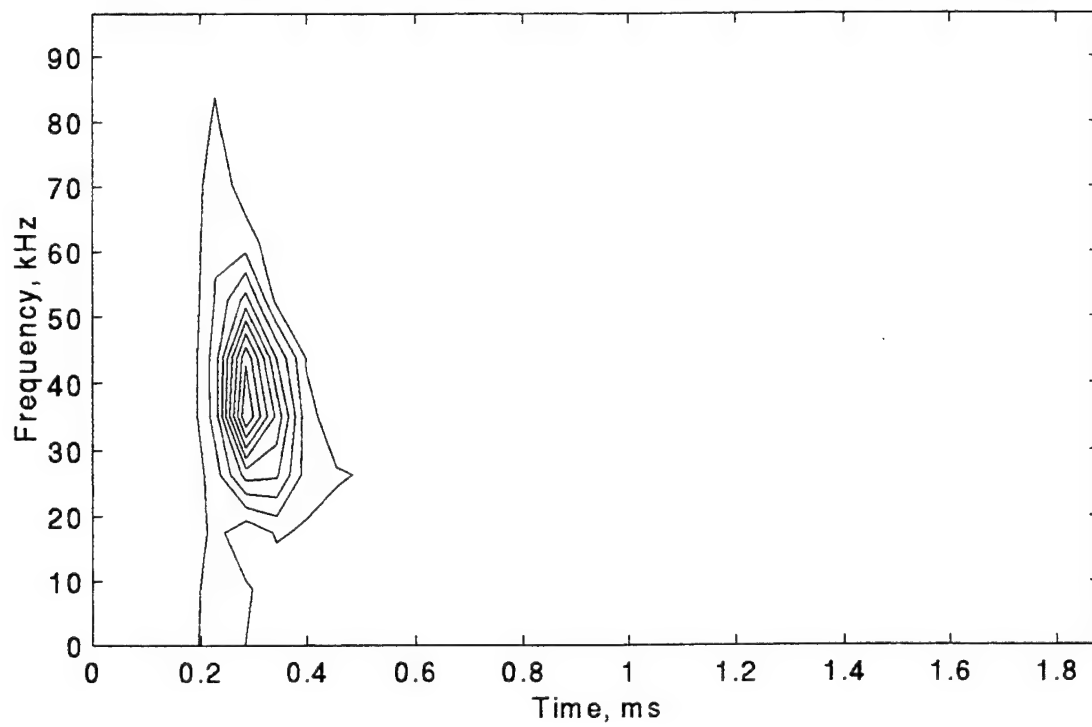


Fig. 5-14 Spectrogram contour plot of waveform at gage C-1

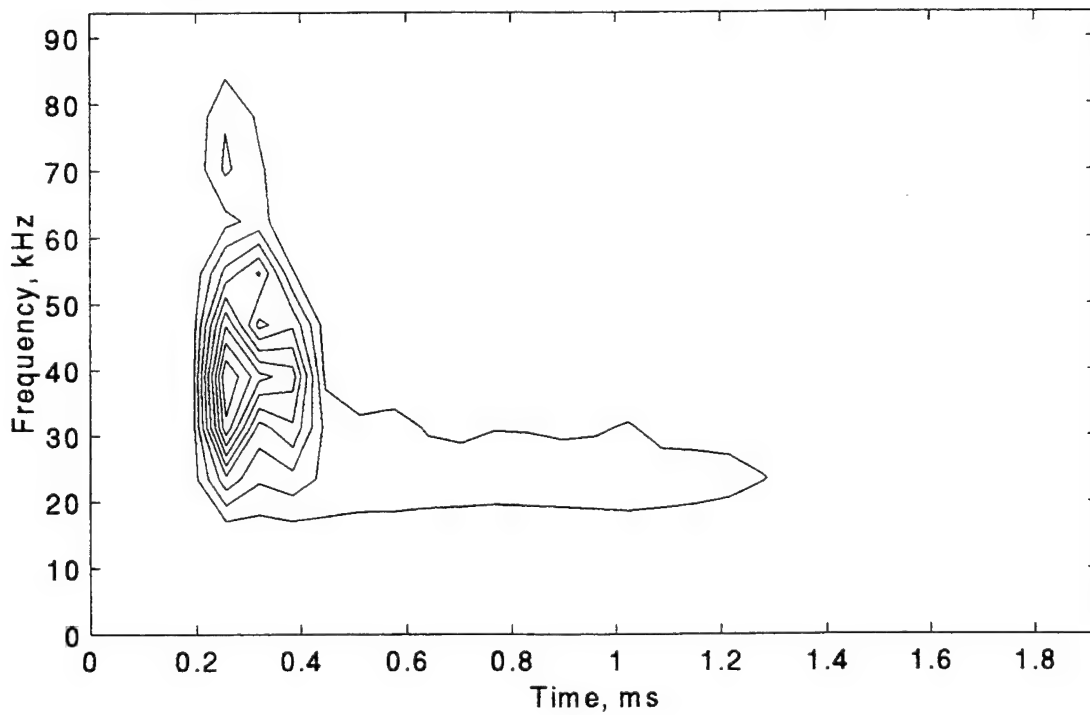


Fig. 5-15 Spectrogram contour plot of waveform at gage C-4

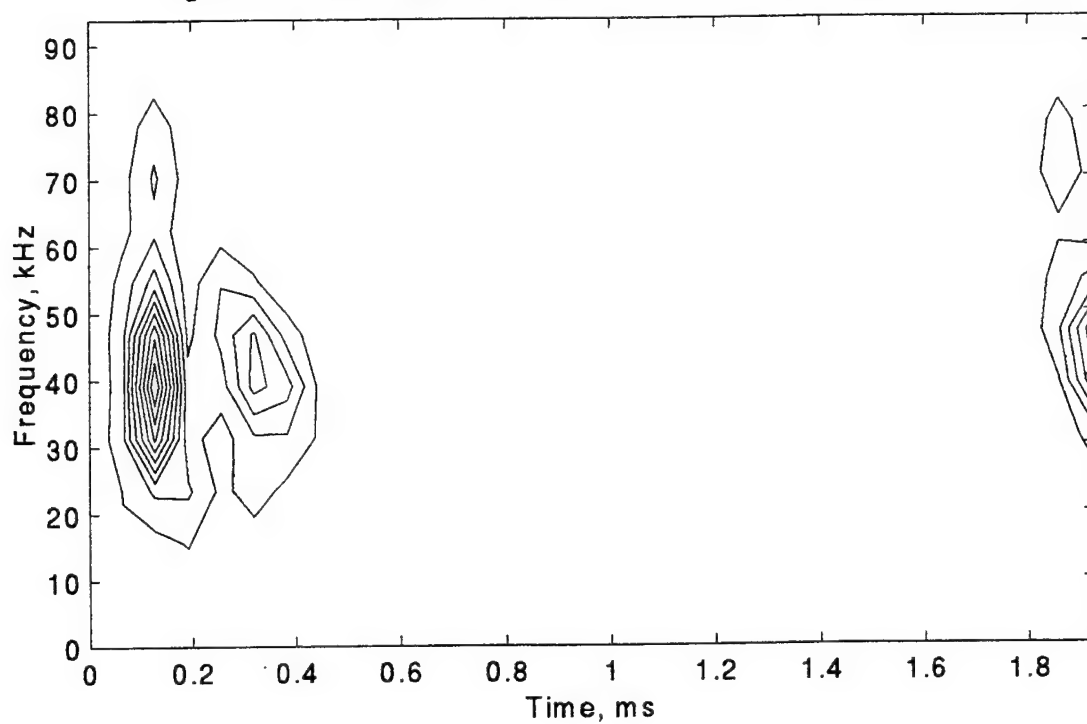


Fig. 5-16 Spectrogram contour plot of waveform at gage C-2

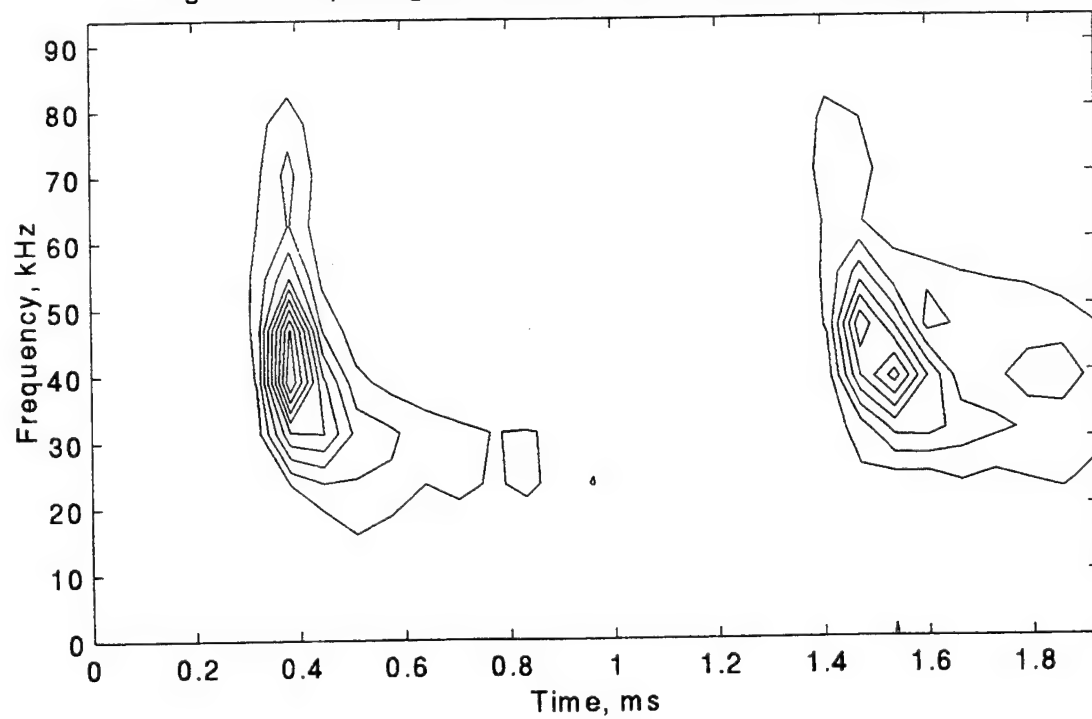


Fig. 5-17 3 D Contour plot of spectrogram of waveform at gage C-3

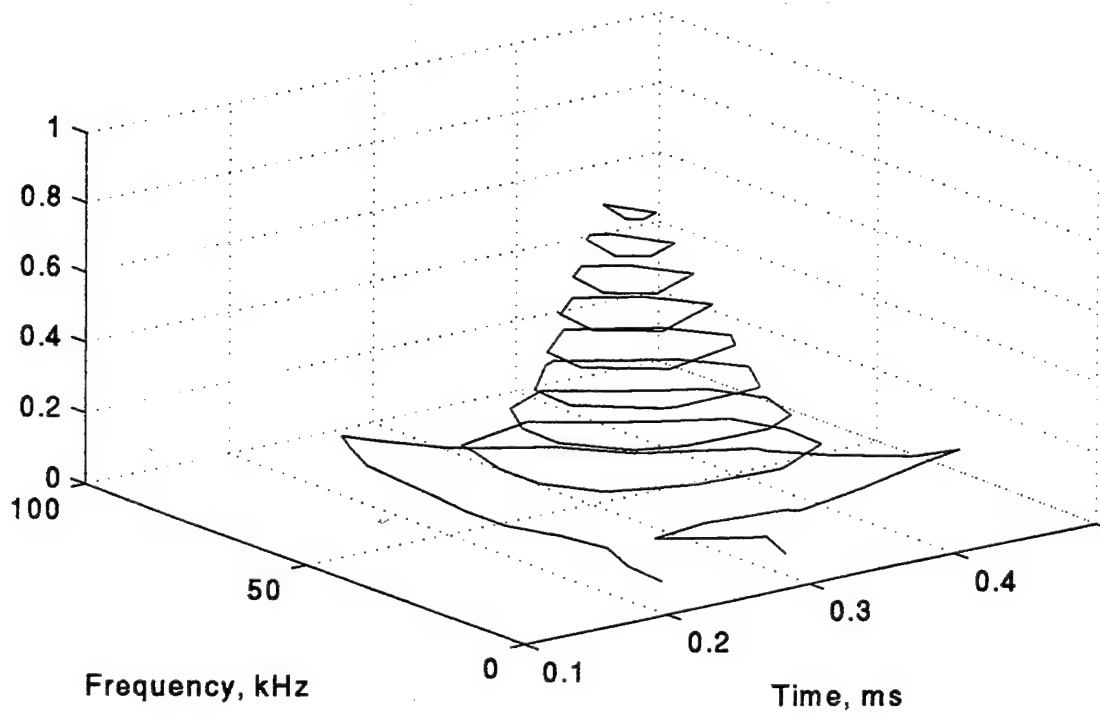


Fig. 5-18 3 D Contour plot of spectrogram of waveform at gage C-1

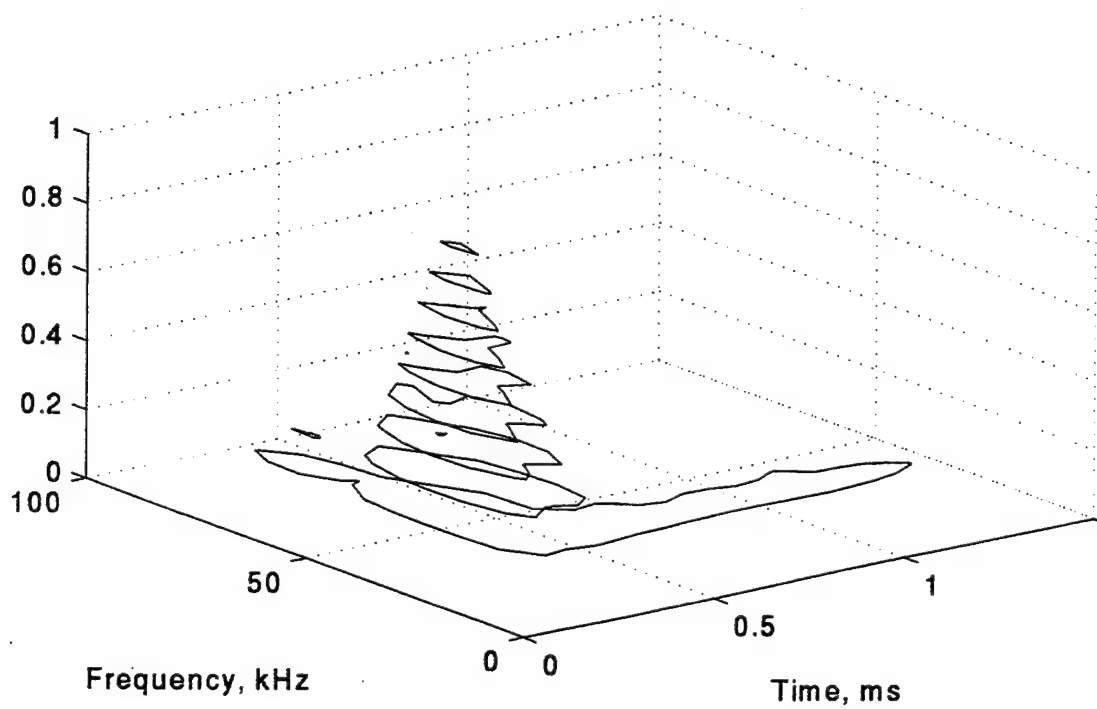


Fig. 5-19 3 D Contour plot of spectrogram of waveform at gage C-4

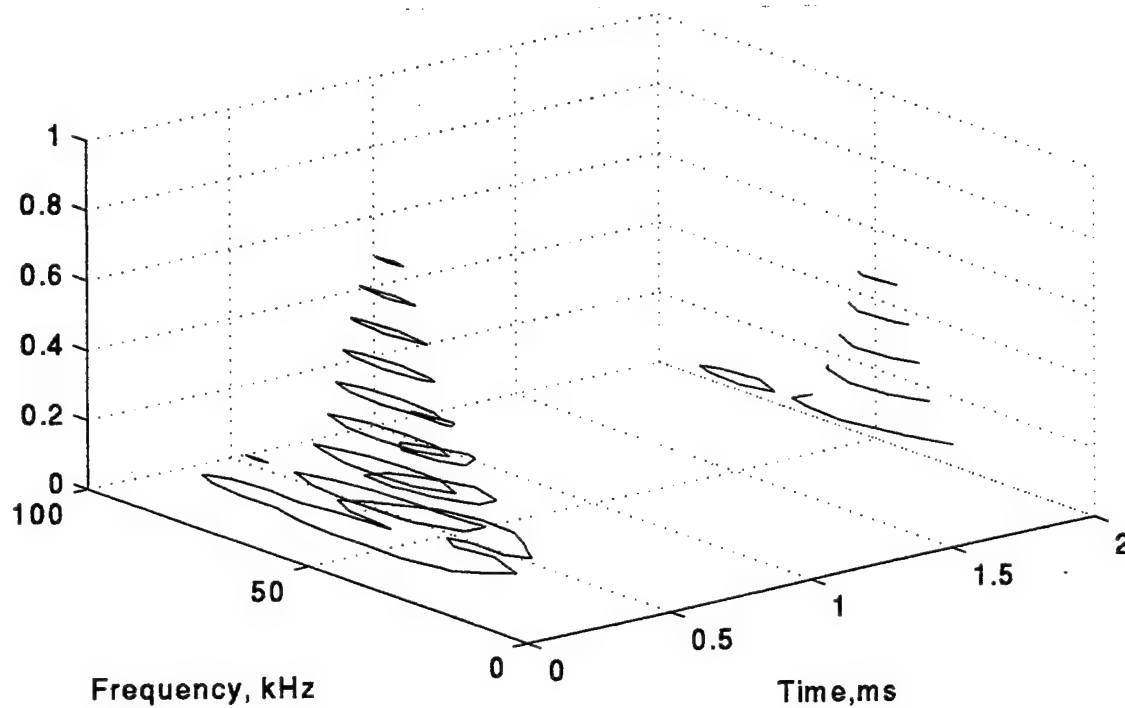


Fig. 5-20 3 D Contour plot of spectrogram of waveform at gage C-2

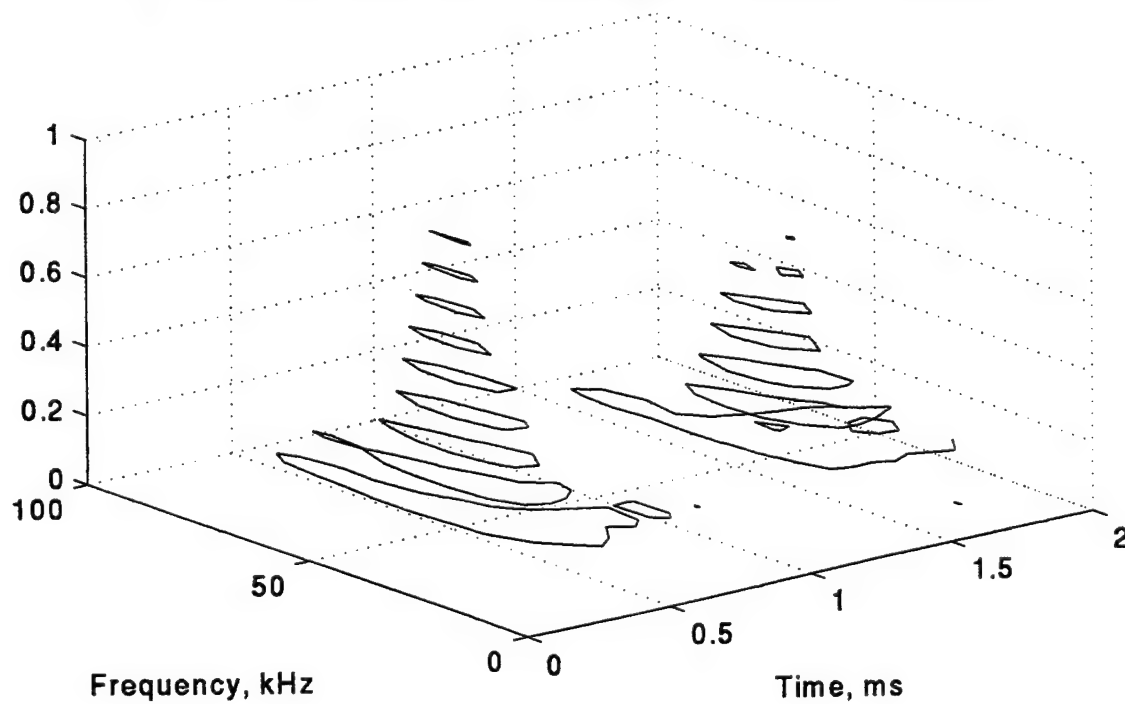


Fig. 5-21 Computed waveform at gage C-1

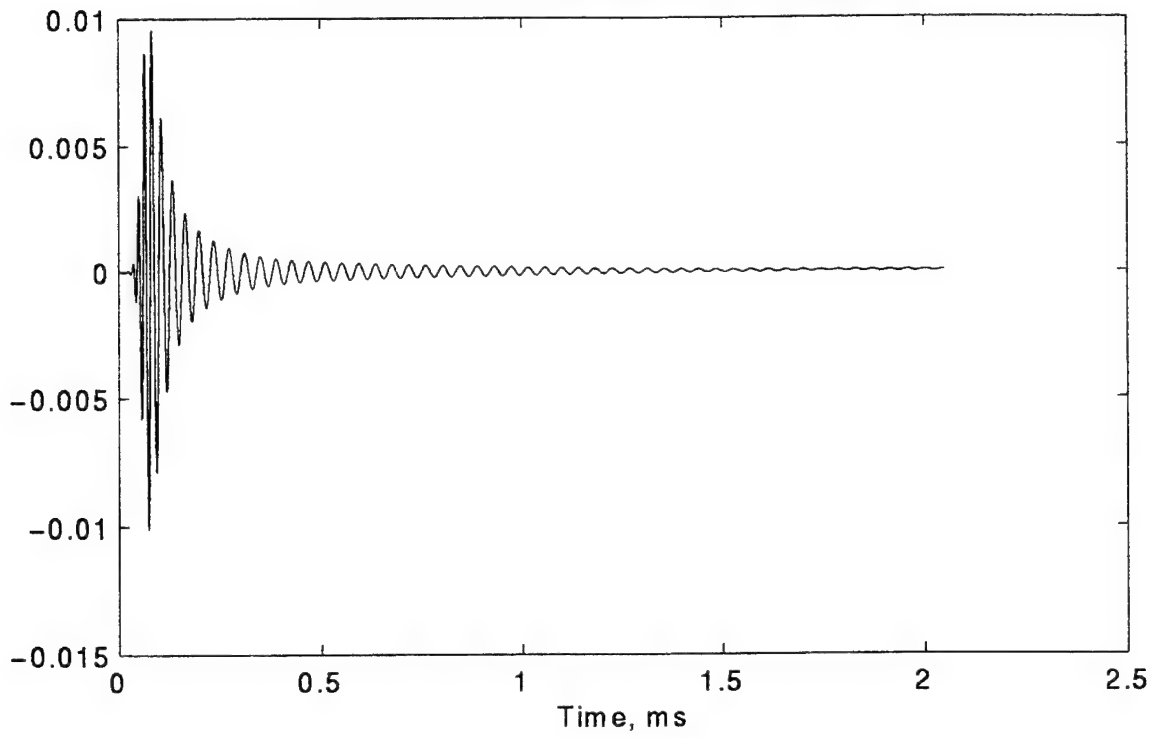
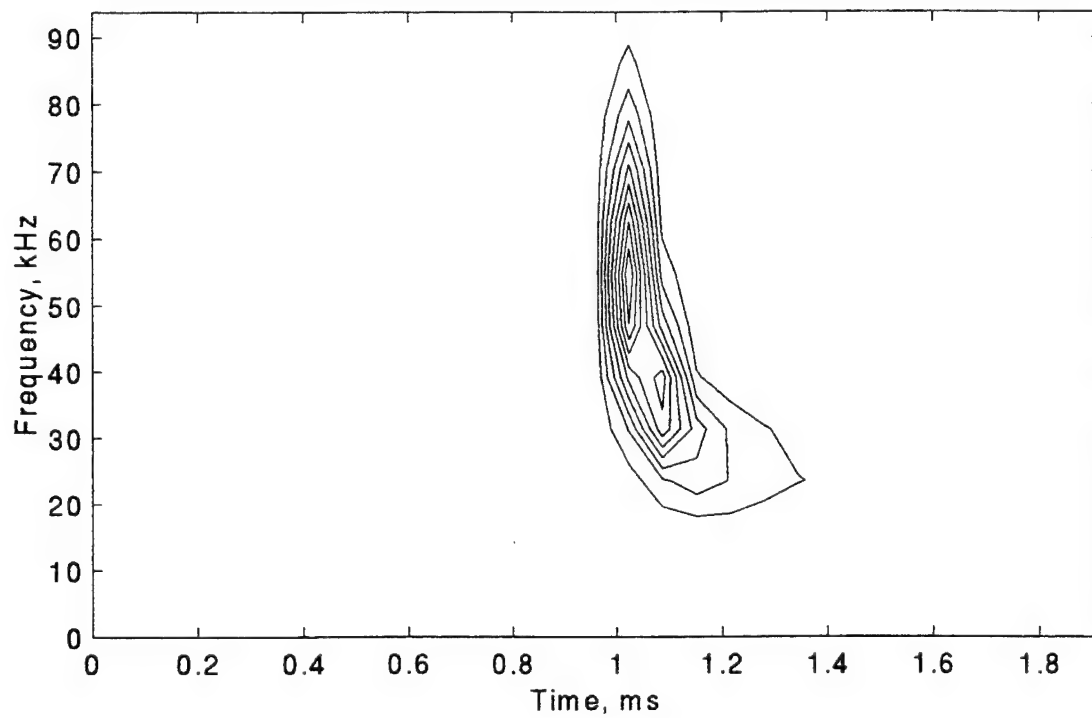


Fig. 5-22 Spectrogram contour plot of computed waveform at gage C-1



TABLES

Table 2-1

Roots of the characteristic equation for free wave propagation in a fluid tube with free-free radial boundaries, for four values of radii ratio s . Columns labeled "Root()" show the exact value of the root for the mode indicated. Columns labeled "E ()" show the error between the asymptotic estimate and the exact root, expressed as a percent of the exact root.

Mode
Number

$s = 1.5$

$s = 2$

m	Root1 _m	E1 _m	Root2 _m	E2 _m
1	6.27	0.207	3.123	0.599
2	12.56	0.053	6.273	0.156
3	18.845	0.023	9.418	0.07
4	25.129	0.013	12.561	0.039
5	31.413	0.008	15.704	0.025
6	37.697	0.006	18.846	0.018
7	43.98	0.004	21.988	0.013
8	50.264	0.003	25.13	0.01
9	56.547	0.003	28.272	0.008
10	62.831	0.002	31.414	0.006

Mode
Number

$s = 3$

$s = 5$

m	Root3 _m	E3 _m	Root4 _m	E4 _m
1	1.548	1.465	0.763	3.001
2	3.129	0.402	1.557	0.889
3	4.704	0.183	2.346	0.419
4	6.277	0.104	3.134	0.242
5	7.849	0.067	3.921	0.157
6	9.42	0.047	4.707	0.11
7	10.992	0.034	5.493	0.081
8	12.563	0.026	6.279	0.063
9	14.134	0.021	7.065	0.05
10	15.705	0.017	7.851	0.04

Table 2-2

Roots of the characteristic equation for free wave propagation in a fluid tube with free boundary at inner radius and fixed boundary at outer radius, for four values of radii ratio s .

Mode Number	$s = 1.5$		$s = 2$	
	m	Root1_m	Root2_m	$E2_m$
1	9.344	0.865	4.645	1.455
2	15.66	0.307	7.814	0.513
3	21.957	0.156	10.967	0.26
4	28.248	0.094	14.115	0.157
5	34.536	0.063	17.261	0.105
6	40.822	0.045	20.405	0.075
7	47.108	0.034	23.549	0.056
8	53.393	0.026	26.692	0.044
9	59.678	0.021	29.835	0.035
10	65.962	0.017	32.977	0.029

Mode Number	$s = 3$		$s = 5$	
	m	Root3_m	Root4_m	$E4_m$
1	2.303	2.326	1.139	3.408
2	3.895	0.819	1.939	1.275
3	5.475	0.416	2.731	0.654
4	7.051	0.251	3.52	0.397
5	8.625	0.168	4.308	0.266
6	10.198	0.12	5.095	0.191
7	11.77	0.09	5.882	0.144
8	13.342	0.07	6.668	0.112
9	14.914	0.056	7.455	0.09
10	16.486	0.046	8.241	0.073

Table 2-3

Roots of the characteristic equation for free wave propagation in a fluid tube with fixed boundary at inner radius and free boundary at outer radius, for four values of radii ratio s .

Mode
Number

$s = 1.5$

$s = 2$

m	Root1 _m	E1 _m	Root2 _m	E2 _m
1	3.401	-7.636	1.794	-12.439
2	9.52	-0.998	4.801	-1.838
3	15.766	-0.367	7.909	-0.692
4	22.033	-0.189	11.035	-0.357
5	28.307	-0.114	14.168	-0.217
6	34.584	-0.077	17.304	-0.146
7	40.863	-0.055	20.442	-0.105
8	47.143	-0.041	23.58	-0.079
9	53.424	-0.032	26.72	-0.061
10	59.706	-0.026	29.86	-0.049

Mode
Number

$s = 3$

$s = 5$

m	Root3 _m	E3 _m	Root4 _m	E4 _m
1	0.959	-18.129	0.515	-23.706
2	2.435	-3.238	1.246	-5.483
3	3.978	-1.275	2.009	-2.264
4	5.535	-0.669	2.783	-1.227
5	7.098	-0.409	3.561	-0.763
6	8.663	-0.276	4.342	-0.519
7	10.23	-0.198	5.124	-0.375
8	11.799	-0.149	5.907	-0.283
9	13.367	-0.116	6.691	-0.221
10	14.936	-0.093	7.475	-0.178

Table 2-4

Roots of the characteristic equation for free wave propagation in a fluid tube with fixed boundaries at both inner and outer radii, for four values of radii ratio s .

Mode
Number

$s = 1.5$

$s = 2$

m	Root1 _m	E1 _m	Root2 _m	E2 _m
1	6.322	-0.609	3.196	-1.693
2	12.586	-0.157	6.312	-0.46
3	18.863	-0.07	9.444	-0.208
4	25.143	-0.04	12.581	-0.118
5	31.424	-0.025	15.72	-0.076
6	37.706	-0.018	18.859	-0.053
7	43.988	-0.013	22	-0.039
8	50.27	-0.01	25.14	-0.03
9	56.553	-0.008	28.281	-0.023
10	62.836	-0.006	31.422	-0.019

Mode
Number

$s = 3$

$s = 5$

m	Root3 _m	E3 _m	Root4 _m	E4 _m
1	1.636	-3.957	0.847	-7.253
2	3.178	-1.161	1.61	-2.455
3	4.738	-0.54	2.385	-1.211
4	6.303	-0.309	3.164	-0.712
5	7.87	-0.2	3.945	-0.466
6	9.438	-0.139	4.728	-0.328
7	11.007	-0.103	5.511	-0.243
8	12.576	-0.079	6.295	-0.187
9	14.146	-0.062	7.079	-0.148
10	15.716	-0.051	7.863	-0.12

Table 5-1 Published Data on Brass

Data Source	Young's Modulus N/sq m	Density Kg/cu m	Poisson's Ratio	Long. Wavspd m/s	Plate Wavspd Cp, m/s	Thin Bar Wavspd Cb, m/s	Shear Wavspd Cs, m/s	Shear Modulus N/sq m	Bulk Modulus N/sq m	Lame Lambda N/sq m
Fahy	1.00E+11	8.50E+03	0.36	4450	3677	3430	2080	3.67E+10	1.19E+11	9.45E+10
Elmore & Heald	1.04E+11	8.53E+03	0.37	4644	3759	3492	1948	3.80E+10	1.30E+11	1.08E+11
Kinsler & Frey	1.04E+11	8.50E+03	0.37	4700	3765	3498	1948	3.80E+10	1.36E+11	1.08E+11
Metrotek, Brass	9.56E+10	8.56E+03	0.35	4280	3574	3342	2030	3.53E+10	1.10E+11	8.63E+10
Metro. Half Hard	8.85E+10	8.10E+03	0.30	3830	3463	3305	2050	3.04E+10	7.10E+10	5.07E+10
Metro. Naval Brass	1.02E+11	8.42E+03	0.35	4430	3723	3485	2120	3.78E+10	1.15E+11	8.96E+10
Cartridge Brass	1.10E+11	8.53E+03	0.37	4784	3872	3597	2173	4.03E+10	1.95E+11	1.15E+11
AVERAGE	1.01E+11	8.45E+03	0.35	4445	3690	3450	2050	3.66E+10	1.25E+11	9.31E+10
STD. DEVIATION	6.46E+09	1.48E+02	0.02	299	125	93	78	2.90E+09	3.45E+10	1.99E+10
% Deviation	6.42	1.75	6.60	6.72	3.39	2.69	3.78	7.91	27.60	21.34
Modal Tests	1.14E+11	8.52E+03	0.37	4868	3939	3660	2211	4.17E+10	2.02E+11	1.19E+11

Table 5-2

Comparison of measured and calculated modal frequencies (in Hz)

Measured modal frequencies	Modal frequencies calculated from membrane model	Modal frequencies calculated for free-free bar
$f_{\text{meas}} = \begin{bmatrix} 506.38 \\ 1014.937 \\ 1523.59 \\ 2029.92 \\ 2535.514 \\ 3042.169 \\ 3543.690 \\ 4044.796 \end{bmatrix}$	$f_{\text{model}} = \begin{bmatrix} 506.834 \\ 1013.569 \\ 1520.106 \\ 2026.346 \\ 2532.185 \\ 3037.519 \\ 3542.236 \\ 4046.225 \end{bmatrix}$	$f_{\text{nd}} = \begin{bmatrix} 506.85 \\ 1013.7 \\ 1520.55 \\ 2027.399 \\ 2534.249 \\ 3041.099 \\ 3547.949 \\ 4054.799 \end{bmatrix}$

The calculated modal frequencies were computed using an extensional wave speed of 3939 meters/second.

BIBLIOGRAPHY

- Anderson, D. V. and Barnes, C., (1953) "Pulse Dispersion in a Cylindrical Fluid Tube," Journal of the Acoustical Society of America, Volume 25, Number 3
- Beranek, Leo L., (1954) Acoustics, McGraw-Hill Book Company
- Berkowitz, H. M., (1963) "Longitudinal Impact of a Semi-Infinite Elastic Cylindrical Shell," Journal of Applied Mechanics
- Berlincourt, D., and Krueger, H. H. A., (1964) "Properties of Clevite Ceramics," Technical Paper TP-226, Clevite Corporation, Bedford, Ohio
- Biot, M. A., (1952) "Propagation of Elastic Waves in a Cylindrical Bore Containing a Fluid," Journal of Applied Physics, Vol. 23, No. 9
- Bird, J. F., Hart, R. W., and McClure, F. T., (1960) "Vibrations of Thick-walled Hollow Cylinders: Exact Numerical Solutions," Journal of the Acoustical Society of America Vol. 32, No. 11, 1404-1412
- Bracewell, Ron, (1965) The Fourier Transform and Its Applications, McGraw-Hill Book Company
- Brekhovskikh, L. M., (1960) Waves in Layered Media, Academic Press
- Brevart, B. J., and Fuller, C. R., (1994) "Radial Impulsive Excitation of Infinite Fluid-Filled Elastic Cylindrical Shells," Journal of Sound and Vibration, Volume 177, Number 3
- Claasen, T. A. C. M., and Mecklenbräuker, W. F. G., (1980) "The Wigner Distribution - A Tool for Time-Frequency Signal Analysis, Part I: Continuous - Time Signals," Philips Journal of Research, Volume 35, Number 3
- Claasen, T. A. C. M., and Mecklenbräuker, W. F. G., (1980) "The Wigner Distribution - A Tool for Time-Frequency Signal Analysis, Part II: Discrete-Time Signals," Philips Journal of Research, Volume 35, Number 4/5
- Claasen, T. A. C. M., and Mecklenbräuker, W. F. G., (1981) "Time-Frequency Signal Analysis by Means of the Wigner Distribution," Proceedings of the Institute of Electrical and Electronic Engineers International Conference on Acoustics, Speech, and Signal Processing
- Claasen, T. A. C. M., and Mecklenbräuker, W. F. G., (1983) "The Aliasing

Problem in Discrete-Time Wigner Distributions," The Institute of Electrical and Electronic Engineers International Transactions on Acoustics, Speech, and Signal Processing, Volume ASSP-31, Number 5, October

Claasen, T. A. C. M., and Mecklenbräuker, W. F. G., (1980) "The Wigner Distribution - A Tool for Time-Frequency Signal Analysis, Part III: Relations with Other Time-Frequency Signal Transformations," Philips Journal of Research, Volume 35, Number 6

Claasen, T. A. C. M., and Mecklenbräuker, W. F. G., (1984) "On the Time-Frequency Discrimination of Energy Distributions: Can They Look Sharper than Heisenberg?," Proceedings of the Institute of Electrical and Electronic Engineers International Conference on Acoustics, Speech, and Signal Processing

Cohen, Leon, (1989) "Time-Frequency Distributions - A Review," Proceedings of the Institute of Electrical and Electronic Engineers, Volume 77, Number 7

Cooper, R. M., and Naghdi, P. M., (1957) "Propagation of Nonaxially Symmetric Waves in Elastic Cylindrical Shells," Journal of the Acoustical Society of America, Vol. 29, No. 12, 1365-1371

Davies, R. M., (1948) "A Critical Study of the Hopkinson Pressure Bar," Philosophical Transactions of the Royal Society, Volume 240

Donnell, L. H., (1933) "Stability of Thin Walled Tubes Under Torsion," NACA Report Number 479

Elmore, W. C., and Heald, M. A., (1985) Physics of Waves, Dover Publications Inc.

Fahy, Frank, (1985) Sound and Structural Vibration, Academic Press

Fay, R. D., Brown, R. L., and Fortier, O. V., (1947) "Measurement of Acoustic Impedances of Surfaces in Water," Journal of the Acoustical Society of America, Vol. 19, No. 5

Folds, D. L., and Loggins, C. D., (1977) "Transmission and Reflection of Ultrasonic Waves in Layered Media," Journal of the Acoustical Society of America, Vol. 62, No. 5

Fuller, C. R., (1981) "The Effects of Wall Discontinuities on the Propagation of Flexural Waves in Cylindrical Shells," Journal of Sound and Vibration, Volume 75, Number 2

Fuller, C. R., and Fahy, F. J., (1982) "Characteristics of Wave Propagation and

Energy Distributions in Cylindrical Elastic Shells Filled with Fluid," Journal of Sound and Vibration, Vol. 81, No. 4

Fuller, C. R., (1988) "The Input Mobility of an Infinte Circular Cylindrical Elastic Shell Filled with Fluid," Journal of Sound and Vibration, Volume 87, Number 3

Gazalet, M. G., Houze, M., Logette, P., Bruneel, C., and Torguet, R., (1987) "Dummy Load Backing of Ultrasonic Transducers for Bandwidth Enhancement," Journal of the Acoustical Society of America, Vol. 83, No. 3

Gazis, D. C., (1958) "Exact Analysis of the Plane-Strain Vibrations of Thick-Walled Hollow Cylinders," Journal of the Acoustical Society of America, Vol. 30, No. 8

Gazis, D. C., (1959) "Three-Dimensional Investigation of the Propagation of Waves in Hollow Circular Cylinders. I. Analytical Foundation," Journal of the Acoustical Society of America, Vol. 31, No. 5

Gradshteyn, I. S., and Ryzhik, I. M., (1980) Table of Integrals, Series, and Products, Academic Press

Greenspon, J. E., (1958) "Flexural Vibrations of a Thick Walled Circular Cylinder," Proceedings of the Third U. S. National Congress of Applied Mechanics

Greenspon, J. E., (1960) "Axially Symmetric Vibrations of a Thick Cylindrical Shell in an Acoustic Medium," Journal of the Acoustical Society of America, Vol. 32, No. 8

Greenspon, J. E., (1960) "Flexural Vibrations of a Thick-Walled Circular Cylinder According to the Exact Theory of Elasticity,," Journal of the Aero/Space Sciences

Herrmann, G., and Mirsky, I., (1956) "Three-Dimensional and Shell-Theory Analysis of Axially Symmetric Motions of Cylinders," Journal of Applied Mechanics, Vol. 23

Hildebrand, Francis B., (1962) Advanced Calculus for Applications, Prentice-Hall, Inc.

Hoyt, S. L., (editor), (1954) Metals Properties, American Society of Mechanical Engineers Handbook, McGraw-Hill Book Company

Hughes, William F., and Gaylord, Eber W., (1964) Basic Equations of Engineering Science, McGraw-Hill Book Company

IEEE (1984) "IEEE Standard on Piezoelectricity," The Institute of Electrical and Electronics Engineers Transactions on Sonics and Ultrasonics, Volume SU-31, Number 2

Jackson, Leland B., (1991) Signals, Systems, and Transforms, Addison-Wesley Publishing Company

Jackson, Leland B., (1986) Digital Filters and Signal Processing, Kluwer, Academic Publishers

Jacobi, W. J., (1949) "Propagation of Sound Waves Along Liquid Cylinders," Journal of the Acoustical Society of America, Vol. 21, No. 2

Janse, Cornelis P., and Kaizer, J. M., (1983) "Time-Frequency Distributions of Loudspeakers: The Application of the Wigner Distribution," Journal of the Audio Engineering Society, Volume 31, Number 4

Junger, M. C., (1952) "Radiation Loading of Cylindrical and Spherical Surfaces," Journal of the Acoustical Society of America, Vol. 24, No. 3

Junger, M. C., (1953) "The Physical Interpretation of the Expression for an Outgoing Wave in Cylindrical Coordinates," Journal of the Acoustical Society of America, Vol. 25, No. 1

Junger, M. C., and Feit, D., (1986) Sound, Structures, and Their Interactions, Second Edition, the M. I. T. Press

Kinsler, Lawrence E., Frey, Austin R., Coppens, Alan B., and Sanders, James V., (1982) Fundamentals of Acoustics, Third Edition, John Wiley and Sons, Inc.

Kraus, Harry, (1967) Thin Elastic Shells, John Wiley and Sons, Inc.

Kumar, R., (1966) "Axially Symmetric Vibrations of a Thin Cylindrical Elastic Shell Filled with Non-viscous Fluid," Acustica, Vol. 17

Lamont, H. R. L., (1950) Wave Guides, John Wiley and Sons, Inc.

Leissa, A. W., (1973) Vibrations of Shells, NASA SP-288, National Aeronautics and Space Administration

Lin, T. C., and Morgan, G. W., (1956) "A Study of Axisymmetric Vibrations of Cylindrical Shells as Affected by Rotatory Inertia and Transverse Shear," Journal of Applied Mechanics, Vol. 23, No. 10

Lin, T. C., and Morgan, G. W., (1956) "Wave Propagation Through Fluid

Contained in a Cylindrical Elastic Shell," Journal of the Acoustical Society of America, Vol. 28, No. 6

Love, A. E. H., (1888) "On the Small Free Vibrations and Deformations of Thin Elastic Shells," Philosophical Transactions of the Royal Society (London), Vol. 179A

Love, A. E. H., (1944) A Treatise on the Mathematical Theory of Elasticity, Fourth Edition, Dover Publications

Mason, Warren P. (Editor), (1964) Physical Acoustics, Volume I, Part A, Academic Press

Meitzler, Allen H., O'Bryan, Henry M. Jr., and Thiersten, Harry F., (1973) "Definition and Measurement of Radial Mode Coupling Factors in Piezoelectric Ceramic Materials with Large Variations in Poisson's Ratio," Institute of Electrical and Electronic Engineers Transactions on Sonics and Ultrasonics, Volume SU-20, Number 3

Merkulov, V. N., Prihod'ko, V. U., and Tyutekin, V. V., (1978) "Excitation and Propagation of Normal Modes in a Thin Cylindrical Elastic Shell Filled with Fluid," Soviet Physics - Acoustics, Vol. 24, No. 5

Metrotek, Inc. (1982) "Tables of Ultrasonic Properties," Metrotek Application Note AN 23, Box 8500, Richland, WA

Mirsky, I., and Herrmann, G., (1957) "Nonaxially Symmetric Motions of Cylindrical Shells," Journal of the Acoustical Society of America, Vol. 29, No. 10

Morse, P. M., (1948) Vibration and Sound, McGraw-Hill

Morse, P. M., and Ingard, K. U., (1968) Theoretical Acoustics, McGraw-Hill

Naghdi, P. M., and Cooper, R. M., (1956) "Propagation of Elastic Waves in Cylindrical Shells, Including the Effects of Transverse Shear and Rotatory Inertia," Journal of the Acoustical Society of America, Vol. 28, No. 1

Nyquist, H., (1928) "Certain Topics in Telegraph Transmission Theory," Transactions of the American Institute of Electrical Engineers

Oberg, E. and Jones, F. D., (1959) Machinery's Handbook, 16th edition, The Industrial Press

Onoe, Morio, (1958) Tables of Modified Quotients of Bessel Functions of the First Kind for Real and Imaginary Arguments, Columbia University Press, New York

Onoe, Morio, (1956) "Contour Vibrations of Isotropic Circular Plates," Journal of the Acoustical Society of America, Volume 28, Number 6

Oppenheim, Alan V., and Schafer, Ronald W., (1989) Discrete-Time Signal Processing, Prentice Hall

Papoulis, Athanasios, (1977) Signal Analysis, McGraw Hill Book Company

Pathak, Ardhendu G., (1993) "Acoustic Harmonic Radiation and Scattering from Fluid-Loaded Plates and Shells with Impedance Discontinuities," doctoral dissertation submitted to the University of Rhode Island

Photiadis, Douglas M., (1990) "Waves in Fluid-Loaded Cylindrical Shells," Journal of the Acoustical Society of America, Volume 88, Number 1

Proud, J. M., Tamarkin, P., and Kornhauser, E. T., (1956) "Dispersion in Rectangular Fluid Waveguides," Journal of the Acoustical Society of America, Volume 28, Number 1

Rao, Preeti, Taylor, Fred, and Harrison, Gregory, (1990) "Real-Time Monitoring of Vibration Using the Wigner Distribution," Sound and Vibration

Redwood, Martin, (1960) Mechanical Waveguides, Pergamon Press

Rossano, Graham W., Shin, Y. S., and Hamilton, J., (1990) "A Method for Machinery Condition Monitoring of Transient Phenomena Using the Pseudo Wigner-Ville Distribution," MS Thesis, Naval Postgraduate School

Rschewkin, S. N., (1963) A Course of Lectures on the Theory of Sound, (translated by O. M. Blunn), The Macmillan Company

Sharma, Roshan Lal, (1956) "Equivalent Circuit of a Resonant, Finite, Isotropic Elastic Circular Disk," Journal of the Acoustical Society of America, Volume 28, Number 6

Shaw, R. P., and Bugl, P., (1969) "Transmission of Plane Waves Through Layered Linear Viscoelastic Media," Journal of the Acoustical Society of America, Vol. 46, No. 3

Skalak, R., (1956) "An Extension of the Theory of Water Hammer," Transactions of the American Society of Mechanical Engineers

Skalak, R., (1957) "Longitudinal Impact of a Semi-Infinite Circular Elastic Bar," American Society of Mechanical Engineers Journal of Applied Mechanics

Skolnik, M. I., (1980) Introduction to Radar Systems, McGraw-Hill Book Company

Soedel, W., (1981) Vibrations of Shells and Plates, Marcel Dekker, Inc.

Spiegel, Murray R., (1971) Advanced Mathematics, McGraw-Hill Book Company

Spiegel, Murray R., (1968) Mathematical Handbook, McGraw-Hill Book Company

Stepanishen, P. R., (1978) "Radiated Power and Radiation Loading of Cylindrical Surfaces with Nonuniform Velocity Distributions," Journal of the Acoustical Society of America, Vol. 63, No. 2

Stepanishen, P. R., and Strozeski, B., (1982) "Reflection and Transmission of Acoustic Wideband Plane Waves by Layered Viscoelastic Media," Journal of the Acoustical Society of America, Vol. 71, No. 1

Stepanishen, P. R., and Chen, H. W., (1984) "Nearfield Pressures and Surface Intensity for Cylindrical Vibrators," Journal of the Acoustical Society of America, Vol. 76, No. 3

Stepanishen, Peter R., (1985) "Wave-Vector-Frequency Filtering Characteristics of Multilayer Plate Systems vis Two-Port Methods," Journal of the Acoustical Society of America, Supplement 1, Volume 78

Stepanishen, P. R., (1982) "Modal Coupling in the Vibration of Fluid-Loaded Cylindrical Shells," Journal of the Acoustical Society of America, Volume 71, Number 4

Strum, Robert D., and Kirk, Donald E., (1995) Contemporary Linear Systems, PWS Publishing Company

Thomson, W. T., (1950) "Transmission of Elastic Waves Through a Stratified Solid Medium," Journal of Applied Physics, Vol. 21

Thomson, W. T., (1953) "Transmission of Pressure Waves in Liquid Filled Tubes," Proceedings of the First U. S. National Congress on Applied Mechanics, Chicago

Ujihashi, S., Matsumoto, H., Nakahara, I., and Shigeta, M., (1987) "Axisymmetrical Impulsive Responses of an Infinite Circular Cylindrical Shell Filled with Liquid," Japanese Society of Mechanical Engineers International Journal, Volume 30, Number 262

Vernitron Piezoelectric Division, (1984) "Modern Piezoelectric Ceramics," Bedford, Ohio

Vogelsong, Richard D., (1988) "Nearfield Acoustic Radiation from a Point-Excited Cylindrical Shell," doctoral dissertation submitted to Pennsylvania State University

White, P. H., and Sawley, R. J., (1972) "Energy Transmission in Piping Systems and Its Relation to Noise Control," Transactions of the American Society of Mechanical Engineers

Yen, N., (1987) "Time and Frequency Representations of Acoustic Signals by Means of the Wigner Distribution Function: Implementation and Interpretation," Journal of the Acoustical Society of America, Volume 81, Number 6

INITIAL DISTRIBUTION LIST

Addressee	No. of Copies
Defense Technical Information Center	12
Advanced Research Projects Agency	2
Office of Naval Research	3
Naval Undersea Warfare Center, Orlando Detachment (J. E. Blue)	1
Naval Surface Warfare Center, Carderock Division (D. Feit)	1
Naval Research Laboratory (D. M. Photiadis)	1
Aegis Program Office, PMS 400R (R. P. Radlinski)	1
Office of Naval Research (R. D. Vogelsong, ONR 334)	1
H. K. Farr	1
W. A. Von Winkle	1